Cluster Multi-Spacecraft Observations of Flux Transfer Events

Robert Charles Fear

Mullard Space Science Laboratory
Department of Space and Climate Physics
University College London

A thesis submitted to the University of London
for the degree of Doctor of Philosophy

April 2006

I, Robert Charles Fear, confirm that the work presented in this thesis is my own. Where information has been derived from other sources, I confirm that this has been indicated in the thesis.

Abstract

This thesis presents observations of flux transfer events (FTEs) from the four-spacecraft Cluster mission. FTEs are a signature of transient, or variable rate, magnetic reconnection at the Earth's magnetopause causing a bipolar variation in the component of the magnetic field normal to the magnetopause (B_N). The presence of four spacecraft allows the velocities of FTEs observed by all four spacecraft to be determined to much greater accuracy than previously possible.

Three studies are presented. First, a crossing from the high-latitude dayside magnetosphere into the magnetosheath is studied. A series of bursts of field-aligned magnetosheath-energy plasma were observed in the magnetosphere, but no bipolar B_N signature was present. When the Cluster quartet straddled the magnetopause, traditional bipolar FTE signatures were observed in the magnetosheath, demonstrating that the magnetospheric signatures were unorthodox FTEs.

The remainder of the thesis contains a survey of FTEs observed by Cluster in 2002/3. Many FTEs were found which occurred under strongly northward IMF, the majority of which occurred on three particular magnetopause crossings. The observed velocities are compared with a model of reconnected flux tube motion. The velocities are consistent with a reconnection line which originates at high latitudes, in a region of high magnetic shear. However, the strict antiparallel reconnection hypothesis does not explain all of the observed velocities; a component reconnection line must extend to regions of lower shear.

Finally, the velocities of 81 FTEs observed under southward or dawn/dusk-dominated IMF conditions are examined. The observed velocities are generally explained well by the Cooling *et al.* (2001) model. In a small number of cases it is possible to distinguish, within the constraints of the model, between some events which were only consistent with component reconnection, and others which were solely consistent with an antiparallel reconnection site.

Acknowledgements

I am grateful to various people for their help and support over the last three to twenty-six years.

Thanks to my parents for encouraging me down this path, and not once telling me to get a proper job. There are consequences to letting your children watch *The Clangers*. Thanks to Charlotte, too, for her support (and tolerance), particularly over the last three years.

On the academic side, I'd like to thank Dr. Andrew Fazakerley and Dr. Chris Owen, my principal and secondary supervisors, for their advice over the course of my Ph.D.. I'm grateful to my office mates, past and present (Rob Wilson, Jason Dewhurst, Yulia Bogdanova, Aurélie Marchaudon and Hazel McAndrews), for being prepared to answer the odd stupid question, and to others in the Space Plasma Physics Group for valuable conversations and advice.

Like everyone working with PEACE data, I owe a lot to the PEACE operations team, for their frequently-requested and invaluable assistance. Without data, this thesis would be considerably shorter. I am therefore similarly grateful to the other instrument teams who provided data.

Finally, I'd like to thank the Particle Physics and Astronomy Research Council (PPARC) for their financial support over the last three years.

Contents

List of Figures

List of Tables

Chapter 1

Introduction

> This year, after Christmas, on a Monday night, at the first sleep, was the heaven on the northern hemisphere all as if it were burning fire; so that all who saw it were so dismayed as they never were before.
> *Record of an auroral sighting in the Anglo Saxon Chronicle, 1131 A.D.*

1.1 Historical Background and Overview

Phenomena of space plasma physics have been observed for millennia. The term '*aurora*[1] *borealis*[2]' (northern lights, or more literally 'dawn of the north') is believed to have been introduced by Galileo Galilei, who thought that the aurora was caused by illumination of air outside the Earth's shadow. However, the earliest known observations were recorded in ancient China, around 2000 B.C.. Unsurprisingly, auroral observations and folklore were common in Scandinavian cultures, such as the Norwegian chronicle *Konungs skuggsjá*[3] in 1250 A.D., but they were also observed on occasion at lower latitudes; a sighting in England was recorded in the Anglo Saxon Chronicle of 1131.

In 1773, Captain Cook and the crew aboard HMS Resolution became the first to observe the southern hemisphere equivalent, the *aurora australis*[4] or southern lights, on what is believed to be the first voyage to cross the Antarctic Circle.

A London instrument maker, George Graham, was the first to observe that a compass needle is constantly in motion, which is now known to be a response to

[1] Latin: *aurora*, meaning 'dawn', from the name of the Roman goddess of dawn
[2] Latin: *borealis*, from *boreas*, the north wind named after the Greek god *Boreas*
[3] Old Norse: *King's mirror*
[4] Latin: *australis*, from *Auster*, the Roman god of the south wind

variations in current systems in the upper atmosphere. Later observations by Hiorter in Sweden revealed a regular daily (diurnal) variation in the direction in which the needle points, as the Earth rotates beneath the current systems. Hiorter was also the first to note the correlation between magnetic variations and auroral activity, in 1741.

Both of these processes arise as a result of the interaction between the solar wind, a plasma ejected by the Sun which flows throughout the Solar System, and the magnetosphere, which is the Earth's magnetic field and natural plasma environment. The major interaction process between the solar wind and magnetosphere is magnetic reconnection, which occurs at the dayside boundary between the two regions (the magnetopause). When magnetopause reconnection occurs at a variable rate, it gives rise to data signatures called 'flux transfer events' (FTEs), which can be observed by spacecraft near the magnetopause and which form the subject of this thesis.

In this chapter, an overview of basic plasma physics concepts of relevance to the thesis is given, followed by an introduction to reconnection, a brief tour of solar system plasmas, an overview of magnetopause reconnection and the magnetospheric convection cycle and a summary of previous FTE observations.

1.2 Plasma Physics Concepts

1.2.1 Definition

> A plasma is a quasi-neutral gas of charged (and possibly neutral) particles which exhibit collective behaviour (Chen, 1974, p. 3).

A plasma is *quasi-neutral* as small scale concentrations of net charge may exist. However, such concentrations are transient as regions of like charges are dispersed by electrostatic repulsion. When the plasma is in steady state it appears neutral on a large scale, as the electrical charges of the constituent charged particles (ions and electrons) cancel.

Each charged particle generates an electric and, if in motion, magnetic field. If many particles are concentrated or move in an organised manner, the fields of the individual particles may be combined, resulting in strong overall electromagnetic fields. Other particles are subjected to these electromagnetic fields, leading to *collective behaviour*. For a particle to be significantly affected by these large-scale

electromagnetic fields, it must be free from the influence of its neighbours; in other words it must be a *free particle*. A particle is free if its potential energy due to its nearest neighbour is much smaller than its thermal energy. To avoid any influence by other particles, it must also avoid direct collisions.

Hence there are three specific conditions that must be met: the plasma must appear neutral on a large scale, consist of free charged particles and the particles must be collisionless on the timescale of collective processes. These conditions will briefly be examined further.

1.2.1.1 Quasi-neutrality and Debye Shielding

An individual charged particle with charge q has an electric Coulomb potential field ϕ_c:

$$\phi_c(r) = \frac{q}{4\pi\varepsilon_0 r} \tag{1.1}$$

where ε_0 is the permittivity of free space. If this charge is placed in a plasma, it attracts oppositely charged particles, and repels like-charges, to restore quasi-neutrality on the larger scale. This process is a collective effect, and is known as Debye shielding. The net (Debye) potential (ϕ_D) takes the form:

$$\phi_D(r) = \phi_{D0} \exp\left(\frac{r}{\lambda_D}\right) \tag{1.2}$$

where:

$$\lambda_D = \sqrt{\frac{\varepsilon_0 k_B T_e}{n_0 e^2}} \tag{1.3}$$

and k_B is the Boltzmann constant, T_e is the electron temperature, n_0 is the unperturbed electron density and e is the electronic charge (Baumjohann and Treumann, 1997, pp. 2, 206; Kivelson and Russell, 1995, p. 39). λ_D is called the Debye length; it is the scale size on which Debye shielding occurs, and hence the scale size on which charge fluctuations are removed. For a plasma to be quasi-neutral, the scale size of the plasma, L, must be large compared with the Debye length. Hence the first plasma criterion may be expressed as:

$$L \gg \lambda_D \tag{1.4}$$

1.2.1.2 Free Particles and the Plasma Parameter

For Debye shielding to occur, there must be a significant number of particles within a sphere of radius λ_D (a Debye sphere). Since the number of particles in a Debye sphere is

$$N_D = \frac{4\pi}{3} n_e \lambda_D^3 \tag{1.5}$$

N_D is referred to as the plasma parameter, and another criterion may be written:

$$N_D = \frac{4\pi}{3} n_e \lambda_D^3 \gg 1 \tag{1.6}$$

This can be shown to be equivalent to the free particle criterion; the thermal energy of the particles must be greater than the potential energy due to other particles (Baumjohann and Treumann, 1997, p. 3):

$$k_B T_e \gg \frac{e^2}{4\pi\varepsilon_0 r} \tag{1.7}$$

1.2.1.3 Collisions and the Plasma Frequency

The typical oscillation frequency of a plasma is the *electron plasma frequency*, ω_{pe}. If an external force disturbs the quasi-neutrality of a plasma, the electrons will be accelerated back by the resulting electric field, but will then oscillate about the ions (which can be assumed to be stationary) at this frequency (Baumjohann and Treumann, 1997, pp. 4, 201; Kivelson and Russell, 1995, p. 40):

$$\omega_{pe}^2 = \frac{n_e e^2}{m_e \varepsilon_0} \tag{1.8}$$

For the collision criterion to be fulfilled, the timescale of particle collisions (τ_c) must be much greater than the timescale of the collective behaviour processes (such as plasma oscillation):

$$\omega_{pe} \tau_c \gg 1 \tag{1.9}$$

1.2.2 Single Particle Motion

There are several different theoretical approaches to describing plasma processes. The first is the single particle approach; here it is assumed that individual charged

particles do not affect the external magnetic field significantly (i.e. the external field is strong), and collective effects are regarded as negligible.

The particles are subject to the Coulomb and Lorentz forces which act upon them:

$$\boldsymbol{F} = q(\boldsymbol{E} + \boldsymbol{v} \times \boldsymbol{B}) \tag{1.10}$$

and the electric and magnetic fields $\boldsymbol{E}$ and $\boldsymbol{B}$ are governed by Maxwell's laws (Maxwell, 1891):

$$\text{Gauss's Law} \qquad \nabla \cdot \boldsymbol{E} = \frac{\rho}{\varepsilon_0} \tag{1.11}$$

$$\text{Faraday's Law} \qquad \nabla \times \boldsymbol{E} = -\frac{\partial \boldsymbol{B}}{\partial t} \tag{1.12}$$

$$\nabla \cdot \boldsymbol{B} = 0 \tag{1.13}$$

$$\text{Ampère's Law} \qquad \nabla \times \boldsymbol{B} = \mu_0 \boldsymbol{J} + \varepsilon_0 \mu_0 \frac{\partial \boldsymbol{E}}{\partial t} \tag{1.14}$$

where $\boldsymbol{J}$ is the current density, ρ is the charge density, ε_0 is the permittivity of free space and μ_0 is the permeability of free space.

1.2.2.1 Particle Gyration and Drifts

Combining Equation 1.10 with Newton's second law, the equation of motion of a charged particle in electromagnetic fields is:

$$m\frac{d\boldsymbol{v}}{dt} = q(\boldsymbol{E} + \boldsymbol{v} \times \boldsymbol{B}) \tag{1.15}$$

If there is a magnetic, but no electric field, then a charged particle is accelerated perpendicular to $\boldsymbol{v}$ and $\boldsymbol{B}$, and there is no increase in the kinetic energy of the particle. The result is a gyration of the particle about the magnetic field line with a gyrofrequency, or cyclotron frequency of ω_g (Baumjohann and Treumann, 1997, p. 13; Kivelson and Russell, 1995, p. 29):

$$\omega_g = \frac{q|\boldsymbol{B}|}{m} \tag{1.16}$$

and the electron is bound to a magnetic field line. If the particle has a velocity component along the magnetic field ($v_\parallel$), then this component remains constant and the particle's path describes a helix. The centre of the orbit (which follows the axis of the helix) is known as the guiding centre. The angle between the velocity

vector and the magnetic field is the pitch angle, α:

$$\alpha = \arctan\left(\frac{v_\perp}{v_\parallel}\right) \tag{1.17}$$

The presence of an electric field parallel to the magnetic field leads to a straightforward acceleration along $\boldsymbol{B}$. However, in a plasma such a field is likely to be cancelled quickly by the mobile electrons. The presence of a perpendicular electric field, or gradients/time variations in the electromagnetic fields, leads to drift motion relative to the helical orbit of the particles.

1.2.2.2 The Magnetic Moment and Magnetic Mirrors

The magnetic moment of a particle, μ, is defined as the ratio between its perpendicular kinetic energy and the magnetic field (Baumjohann and Treumann, 1997, p. 20; Kivelson and Russell, 1995, p. 33):

$$\mu = \frac{mv_\perp^2}{2B} = \frac{mv^2 \sin^2 \alpha}{2B} \tag{1.18}$$

μ is an adiabatic invariant: it remains constant if the electromagnetic fields do not vary rapidly. In the absence of an electric field, the kinetic energy of the particle (and hence v) is also constant. Hence the pitch angles, α, of a particle which moves between two regions with different magnetic field strengths are related by:

$$\frac{\sin^2 \alpha_1}{\sin^2 \alpha_2} = \frac{B_1}{B_2} \tag{1.19}$$

Thus the pitch angle increases as the magnetic field strength increases; at a critical value called the mirror point, the pitch angle reaches 90° and the particle is reflected and travels in the opposite direction along $\boldsymbol{B}$.

1.2.3 Kinetic Theory

A second approach to describing plasma behaviour is to consider the whole system, but take a similar statistical approach to that used when studying gas behaviour. An individual particle can be described by its position $\boldsymbol{x}$ and velocity $\boldsymbol{v}$ at time t. The six-dimensional space ($\boldsymbol{x}$,$\boldsymbol{v}$) is called *phase space*; a plasma distribution can be described by the *phase space density* $f(\boldsymbol{x}, \boldsymbol{v}, t)$, and macroscopic parameters (e.g. density, velocity, pressure) are derived by taking moments of this distribution.

This is of particular interest in deriving physical parameters from the plasma distribution observed by an electron or ion spectrometer, and is discussed in Chapter 2.

1.2.4 Magnetohydrodynamics (MHD)

The third major approach is to treat the plasma as a fluid. The MHD approximation is valid for long timescales and length scales compared with the gyrofrequency and gyrolength. Maxwell's equations are combined with the hydrodynamic continuity equation:

$$\frac{\partial n}{\partial t} + \nabla \cdot (n\boldsymbol{v}) = 0 \tag{1.20}$$

and the equation of motion:

$$\frac{\partial (n\boldsymbol{v})}{\partial t} + \nabla \cdot (n\boldsymbol{v}\boldsymbol{v}) = -\frac{1}{m}\nabla \cdot \mathbf{P} + \frac{nq}{m}(\boldsymbol{E} + \boldsymbol{v} \times \boldsymbol{B}) + \frac{\boldsymbol{R}}{m} \tag{1.21}$$

where the forces on the right-hand side are those due to a pressure gradient, electromagnetic fields and collisions respectively. Here, n is the plasma density, $\boldsymbol{v}$ is the bulk flow velocity, m is the particle mass, $\mathbf{P}$ is the pressure tensor, q the charge and $\boldsymbol{R}$ is a collisional term.

Combining the equations of motion for electrons and ions (neglecting, for small current densities, the quadratic terms in velocity) leads to the Generalised Ohm's Law:

$$\boldsymbol{E} + \boldsymbol{v} \times \boldsymbol{B} = \eta \boldsymbol{j} - \frac{1}{ne}\nabla \cdot \mathbf{P}_e + \frac{m_e}{ne^2}\frac{\partial \boldsymbol{j}}{\partial t} + \frac{1}{ne}\boldsymbol{j} \times \boldsymbol{B} \tag{1.22}$$

where $\boldsymbol{j}$ is the current density and η is the resistivity (Baumjohann and Treumann, 1997, pp. 139-142; Kivelson and Russell, 1995, p. 41-48)

In the case of ideal MHD, the plasma is assumed to conduct ideally ($\eta = 0$), there is no electron pressure gradient, and the current density is assumed to vary only slowly with time. Then the Generalised Ohm's Law simplifies to:

$$\boldsymbol{E} = -\boldsymbol{v} \times \boldsymbol{B} \tag{1.23}$$

The electric field cannot have a component parallel to the magnetic field, and there is no electric field in the rest-frame of the plasma. Furthermore, the magnetic flux through a surface S (which lies perpendicular to $\boldsymbol{B}$) remains constant, even if S changes shape or location. This is the 'frozen-in-flow' assumption.

If, however, the conductivity is finite, then:

$$\boldsymbol{E} + \boldsymbol{v} \times \boldsymbol{B} = \eta \boldsymbol{j} \tag{1.24}$$

and diffusion may occur. Hence a plasma with finite resistivity, which contains regions of concentrated/reduced magnetic field strength, will tend towards a state where the flux is evenly distributed.

1.2.4.1 Magnetic Pressure and Tension

If we take Ampère's law and assume that time variations are slow, then:

$$\boldsymbol{j} \times \boldsymbol{B} = \frac{1}{\mu_0}(\nabla \times \boldsymbol{B}) \times \boldsymbol{B} \tag{1.25}$$

$$= -\nabla\left(\frac{B^2}{2\mu_0}\right) + \frac{1}{\mu_0}(\boldsymbol{B} \cdot \nabla)\boldsymbol{B} \tag{1.26}$$

The last term in Equation 1.26 can be split into components parallel and perpendicular to the magnetic field:

$$\boldsymbol{j} \times \boldsymbol{B} = -\nabla\left(\frac{B^2}{2\mu_0}\right) - \hat{\boldsymbol{n}}\frac{B^2}{\mu_0}\frac{1}{R_c} + \nabla_{\parallel}\left(\frac{B^2}{2\mu_0}\right) \tag{1.27}$$

$$= -\nabla_{\perp}\left(\frac{B^2}{2\mu_0}\right) - \hat{\boldsymbol{n}}\frac{B^2}{\mu_0}\frac{1}{R_c} \tag{1.28}$$

where R_c is the radius of curvature of the magnetic field (Baumjohann and Treumann, 1997, p. 144; Kivelson and Russell, 1995, p. 50). When Equation 1.28 is substituted into Equation 1.21, the first term on the right-hand side corresponds to a pressure term, which is referred to as the magnetic pressure and which acts perpendicular to the magnetic field:

$$p_B = \frac{B^2}{2\mu_0} \tag{1.29}$$

The total pressure of a plasma is the sum of the thermal, dynamic and magnetic pressures ($p_{total} = nkT + nmv^2 + \frac{B^2}{2\mu_0}$). The 'plasma beta' is defined as the ratio of magnetic pressure to the plasma pressure:

$$\beta = \frac{p_{gas}}{B^2/(2\mu_0)} \tag{1.30}$$

In a high-beta (hot) plasma, the gas pressure dominates, whereas in a low-beta (cool) plasma the magnetic pressure has a larger effect.

The last term in Equation 1.28 corresponds to a 'magnetic tension' or 'curvature' force, which acts to straighten kinked magnetic field lines.

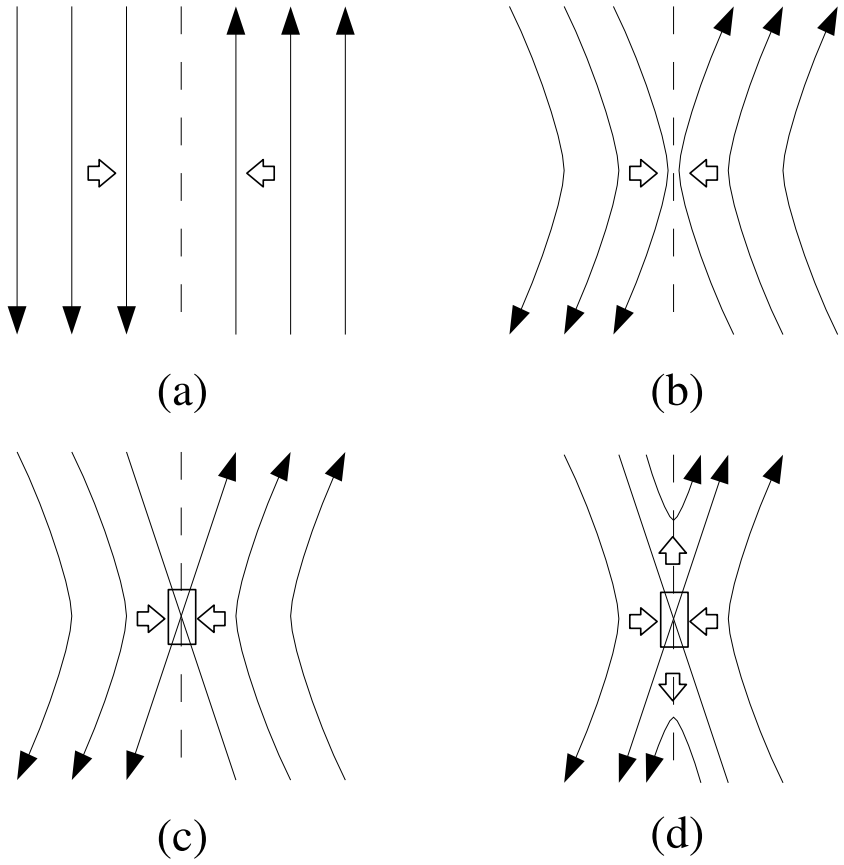

Figure 1.1: The reconnection process. (a) A current sheet (dotted line) forms at the interface between two regions with different magnetic field strengths and/or directions. (b) If the two plasma regions are compressed at some point on the current sheet, an 'X'-type configuration of the magnetic fields is formed (the X-point). (c) If the density of the plasmas in this compression region is high enough, the resistivity may be increased to a level sufficient to break the frozen-in-flow assumption. This region is known as the diffusion region (marked by a box). (d) If diffusion occurs, the magnetic field lines may realign to form two oppositely directed field lines which cross the current sheet (reconnection). These field lines are highly kinked, and are thus pulled away from the X-point at the Alfvén speed (the kink is an Alfvén wave) by the $\boldsymbol{j} \times \boldsymbol{B}$ forces (outflow). The reconnected field lines are replaced by other, unreconnected field lines (inflow).

1.2.5 Magnetic Reconnection

At an interface between two highly conductive plasmas with different magnetic field orientations, the two particle populations are initially prevented from mixing by being frozen to their respective magnetic field lines whilst the MHD approximation remains valid. The two regions will be separated by a current sheet as a consequence of Ampère's law (shown in Figure 1.1a). However, if the magnetic fields are oppositely directed, and if external forces push the plasma and magnetic field lines on either side of the current sheet closer together (Figure 1.1b), a region of enhanced resistivity may develop due to anomalous collisions. In this case, the frozen-in-flow assumption breaks down and diffusion of the magnetic field may occur (the diffusion region). This results in the situation shown in Figure 1.1c, where there is an 'X'-

type configuration of the magnetic fields. At the central point (the neutral point or X-point), the magnetic field strength is zero. Here, the magnetic field lines may become re-orientated, generating two highly-kinked field lines which cross the current sheet. The $\boldsymbol{j} \times \boldsymbol{B}$ forces then act to straighten the newly oriented lines, ejecting them from the diffusion region (Figure 1.1d). This process is called reconnection (or merging) (Sweet, 1958; Dungey, 1961; Parker, 1963; Petschek, 1964; Vasyliunas, 1975; Hill, 1975; Cowley, 1976).

Once the kinked part of the ejected field line has left the diffusion region the frozen-in-flow assumption once again applies to the field line, but now plasma is free to move along the field line across the current sheet. Hence the reconnection process is capable of transferring mass and energy (and therefore momentum) across the current sheet which initially separated the two regions. The reconnection process also accelerates plasma; the plasma speed in the outflow region is increased relative to the inflow region by the Alfvén speed. Extending the simple 2D cartoon in Figure 1.1 to three dimensions, the X-point becomes an X-line (or reconnection line). The boundary separating the field lines which have undergone reconnection from those which have not is referred to as the separatrix.

1.3 Solar System Plasmas

As will be discussed later, reconnection is the major source of energy and momentum exchange between the plasma ejected by the Sun and that locked within the Earth's magnetic field region. First, an overview of the different plasma domains in the Solar System is given.

1.3.1 The Solar Wind

The solar wind is a supersonic plasma emitted by the Sun. Birkeland (1909) first postulated that bursts of negatively charged particles from the Sun could penetrate the Earth's atmosphere, causing the northern lights, although he later concluded that positively charged particles were also emitted in order for the Sun to remain electrically neutral (Birkeland, 1916). Calculations of the properties of the solar corona by Chapman (1957) led to the conclusion that the corona must be carried further out into space than the orbit of Earth. Furthermore, the hypothesized presence of a gaseous/ionised flow through the solar system was used by Biermann (1951) to explain the presence and motion of a second 'plasma' tail frequently possessed by comets.

Parker (1958) demonstrated that a continuous outflow of plasma was possible, and coined the name 'solar wind'. The first direct spacecraft observations of the solar wind were made by Gringauz *et al.* (1960) on Lunik 2 and 3. Typical electron temperatures and densities are now known to be of order 10^5 K and 5 cm^{-3} respectively (Baumjohann and Treumann, 1997, p5). The plasma consists mainly of protons and electrons, but contains low levels of helium ions ($\sim$5%) and trace amounts of heavier ions. The solar wind flow consists of 'slow' and 'fast' streams, with velocities of order 300–450 kms^{-1} and 600–900 kms^{-1} respectively (Phillips *et al.*, 1995). The flow is directed radially outward from the Sun, but the orbital motion of the Earth causes an aberration of $\sim5^\circ$ in a terrestrial frame of reference.

Parker (1958) also showed that the solar wind speed increases with radial distance from the Sun, becoming supersonic before reaching the orbit of Mercury. The generation mechanism of the solar wind is unclear; however since the solar photosphere has a comparatively low temperature of $\sim$6000 K, it is likely that the solar wind is accelerated in the solar corona, which is a relatively hot region with temperatures and densities of order 1.6×10^6 K and 5×10^{17} cm^{-3} respectively. However, the reason for the observed high coronal temperatures, and hence the temperature of the solar wind, also remains unclear.

As the solar wind plasma is highly conductive, a magnetic field of solar origin is frozen into the solar wind (see Section 1.2.4). This magnetic field is called the interplanetary magnetic field (IMF), and has a typical magnitude of 5–10 nT at 1 Astronomical Unit (AU) from the Sun. As the Sun rotates whilst the solar wind propagates radially outwards and the feet of the field lines remain frozen into the photosphere/corona plasma, the IMF is formed into a 'Parker' spiral (Figure 1.2). Hence there is an angle between the IMF and a radial vector from the Sun which is typically $\sim45^\circ$ at 1 AU.

When the solar magnetic field is in its simplest orientation (during periods of minimum activity in the 11-year solar activity cycle), the radial component of the field lines in the magnetic northern hemisphere is directed outwards. At the minimum activity period of one solar cycle, the magnetic field is directed inwards in the magnetic southern hemisphere; the radial direction is then reversed in the next cycle. This hemispheric division extends into the solar wind; consequently there is a current sheet near the solar magnetic equatorial plane which separates radially outward and inward regions of the IMF. In practice, the current sheet is warped and may move across the Earth several times during the 27-day solar rotation period. This results in variations in the radial direction of the IMF, which is referred to as 'sector structure'. The sector structure becomes more complicated at periods of maximum activity in the solar activity cycle.

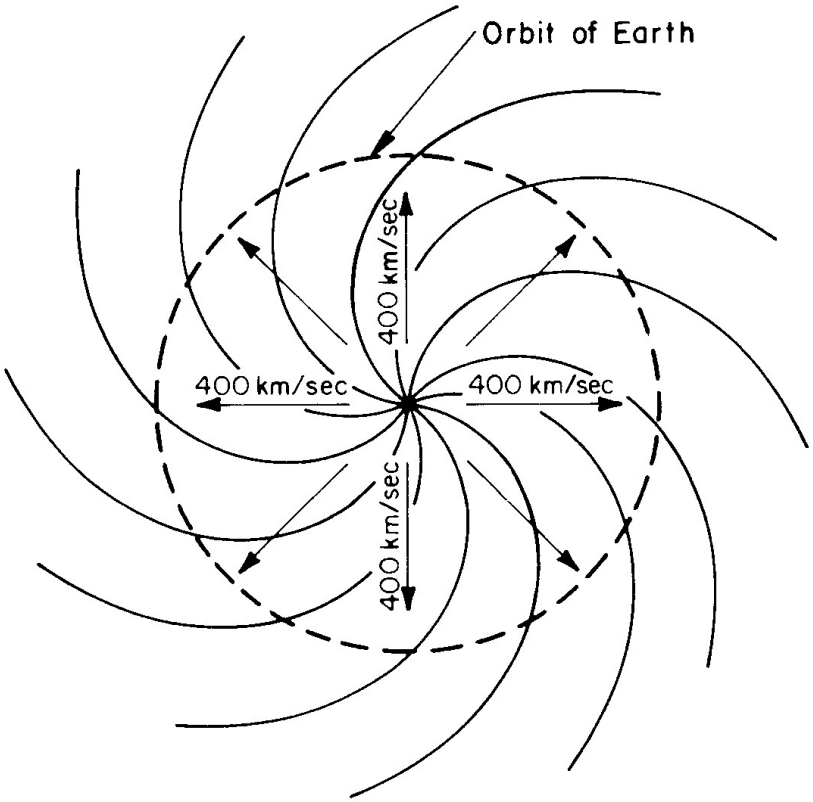

Figure 1.2: The Parker spiral assuming a constant radial speed of 400 kms^{-1}, and a radial magnetic field at the solar surface (from Kivelson and Russell, 1995). The solar wind flows radially outward from the Sun as the Sun rotates. This causes a spiral orientation of the interplanetary magnetic field (IMF). The typical angle between the IMF observed at Earth and the Sun-Earth line is about 45°.

At the heliopause, the solar wind flow is finally stopped by the interstellar plasma environment (the interstellar wind). Since the solar wind flow is supersonic, solar wind must drop to subsonic speeds at a 'termination shock' within the heliopause. Various models place the termination shock between 80 and over 100 AU (Stone, 2001), compared with the orbital radius of Pluto which is 40 AU. Krimigis *et al.* (2003) argued that recent Voyager 1 observations of anomalous cosmic rays were consistent with a crossing of the terminator shock at 87 AU from the Sun, although McDonald *et al.* (2003) contended that these observations represented a precursor to the shock crossing. In 2005, a factor of three enhancement in the magnetic field was observed by the Voyager magnetometer; this is consistent with an enhancement in the solar wind density as it is slowed down and suggests that the spacecraft has now crossed the termination shock (Kerr, 2005). Subsequent estimates predict that the heliopause will be crossed at a heliocentric distance of 125 AU, which Voyager 1 will reach in around 2014. Voyager 1 will run out of power from its radioisotope thermal generator in about 2020.

1.3.2 Earth: The Bow Shock, Magnetosheath and Magnetopause

The Earth's magnetic field region (the magnetosphere) presents an obstacle to the solar wind (Chapman and Ferarro, 1930), since the interplanetary magnetic field lines cannot penetrate the terrestrial magnetic field cavity and the solar wind particles are frozen to the IMF. As the solar wind flow is supersonic, a shock wave is generated upstream of the Earth (the bow shock). At this shock, the solar wind speed is reduced to subsonic values in order to pass around the Earth. Consequently, plasma 'piles up', and the plasma density increases. Much of the bulk kinetic energy of the solar wind is converted to thermal energy, so the temperature also increases across the shock. This region of shocked, dense plasma of solar wind origin is called the magnetosheath. The magnetosheath plasma flows around the magnetosphere; the boundary between the magnetosheath and magnetosphere is called the magnetopause.

As the magnetosheath plasma is simply the shocked solar wind, it also consists largely of electrons and protons, but with some He^{++} ions and trace amounts of heavier ions. Typical plasma densities are between 10 and 30 cm^{-3}, and particle energies are of order 10-100 eV for electrons and 1 keV/q for ions (e.g. Phan *et al.*, 1994). As the plasma density is larger than in the solar wind, and the magnetic flux is frozen into the plasma, the magnetic field magnitude is also enhanced compared with the IMF. The magnetic field lines drape over the magnetosphere; a simple assumption that is often made is that the angle between the field components in the plane perpendicular to the radial vector from the Sun (the clock-angle plane) remains constant across the bow shock. There are, however, more advanced models of the draping of the magnetosheath magnetic field (such as Kobel and Flückiger (1994), which will be used in later chapters of this thesis).

1.3.3 Earth: The Magnetosphere

The Earth's magnetic field creates a cavity in the solar wind (Chapman and Ferarro, 1930), which is called the magnetosphere. The dynamic pressure of the solar wind distorts the otherwise dipolar terrestrial magnetic field, which is compressed on the dayside, and extended on the nightside. The regions of the magnetosphere and magnetospheric currents are illustrated in Figure 1.3. Of the other eight planets in the Solar System, five (Mercury, Jupiter, Saturn, Uranus and Neptune) are known to have magnetic fields which are significant enough to form a magnetosphere; their interactions with the solar wind are similar in many respects to that of Earth.

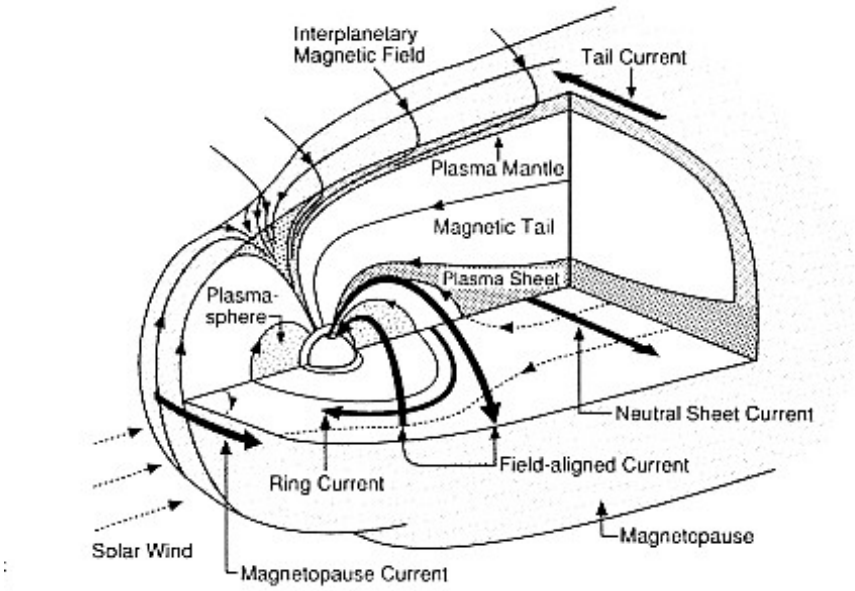

Figure 1.3: The magnetosphere (from Kivelson and Russell, 1995).

1.3.3.1 The Dayside Outer Magnetosphere

The dayside outer magnetosphere consists of a relatively hot, rare plasma. Typical electron energies are between 1–10 keV, whilst densities are much lower than 1 cm^{-3}. Again, the plasma consists mainly of electrons and protons, of both solar wind and terrestrial ionospheric origin, but there are also small quantities of He^{+} and O^{+} ions from the ionosphere, and some He^{++} from the solar wind. The magnetic field lines are generally closed: the field lines can be traced from the Earth's surface in one hemisphere to the Earth's surface in the other hemisphere. The separation regions between the noon-midnight meridian field lines which cross the equator on the day- and night-sides are called the cusps. The cusps have a finite extent perpendicular to the noon-midnight meridian (i.e. in local time). Since the geomagnetic field lines are generally closed, plasma particles are trapped and mirror between hemispheres (see Section 1.2.2.2).

On a given magnetospheric field line, the altitude of a particle's mirror point depends only on the pitch-angle of the particle at the equator (Equation 1.19). Those particles which are more closely field-aligned at the equator penetrate to a lower altitude in the polar regions. If the mirror point of a particle is below about 100 km above the surface of the Earth, that particle is likely to collide with neutral particles (i.e. atoms/molecules) in the atmosphere. In this case, the ionised particle will be absorbed by the atmosphere, rather than being mirrored. Hence, particles with a pitch angle below a certain threshold (α_{loss}) are generally absorbed, and are less likely to be observed. The range of pitch-angles which are not usually seen is known as the 'loss cone'. This applies to both particles with parallel and antiparallel

motion relative to the magnetic field; the loss cone consists of the pitch-angle range $0 \leq \alpha \leq \alpha_{loss}$ and $(180° - \alpha_{loss}) \leq \alpha \leq 180°$. Consequently electron and ion fluxes in the outer magnetosphere are highest at pitch angles close to perpendicular to the magnetic field.

1.3.3.2 The Magnetotail

On the night-side of the Earth, the magnetosphere is extended into a structure called the magnetotail, which extends approximately 1000 R_E downstream (Dungey, 1965), where 1 R_E is one Earth radius (∼6378 km). The region of space containing field lines connected to higher latitude regions is called the lobe. The electron density in the lobe is particularly low (∼0.01 cm^{-3}), and the magnetic field, which extends predominantly anti-Sunward in the southern hemisphere, and Sunward in the northern hemisphere, has a typical magnitude of about 30 nT (Baumjohann and Treumann, 1997, p. 7).

At low latitudes there is a ∼10 R_E thick region called the plasma sheet. Most of the magnetotail plasma is contained in this region; electron densities the order of 1 cm^{-3} and energies of several keV are observed. The plasma sheet magnetic field strength is of order 10 nT (Baumjohann and Treumann, 1997, p. 7).

1.3.3.3 The Inner Magnetosphere

At lower altitudes, the terrestrial magnetic field is more dipolar. Moving radially outwards from the Earth's surface, the inner magnetosphere contains the ionosphere, the plasmasphere and the radiation belts.

The ionosphere consists of the fraction of the terrestrial atmosphere which is ionised by solar ultraviolet radiation. If an ionised particle collides with a free electron, it may recombine to form a neutral atom. At higher altitudes (above 80 km), the atmosphere is rare enough that collisions between particles and free electrons are infrequent and recombination occurs at a low enough rate to allow a permanently ionised population.

Above the ionosphere, at low and mid latitudes, lies the plasmasphere. The boundary between the ionosphere and plasmasphere is not clearly defined, but the plasmasphere has a lower density. The plasmasphere consists of plasma from the ionosphere, and co-rotates with the Earth. The outer limit of the plasmasphere, where the density drops down sharply from ∼10^3 to ∼1 cm^{-3}, is called the plasma-

pause (Baumjohann and Treumann, 1997, p. 84). Magnetospheric field lines are often referred to by their L-shell number, which is the radial distance (in R_E), from the centre of the Earth at which they cross the equatorial plane; the plasmapause lies at about $L = 4$.

The magnetic field lines which contain the plasma sheet map down to the atmosphere at high latitudes and define the 'auroral oval'. Here, energetic plasma sheet particles can collide with and excite the electrons of neutral atoms/molecules. When the excited electrons 'relax', light at distinct wavelengths (both ultraviolet and visible) is emitted. These lights are the aurora. The commonly-observed green aurora is a manifestation of the 557.7 nm emission line in atomic oxygen; at higher altitudes the red 630.0 nm oxygen emission line is observed (Vallance Jones, 1974). Further poleward of the auroral oval lies the polar cap, which is magnetically connected to the lobes.

The radiation belts consist of energetic electrons and ions which are trapped on magnetic field lines between $2 < L < 6$ (Baumjohann and Treumann, 1997, p. 7).

1.4 The Magnetopause and Reconnection

Since the IMF observed near Earth varies frequently as a result of various factors such as sector structure and passing coronal mass ejections (CMEs), the magnetosheath magnetic field also varies. Thus there is always a region of the magnetopause where the magnetosheath and magnetospheric magnetic fields have antiparallel components, and reconnection may occur.

1.4.1 The Magnetospheric Convection Cycle

Chapman and Ferarro (1930) envisaged a 'closed' magnetosphere. In their model there was no interconnection between terrestrial and solar magnetic field lines, but they proposed that geomagnetic storms were caused by the potential difference set up as packets of solar wind passed the Earth, which set up a ring current at lower latitudes (Figure 1.4a). Axford and Hines (1961) proposed a viscous interaction between the solar wind and magnetosphere, modulated by enhancements in the solar wind speed.

Dungey (1961) proposed that when the draped IMF in the magnetosheath was directed southward, reconnection could occur between the magnetosheath and mag-

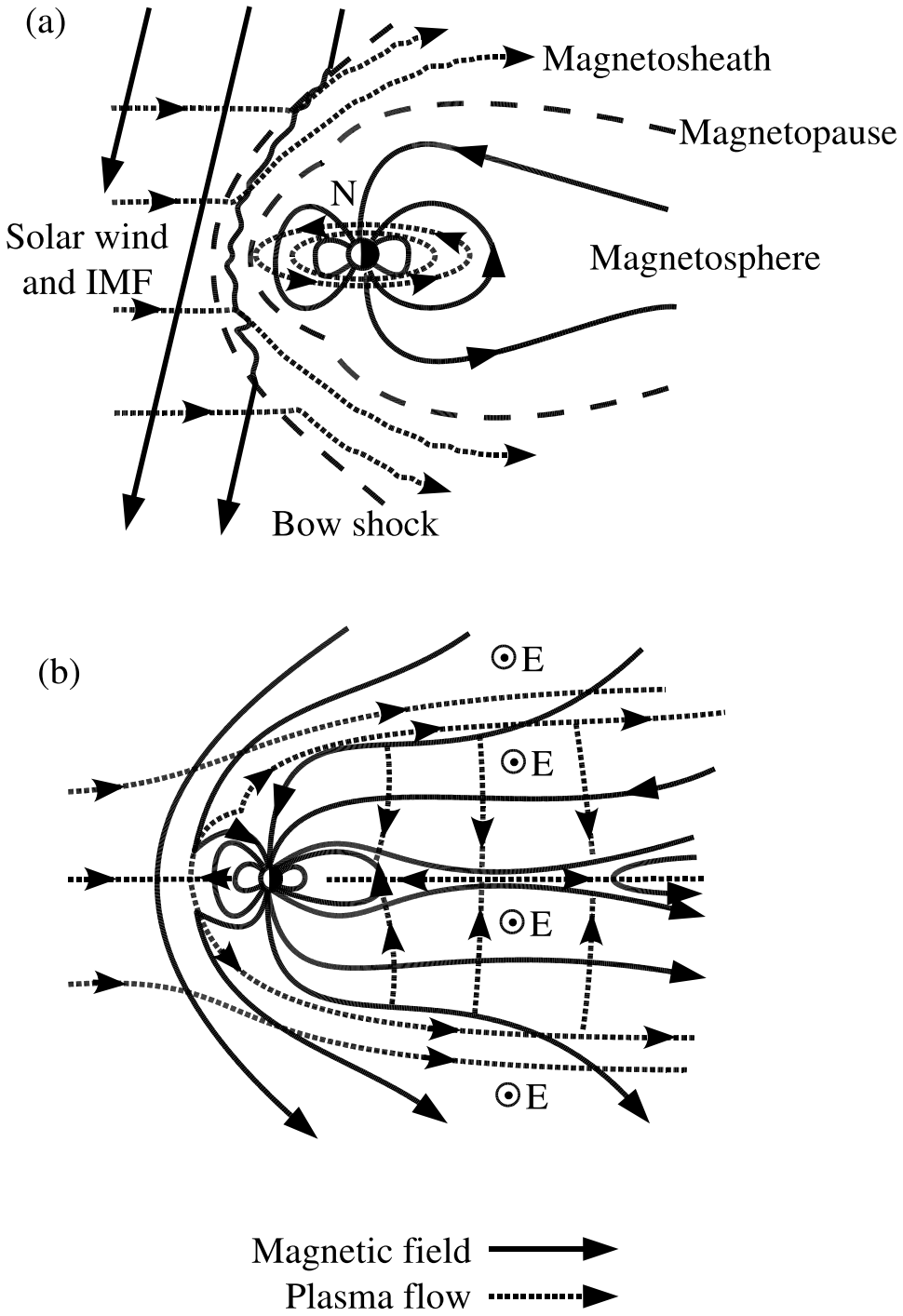

Figure 1.4: (a) The Chapman-Ferraro closed magnetosphere. (b) The Dungey open magnetosphere. When the IMF is southward, IMF and magnetospheric field lines reconnect near the subsolar point (left). The opened field lines move tailward as a result of the magnetic tension in the kinked field lines and magnetosheath flow. In the tail, open field lines are compressed toward each other and reconnect to form a field line with both feet in the solar wind, and a closed field line. The closed field line initially contracts Earthward in order to reduce the magnetic tension. It then moves around the flank to the dayside, where the cycle continues. (After Cowley, 1996).

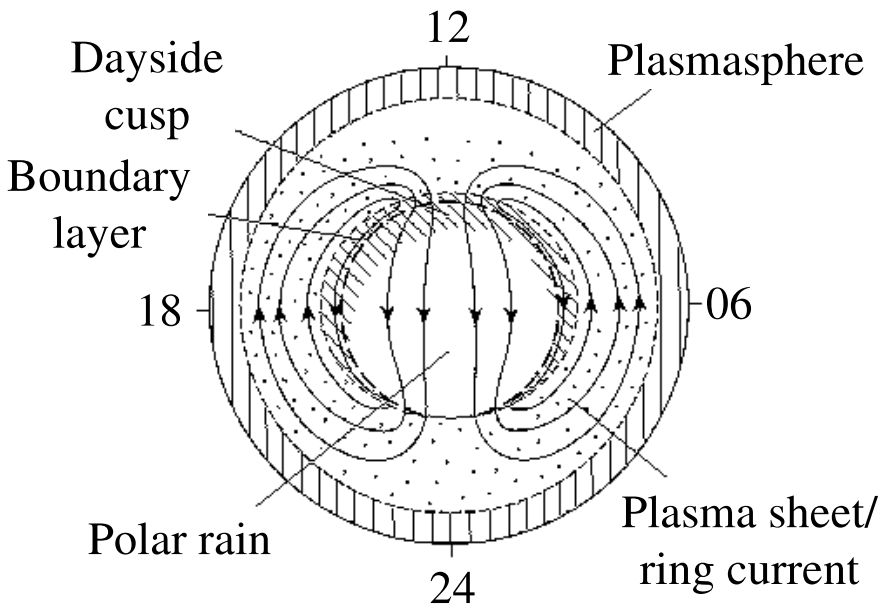

Figure 1.5: The convection cycle in the ionosphere, for southward IMF. This figure shows a view of the polar ionosphere from above the Earth's surface. Local noon is at the top, and midnight at the bottom. Newly opened magnetic field lines near local noon are dragged tailward to local midnight across the polar cap, where they reconnect again. The closed portions of the reconnected field lines then move Earthward and round the flanks to the subsolar point to replace the tailward-moving field lines. The feet of the field lines which move around the flank are thus dragged around the poles at lower latitudes than the tailward flow. (After Cowley, 1996).

netospheric magnetic fields near the subsolar point (Figure 1.4b). This leads to an 'open' magnetosphere. (In reality, since $\nabla \cdot \boldsymbol{B} = 0$, field lines cannot truly be open, and the reconnected terrestrial field lines close via the Sun). The reconnection process drives a similar convection cycle in the ionosphere to that proposed by Axford and Hines (1961), shown in Figure 1.5, but the Dungey (1961) convection cycle is controlled by the IMF. The motion of the convecting magnetic field lines and the plasma which is frozen to them gives rise to a convection electric field which will be seen by an external observer. The convection electric field $\boldsymbol{E}$ is directed from dawn to dusk, and is shown in Figure 1.4b.

Newly opened field lines near the subsolar point are dragged tailward by two effects: the solar wind flow and the $\boldsymbol{j} \times \boldsymbol{B}$ force which acts to straighten the highly-kinked field lines. Consequently, the ionospheric ends of the field lines are dragged across the magnetic pole (the polar cap region). Once the kink in the magnetic field is straightened, the solar wind flow continues to drag the open end of the field line tailward; this creates a new kink in the field line and the $\boldsymbol{j} \times \boldsymbol{B}$ force acts to slow down the tailward motion of the field line. However, the force exerted by the solar wind is greater, and the magnetospheric portion of the field line (between the kink and the ionosphere) is extended tailward, forming the lobe. It can be inferred from the estimates in Dungey (1965) that the magnetic field lines remain open for

approximately 4 hours. The addition of magnetic flux to the lobe increases the magnetic pressure in the magnetotail. When the pressure becomes sufficient, two open field lines then reconnect at the current sheet (the plasma sheet) which separates the Earthward field in the northern lobe from the anti-Sunward field in the southern lobe. The nightside reconnection site generates an entirely 'open' solar wind field line (which has both feet in the solar corona) and a closed magnetospheric field line, which is highly stretched. The solar wind field line continues its journey radially outwards through the solar system, whilst the magnetospheric field line contracts, moving Earthward, under the $\boldsymbol{j} \times \boldsymbol{B}$ force. The convection cycle is completed as the closed field line moves around the flank to replace dayside field lines which have been reconnected. The ionospheric ends of these field lines move Sunward at lower latitudes (Figure 1.5). The newly-closed magnetic field lines take about 8 hours to return to the subsolar sector (Cowley *et al.*, 2003).

In practice this process does not always occur in such a steady cycle. When the IMF turns southward and remains steady, reconnection commences on the dayside and initially occurs at a greater rate than in the magnetotail. This results in magnetic flux being added to the lobe which builds up before being released in a burst of reconnection, injecting large quantities of charged particles into the atmosphere. Such variable-rate reconnection is known as the substorm cycle (Russell and McPherron, 1973).

There is plenty of observational evidence for the convection cycle as broadly suggested by Dungey (1961). Accelerated flows are often observed at the magnetopause (e.g. Paschmann *et al.*, 1979; Gosling *et al.*, 1991), and the ionospheric convection pattern outlined above, along with substorm activity and auroral displays, correlate well with periods of southward IMF (Fairfield and Cahill, 1966).

Dungey (1963) proposed that reconnection may also occur when the IMF is northward (Figure 1.6). In this scenario, the magnetosheath and magnetospheric magnetic fields are oppositely directed at the magnetopause tailward of the cusp, hence the magnetospheric field lines that reconnect are in the lobe and already open. Thus one field line is generated which has both ends in the solar wind; this therefore eventually passes into the solar wind-proper. The other field line has one foot in the ionosphere, and the other end in the solar wind. If the tension force on this highly-kinked field line is initially greater than the force exerted by the solar wind, then the field line is dragged initially Sunward before being swept tailward round the flank by the solar wind. This convection cycle is called 'reverse convection'.

It seems sensible, therefore, that if reconnection may occur for both southward- and northward-directed IMF, then it may occur for intermediate cases where there

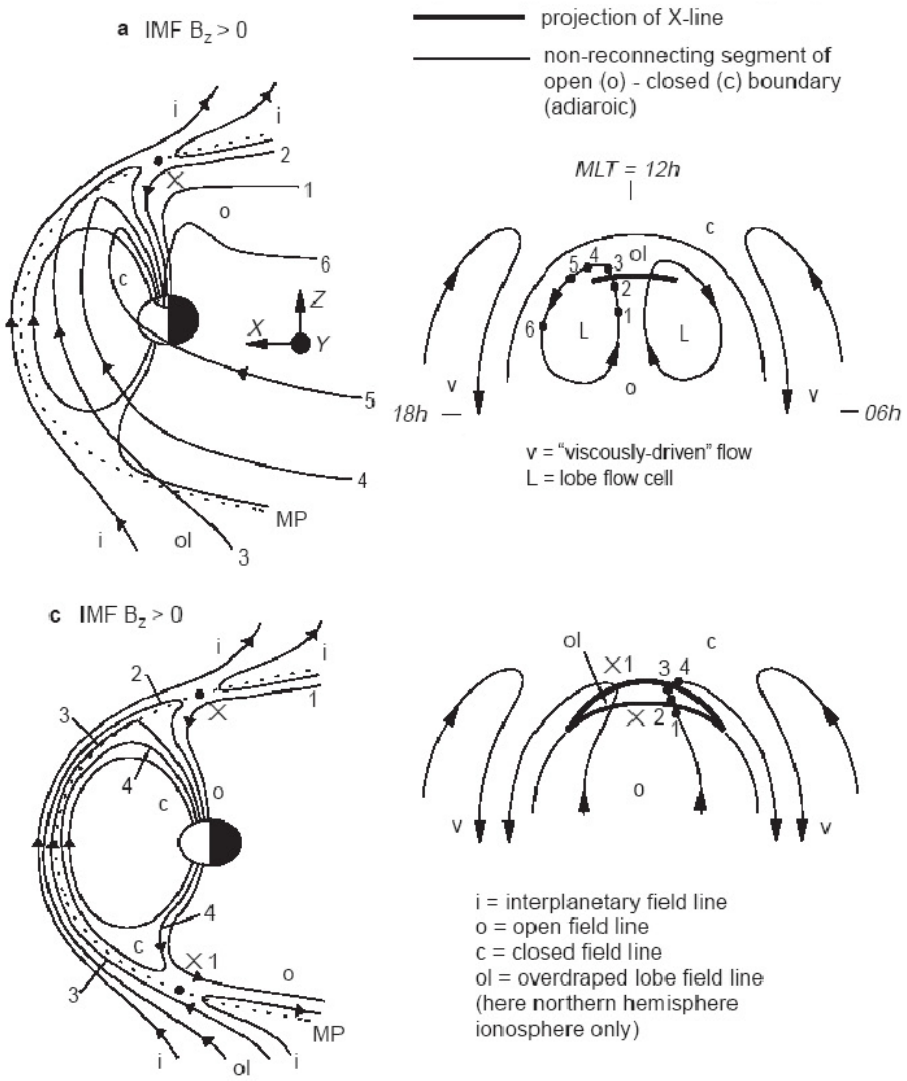

Figure 1.6: Northward IMF reconnection (from Lockwood and Moen, 1999). (a) The IMF may reconnect with the open lobe field lines in one hemisphere. In this case, the (open) reconnected field lines may initially be dragged Sunward (if the tension in the field line kink is able to pull harder than the force exerted by the magnetosheath flow), and then tailward at lower latitudes, creating a 'reverse convection' pattern in the ionosphere. (b) Alternatively, double lobe reconnection may occur, forming a closed, reconnected field line. The feet of the newly closed field line may still initially move Sunward as the field line contracts, before being forced tailward as part of the reverse convection cycle.

is a dawn-dusk component of the IMF. There are two major hypotheses of where reconnection may occur as a function of B_Y. The first is the component reconnection model (Gonzalez and Mozer, 1974), which gives a tilted reconnection line which passes through or near the subsolar point irrespective of the value of the IMF B_Y component, so long as B_Z is negative. The tilt angle is given by the bisector between the magnetosheath and geomagnetic fields at the magnetopause. The second hypothesis is that reconnection occurs only in regions where the shear between the magnetosheath and geomagnetic fields is equal to (or close to) 180° (Crooker, 1979). The accuracy to which antiparallel fields at a site are required to be 'consistent'

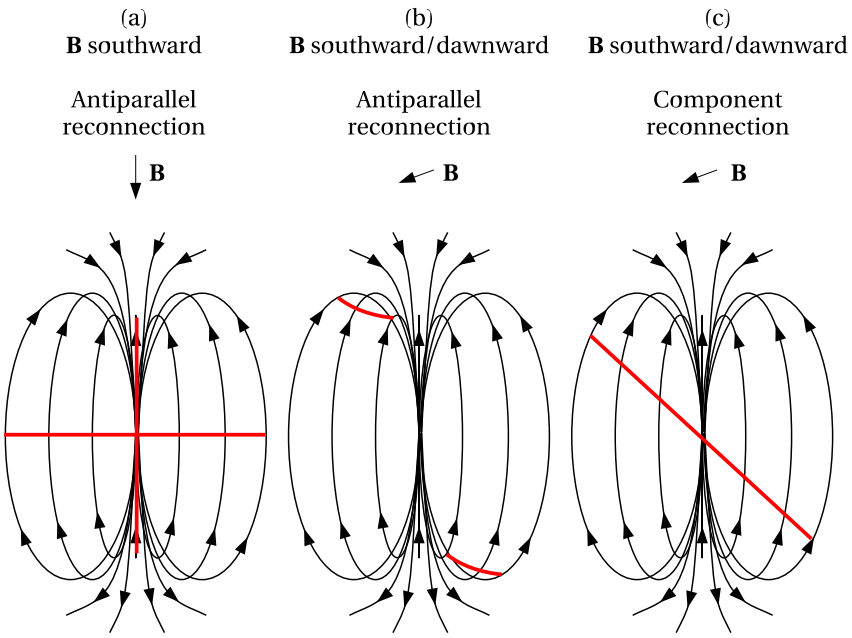

Figure 1.7: Antiparallel and component reconnection. The three figures are sketches of magnetospheric field lines as viewed from the Sun. Hence local dawn is on the left, and local dusk on the right of each figure. The field lines at the top and bottom are part of the lobes; these field lines are open and extend into the solar wind downtail. The field lines in the middle are closed, dayside field lines. If the IMF is directed close to due south (a), then the magnetospheric and magnetosheath magnetic field lines are oppositely directed at all latitudes near the midday magnetic meridian, and at all local times near the magnetic equator. Reconnection may occur along these lines according to the antiparallel reconnection hypothesis (red lines). A subsolar, component reconnection line for exactly southward IMF is identical, except that it does not extend to high latitudes at local noon. If there is a significant dawn-dusk component of the IMF, then according to the antiparallel reconnection hypothesis (b), reconnection may not occur at low latitudes, but takes place at higher latitudes where the magnetic shear is equal to (or near to) 180°. On the other hand, the component reconnection hypothesis (c) allows reconnection to occur near the subsolar point, but the reconnection line becomes tilted.

with the antiparallel hypothesis varies from study to study; an arbitrary threshold is usually set such as $\theta > 170°$ (Petrinec and Fuselier, 2003). The differences between these two hypotheses are illustrated in Figure 1.7. A third, less common, hypothesis incorporates a more random nature into the location of reconnection (e.g. Nishida, 1989). Coleman and Freeman (2005) examined the possibility that fluctuations in the magnetosheath magnetic field could be described by fractal noise. Following this assumption, they were able to reproduce both large-scale persistent reconnection sites, similar to those of the antiparallel reconnection hypothesis, and more random sites which were not temporally stable.

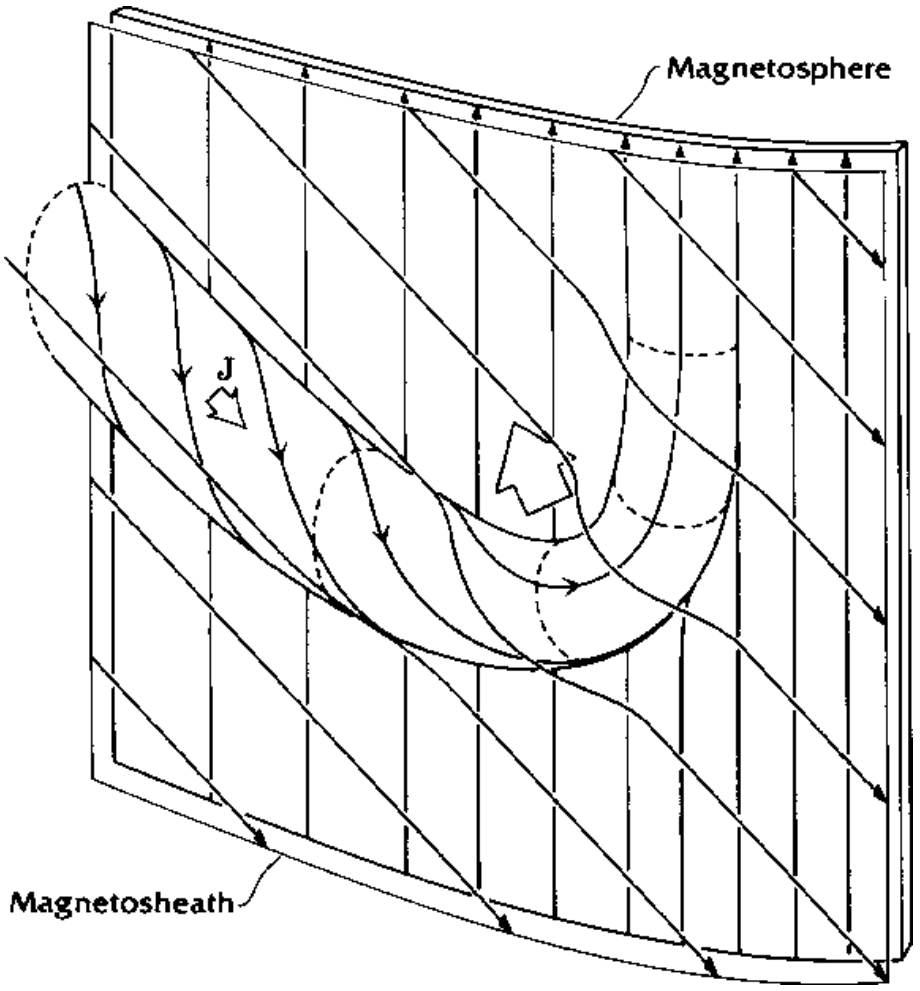

Figure 1.8: The Russell and Elphic (1978, 1979) FTE model. If a burst of reconnection occurs near the subsolar point, two flux tubes of reconnected field lines are generated. One (shown in this figure) moves northward, whilst the other moves southward. Their motion in the dawn-dusk direction depends upon the B_Y component in the magnetosheath. Neighbouring, unreconnected field lines on either side of the magnetopause drape over the flux tube, causing a bipolar B_N signature if the FTE moves past an observing spacecraft. The magnetic field is also compressed in the draping regions, causing an increase in $|\boldsymbol{B}|$. Currents within the flux tube, postulated by Sonnerup (1987), ensure that if the spacecraft enters the flux tube a bipolar B_N signature is observed which is consistent with the field-line draping. Furthermore, if the flux tube is entered, then a mixing of plasma from either side of the magnetopause may be observed. The population originating from the opposite side of the magnetopause may be accelerated and will be field-aligned (parallel if the flux tube is connected to the southern hemisphere; antiparallel if connected to the northern hemisphere).

1.5 Flux Transfer Events

Dayside reconnection does not always occur as a steady-state process. Haerendel *et al.* (1978) studied the high-latitude magnetopause region using data from the HEOS-2 satellite. They concluded that reconnection does not usually take place as a large-scale quasi-stationary process in the low latitude magnetopause region. The same conclusion was also reached by Paschmann *et al.* (1979), as most of the cases with magnetic fields favouring reconnection that were studied lacked accelerated plasma signatures. However, Haerendel *et al.* (1978) did note brief enhancements

in the magnetic field strength just Earthward of the magnetopause, which were sometimes coupled with a magnetic field rotation that was inconsistent with the magnetosheath field observed shortly beforehand. These signatures were interpreted as signs of impulsive reconnection at the high-latitude magnetopause, and termed 'flux erosion events'.

At the same time, Russell and Elphic (1978, 1979) studied dayside low-latitude magnetopause crossings in magnetometer data from two of the ISEE mission satellites. Russell and Elphic (1978) introduced boundary normal coordinates, defined such that the unit vector $\hat{\boldsymbol{N}}$ was the outward pointing local magnetopause normal vector (deduced by minimum variance analysis, taking the vector product of the magnetosheath and magnetospheric fields, or from a model), $\hat{\boldsymbol{L}}$ lay parallel to the unperturbed magnetospheric field (i.e. points approximately northward) and $\hat{\boldsymbol{M}}$ completed the right-handed set ($\hat{\boldsymbol{L}} \times \hat{\boldsymbol{M}} = \hat{\boldsymbol{N}}$), directed dawnward. This coordinate system revealed examples of a signature consisting of a bipolar variation in B_N, with simultaneous variations of the components in B_L and B_M. The bipolar B_N signature was always in the same sense (positive then negative, subsequently termed a 'direct' or 'standard' FTE, e.g. Berchem and Russell, 1984; Rijnbeek *et al.*, 1984), and the B_L and B_M variations were not consistent with ordinary crossings of the magnetopause. The signatures were observed both sides of the magnetopause. The authors concluded that these observations were signatures of reconnection, and called them 'flux transfer events' (FTEs). (The 'flux erosion events' observed by Haerendel *et al.* (1978) and argued to be signatures of near-cusp reconnection were shown to be consistent with equatorially-generated FTEs by Rijnbeek and Cowley, 1984). Similar signatures have subsequently been reported at Jupiter (Walker and Russell, 1985) and Mercury (Russell and Walker, 1985).

The Russell and Elphic (1978, 1979) model was that of two open, kinked flux tubes formed by reconnection near the subsolar point, propagating tailward (one northward, one southward) in response to solar wind drag and changing form to reduce the magnetic tension ($\boldsymbol{j} \times \boldsymbol{B}$ force). This is shown in Figure 1.8. Neighbouring unreconnected field lines would drape over the reconnected flux tubes causing the bipolar B_N signature and characteristic deviations in B_L and B_M as the FTE moved past the spacecraft. (A more detailed modelling of the field line draping was carried out by Farrugia *et al.*, 1987a). Paschmann *et al.* (1982) also observed a bipolar B_N signature when the reconnected flux tube was crossed; this was explained by a helicity which was added to the Russell and Elphic (1978, 1979) flux tube model by Sonnerup (1987). Other models have since been proposed and debated; these will be discussed after an overview of other observations.

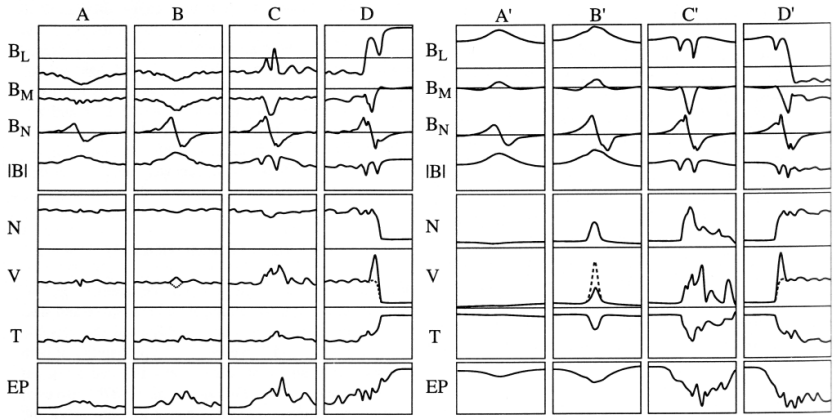

Figure 1.9: Taxonomy of magnetosheath (left) and magnetospheric (right) FTEs by Paschmann *et al.* (1982) and Elphic (1995). $\boldsymbol{B}$ is the observed magnetic field, N the plasma density, V the bulk speed, T the temperature and EP the energetic particle flux. In both environments, class 'A' corresponds to the grazing of an FTE, where the observed effects are due to observations of unreconnected field lines draping over the reconnected flux tube. 'B' is a closer pass - the flux tube is crossed away from the 'kink' in Figure 1.8. 'C' crosses the flux tube near the kink, where the flux tube changes from being directed northward (in the magnetosphere) to southward (in the magnetosheath). 'D' corresponds to an FTE which is observed at the same time as a magnetopause crossing.

1.5.1 FTE Characteristics

Daly *et al.* (1981) confirmed that ions and electrons typical of magnetospheric distributions were observed in magnetosheath FTEs, and Paschmann *et al.* (1982) extended this observation of mixed ion and electron distributions to magnetospheric FTEs. Such observations are consistent with the reconnection model of FTEs.

Paschmann *et al.* (1982) noted the following 'essential' features observed in all low-latitude FTEs: a southward component in the undisturbed magnetosheath magnetic field (negative B_L); a bipolar variation in B_N; an enhanced magnetic field strength $|\boldsymbol{B}|$ and an imbalance in the total pressure ($p_{gas} + B^2/2\mu_0$) within both the flux tube and the draping region, countered by the tension in the draped magnetospheric/magnetosheath field lines. Simultaneous observations of the same FTEs on both sides of the magnetopause were first presented by Farrugia *et al.* (1987b).

Paschmann *et al.* (1982) also noted other characteristics observed in three different classes of 'direct' magnetosheath FTEs (Figure 1.9). In the first class (A), there is very little change other than a small bipolar B_N signature, a small energetic particle signature and a more southward B_L component than in the ambient magnetosheath field. This class represents an event where an FTE is merely 'grazed': the observed effects are due entirely to the draped magnetic field. There were, however, some magnetosheath FTEs in class A which exhibited slight energetic electron signatures (such as shown in the left-hand column of Figure 1.9); accordingly Paschmann *et al.*

(1982) concluded that some form of leakage process allows escaping magnetospheric particles to move onto non-reconnected field lines.

In class B of the Paschmann *et al.* (1982) taxonomy, there is an increase or decrease in the plasma bulk speed, a slight temperature change, and a more pronounced energetic particle flux increase and B_N signature than in class A. The deviations in the B_L and B_M components may be comparable. This taxon represents a full crossing of the flux tube, but away from the point at which the flux tube bends northward to enter the magnetosphere. The final Paschmann *et al.* (1982) class (C) is commonly known as the 'crater' FTE (e.g. Farrugia *et al.*, 1988). This is a crossing of the flux tube near where it enters the magnetosphere, thus taking a northward orientation. Here there is a positive change in B_L, which may be so large as to result in a northward field. The plasma bulk velocities substantially increase (perhaps doubling), for the duration of the event. The B_N signature is of larger amplitude than taxa A and B, and there are often local minima in $|B|$ at one or both edges of the FTE (the 'crater'). This taxonomy was extended by Elphic (1995) to equivalent magnetospheric events, and an additional class (D) of an FTE observed on the magnetopause itself.

Rijnbeek *et al.* (1982) reported the first observations of 'reverse polarity' FTEs: the bipolar B_N was reversed (–/+) compared with the (+/–) 'standard' or 'direct' polarity signature observed by Russell and Elphic (1978). The reverse FTEs were observed at low latitude; the negative/positive B_N signature combined with the southward deviations in the plasma flow and parallel flowing energetic (magnetospheric) particles led them to conclude that these FTEs were connected to the southern hemisphere – the second flux tube formed under the Russell and Elphic (1978) model.

1.5.2 FTE Surveys

The first surveys of FTEs were published by Rijnbeek *et al.* (1984) and Berchem and Russell (1984). Both surveys studied the pre-terminator magnetopause ($X_{GSM} > 0$). Rijnbeek *et al.* (1984) showed standard FTEs to be more common at northern latitudes, whilst reverse events prevailed at low and southern latitudes. Berchem and Russell (1984) used a larger data set, extending to more southern latitudes, and reported that standard and reverse FTEs occurred predominantly in the northern dawn and southern dusk sectors respectively, although some events (less than 10%) deviated from this pattern. The dividing line between standard and reverse events was thus inclined to the magnetospheric equator. Almost all of the events were observed during periods of southward IMF, with the largest number being observed

in the due south IMF bin.

Daly *et al.* (1984) analysed 52 magnetopause crossings which contained FTEs between 6 and 18 hours MLT, and between -20 and +45° latitude. They observed in some cases a contradiction between the motion inferred from the polarity of the B_N signature (e.g. standard polarity implies northward) and the hemisphere of connection deduced from the particle anisotropy (e.g. a parallel beam implies a flux tube connected to the southern hemisphere). This was resolved by the possibility that the bulk speed could exceed the Alfvén speed; if the two velocities were oppositely directed, a flux tube connected to the southern hemisphere could be dragged northward by the magnetosheath flow faster than magnetic tension could pull it southward. Therefore B_N can not be used to determine the hemisphere of connection on its own. Considering this factor, Daly *et al.* (1984) concluded that the FTEs in their survey had an equatorial, rather than high-latitude source. Southwood *et al.* (1986) presented another survey, which also showed a correlation with southward IMF and concluded that the source region was at low latitudes.

More recent statistical studies of pre-terminator FTEs (e.g. Kuo *et al.*, 1995; Kawano and Russell, 1997a,b) have also shown that FTEs occur predominantly when IMF $B_Z < 0$, but have not found a strong peak around due south IMF. Russell *et al.* (1985) and Kawano and Russell (1997a) have shown the polarity, and hence motion, of southward IMF FTEs to be consistent with low-latitude merging even when there is a dominant IMF B_Y component. This is the major piece of evidence for the component merging model (Gonzalez and Mozer, 1974), as opposed to strictly antiparallel merging (Crooker, 1979). Kawano and Russell (1997a,b) extended coverage to the post-terminator magnetopause, and observed a significant number of northward IMF FTEs. This survey will be discussed further in Chapter 4.

Lockwood and Wild (1993) measured the times between FTEs on 172 crossings, and calculated a mean of 8 minutes, and a mode of 3 minutes. Whilst Kuo *et al.* (1995) calculated similar averages (mean: 10.5 mins, median: 8 mins, mode: 4 mins), the distributions observed are broad and there is no regular separation time. Furthermore, the inter-FTE time will presumably depend upon the threshold (if any) applied to the peak-to-peak size of the B_N signature. Recently, Wang *et al.* (2005) has shown that varying a peak-to-peak threshold does not significantly impact on the IMF dependency of FTE occurrence, implying that there is no fundamental lower limit. Kuo *et al.* (1995) also investigated the dependency of FTEs on solar wind parameters (plasma beta, dynamic pressure and upstream magnetosonic Mach number); there was a weak, but observable, correlation between FTE occurrence and the upstream magnetosonic Mach number, but no correlation with the solar wind plasma beta or dynamic pressure.

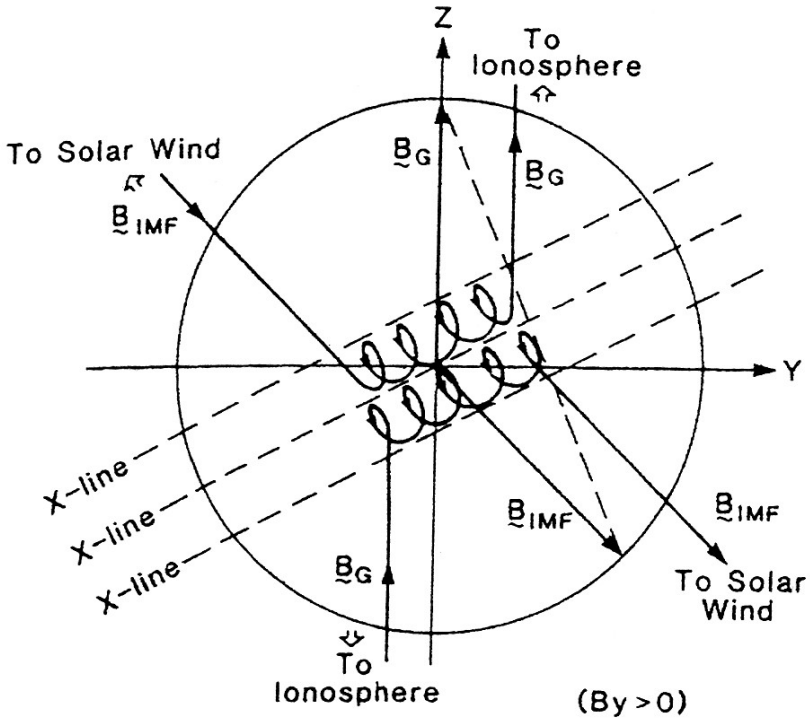

Figure 1.10: The Lee and Fu (1985) multiple X-line FTE model.

1.5.3 Other models

Other reconnection models of FTEs have been proposed that are consistent with these observations. Lee and Fu (1985) suggested that the observed signatures could be caused by flux tubes generated by multiple X-lines at the dayside magnetopause (Figure 1.10). In this model, if n parallel reconnection lines are formed, then $n-1$ flux tubes are generated. In the absence of a magnetosheath B_Y component, only isolated magnetic loops are formed, but if there is a B_Y component a helical field is generated. As it is unlikely that all of the X-lines will reconnect field lines at exactly the same rate, one X-line will become more active than the others; those flux tubes generated either side of the dominant X-line will be swept in opposite directions. The multiple X-line model is perhaps most-often quoted in the context of travelling compression regions (TCRs), which are believed to be reconnection-generated structures in the magnetotail (e.g. Slavin *et al.*, 1984, 2005). As such, TCRs are the magnetotail equivalent of FTEs. The principal difference between the Lee and Fu (1985) and Russell and Elphic (1978, 1979) models is that in the former, the axis of the flux tube is parallel to the reconnection line and straddles the magnetopause along the length of the flux tube. In the Russell and Elphic (1978, 1979) model, the flux tube is generated perpendicular to a short X-line (when the IMF is directed due south), and crosses the magnetopause at the 'kink'. The axis of the flux tube proposed by Lee and Fu (1985) is perpendicular to that proposed

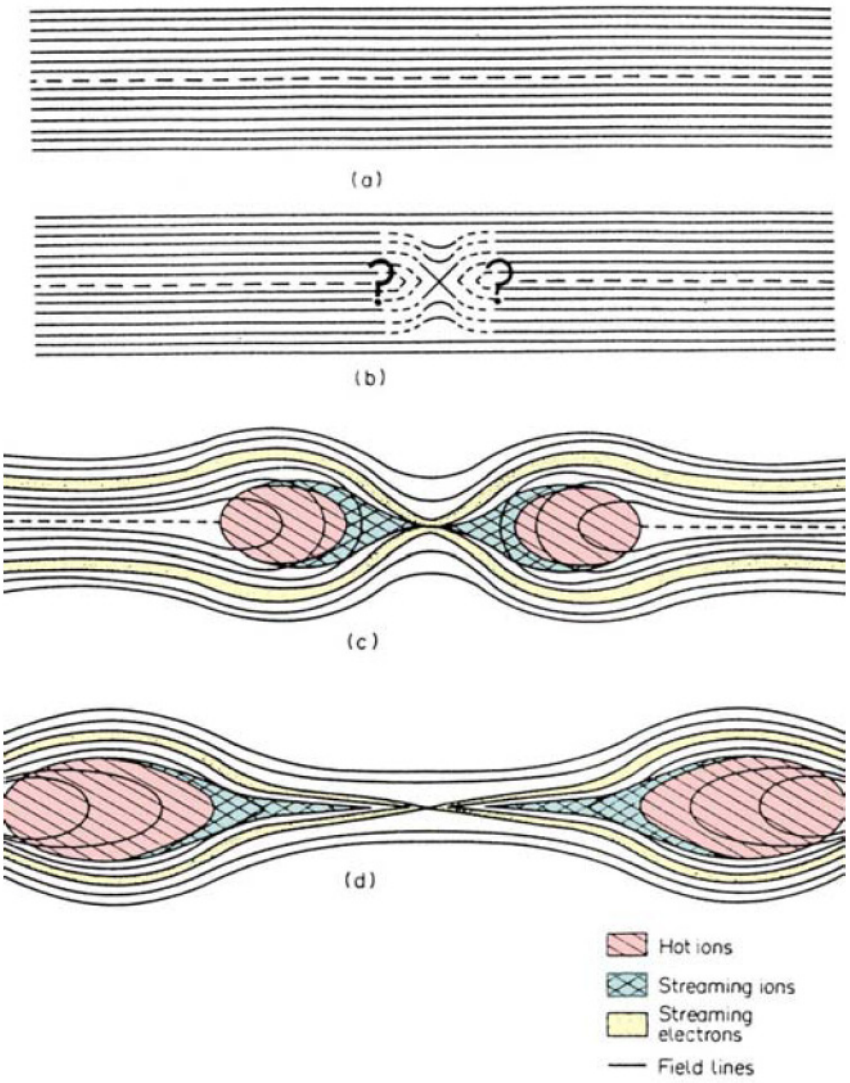

Figure 1.11: The 'reconnection bubble' FTE model, as proposed by Southwood *et al.* (1988). A similar version was proposed independently by Scholer (1988a). In this model an enhancement, then decrease, in the reconnection rate produces two 'bubbles' of reconnected flux, which move away from the reconnection line under the same forces as act on the Russell and Elphic (1978, 1979) flux tube. These bulges also cause a bipolar B_N signature and an enhancement in $|\boldsymbol{B}|$, but the internal FTE currents are initially parallel to the reconnection line, and hence perpendicular to those in the Russell and Elphic (1978, 1979) model. (From Marchaudon, 2003).

by Russell and Elphic (1978, 1979). Consequently internal currents will also be perpendicular in the two models, although both models lead to bipolar magnetic field signatures in the component normal to the magnetopause plane.

Southwood *et al.* (1988) and Scholer (1988a) independently proposed a 'reconnection bubble' model of FTEs (Figure 1.11). This model does not contain a reconnected flux tube at the core of the event. Instead, as the reconnection rate at a single X-line increases, then decreases, the region occupied by reconnected field lines thickens and then thins. Scholer (1988b) used this model to explain the strong core fields often seen at FTE centres.

Like the other models, the reconnection 'bubble' leads to a bipolar B_N signature, but the FTE structure is initially aligned parallel to the X-line (as in the Lee and Fu (1985) model). This means that at a low-latitude reconnection site with a dominant southward B_Z component, an FTE may have a long latitudinal length, as opposed to the Russell and Elphic (1978) flux tube which has a short latitudinal extent. Another important point is that the Southwood *et al.* (1988)/Scholer (1988a) model is not simply a longitudinally extended Russell and Elphic (1978) flux tube; in the latter model the bipolar B_N signature arises as a consequence of draping and internal structure over the FTE's short longitudinal extent, whereas in the former it is a consequence of a short latitudinal length-scale.

Two alternative groups of non-reconnection models were also proposed to explain the observed bipolar signatures. The first hypothesis was that impulsive plasma penetration (Lemaire and Roth, 1978; Lemaire *et al.*, 1979; Heikkila, 1982) could be a source mechanism for FTE signatures. These authors argued that impulsive penetration may occur when a plasma element in the solar wind has a larger momentum density compared with the background plasma. However, Smith and Curran (1990) showed that there is a poor correlation between FTE occurrence and the magnetopause penetration parameter derived by Lemaire *et al.* (1979), compared with the correlation between FTEs and magnetosheath B_L (although they referred to the magnetosheath magnetic field as the interplanetary magnetic field). This suggests that impulsive penetration is not the main cause of FTEs, although it continues to be discussed as a possible source (e.g. Lundin *et al.*, 2003). Furthermore, Owen and Cowley (1991) disputed the mechanism proposed by Heikkila (1982).

The second group of non-reconnection models was proposed by Sibeck and colleagues (Sibeck *et al.*, 1989; Sibeck, 1990, 1992), who suggested that magnetopause waves generate signatures similar to those observed by Russell and Elphic (1978) as spacecraft undergo successive crossings of near-magnetopause regions (Figure 1.12). These authors argued that the magnetopause waves are caused by brief, impulsive, large-amplitude solar wind pressure pulses. The pressure pulse compresses the magnetopause Earthward, causing a trough in the magnetopause surface. They argued that the pulse may be outrun by a fast-mode wave within the magnetosphere, since southward magnetosheath fields are associated with a thin low-latitude boundary layer (LLBL), as reported by Haerendel *et al.* (1978). The fast-mode wave consists of a region of increased magnetic field, and hence pressure, which forms a peak ahead of the trough. This, according to Sibeck (1990, 1992), causes the spacecraft to observe a bipolar B_N signature as the pulse passes, along with enhancements in B_L and B_M. The plasma signatures are explained in this model by two factors: adiabatic heating of plasma on compressed field lines, and the passage of the spacecraft through two or more successive regions (the magnetosphere, low-latitude boundary

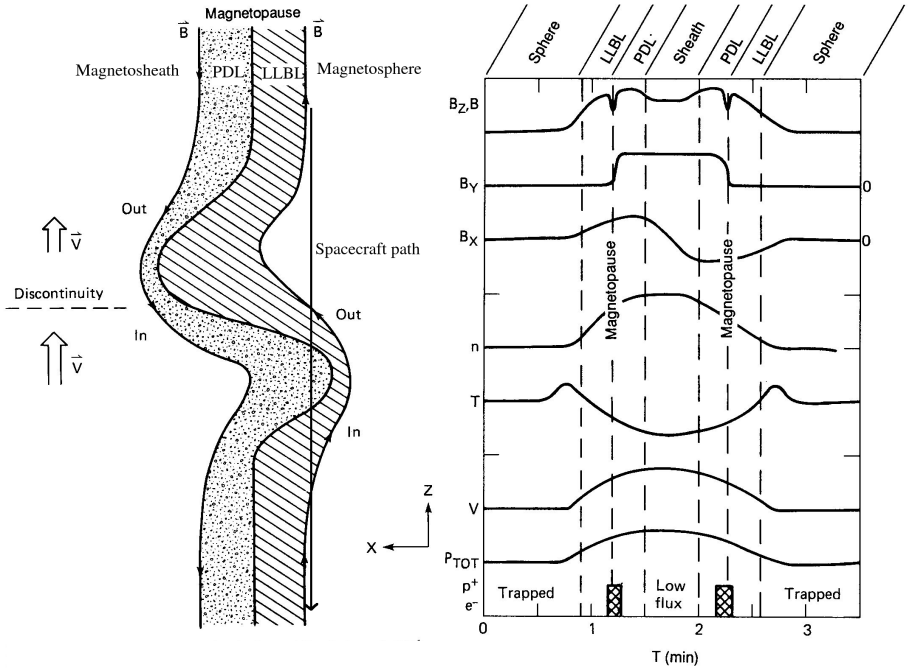

Figure 1.12: A variant of the boundary wave model of FTE signatures. This group of models is not based on reconnection, but assumes that if a spacecraft passes through a group of magnetopause layers (left) then the FTE-like signatures are observed (right). (After Sibeck, 1990).

layer, energetic particle layer, plasma depletion layer, magnetosheath).

The pressure pulse/pulsed boundary layer models have been the cause of much debate. Lanzerotti (1989) noted that reconnection and pressure pulses might be expected to be correlated as pressure pulses could lead to enhancements in the reconnection rate, hence the pressure pulses could correlate with reconnection-generated FTEs. Furthermore, Lanzerotti (1989) argued that previous studies had argued that reconnection could theoretically produce boundary oscillations (Holzer and Reid, 1975; Southwood, 1987; Lee *et al.*, 1988), and Sibeck *et al.* (1989) had not provided any evidence to negate reconnection as a cause of the magnetopause oscillations. Elphic (1990) argued that the correlation with southward IMF, accelerated flows along the magnetopause and mixing of solar wind and magnetospheric plasmas were not explained by the pressure pulse model. Furthermore, the pressure pulse model required an enhancement in the magnetic field strength to be observed ahead of magnetospheric FTEs, which was not consistent with ISEE observations. Lockwood (1991) proposed that the B_N signature of the Sibeck (1990) model (Figure 1.12) would be tripolar under southern IMF, although the third peak might be too small to be observed. Lockwood (1991) also concluded that whilst most individual FTEs (except those observed simultaneously on either side of the magnetopause) could be explained in principle by the Sibeck (1990) model, the probability of observing the majority of events during negative IMF B_Z, as noted by earlier surveys, was minuscule if FTEs were in general caused by pressure pulses, since pressure variations and

IMF orientation are not correlated (Bowe *et al.*, 1990).

Smith and Owen (1992) analysed the ion velocity distribution functions within an event previously described as both an FTE (Rijnbeek *et al.*, 1987; Farrugia *et al.*, 1988) and a magnetopause crossing (Sibeck, 1992), and argued that the distributions were inconsistent with a simple magnetopause crossing unless reconnection was taking place.

Kawano *et al.* (1992) studied bipolar signature events over a range of magnetic L-shells ($6.0 < L < 9.4$). They observed that long events (with a 'characteristic' B_N peak-to-peak time-scale that was greater than 90 s) showed no correlation with the interplanetary magnetic field (IMF) or AE index and occurred over a wide range of L-shells. These were attributed to solar wind pressure variations. However short events (time-scale $<$ 90 s) tended to be observed near the magnetopause during periods of southward IMF and high AE index, and were ascribed to reconnection.

Elphic *et al.* (1994) examined an interval when the AMPTE UKS and IRM satellites were in the near-subsolar magnetosheath, whilst ISEE-1 and -2 observed FTEs near the magnetopause. Using a superposed epoch analysis, they found no correlation between the pressure pulses and FTEs. Furthermore, the magnetic pressure and tension observed in the FTEs were much larger than the pressure variation in the magnetosheath pulses. Song *et al.* (1994, 1996) carried out a spectral analysis of the solar wind for six FTE case studies (not including the interval presented by Elphic *et al.*, 1994), and also found no suitable pulses. They sought to distinguish between signatures due to reconnection FTEs and those due to pressure pulses by comparing the duration of events with the inter-event period. They suggested that a sinusoidal surface wave that could realistically be expected to be generated by a pressure pulse would have a much longer wavelength than amplitude, and they assumed that the scale lengths of an FTE along the convection direction and normal to the magnetopause are of the same order. Consequently they argued that a spacecraft observation of an FTE will have a short time duration compared with the inter-FTE period, whereas on multiple magnetopause crossings due to surface waves the relative times spent in the magnetosphere and magnetosheath will vary as the spacecraft moves across the mean magnetopause, but will be of the same order. However, Sibeck and Newell (1995, 1996) refuted these arguments. They contended that a sinusoidal waveform should not be assumed, as earlier work (Sibeck *et al.*, 1989; Fairfield *et al.*, 1990) had revealed a correspondence between impulsive pressure variations generated in the foreshock with characteristic timescales greater than 1 minute and magnetospheric magnetic field enhancements. Consequently they argued that the effect of large, irregular, rapid pulses in the foreshock had been underestimated by Song *et al.* (1994). Such pulses could lead to a non-sinusoidal mag-

netopause wave which could have a comparable wavelength and amplitude. Song *et al.* (1996) claimed that Sibeck and Newell (1995) used extreme observations of parameters to justify everyday behaviour, by quoting the largest pulse amplitudes in the interval studied but counting much smaller pulses when estimating the frequency. Although Sibeck and Newell (1995) identified a correspondence between foreshock pressure pulses and enhancements in the magnetic field observed by the GOES-5/6 and AMPTE CCE satellites, Song *et al.* (1996) claimed that none of these enhancements were FTEs.

Other studies, such as Hapgood and Lockwood (1995) and Lockwood and Hapgood (1998), have used the magnetopause transition parameter (τ, Bryant and Riggs, 1989; Hapgood and Bryant, 1990, 1992) to distinguish between different FTE models. τ is a proxy for the relative position of a spacecraft within boundary layers between the magnetosphere and the magnetosheath. It is derived by fitting a curve to plasma temperature and density moments (usually electron data), projecting each data point onto the nearest point of the best-fit curve and measuring the distance along the curve to each projection. These values are then normalised to extreme values on the curve, with 0 equating to the coolest/densest part of the magnetosheath and 100 the hottest/rarest point observed in the magnetosphere. Lockwood and Hapgood (1997) showed the behaviour of τ to be consistent with a model of the observations of a spacecraft as it passes across magnetic field lines which have been reconnected for different lengths of time.

Hapgood and Lockwood (1995) examined the thickness of the LLBL in the time surrounding an FTE observed by two AMPTE spacecraft. As the FTE passed, there was very little difference between the values of τ observed by the two spacecraft, which were separated by 400 km (mostly along the magnetopause normal direction). However, ten minutes later the spacecraft observed further entries into the LLBL which were not coupled with bipolar B_N signatures; during these crossings there was often a large difference between the values of τ observed at each spacecraft, indicating that at times the boundary scale length was of the same order as the spacecraft separation. This relative thickening of the LLBL as the FTE passed was cited as evidence for the Southwood *et al.* (1988)/Scholer (1988a) reconnection FTE model, as opposed to the Sibeck (1990, 1992) model which would predict thinning of the LLBL as the surface wave passes. The LLBL entries observed later were consistent (in terms of τ) with a Sibeck (1990, 1992) wave, but no FTEs were identified in this interval. Furthermore, Hapgood and Lockwood (1995) noted that the two spacecraft should observe nested plasma and field signatures when a surface wave passes, but not when an FTE convects past. The FTE signatures were not nested, but the later LLBL crossings were.

Finally, Lockwood and Hapgood (1998) analysed the consistency of another FTE observed by AMPTE in terms of all of the above-mentioned models. Using the ion precipitation model developed by Lockwood and Hapgood (1997), they concluded that the FTE was well explained by a brief entry onto open LLBL field lines, which was predicted by both the Southwood *et al.* (1988)/Scholer (1988a) model and the pressure pulse model in the presence of ongoing reconnection.

1.5.4 Recent Developments: Four-Spacecraft Studies

The four-spacecraft Cluster mission allows the first multi-point observations in three dimensions. Initial Cluster observations of high-latitude FTEs were presented by Bosqued *et al.* (2001), Owen *et al.* (2001) and Wild *et al.* (2001). Lockwood *et al.* (2001) presented a study of a series of transient entries into the LLBL observed by Cluster during an interval of predominantly northward IMF. These entries correlated well with IMF clock angle ($\arctan[B_Y/B_Z]$) swings to near 90°, typically from less than 60°, and with ground-based observations of transient reconnection signatures. Their occurrence was consistent with sub-solar reconnection (i.e. between magnetosheath and closed magnetospheric magnetic field lines, which may occur away from the equatorial plane). Whilst the events occurring in the 'exterior' boundary layer (the newly-opened, northward-pointing magnetic field lines at the magnetopause) exhibited a weak bipolar B_N signature, those events occurring in the 'interior' boundary layer (southward-pointing field lines on the edge of the interior magnetic cusp) did not have a bipolar B_N signature at all. Lockwood argued that this was because the bipolar signature is caused (under the Southwood/Scholer bursty reconnection model) by a pressure imbalance. In the interior boundary layer events, the enhanced magnetic pressure inside the events was approximately cancelled by an observed decrease in the ion gas pressure, whereas there was a net pressure increase in the exterior boundary layer events. Cluster observations have also been been presented of FTE signatures in the cusp (Vontrat-Reberac *et al.*, 2003; Marchaudon *et al.*, 2004).

Thompson *et al.* (2004) reported a series of transient magnetic field signatures, including GSM B_Z reversals, which were observed by Cluster whilst the spacecraft were on open magnetospheric lobe field lines. The events each lasted about 1 minute, and had an approximate periodicity of 8 minutes, reminiscent of the average values calculated by Lockwood and Wild (1993) and Kuo *et al.* (1995), however they did not exhibit bipolar B_N signatures.

More recent papers have taken advantage of conjunctions between Cluster and other spacecraft. Wild *et al.* (2005) presented simultaneous observations of FTEs

at the high- and low-latitude magnetopause, using data from both Cluster and Geotail. The authors compared the location of their observations with the paths of reconnected flux tubes predicted by the model developed by Cooling *et al.* (2001), and showed that the FTEs at both latitudes could be explained by a single near-equatorial reconnection line lying between the two spacecraft. As a further test of Cooling *et al.* (2001), Wild *et al.* (2005) calculated the velocity of two of the FTEs observed by Cluster; whilst one matched that predicted by the model very well, the velocity of the other FTE was 30° from the model value. Finally, Marchaudon *et al.* (2005) presented Cluster and Double Star (TC-1) observations of FTEs on the dawn flank of the magnetopause, with TC-1 near the equatorial plane, and Cluster at higher latitudes in the southern hemisphere. The reconnection site appeared to remain active and stable in location for several hours, despite varying IMF conditions (although the IMF clock angle remained above 70°).

1.5.5 Outstanding Questions

Cluster is a valuable tool to help our understanding of many space physics phenomena, including FTEs. Four-point spacecraft observations allow advances to be made in many topics in space physics, for two reasons. First, it can help further our understanding to be able to observe processes which are occurring in two nearby regions. For example, observations can be made either side of the magnetopause; alternatively the presence of some signature on one spacecraft and its absence on another can give some idea of the scale size of a phenomenon. Second, there are several techniques which return individual physical quantities based on the variations between other quantities observed at the different spacecraft. For example, the motion of a structure, along with its gradient may be inferred from the difference in timing between observations of a parameter (e.g. plasma density, or a magnetic field component) and the knowledge of the spacecraft separation (Harvey, 1998), or the averaged currents over the volume defined by the spacecraft tetrahedron may be deduced from the curl of the magnetic field (Dunlop *et al.*, 2002).

It is clear from discussion in this chapter that much research has been carried out into FTEs in the last 27 years. However, the outstanding questions can still be phrased at a fundamental level. First, "What is an FTE?". The body of research seems to side with FTEs being generated at the dayside magnetopause preferentially under southward IMF, suggestive of a reconnection source as opposed to a pressure pulse generation mechanism. Cluster provides the opportunity to verify this, since the velocity of structures can be measured, and the motion of reconnected flux tubes will often differ from that of the surrounding magnetosheath. However, there is still the question of which of the various reconnection models (latitudinally narrow

flux tube, reconnection 'bubble' or multiple X-line) best describes the spacecraft observations at the magnetopause.

Second, "Where are FTEs created?". As noted above, there are two major models of where reconnection takes place at the Earth's magnetopause: antiparallel and subsolar component reconnection. The presence of FTEs at low latitudes during periods of B_Y-dominated IMF has been argued as evidence for subsolar component reconnection, but it is worthwhile testing this by combining four-spacecraft observations with models of FTE motion that are now available (e.g. Cooling *et al.*, 2001). Furthermore, the orbit of Cluster crosses the magnetopause at high latitudes near local noon, so it is possible to examine whether the antiparallel and component reconnection hypotheses can be distinguished when the IMF B_Y component is strong. Although one statistical study (Kawano and Russell, 1997a,b) has investigated the occurrence of FTEs during intervals of northward IMF at the post-terminator magnetopause, questions still remain from this study as to where these FTEs were generated, as they were observed at lower latitudes than would be expected.

1.6 Overview of Thesis

In Chapter 2, an introduction to the instrumentation used in this thesis. This is followed in Chapter 3 by a case study of a series of transient bursts of magnetosheath-energy plasma observed in the magnetosphere, near the high-latitude magnetopause. The magnetospheric signatures are accompanied by distinct magnetic field rotations, which are not consistent with the low-latitude understanding of FTEs as outlined above. Use of the transition parameter reveals the plasma bursts to be part of a stable boundary layer structure, and their relationship to FTE signatures observed in the magnetosheath is discussed. Chapters 4 and 5 present the results of a survey of FTEs made during the 2002/3 Cluster dayside magnetopause crossing season. Contrary to most of the earlier surveys discussed in Section 1.5.2, but similar to the results of Kawano and Russell (1997a,b), a significant number of events were observed during periods of strongly northward IMF. In Chapter 4, four-spacecraft timing analysis was used to derive the velocities of some of these northward IMF FTEs, which were compared with the model of reconnected flux tube motion developed by Cooling *et al.* (2001). In Chapter 5, the velocities of those FTEs which were observed during periods of southward or dawn/dusk-dominated IMF are studied in more detail along with the predictions of the Cooling *et al.* (2001) model, and the proportion of events which fit the antiparallel and component reconnection models is quantified. Finally, a summary of the thesis is presented along with some conclusions and potential further research in Chapter 6.

Chapter 2

Instrumentation

> The gods are just, and of our pleasant vices
> Make instruments to plague us.
> *William Shakespeare, "King Lear", Act 5 Scene 3*

2.1 The Cluster Satellites

In this chapter, an introduction to the Cluster mission is provided, along with an overview of the main instruments that produced the data that were used in the preparation of this thesis.

The European Space Agency's Cluster mission consists of a quartet of satellites. The initial launch was aborted in June 1996, destroying all four spacecraft. However, four replacement satellites were built and Cluster II[1] was launched from the Baikonur Cosmodrome on the 16th July and 9th August 2000. The satellites were launched in pairs by two Soyuz rockets into an elliptical polar orbit with an initial perigee of 4 R_E (26,000 km) and an apogee of 19.6 R_E (125,000 km) (Escoubet *et al.*, 2001). The orbital period is 57 hours.

The orbit is fixed in inertial space. As the Earth orbits the Sun, the orbital plane rotates with respect to the Sun-Earth line, and different regions of the near-Earth environment are observed through the year. The magnetopause is crossed on each orbit between November and June (the 'dayside' season); between December and May, the bow shock is also crossed, providing observations of the solar wind. The apogee of the orbit crosses the Sun-Earth line (12:00 local time) in late February. From June to November, Cluster is predominantly in the magnetotail (the 'nightside'

[1]Since launch, Cluster II has generally been referred to simply as 'Cluster'

season). Two sets of cusp crossings are made each year: at high altitudes in the dayside season, and at mid altitudes in the nightside season.

During the dayside season, the Cluster spacecraft cross the magnetopause twice per orbit, although each 'crossing' may in fact consist of several crossings if the magnetopause moves in and out across the spacecraft in response to varying solar wind conditions whilst the spacecraft are in the vicinity. The spacecraft cross the magnetopause heading outwards in the northern hemisphere, and inwards in the southern hemisphere. As a result of the high inclination of the orbit, the magnetopause is observed only at high latitudes near local noon, and at lower latitudes along the flanks. The orbits of the individual spacecraft are designed such that the quartet generally forms a tetrahedron at both magnetopause crossings each orbit, although during periods of orbital manoeuvres (to change the tetrahedron separation scale) other formations occur.

Each Cluster satellite carries an identical suite of eleven instruments which collect data that can be used to study the Earth's near-space environment. These instruments are summarised in Table 2.1.

In this thesis, data from the PEACE, FGM, CIS and EFW instruments are used. These instruments will now be discussed in more detail.

2.2 The Plasma Electron and Current Experiment (PEACE)

The PEACE instrument is an electron spectrometer which measures the three-dimensional velocity distribution of the electron population in the energy range from 0.59 eV to 26.4 keV (Fazakerley *et al.*, 2006[2]; Johnstone *et al.*, 1997). The instrument on each spacecraft consists of two 'top hat' detectors (HEEA: the High Energy Electron Analyser, and LEEA: the Low Energy Electron Analyser) and a Data Processing Unit (DPU).

2.2.1 Top Hat Analysers

A cross-section of a top hat analyser is shown in Figure 2.1. When an electron enters the aperture, it passes through a collimator and is then deflected by an electric field applied between the inner and outer deflection plates ($\boldsymbol{E}$). Only electrons with a

[2]Manuscript in preparation

PEACE	Plasma Electron And Current Experiment *Measures the electron distribution between 0.59* eV *and 26.4* keV
FGM	Fluxgate Magnetometer *Measures the 3D magnetic field with a time resolution of up to 67* Hz
CIS	Cluster Ion Spectrometry experiment *Measures the composition, mass and distribution of ions from ∼0 to 40* keV/q
EFW*	Electric Field and Wave experiment *Measures the electric field and plasma density at up to 36* kHz
EDI	Electron Drift Instrument *Measures the electric field and gradient of the magnetic field by emitting weak beams of test electrons and detecting them on their return to the spacecraft*
ASPOC	Active Spacecraft Potential Control experiment *Reduces the spacecraft potential by emission of positive ions*
STAFF*	Spatio-Temporal Analysis of Field Fluctuation experiment *Measures high-frequency (up to 4* kHz*) magnetic field fluctuations*
DWP*	Digital Wave Processing experiment *Coordinates and processes WEC measurements*
WHISPER*	Waves of High frequency and Sounder for Probing of Electron density by Relaxation experiment *Measures the total electron density by active stimulation of plasma and detection of resonances, and detects natural plasma waves between 2 and 80* kHz
WBD*	Wide Band Data instrument *Provides high-resolution measurements of electric and magnetic field oscillations between 25 and 577* kHz
RAPID	Research with Adaptive Particle Imaging Detectors *Measures suprathermal distributions of electrons (20–400* keV*), protons (40–1500* keV*) and heavier ions (10–1500* keV*)*

Table 2.1: Instruments aboard Cluster
* denotes an instrument that is part of the Wave Experiment Consortium (WEC)

specific energy, which is dependent upon $\boldsymbol{E}$, will follow the path shown in Figure 2.1 and hit a stack of two microchannel plates (MCPs). When an electron hits the MCPs, it causes a cascade of secondary electrons which amplify the signal detected by the anode by a factor of ∼1000. If an electron enters the aperture, but has too little or too much energy, it will hit one of the deflection plates and will not be detected by the anode.

In principle, a top hat analyser has a 360° field of view. However, each PEACE analyser is mounted on the side of the spacecraft such that the field of view is restricted to a 180° fan perpendicular to the spacecraft spin axis (Figure 2.2). The direction of arrival of the electron in the plane of the aperture (the polar angle) is determined from the position at which the cascade of secondary electrons hits the anode. The polar angle resolution is fixed by the fact that there are 12 separate

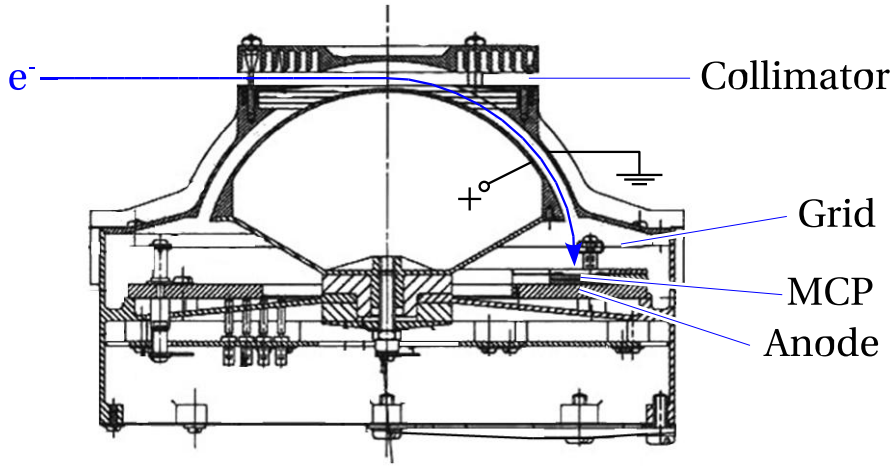

Figure 2.1: A cross-section of a top hat analyser on the PEACE instrument (after Fazakerley *et al.*, 2006[3])

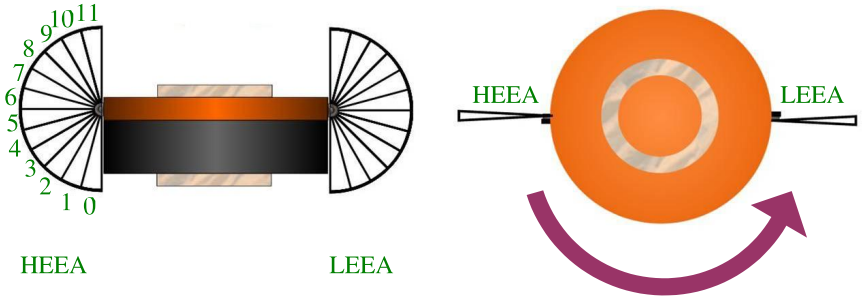

Figure 2.2: A sketch of HEEA and LEEA on the spacecraft (after Fazakerley *et al.*, 2006[3]). The analysers are mounted on opposite sides of the spacecraft. Each analyser has 12 polar bins and completes an azimuthal sweep of 2π radians every spin (4 ± 0.4 s).

polar anode segments, providing 15° resolution. As the spacecraft spins, the analyser samples varying azimuthal angles (Figure 2.2); the azimuthal angular resolution is determined by a trade-off with the energy range and resolution described below.

2.2.2 Energy and Azimuthal Angular Resolution

By varying the field $\boldsymbol{E}$, the selection energy can be adjusted. Both HEEA and LEEA are able to cover the full energy range of 0.59 eV to 26.4 keV, which is split into 88 levels. The first 16 energy levels are equally spaced linearly from 0.59 to 9.45 eV. The remaining levels are spaced logarithmically by a factor of 1.165. The major difference between the two detectors is the smaller geometric factor on LEEA; this enables the higher fluxes typical at lower energies to be observed without saturating

[3]Manuscript in preparation

the instrument and reduces MCP degradation.

The electron energy range covered by each analyser is set by commands telemetered to the spacecraft. During the first few accumulation bins of each sweep, the voltage is increased to the starting level; the selection energy is swept downwards from the top of the range (Figure 2.3). The sweep rate is synchronised to the spin period (specified to be 4 ± 0.4 s) to ensure that an integer number of sweeps are carried out each spin. The starting point of the spin is defined relative to the Sun pulse received from the spacecraft; the sweeps can be offset relative to this pulse to ensure that higher energies are being sampled when the aperture points Sunward to minimise the effect of internal photoelectrons (see Section 2.2.3). Four sweep modes are possible, which vary the azimuthal angular resolution of the instrument; the main three modes are illustrated in Figure 2.3:

- Low Angular Resolution (LAR): the instrument sweeps through 60 energy levels, at 16 sweeps per spin, resulting in an azimuthal angular resolution of 22.5°.
- Medium Angular Resolution (MAR): the instrument sweeps through 60 energy levels at 32 sweeps/spin. The energy levels are paired, so 30 energy bins are returned per sweep. This results in an azimuthal angular resolution of 11.25°.
- High Angular Resolution (HAR): the instrument sweeps through 30 energy levels at 64 sweeps/spin; azimuthal angular resolution 5.625°.
- Fixed Energy (FE): a constant energy up to 1800 eV may be maintained and high time resolution data returned at this energy. FE mode is provided for operations use.

LEEA and HEEA are commanded independently; they may operate in different modes and/or start at different energy levels. Possible combinations of energy sweep patterns are illustrated in Figure 2.4. Whilst it is usual for the instruments to operate with HEEA at a higher, but overlapping, energy range than LEEA (Figure 2.4a), it is also possible for the two sensors to sample the same energy ranges (Figure 2.4b), or two non-contiguous energy ranges (Figure 2.4c). Finally, if the two analysers operate in different angular resolution modes (LAR/MAR/HAR), one may sample a different size energy range (Figure 2.4d).

Each analyser observes the entire 3D electron plasma distribution within its energy range once every spacecraft spin, but in the overlap energy range a complete distribution can be returned every half-spin by combining the observations of the two analysers.

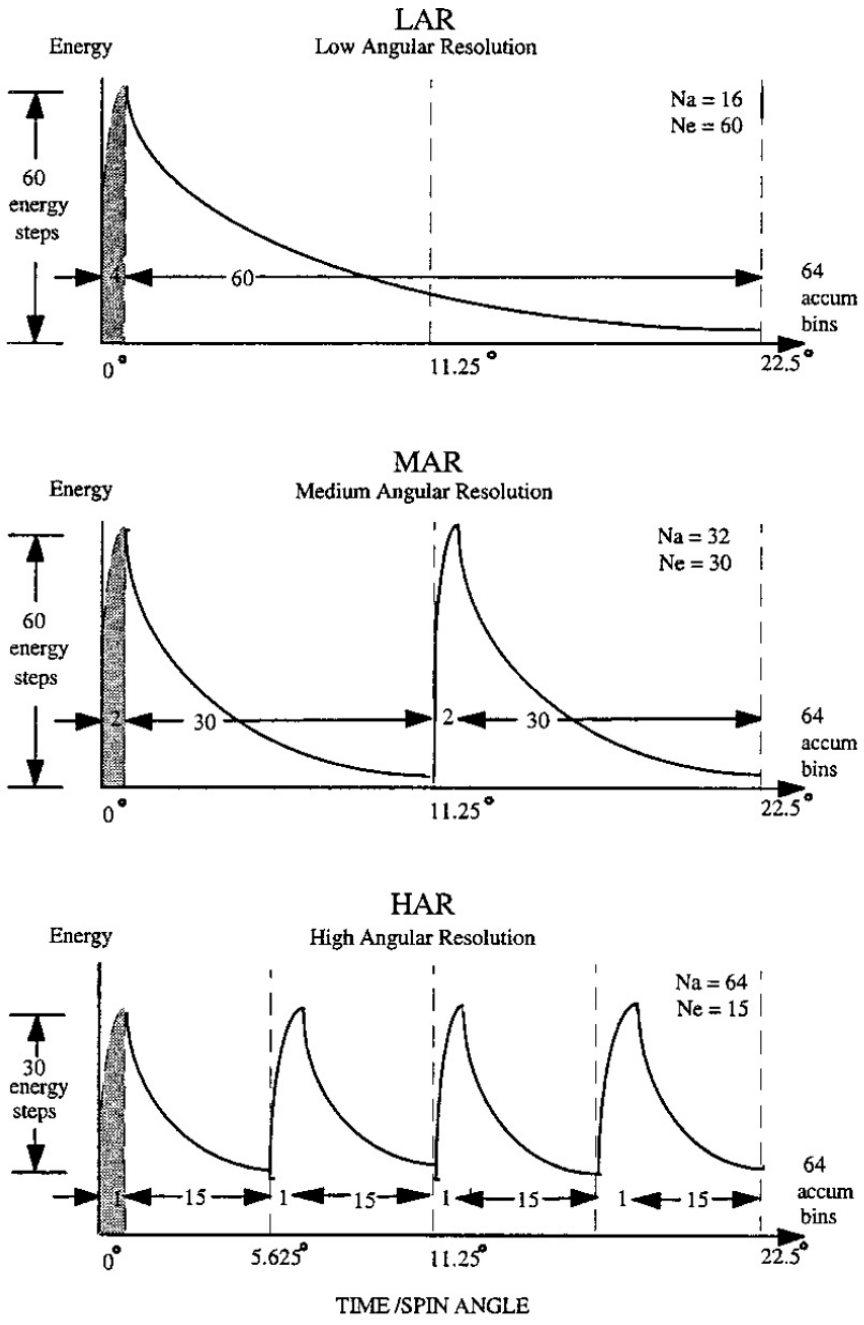

Figure 2.3: The Low, Medium and High Angular Resolution modes (from Johnstone *et al.*, 1997). These modes enable a trade-off between azimuthal angular and energy resolution.

2.2.3 Secondary Electrons and Photoelectrons

When measuring the electron plasma environments at low energies, care must be taken to remove secondary electrons and photoelectrons (Hertz, 1887; Einstein, 1905), which are not part of the natural plasma environment.

Internal secondary electrons arise from two sources within the detectors themselves. First, electrons with a higher energy than the analyser is set to measure may strike the outer deflection plate as they have not been sufficiently deflected by the

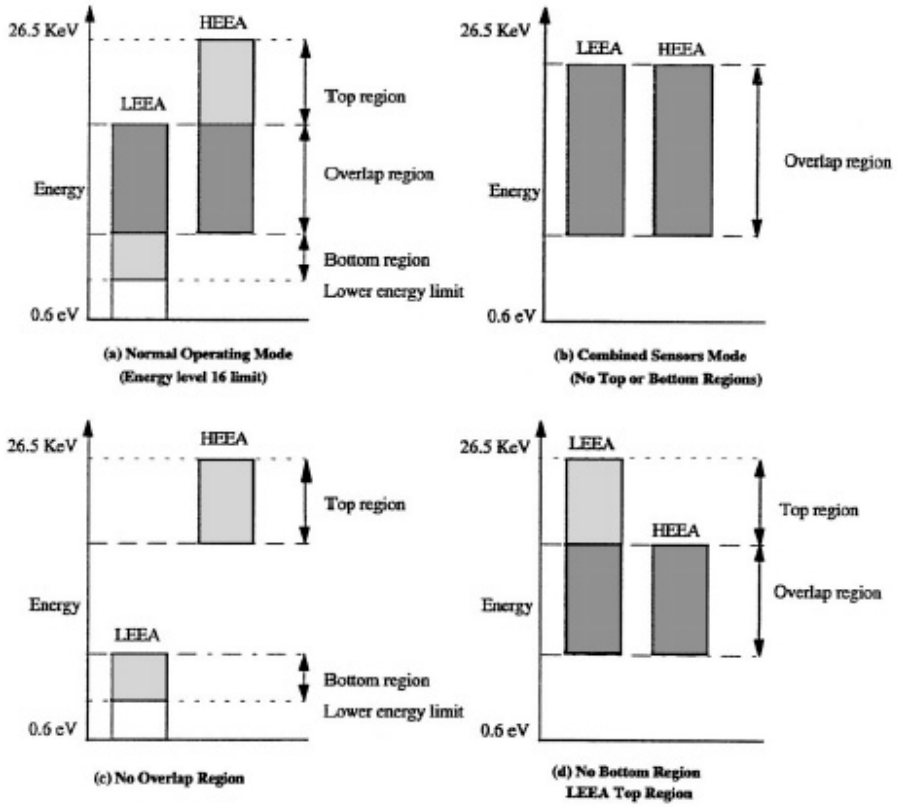

Figure 2.4: Combinations of energy sweep schemes for HEEA and LEEA (from Johnstone *et al.*, 1997). This figure also shows the names of the regions used in moment calculations: 'Overlap' refers to the energy range sampled by both instruments, 'Top' refers to the range of the higher-energy detector (usually HEEA) that is above the range of the other analyser, and 'Bottom' refers to the range of the lower-energy analyser that is below the range of the higher-energy analyser (excluding energies below 10 eV).

electric field $\boldsymbol{E}$. This may generate secondary electrons with energies between about 1 and 10 eV (Johnstone *et al.*, 1997). If this energy coincides with the selection energy determined by $\boldsymbol{E}$, the secondary electrons may pass through the analyser and be detected at the MCP. Second, internal photoelectrons of a similar energy may be generated by entry of solar ultraviolet radiation into the analyser. The effect of the latter source is minimised by offsetting the energy sweep relative to the spacecraft Sun pulse. The effect of both sources is reduced by a baffle, visible in Figure 2.1, which consists of a series of parallel plates just inside the aperture. Furthermore, the smaller aperture and field of view of the LEEA analyser also reduces the amount of solar ultraviolet radiation and number of high energy particles which can penetrate and cause secondary electrons.

Both types of secondary electron that are generated inside the instrument can be generated on the spacecraft surface. If electrons are emitted by the spacecraft, a positive electric potential will develop, and the spacecraft will attract other electrons. This continues until the net charge leaving the spacecraft equals that arriving, and the potential will be maintained. The steady state can be expressed as a current

balance:

$$I_i + I_e + I_{pe} + I_{se} = 0 \tag{2.1}$$

where I_i and I_e are the ion and electron currents in the ambient plasma environment, I_{pe} is the current due to the photoelectric effect, and I_{se} is the secondary electron current (Johnstone *et al.*, 1997). In the regions studied in this thesis (the dayside plasma sheet, lobe and magnetosheath), the major term in this current balance is the photoelectron effect. Solar ultraviolet radiation excites electrons which are emitted from the spacecraft surface (causing the current I_{pe}). This leads to a small positive spacecraft potential Φ_{sc}, which is typically up to the order of ten volts in the dayside magnetosphere, but may reach 100 V in the lobe. Spacecraft photoelectrons with an energy greater than $e\Phi_{sc}$ escape (where e is the electronic charge), but those with a lower energy are trapped in the region around the spacecraft. Some of these photoelectrons enter the analyser apertures and are detected. The net effect of the secondary electrons and photoelectrons is shown in Figure 2.5.

2.2.4 Telemetry, Commanding and Data Products

The PEACE instrument is allocated a fixed telemetry rate which depends upon the spacecraft telemetry mode (Table 2.2). Therefore a series of data products are available, which are prioritised by uploaded commands. The data products are listed in Table 2.3, and discussed in more detail below.

Telemetry mode	Bits s^{-1}	Bytes per spin (4 s spin)	
Normal mode 1	2515.42	1257.7	
Normal mode 2	1521.67	760.8	CIS priority
Normal mode 3	3540.22	1770.1	PEACE priority
Burst mode 1	15980.68	7990.3	
Burst mode 2	3658.23	1829.1	
Burst mode 3	1926.00	963.0	

Table 2.2: PEACE telemetry rates (from Johnstone *et al.*, 1997). In addition, the PEACE instruments receive extra telemetry on Cluster 2 (as a consequence of the fact that the CIS instrument does not work) and Cluster 4 (from EDI).

(a) CORE, Onboard Moments and PAD

The CORE data product is allocated the highest telemetry priority. It contains the onboard moment sums and estimated spacecraft potential. CORE is small enough in terms of bandwidth to be telemetered every spin, even when the spacecraft is allocated the lowest telemetry rate (normal mode 2) at the fastest spin rate (3.6 s).

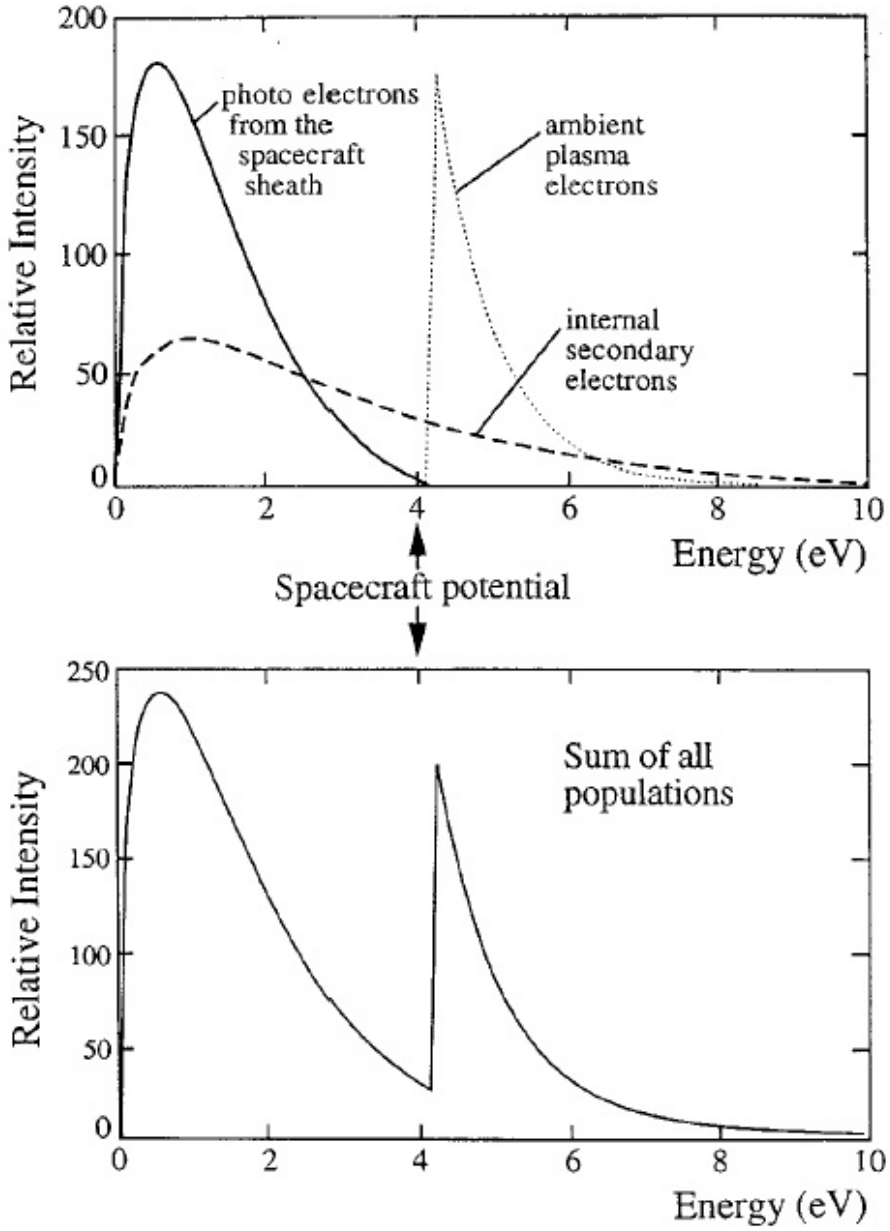

Figure 2.5: The effect of photoelectron and secondary electron populations (from Johnstone *et al.*, 1997). Photoelectrons and secondary electrons are observed with energies lower than a few electron volts, causing higher fluxes than would be otherwise be observed at such energies. These high fluxes at low energies lead to a significant effect on moment calculations (Section 2.2.4) and must therefore be corrected.

Macroscopic plasma parameters (e.g. density, velocity, temperature) are derived by integrating (taking moments) over the 3D plasma distribution in phase space ($f(\mathbf{v})$, with units of $\mathrm{cm}^{-6}\mathrm{s}^{6}$) (Baumjohann and Treumann, 1997, pp. 125-126):

The zeroth order moment gives the number density, n:

$$n = \int f(\mathbf{v}) d^3v \tag{2.2}$$

Abbreviation	Name	Size (bytes per spin)
CORE	Moments	168 (Both analysers)
CORE	Spacecraft potential	7 (Single analyser)
PAD	Pitch Angle Distribution	780 (Both analysers)
LER	Low Energy Reduced	192 (Single analyser)
3DR	3D Reduced resolution	2880 per analyser
3DX	3D reduced resolution	Variable
3DF	Full 3D resolution	23040 (Both analysers)

Table 2.3: PEACE data products, (from Johnstone *et al.*, 1997).

The first order moment gives the bulk flow velocity, $\mathbf{v}_b$:

$$\mathbf{v}_b = \frac{1}{n}\int \mathbf{v} f(\mathbf{v}) d^3v \tag{2.3}$$

The second order moment gives the pressure tensor, $\mathbf{P}$:

$$\mathbf{P} = m_e \int (\mathbf{v} - \mathbf{v}_b)(\mathbf{v} - \mathbf{v}_b) f(\mathbf{v}) d^3v \tag{2.4}$$

The trace of the third order moment gives the heat flux vector, $\mathbf{q}$:

$$\mathbf{q} = \frac{m_e}{2}\int (\mathbf{v} - \mathbf{v}_b) \cdot (\mathbf{v} - \mathbf{v}_b)(\mathbf{v} - \mathbf{v}_b) f(\mathbf{v}) d^3v \tag{2.5}$$

where m_e is the mass of an electron.

A 3D distribution is not usually telemetered on each spin, so the following on-board 'standard' moments are calculated and telemetered with the total number of counts[4] (Johnstone *et al.*, 1997):

Density (one value):

$$n = \int f(\mathbf{v}) d^3v \tag{2.6}$$

Particle flux (three values):

$$n\mathbf{v}_b = \int \mathbf{v} f(\mathbf{v}) d^3v \tag{2.7}$$

Stress tensor $\mathbf{P}'$ (six independent values):

$$\frac{\mathbf{P}'}{m_e} = \int \mathbf{v}\mathbf{v} f(\mathbf{v}) d^3v \tag{2.8}$$

Generalised heat flux $\mathbf{q}'$ (three values):

$$\frac{2\mathbf{q}'}{m_e} = \int (\mathbf{v})^2 \mathbf{v} f(\mathbf{v}) d^3v \tag{2.9}$$

[4]Standard moments are telemetered in raw units, and are calibrated and converted to the scientific formats quoted in Equations 2.6 to 2.9 on the ground before being used to calculate the bulk plasma moments in Equations 2.2 to 2.5

These moments are calculated separately on the two analysers and in three different energy ranges:

- HEEA: From the top of the HEEA energy range to the top of the LEEA energy range (Top - once per spin)
- HEEA: Energy levels overlapping LEEA (Overlap - twice per spin)
- LEEA: Energy levels overlapping HEEA (Overlap - twice per spin)
- LEEA: From the bottom of the HEEA energy range to the bottom of the LEEA energy range (Bottom - once per spin). Values below energy level 17 (approximately 10 eV) are neglected to reduce the influence of photoelectrons.

The bulk parameters (Equations 2.2–2.5) are calculated from the standard moments (Equations 2.6–2.9) as follows (Gowen and Birdseye, 1988):

$$n = n \tag{2.10}$$

$$\mathbf{v}_b = \mathbf{v}_b \tag{2.11}$$

$$\mathbf{P} = \mathbf{P}' - m_e n \mathbf{v}_b \mathbf{v}_b \tag{2.12}$$

$$\mathbf{q} = \mathbf{q}' - \mathbf{v}_b \frac{trace(\mathbf{P}')}{2} - \mathbf{v}_b \cdot \mathbf{P}' + m_e n v_b^2 \mathbf{v}_b \tag{2.13}$$

The moments calculated onboard are not always accurate. One reason is that, although the energy levels below approximately 10 eV are discarded, the presence of photoelectrons can still affect the moment calculations. The spacecraft potential can sometimes rise above 10 V; even when Φ_{sc} is below this level, the consequent acceleration of low-energy electrons within the natural plasma environment can cause a significant error. Secondly, onboard calibrations may be incorrect. Whilst new calibrations can be uploaded, once the moments have been calibrated it is not possible to correct for this factor without re-calculating new moments from a 3D distribution (see Section 2.2.4). It is therefore important to check onboard moments against moments calculated on the ground (which are not always available at spin resolution) and against similar data measured by other instruments (such as the ion velocity measured by CIS, or the electron density which can be calculated from the plasma frequency measured by EFW).

The pitch angle distribution (PAD) has the second highest telemetry priority; consequently it is received from both analysers every spin. PAD is a 2D distribution constructed from the polar bin data from the two occasions on each spin when

the magnetic field direction is within the azimuthal field of view of the analyser (Figure 2.6). To evaluate PAD in Spin 1, the DPU takes the magnetic field azimuth, evaluated at the LEEA spin boundary in Spin 0, from the FGM instrument via the inter-experiment link (IEL). The DPU selects the two azimuthal sectors which contain the field vector. The azimuthal sectors either side are also selected, and polar bin data from the six selected azimuths are stored. In Spin 2, the closest pair of azimuthal sectors stored in Spin 1 are selected using the Spin 1 magnetic field azimuth. The polar data stored from these sectors are then telemetered. Meanwhile, the azimuths stored in Spin 2 are selected based on the magnetic field azimuth from Spin 1. In the example in Figure 2.6, the magnetic field in Spin 0 lies in azimuthal sectors 3 and 19, and in polar bins 8 and 3. Therefore, in Spin 1 polar bins 8 to 11 are stored from azimuthal sectors 2 to 4, and polar bins 11 to 3 are stored from azimuthal sectors 18 to 20 (half a spin later). The magnetic field in Spin 1 (red dashed arrow) lies in azimuthal sectors 4 and 20, so these sectors would be telemetered in Spin 2 and the other stored sectors would be discarded. Polar bin 8 from the first accumulation period represents electrons moving parallel to the magnetic field, and bin 3 from the second period (half a spin later) represents antiparallel-moving electrons.

In this way, the PAD selection algorithm is able to cope with small changes in the magnetic field azimuth with time. On the ground, the PAD data is rebinned relative to the magnetic field provided by the IEL; this product is known as SPINPAD. This binning process assumes that the magnetic field has remained constant (to within ± 1 azimuthal bin) from the spin beforehand. Since this is not always a reasonable assumption, this can lead to error in the pitch-angle binning. If the magnetic field azimuth changes by more than one sector in a spin, the closest azimuthal sector data from those stored will be telemetered, but the 'correct' azimuthal data will have already been discarded. Secondly, the time stamp is that of the central azimuthal sector in the initial selection process, even if one of the adjacent sectors was telemetered; this is a discrepancy if sub-spin time resolution is required. Thirdly, when the magnetic field crosses the 180° or 360° azimuth, the algorithm fails: if the Spin 1 magnetic field in Figure 2.6 had fallen in azimuthal sectors 31 and 15 ($\boldsymbol{B'}$ – blue arrow), data from sectors 4 and 20 would still have been telemetered rather than sectors 2 and 18, as 4 & 20 are numerically closer to the field azimuth sectors. Consequently the returned data lies out of the plane of the observed magnetic field. A final point to note is that the parallel and antiparallel bins will contain the magnetic field vector if the selection process has been successful, but the vector will not necessarily lie at the centre of these bins.

It is also possible to re-bin the PAD data on the ground using high resolution magnetic field data, which is interpolated to 5 ms resolution (approximately one vector per energy step, where a step consists of a change of one energy level in

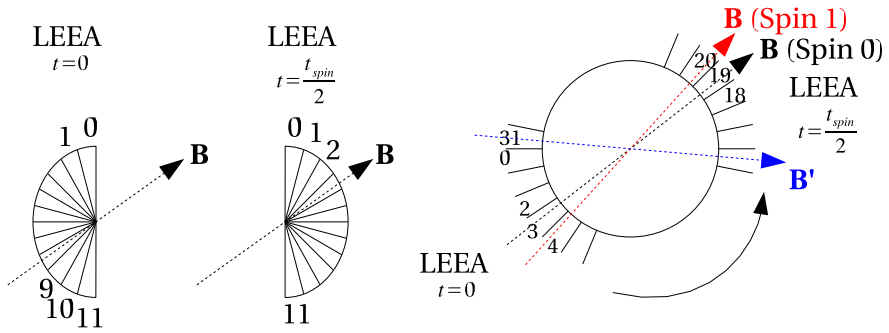

(a) Polar view (b) Azimuthal view

Figure 2.6: Selection of PAD. A magnetic field direction from the spin beforehand (Spin 0 - black dashed arrow) is passed to the DPU. This direction lies within the azimuthal field of view of the analyser twice per spin. The DPU determines these times, and returns 13 polar bins of data from the corresponding azimuthal sector and the adjacent sectors in Spin 1. In the following spin (Spin 2), the closest azimuthal sectors (stored in Spin 1) to the magnetic field from Spin 1 (red dashed arrow) are selected and the corresponding polar data are telemetered. In the example shown, the polar bins returned will be 8 to 11 from azimuthal sectors 2 to 4, and polar bins 11 to 3 from azimuthal sectors 18 to 20. The magnetic field measured in Spin 1 lies in azimuthal sectors 4 and 20, so in Spin 2 these sectors are selected from those stored and telemetered. Counts returned from polar bin 8 represent electrons observed moving parallel to the magnetic field, and counts from polar bin 3 represent antiparallel-moving electrons. If the magnetic field observed in Spin 1 is that denoted by $\boldsymbol{B'}$ (blue dashed arrow), azimuthal sectors 2 and 18 should be selected from those stored in Spin 1; however, as the magnetic field has crossed the 180° azimuth (between azimuthal sectors 15 and 16), sectors 4 and 20 are erroneously returned.

LAR mode, or two in MAR/HAR). An example of a case where SPINPAD has been incorrectly selected is shown in Figure 2.7. The left-hand half of the plot shows the SPINPAD distribution returned for one spin which encompasses 10:08:30 UT on the 25th January 2002. The bin parallel to the magnetic field is at the top of the plot; the pitch angle then increases anticlockwise to 180° which is at the bottom. A region of high differential energy flux (DEF) is present, which is centred at a pitch angle of approximately 135°. However, the magnetic field at this time changed rapidly; when the PAD data is rebinned to the high-resolution magnetic field on the ground, this region of high DEF becomes field-aligned (0° pitch angle). The rebinned distribution is shown in the right-hand half of the plot, which shows pitch angle bins clockwise from 0 to 180°. The part of the plasma distribution that was antiparallel to the actual measured magnetic field (as opposed to the field from the previous spin, returned by the IEL) was discarded in the selection of the PAD azimuth. Hence there is a data gap between 150-180°. Note, however, the start of a region of higher DEF antiparallel to the magnetic field in the 135° pitch-angle bin.

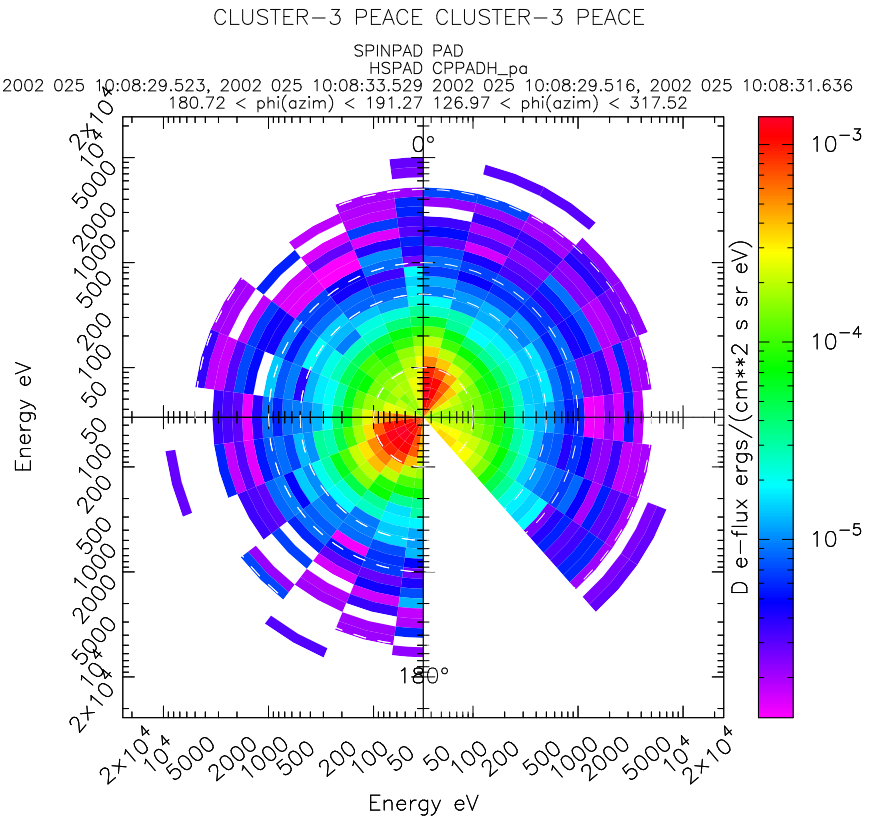

Figure 2.7: An example of SPINPAD and rebinned PAD. The left-hand half of the figure shows the SPINPAD distribution from the spin encompassing 10:08:30 UT on the 25th January 2002. The segment immediately at the top (marked 0°) is the parallel bin; pitch-angle increases anticlockwise until the bottom of the figure (180°). The right-hand half of the figure is a mirror image in pitch-angle, but shows the PAD data rebinned on the ground to the high resolution magnetic field data. A peak in differential energy flux around the 135° bin in the SPINPAD data (left) is shown to be incorrectly binned; in the rebinned PAD data (right), the peak exists around 0°. This error arises from the fact that the magnetic field cannot be assumed to be constant between spins; consequently the PAD azimuth was incorrectly selected on board, and a data gap exists in the rebinned data from 150-180°.

(b) LER

Low Energy Resolution (LER) data is usually allocated priority immediately after CORE. This product consists of the linear section of the energy sweep (0.59 to 9.45 eV); it is provided for operations use as it can be used to evaluate the spacecraft potential in case the EFW instrument fails. The potential is necessary to remove the effects of photoelectrons (discussed in Section 2.2.3).

32 count spectra are obtained (8 successive azimuth sweeps and 4 successive polar bins) with an energy range of the lowest 16 bins in the sweep. The spacecraft potential can be evaluated from these spectra by locating first the maximum count rate in this energy range (the peak of the secondary electron distribution) and then the energy of the minimum count rate which follows (marked in Figure 2.5). This provides 64 values; the mean, variance, and maximum/minimum values are then

telemetered.

Whenever possible a 3D distribution of the low-energy range (the lowest 16 energy bins, in 8 azimuthal sectors per spin, which are alternated on a spin-by-spin basis) is telemetered for further analysis on the ground.

(c) 3D Distributions and Ground Moments

Occasionally, a full 3D distribution is transmitted, primarily for cross-calibration (3DF). 3DF consists of all 12 polar bins and all energy and azimuthal angular bins (the number of which depends on the angular resolution mode, as discussed in Section 2.2.2). Alternatively the distribution can be halved in each dimension (resulting in a one-eighth distribution), which is known as 3DR. A reduction in the energy range can be specified by the instrument commands, or pairs of energy/polar angle bins can be summed to reduce the telemetry bandwidth (3DX).

If a 3D distribution has been received on the ground, the moment integrals (Equations 2.2–2.5) can be re-evaluated. This has two major advantages: first, the measured spacecraft potential can be accounted for. All electrons observed with energies below the spacecraft potential are photoelectrons, and are therefore discarded. Furthermore, the observed energy of the remaining (ambient) electrons is corrected by subtracting the spacecraft potential. Second, ground calibrations for the analysers can be used, improving accuracy. Hence ground moments can be produced at the time resolution with which 3D distributions are received. This is typically spin rate in burst mode, and in normal mode on Cluster 2 (where PEACE has a higher telemetry rate due to the fact that the CIS instrument does not function on that satellite). In normal mode, 3D distributions are telemetered at a lower time resolution on Cluster 4 (as PEACE receives extra telemetry from the non-functioning EDI instrument), and at an even lower resolution on Clusters 1 and 3 (e.g. 30 s).

All four instruments are currently operational.

2.3 The Fluxgate Magnetometer (FGM)

The FGM instruments (Balogh *et al.*, 1997, 2001) on each of the Cluster spacecraft measure the magnetic field in the plasma environment around the spacecraft. Each instrument consists of two tri-axial magnetic field sensors on one of the spacecraft booms (a primary and a secondary sensor), and a Data Processing Unit (DPU).

Either sensor can be designated as the primary/secondary sensor by telemetered command. Each sensor measures the three-dimensional magnetic field at a range of possible resolutions (Table 2.4). All three components are measured using the same range and resolution at any given time. The selection of the instrument range/resolution can either be controlled by telemetered commands, or automatically determined by the DPU. If automatic selection is used, the DPU continuously monitors each component of the magnetic field vector; if a component exceeds 90% of the extreme values measurable in the current resolution mode, the range is increased. If all three components drop below 12.5% of the range extrema, the range is decreased. The ranges were selected to allow good resolution in both the solar wind, where field magnitudes were expected to be between 3 and 30 nT, and magnetosphere, where values can reach about 1000 nT on the orbit of Cluster. The ability to override the automatic range selection is included for test purposes and in case the automation process fails.

Range number	Range	Resolution
2	–64 nT to +63.97 nT	7.8×10^{-3} nT
3	–256 nT to +255.87 nT	3.1×10^{-2} nT
4	–1024 nT to +1023.5 nT	0.125 nT
5	–4096 nT to +4094 nT	0.5 nT
7	–65536 nT to +65504 nT	8 nT

Table 2.4: FGM data range and resolution modes (From Balogh *et al.*, 2001). Ranges 2–5 are used on Cluster; range 7 was only used for ground testing.

The primary sensor on each satellite samples the magnetic field at 201.793 Hz, but the available bandwidth does not allow all vectors to be telemetered. Consequently, the vectors are filtered by the DPU to a lower time-resolution, which varies between the primary and secondary sensors and according to the spacecraft telemetry mode (Table 2.5). Filtered vectors are queued and then telemetered.

The instrument includes a Micro Structure Analyser (MSA), which is normally used for storing short periods of high-resolution data. However, when no telemetry bandwidth is available to the spacecraft the MSA can instead be used to store spin-rate vectors from the primary sensor. The stored vectors are then telemetered in the Burst Mode 3 data dump, which occurs twice per orbit.

The magnetic field vector components are converted from a spinning reference frame to a despun reference frame and converted to science units using calibration data on the ground. The vectors are usually also averaged to a lower time resolution for scientific analysis. In this thesis, FGM data are used at both spin resolution ($\sim$0.25 Hz) and 5 Hz.

Preliminary in-flight calibrations reported by Balogh *et al.* (2001) show that all

Spacecraft telemetry (TM) mode	FGM TM mode	Vectors per second (Primary sensor)	Vectors per second (Secondary sensor)
Nominal modes 1,2,3	A	15.519	1.091
Burst mode 2	B	18.341	6.957
	C	22.416	3.011
Burst mode 1	D	67.249	7.759
Burst mode 3	F	MSA dump	

Table 2.5: FGM time resolution modes (From Balogh *et al.*, 2001). In periods where there is no telemetry bandwidth from the satellite to Earth, spin-rate vectors are stored in the Micro Structure Analyser (MSA), and downloaded later when the spacecraft enters Burst Mode 3.

components of the magnetic field are measured with an accuracy of almost 0.1 nT. At the time of writing this thesis, all four instruments are in full working order.

2.4 The Cluster Ion Spectrometry Experiment (CIS)

The Cluster Ion Spectrometry experiment (Rème *et al.*, 2001) works on similar principles to PEACE. CIS consists of two top-hat analysers on each spacecraft which detect positively charged ions, and a Data Processing System (DPS). The analysers are:

- the Composition and Distribution Function analyser (CODIF), which measures the mass per charge composition with a polar angular resolution of 22.5°, and an azimuthal resolution of 11.25°.
- the Hot Ion Analyser (HIA), which does not provide mass resolution, but which has a better polar angular resolution (5.6°/11.2°) and an azimuthal resolution of 5.6°.

The HIA analyser has two 180° field-of-view sections parallel to the spin axis. The two sections have different sensitivities. The "low gain" section was designed for use in the solar wind, and was intended to be split into eight central anodes with angular resolution of 5.625° and eight other anodes with a resolution of 11.25°. However, calibrations have shown these resolutions to be approximately 5.1° and 9.7° respectively. The "high gain" section was designed to be split into sixteen anodes, each with a resolution of 11.25°, but again calibration has shown the resolution to be nearer 9.7° (Rème *et al.*, 2001). Two-dimensional distributions can be sampled every 62.5 ms, providing an azimuthal resolution of 5.625°, with a complete

three-dimensional distribution being observed once every spacecraft spin. The sensor energy/charge range is fixed at 5 eVq^{-1} to 32 $keVq^{-1}$, and the analyser resolution $\Delta E/E$ is approximately 17%. The analyser has an entrance aperture which collimates the observed ions, determines the geometric factors and reduces the effects of solar UV radiation.

CODIF also consists of two 180° field-of-view sections; each half contains eight polar anodes with 22.5° angular resolution. A two-dimensional distribution can be measured 32 times per spin, resulting in an azimuthal resolution of 11.25°. A complete 3D distribution function is measured by the main sensors each spacecraft spin. The sensor covers the energy/charge range 20 eVq^{-1} to 38 $keVq^{-1}$ with energy resolution $\Delta E/E$ of about 16%. CODIF consists of an electrostatic analyser which provides the energy-per-charge, and a time of flight section which provides the mass/charge ratio. Like HIA, the two halves of CODIF operate at two different sensitivities. The two halves are designed such that at least one half usually has count rates which are statistically meaningful, without saturation occurring. However, in the solar wind H^+ ions often saturate both CODIF detectors; in this region HIA data from the low-gain mode should be used.

CODIF also includes a 'Retarding Potential Analyser' which enables ions with energies as low as the equivalent of the spacecraft potential to be detected. This mode is rarely used. When active, only low energy ions are detected by CODIF.

The following onboard moments are calculated at spin resolution from CODIF (H^+, He^+, He^{++} and O^+) and HIA (c.f. PEACE moments, Section 2.2.4):

- particle density
- the three components of the flow vector
- the six unique components of the momentum flux tensor
- the ion heat flux vector

A large number of scientific telemetry products, listed by Rème *et al.* (2001), are available, a subset of which are telemetered. The products include the onboard moments, one-, two- and three-dimensional distributions and pitch-angle distributions. The priority with which the various products are telemetered can be set according to the spacecraft telemetry mode, the bandwidth-sharing between HIA and CODIF, and the plasma environment. When three-dimensional distributions are telemetered, ground moments may also be calculated (see Section 2.2.4). Whilst use of ground moments allows better calibrations to be applied, onboard moments returned by

CIS are generally more reliable than those telemetered from PEACE for two reasons. First, the absence of an equivalent to the photoelectron population means count rates are not artificially raised. Second, the kinetic energy of typical ions in the plasma environments observed by Cluster is large enough that the spacecraft potential does little to retard the ions. However, near magnetospheric boundaries (such as the magnetopause), the HIA and CODIF sensors are often in the wrong sensitivity mode as mode changes are commanded in advance based on predicted boundary crossings. This can lead to misleading moment data. Furthermore, HIA is only operational on Clusters 1 and 3, whilst CODIF is only operational on Clusters 1, 3 and 4. A degradation of one MCP quadrant on the Cluster 3 CODIF sensor affects the accuracy of V_Z measurements made by this instrument, although this has been improved by onboard software patches made in September 2001.

2.5 The Electric Fields and Waves Experiment (EFW)

The Electric Fields and Waves experiment (EFW: Gustafsson *et al.*, 2001) consists of two pairs of probes on the spacecraft booms. The instrument is therefore able to measure the electric field in the spin plane of the spacecraft, and the probe-to-spacecraft electric potential difference. Whilst there may be a small potential difference between the probes and the background plasma several Debye lengths from the spacecraft (i.e. outside the sheath of electrons formed by spacecraft charging), the probe-to-spacecraft potential does provide a good measurement of the spacecraft potential relative to the background plasma. This helps to illustrate in spectrograms the extent of the photoelectrons; consequently most PEACE spectrograms in this thesis have the EFW probe-to-spacecraft potential overplotted to aid the eye. The potential is also used to determine which parts of the spectrum are removed in the calculation of ground moments, and the energy by which the remainder of the observed electron population is shifted to determine the 'natural' distribution.

2.6 Active Spacecraft Potential Control (ASPOC)

The effects of photoelectron contamination on the PEACE instrument (Section 2.2.3), and to a lesser extent CIS, can be reduced by the operation of the Active Spacecraft Potential Control experiment (ASPOC: Torkar *et al.*, 2001). AS-

POC consists of two emitter modules which each have a four emitters. Each emitter is a solid tungsten needle with a tip radius of between 2 and 5 μm, which ejects a high energy indium ion beam along the spacecraft spin axis. As the ions have a large gyroradius, they do not return to the spacecraft and hence lower the (positive) spacecraft potential. This allows some of the photoelectron population trapped in the spacecraft sheath to disperse, reducing the number of photoelectrons which are detected by the instruments. The emission current can be varied in response to the spacecraft potential, which the instrument receives from EFW via the inter-experiment link; in the event of an EFW instrument failure, the potential can be supplied by PEACE. Each emitter has a reservoir of 250 mg of indium, which allows 4,000 hours at an emission current of 10 μA. Only one emitter per spacecraft is operated at a time, allowing a nominal lifetime of 32,000 hours.

Two of the instruments are now defunct; the other two are still technically operable, but are unreliable and therefore not used. When the instruments were operational, they were active on alternate orbits for a maximum of seven hours at a time (seven hours on the outbound section of the orbit, seven hours on the inbound section and sometimes seven hours near apogee).

Chapter 3

Flux Transfer Events and Boundary Layer Structure

No FT, No Comment.
Financial Times advertising slogan

3.1 Introduction

On the 25th January 2002 between 10:00 and 12:00 UT, the four Cluster spacecraft passed through the northern high-latitude cusp, the dayside magnetosphere and into the magnetosheath in a linear formation. In the magnetosphere the PEACE electron spectrometers on the four spacecraft all observed a series of transient bursts of magnetosheath-like plasma, but without bipolar magnetic signatures in the magnetopause normal component as might be expected if the plasma had been injected by transient reconnection (FTEs). Reordering the data using the magnetopause transition parameter reveals that these plasma observations, the related variations in the magnetic field and the balance of magnetic and thermal gas pressures are consistent with transient entries into a stable high-latitude boundary layer structure. However, once some of the spacecraft entered the magnetosheath, FTE signatures were observed outside the magnetopause at the same time as some of the boundary layer entries occurred at the other spacecraft inside. Thus, (a) the lack of a bipolar B_N signature is inconsistent with the traditional picture of a magnetospheric FTE, and (b) the cause of the observed entry of the spacecraft into the boundary layer (pressure pulse or passing magnetosheath FTE) can only be determined by simultaneous spacecraft observations in the magnetosheath.

So far, the reconnection/pressure pulse debate has largely been constrained to

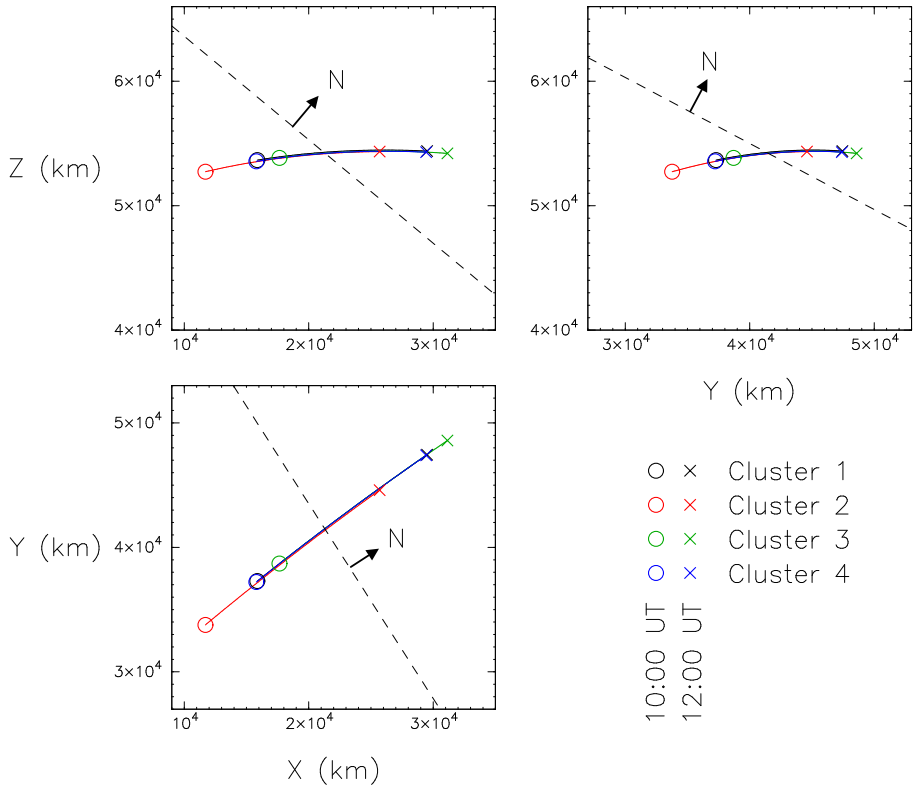

Figure 3.1: The Cluster orbit traces from 10:00 UT (marked by circles) to 12:00 UT (crosses) on the 25th January 2002, in the GSE Z-X (top left), Z-Y (top right) and Y-X (bottom left) planes. The traces are plotted in the standard Cluster colours shown in the key. As this interval occurred during a period of spacecraft manoeuvres, the spacecraft were oriented in a string formation as they crossed the magnetopause (between 10:41 and 11:12 UT), rather than a tetrahedron. Clusters 1 and 4 were within 160 km of each other throughout the interval. The normal vector $\hat{\boldsymbol{N}}$ derived in Section 3.6 has also been projected into the plane of each panel, along with the intersection of the corresponding magnetopause plane with the spacecraft orbits.

lower latitudes (see Section 1.5.3). In this chapter, it is extended it to higher latitudes by an analysis of two events from the 25th January 2002 (also published by Fear *et al.*, 2005a). In both cases, spacecraft that were initially within the magnetosphere observed signatures consistent with the spacecraft moving deeper into the observed boundary layer structure; however in the second example two Cluster spacecraft were in the magnetosheath, and they observed traditional FTE signatures.

3.2 Spacecraft Location

On the 25th January 2002 the four Cluster spacecraft made an outbound pass through the northern magnetosphere into the magnetosheath at 15h MLT. Figure 3.1 shows the positions and relative separations of the spacecraft in GSE during the period of interest between 10:00 UT (denoted by circles) and 12:00 UT (denoted by crosses). A period of orbital manoeuvres was under way, so as the spacecraft crossed the magnetopause they were in a linear formation, rather than a tetrahe-

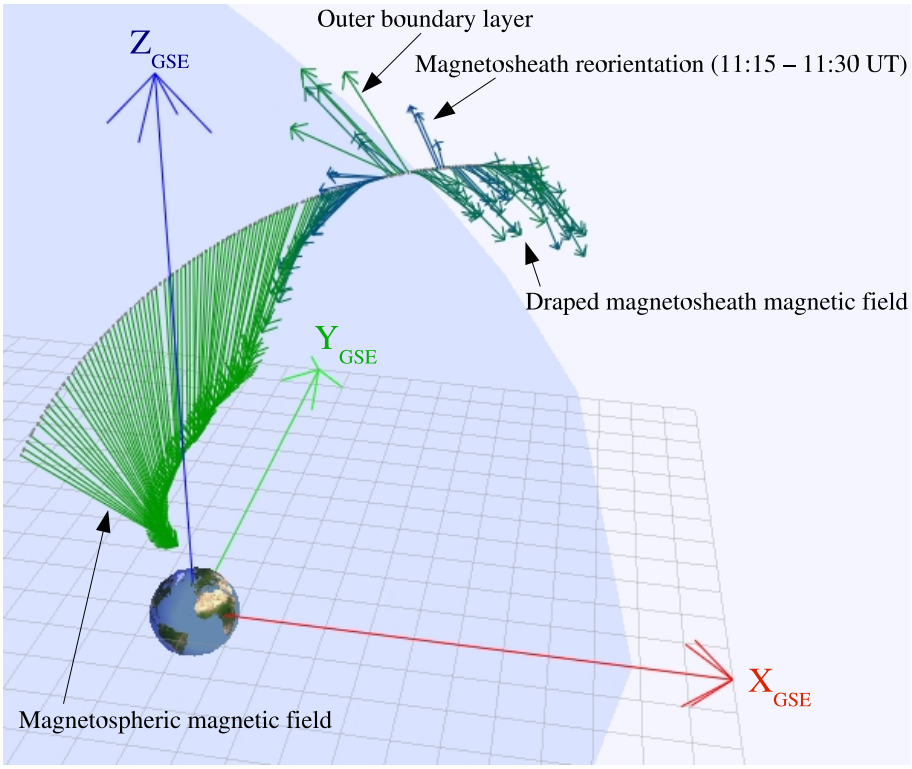

Figure 3.2: The orbit of the Cluster spacecraft from 04:30 to 13:35 UT. The grey line marks the orbit of Cluster 3, and superimposed onto the trace are arrows representing the magnetic field observed by FGM. The magnetic field vectors are sampled at regular intervals, and have been labelled with the interpretation provided in Section 3.5. The magnetopause is denoted by the darker blue shaded surface; it is based on the Sibeck *et al.* (1991) model but has been scaled to fit the observed magnetopause crossing time.

dron. Cluster 3 led the formation, followed by Clusters 1 and 4 (which were relatively close together) and then Cluster 2. A three-dimensional view of the orbit of Cluster 3 is shown in Figure 3.2.

3.3 Instrumentation and Data

In this study, spectra and moments from the Plasma Electron and Current Experiment (PEACE), together with supporting data from the Flux Gate Magnetometer (FGM), the Cluster Ion Spectrometer (CIS) and the Electric Field and Wave experiment (EFW), are employed; these instruments are discussed in Chapter 2. Supporting IMF data are provided by the ACE MAG instrument (Smith *et al.*, 1998), lagged by a delay time calculated from the solar wind velocity observed by the ACE SWEPAM instrument (McComas *et al.*, 1998).

On-board temperature and density moments, calculated using on-board calibrations and not corrected for the spacecraft potential, were telemetered by PEACE on all four spacecraft during the period of interest. These are used in this study as they

are available at spin resolution (4 s), rather than ground moments derived from 3D reduced energy/angular resolution distributions (3DR) which are not available at spin resolution on Clusters 1, 3 and 4 during this interval. The effect of the non-zero spacecraft potential is minimised by the use of on-board moments from HEEA only. During this interval, HEEA covered the energy range of 30 eV to 26 keV; the four spacecraft potentials remained comparatively low, with a peak value of 18 V.

All proton velocities and pressures presented here are derived from CIS-CODIF ground moments, which are available at spin resolution from Cluster 4, and lower time resolution from Clusters 1 and 3. A dead-time correction has been applied to the Cluster 1 and 4 moments to improve accuracy in the magnetosheath, however this correction could not be applied to the data from Cluster 3 due to degradation of one quadrant of the CODIF sensor. Data are unavailable from CIS on Cluster 2. Magnetic field data from the FGM instrument are presented at both 5 Hz and spin resolution (0.25 Hz), as appropriate. The spacecraft potential measured by EFW is over-plotted on all spectrograms at spin resolution.

3.4 Data Overview

Figure 3.3 shows two hours of Cluster and ACE data (10:00 – 12:00 UT). The top four panels are spectrograms of the differential energy flux (DEF) measured by PEACE, averaged over all pitch angles and derived from SPINPAD. This shall be referred to as the omnidirectional DEF. The spacecraft potential is over-plotted on each panel as a red line; all electrons below the equivalent energy are caused by photoionisation of the spacecraft or by secondary electrons, and are not part of the natural plasma environment. The next four panels show (in GSE coordinates) the magnetic field observed by FGM (in standard Cluster colours: Cluster 1 in black, Cluster 2 in red, Cluster 3 in green and Cluster 4 in blue), and the magnetic field observed by the ACE MAG instrument (purple line), which has been lagged by a calculated propagation time of 75 minutes and multiplied by a factor of four. The Cluster FGM and ACE MAG data are shown at 4 and 16 s resolution respectively; a time-sampled subset of the Cluster 3 FGM data are also shown in Figure 3.2. The penultimate panel contains the total pressure observed by Clusters 1 and 4, using data from the FGM and CODIF instruments. The bottom panel shows the transition parameter (τ) for each spacecraft, which will be discussed in detail in Section 3.5. The magnetopause crossing of each satellite is indicated by a red vertical line (Cluster 3: 10:41 UT, Clusters 1 and 4: 10:46 UT, and Cluster 2: final crossing at 11:12 UT), and two periods that will be the subject of detailed discussion in this chapter are highlighted by purple boxes (centred on 10:08 and 10:52 UT).

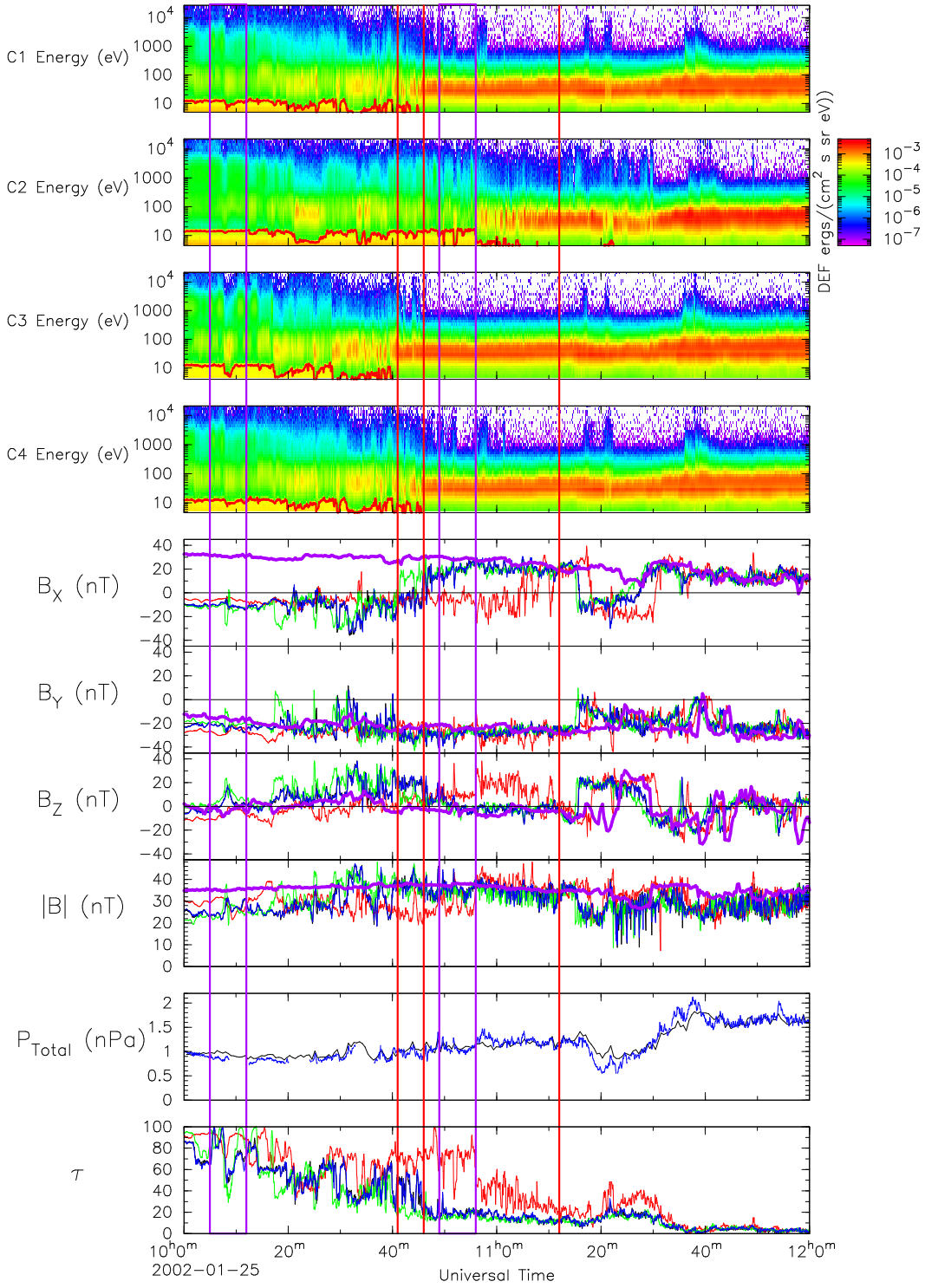

Figure 3.3: An overview of the PEACE and FGM data and the interplanetary magnetic field (IMF). The top four panels are spectrograms of the omnidirectional electron differential energy flux observed by the PEACE instruments on Clusters 1, 2, 3 and 4. The next four panels show the magnetic field observed by FGM on Clusters 1, 2, 3 and 4 in black, red, green and blue respectively in GSE coordinates. The magnetic field observed by ACE, lagged by 75 minutes and multiplied by a factor of 4, is over-plotted in purple. The penultimate panel is the total pressure observed at Clusters 1 and 4 (calculated from the magnetic pressure and the thermal pressure derived from on-board CODIF moments corrected for dead-time effects). The bottom panel shows the magnetopause transition parameter calculated from the PEACE on-board moments. The magnetopause crossings made by Clusters 3, 1 and 4, and 2 are shown by red lines at 10:41, 10:46 and 11:12 UT respectively, and the events analysed at 10:08 and 10:52 UT are indicated by purple boxes.

Between 10:00 and 12:00 UT the lagged interplanetary magnetic field (IMF) was generally stable and dominated in the GSE clock-angle (Y-Z) plane by a negative B_Y component, whilst B_Z varied between slightly positive and slightly negative values. The clock angle (not shown) was close to -90° until 11:20 UT. At the start of the interval shown, the PEACE instrument on each spacecraft observed a magnetospheric electron plasma distribution (a peak differential energy flux of $\sim 10^{-4}$ ergs $(\mathrm{cm}^2\,\mathrm{s}\,\mathrm{sr}\,\mathrm{eV})^{-1}$ at energies of ~ 1 keV) and FGM observed a relatively steady magnetic field of $\sim (-10, -20, 0)_{GSE}$ nT. The near-zero component of the magnetospheric magnetic field in Z_{GSE} indicates that the spacecraft were located near the lip of the magnetospheric cusp, where B_Z changes from positive to negative on closed magnetospheric field lines. (During this interval, the rotation angle between GSE and GSM was under 4°). In the time leading up to the magnetopause crossings, intervals of plasma of magnetosheath energy (~ 100 eV) and differential energy fluxes of up to 10^{-3} ergs $(\mathrm{cm}^2\,\mathrm{s}\,\mathrm{sr}\,\mathrm{eV})^{-1}$ were observed from time to time, some of which corresponded to a rotation of the magnetic field which was enhanced in -B_X and +B_Z. In these rotations, B_Y was diminished, and sometimes turned positive. At the times indicated in red, the spacecraft crossed the magnetopause into the magnetosheath. Magnetopause crossings (defined as the final entry into the magnetosheath on each spacecraft) were determined by the appearance of an isotropic electron distribution at ~ 100 eV and a magnetic field rotation to $\sim (20, -20, -5)_{GSE}$ nT. The Cluster 2 crossing is not as clear in the PEACE spectrogram, however the magnetic field data suggest that there were four transient magnetosheath entries, with the last occurring at 11:12 UT (seen most clearly in the B_X panel). The differential energy fluxes observed at ~ 100 eV in the magnetosheath were higher than for the plasma at similar energies inside the magnetopause. A magnetic field reorientation, corresponding to a similar reorientation observed upstream by ACE, was observed in the magnetosheath between 11:15 and 11:30 UT. The total pressure remained relatively steady at $\sim 1 \pm 0.3$ nPa until the magnetosheath magnetic field reorientation occurred at 11:15 UT.

3.5 Boundary Layers and the Magnetopause Transition Parameter

To aid discussion of this interval, the magnetopause transition parameter (τ) is introduced. It was calculated by fitting a curve to a $\log_{10} - \log_{10}$ scatter plot of electron density against perpendicular electron temperature using all data points between 10:00 and 12:00 UT for each spacecraft (Figure 3.4). Detailed intercalibration between electron moments from different spacecraft would have required

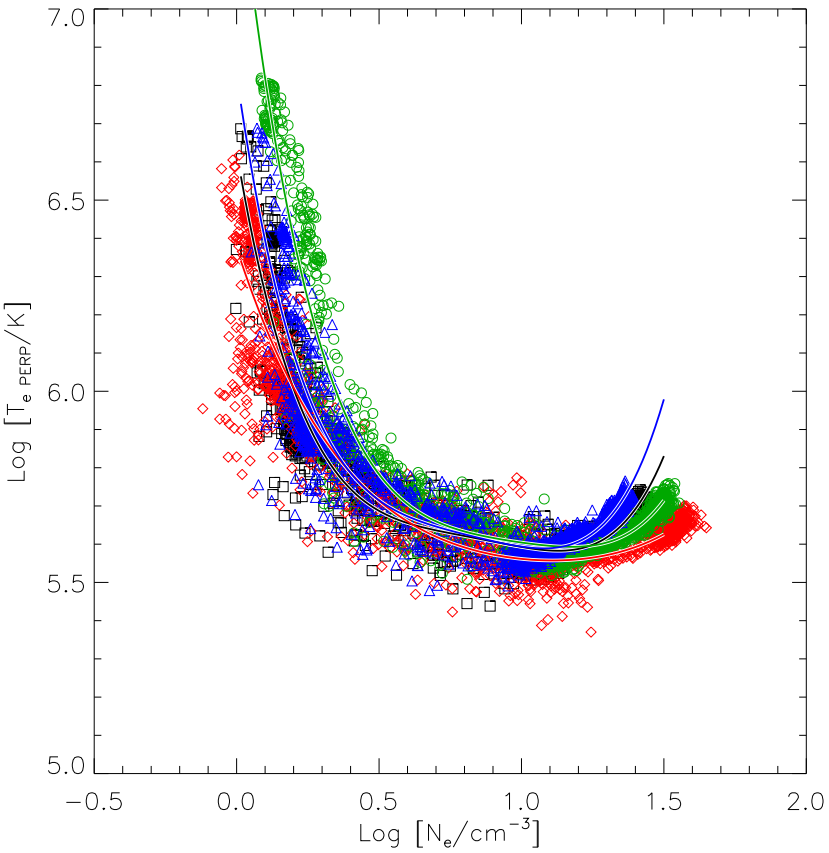

Figure 3.4: A scatter plot of the perpendicular electron temperature against the electron density derived from PEACE on-board moments calculated using data from the HEEA sensor on each Cluster spacecraft. A fourth order polynomial curve was fitted to the points from each spacecraft separately (shown). Each data point was projected onto the curve corresponding to the same spacecraft, and the distance along the curve to each projected point was converted to the transition parameter by normalising to extreme values.

the use of ground moments, which would have lowered the time resolution on Clusters 1, 3 and 4. Since all that is required to define the relative position of a spacecraft within the boundary layer is a consistent variation in the density and temperature as the layer is crossed, on-board moments from HEEA were used. As the data had not been inter-calibrated, there were slight differences in the temperature/density curves for each spacecraft, which are visible in Figure 3.4. Consequently, best fit curves (4th order polynomials shown in Figure 3.4) were calculated separately for each spacecraft. All data points were projected onto the nearest point of the corresponding curve. The projected points at the end of each curve were defined as 0 (in the magnetosheath) and 100 (in the magnetosphere) and the distance of each projected point along the curve, normalised to the extrema, was defined as τ. The resulting transition parameter values for each spacecraft are plotted in the bottom panel of Figure 3.3. The general trend in τ was a decrease until each spacecraft crossed the magnetopause, after which it stayed low. A brief enhancement of τ within the magnetosheath coincided with the magnetic field reorientation observed between 11:15

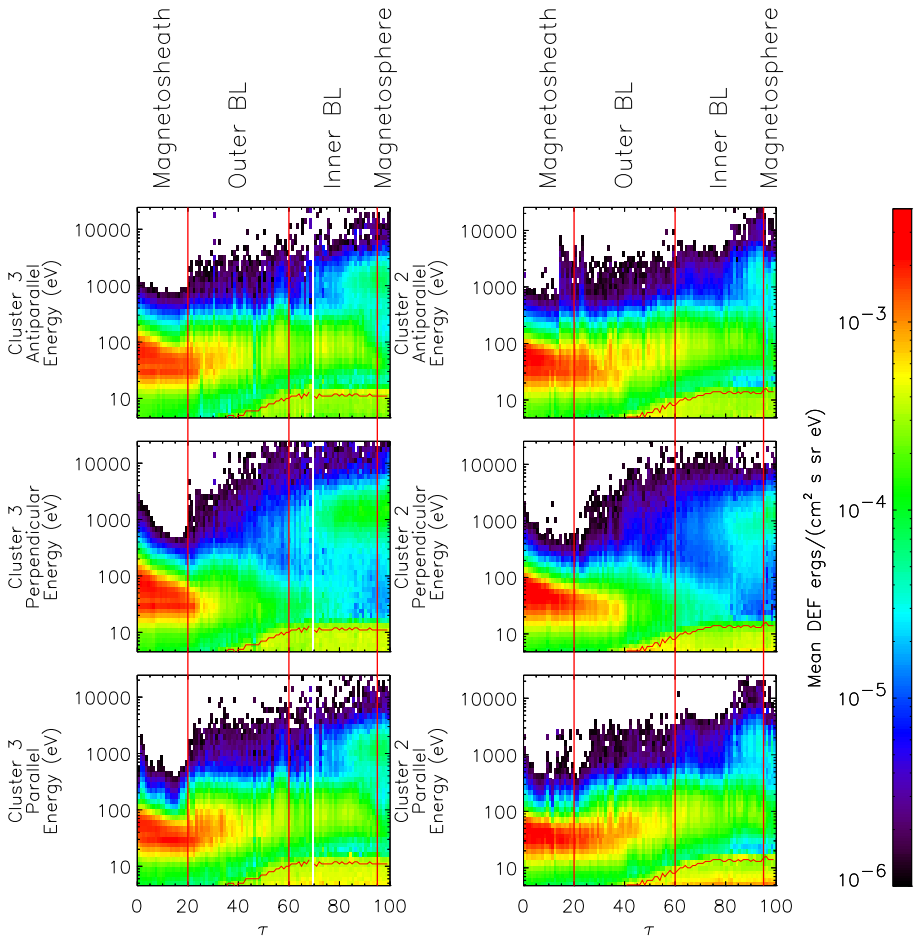

Figure 3.5: Electron spectrograms from the first (Cluster 3, left-hand column) and last (Cluster 2, right-hand column) spacecraft to cross the magnetopause, reordered by transition parameter. Although the transition parameter values were derived from on-board moments from the HEEA sensors, both HEEA and LEEA data are shown in each panel. The top, middle and bottom rows show electron fluxes antiparallel, perpendicular and parallel to the magnetic field respectively. A stable boundary layer structure exists since there is little change between the structure observed at Clusters 3 and 2; similar structure is also observed by Clusters 1 and 4. The regions identified in Section 3.5 (magnetosphere, inner and outer boundary layers and magnetosheath) are labelled, separated by red vertical lines.

and 11:30 UT, as a region of solar wind with lower density arrived. After 11:30 UT, a region of solar wind at higher pressure arrived, which was associated with lower values of τ.

Figure 3.5 shows spectrograms of the PEACE HEEA and LEEA data from the first and last spacecraft to cross the magnetopause (Cluster 3 and Cluster 2, which crossed the magnetopause thirty minutes apart) in the antiparallel, perpendicular and parallel pitch angle bins ordered by transition parameter rather than time. The data have been rebinned to the true pitch angles on the ground (see Section 2.2.4). The mean spacecraft potential is superposed as a red line. The general similarity of the two data sets in this figure demonstrates the persistence of a stable boundary structure for at least 30 minutes in the region of interest, although data from short-lived events can also be identified within this plot. Although the variations in this

structure are gradual, four general regions can be distinguished.

The first region that was observed lay in the range $95 < \tau < 100$. This region was the magnetospheric dayside plasma-sheet, which was seen most clearly on Cluster 3. Here there was a relatively low DEF of order 10^{-5} ergs $(\mathrm{cm}^2\,\mathrm{s}\,\mathrm{sr}\,\mathrm{eV})^{-1}$ at energies just above the spacecraft potential, and a larger flux of $\sim 10^{-4}$ ergs $(\mathrm{cm}^2\,\mathrm{s}\,\mathrm{sr}\,\mathrm{eV})^{-1}$ at energies just above 1 keV. The DEF above 1 keV was strongest perpendicular to the magnetic field, consistent with a trapped magnetospheric electron population.

Between $60 < \tau < 95$ the second region was observed, which will be referred to as the inner boundary layer. As τ decreased within this layer, a low energy (10-100 eV) bidirectional field-aligned population of higher DEF replaced the 1 keV population. The DEF increased at energies between 10 and 100 eV and the anisotropy decreased with decreasing τ. The trapped (90°) 1 keV population disappeared between τ values of 70 and 80.

A lower energy perpendicular population similar to that in the field-aligned directions appeared in the range $20 < \tau < 60$. The mean spacecraft potential also decreased in this region as τ decreased, consistent with an increase in plasma density towards magnetosheath values. The lack of magnetospheric electrons suggests that this plasma was on open magnetic field lines. This region will be referred to as the outer boundary layer.

For $\tau < 20$ the low-energy DEF reached its peak of $\sim 10^{-3}$ ergs $(\mathrm{cm}^2\,\mathrm{s}\,\mathrm{sr}\,\mathrm{eV})^{-1}$ and the distribution became isotropic. This was the fourth region: the magnetosheath. These regions were identified according to the value of τ, which is indicative of the time elapsed since the magnetic field line was reconnected (e.g. Lockwood and Hapgood, 1997). The terms 'inner' and 'outer' boundary layer are used in a completely different sense from the interior and exterior layers of Lockwood *et al.* (2001), discussed in Chapter 1, which was based on B_Z, and hence position relative to the cusp in a GSE X-Y plane. As the spacecraft approached and passed the mean position of the boundary layers, the layers were encountered first intermittently and then more frequently (Figure 3.3), due to the motion of the magnetopause.

Figure 3.6 shows the variation of the magnetic field and CODIF proton parameters in GSE coordinates as a function of corresponding transition parameter. The top four panels show the variation with τ of the magnetic field on all four spacecraft. Data from the period of magnetosheath magnetic field reorientation (11:15 to 11:30 UT on Clusters 1, 3 and 4; 11:16 to 11:32 UT on Cluster 2) have not been plotted in these panels. Whilst a magnetospheric magnetic field orientation was maintained to values as low as $\tau = 60$, in the region $20 < \tau < 60$ (the outer boundary layer) a magnetic field orientation was observed which differed from both the

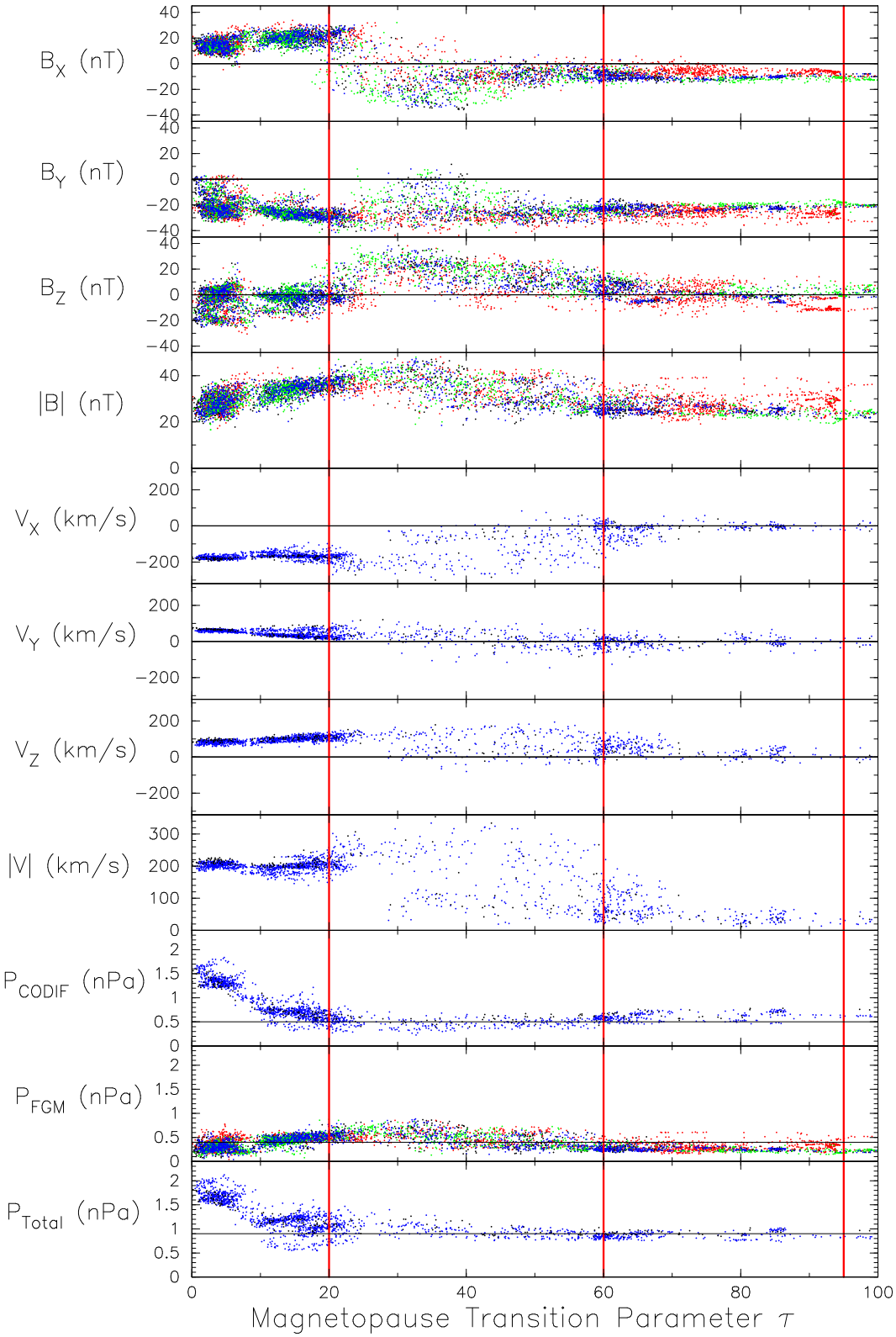

Figure 3.6: The magnetic field, proton velocity and gas, magnetic and total pressure reordered by transition parameter. The proton velocities and pressure are derived from CODIF ground moments which have undergone a dead-time correction to improve their accuracy in the magnetosheath. A period of magnetosheath magnetic field reorientation (11:15 to 11:30 UT on Clusters 1, 3 and 4; 11:16 to 11:32 UT on Cluster 2) has been removed from the top four panels. The boundaries (see Figure 3.5) between the magnetosheath, outer and inner boundary layers and magnetosphere are indicated by vertical lines.

magnetosphere and the magnetosheath. There was a wider spread of values in this region, but the magnitude of the magnetic field was generally stronger than either side, the B_X and B_Z components were enhanced, and B_Y decreased. At $\tau = 20$ there was a clear reversal in B_X and B_Z, and at smaller values of τ there was a consistently Sunward, duskward and generally southward magnetic field orientation.

The next four panels of Figure 3.6 show the dead-time corrected CODIF ground moment velocities from Clusters 1 and 4 (which were located relatively close together). The moments from Cluster 3 are not shown, as without the dead-time correction they are not believed to be accurate in the magnetosheath; therefore it is not possible to demonstrate stability lasting more than a few minutes in the trends of the proton data. In most of the inner boundary layer ($60 < \tau < 95$), there was little deviation from the low bulk velocities observed in the magnetosphere. In the outer boundary layer ion velocities were generally either similar to those observed in the magnetosheath or to those in the magnetosphere. However there were some enhancements, predominantly in -V_X, which increased the magnitude of the ion velocity to greater than that of the magnetosheath flow.

The next three panels show the thermal pressure calculated from the dead-time corrected CODIF density and temperature ground moments [$T = \frac{1}{3}(T_{\parallel} + 2T_{\perp})$], the magnetic pressure and the sum of these two pressures. There was a decrease in the gas pressure and an increase in the magnetic pressure in the outer boundary layer compared with the inner boundary layer and the magnetosphere. Although temporal variations caused a slight spread in values of total pressure ($\pm$0.2 nPa above $\tau = 40$; $\pm$0.5 nPa in the region $18 < \tau < 40$), the mean value of the total pressure remained close to 1 nPa down to $\tau = 18$. Pressure balance was therefore probably conserved both between the magnetosphere and boundary layers, and the boundary layers and the magnetosheath. After the spacecraft entered the magnetosheath, the total pressure varied more in time (penultimate panel of Figure 3.3). This caused a larger spread of values and a general increase in P_{Total} corresponding to $\tau < 18$.

3.6 Boundary Normal Coordinates

In order to examine the two events highlighted in Figure 3.3, a boundary normal coordinate system was established. The linear formation of the spacecraft precluded using a multi-spacecraft timing analysis as a means of establishing the normal vector $\hat{\boldsymbol{N}}$. Therefore $\hat{\boldsymbol{N}} = (0.592, 0.378, 0.712)_{GSE}$ was determined by minimum variance analysis (MVA) performed using high resolution FGM data across the field rotation between the outer boundary layer and the magnetosheath. A variety of inter-

vals were used for MVA on all four spacecraft; the largest intermediate/minimum eigenvalue ratio achieved was 4.3, using Cluster 2 data from 10:50 to 11:50 UT. $\hat{\boldsymbol{L}} = (-0.715, -0.161, 0.680)_{GSE}$ was determined by projecting the Earth's magnetic dipole onto the plane defined by $\hat{\boldsymbol{N}}$, and $\hat{\boldsymbol{M}} = (0.372, -0.912, 0.175)_{GSE}$ was constructed from the vector product of $\hat{\boldsymbol{N}}$ and $\hat{\boldsymbol{L}}$.

Sonnerup and Scheible (1998, p. 198) provide the following estimate of the error due to random variation (i.e. noise) on eigenvector $\boldsymbol{x}_i$ (in radians) in a rotation toward eigenvector $\boldsymbol{x}_j$:

$$|\Delta\phi_{ij}| = \sqrt{\frac{\lambda_3}{(M-1)} \frac{(\lambda_i + \lambda_j - \lambda_3)}{(\lambda_i - \lambda_j)^2}} \tag{3.1}$$

where $i \neq j$, M is the number of data points (18,000) and λ_1, λ_2 and λ_3 are the maximum, intermediate and minimum eigenvalues (which have values of 23.2, 99.1 and 464 $(\mathrm{nT})^2$ and correspond to eigenvectors $\boldsymbol{x}_1$, $\boldsymbol{x}_2$ and $\boldsymbol{x}_3$). The large number of data points used results in small random angular errors: applying this equation to the minimum variance eigenvector $\boldsymbol{x}_3$ ($\hat{\boldsymbol{N}}$) leads to values of $|\Delta\phi_{31}| = 0.1°$ and $|\Delta\phi_{32}| = 0.3°$.

These estimates neglect systematic error (such as a temporal change in the magnetopause shape and/or size). Nonetheless, the MVA frame which was derived did succeed in producing a minimum component of the local magnetosheath magnetic field that is close to zero which is consistent with magnetic field draping over the magnetopause. Furthermore, although current magnetopause models do not account for any effect of the cusp on the magnetopause shape, $\hat{\boldsymbol{N}}$ compares quite well with a normal derived from the Roelof and Sibeck (1993) model of $(0.664, 0.437, 0.607)_{GSE}$. The angle between these two normal vectors is 8°.

The magnetic field and proton velocity variations shown in Figure 3.6 are plotted in boundary normal coordinates as a function of τ in Figure 3.7. As in Figure 3.6, the period of magnetosheath magnetic field reorientation (between 11:15 and 11:30 UT on Clusters 1, 3 and 4; 11:16 to 11:32 UT on Cluster 2) has not been plotted in the magnetic field panels. Since the boundary normal coordinate frame was derived at the entry into the magnetosheath (at $\tau \sim 20$), which does not equate to the exit from the magnetosphere-proper (at $\tau \sim 95$), the magnetospheric magnetic field was not entirely in B_L; there was also a positive B_M component, and B_N was negative as the proximity to the cusp meant that the magnetospheric magnetic field lines observed when τ was greater than 95 had a component away from the magnetopause plane derived from the later crossings. When the spacecraft were in the outer boundary layer, B_L was enhanced, B_M increased slightly but sometimes became negative, and B_N decreased (sometimes becoming positive). On entry into the magnetosheath,

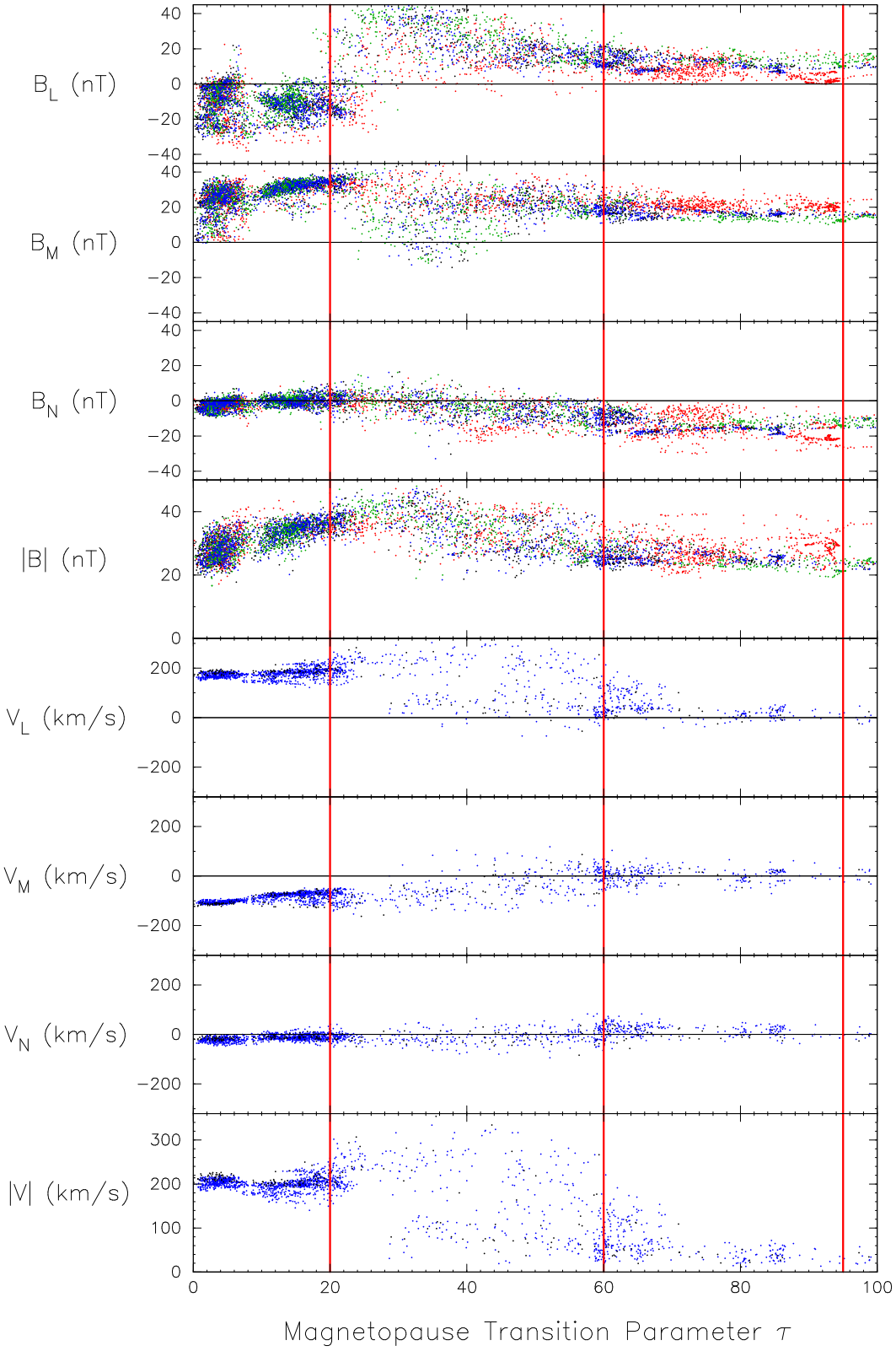

Figure 3.7: The magnetic field and proton velocity data shown in Figure 3.6, rotated into boundary normal coordinates.

B_L reversed direction and became negative, B_M was positive and B_N decreased. As is expected, the magnetosheath flow was almost entirely in the magnetopause plane (positive V_L and negative V_M). As noted in the discussion of Figure 3.6, the boundary layer flow velocity vectors were generally either similar to the flow observed in the magnetosheath or similar to the negligible flow in the magnetosphere. However, there were some enhancements in V_L and V_M and there were a significant number of positive V_M values in the range $\tau > 30$. The V_L enhancements corresponded to enhancements in $|V|$.

3.7 Case Studies

3.7.1 10:08 UT Boundary Layer Entry

The first event to be considered occurred at 10:08 UT. Plasma and magnetic field data for the period 10:00 – 10:15 UT are shown in Figure 3.8. Electron spectra from Cluster 3 in the directions antiparallel, perpendicular and parallel to the magnetic field are plotted in the top three panels. The data in these plots have been rebinned on the ground to the true pitch angles. Rebinning improves the reliability of the pitch-angle selection compared with on-board binning (SPINPAD), which uses on-board FGM calibrations. SPINPAD will also return the wrong pitch angle if the magnetic field changes by more than one azimuthal sector (see Section 2.2.4). In this case some pitch angles, usually near the magnetic field direction, are discarded before the distribution is telemetered; resulting data gaps are seen in Figure 3.8 near 10:08 UT. These spectrograms are followed by similar spectrograms for Cluster 4; the magnetic field did not change rapidly enough to cause problems for on-board pitch angle selection, therefore SPINPAD is shown for this spacecraft. The spacecraft potential is again superposed onto each spectrogram.

The next four panels display the CODIF proton velocity moments in boundary normal coordinates. These panels are followed by the high time-resolution magnetic field data in boundary normal coordinates, the thermal gas pressure derived from CODIF ground moments, the magnetic and total pressures and the transition parameter. The ion moments from Clusters 1 and 4 are dead-time corrected.

Between 10:00 and 10:02 UT, all four spacecraft were near the magnetosphere/inner boundary layer transition. In this interval the magnetic field maintained a steady value of $\sim (10, 10, -20)_{LMN}$ nT, the proton velocity was low and the transition parameter was approximately 90. Between 10:02 and 10:05 UT, the transition parameter on Clusters 1, 3 and 4 dropped to 70. A higher DEF, of or-

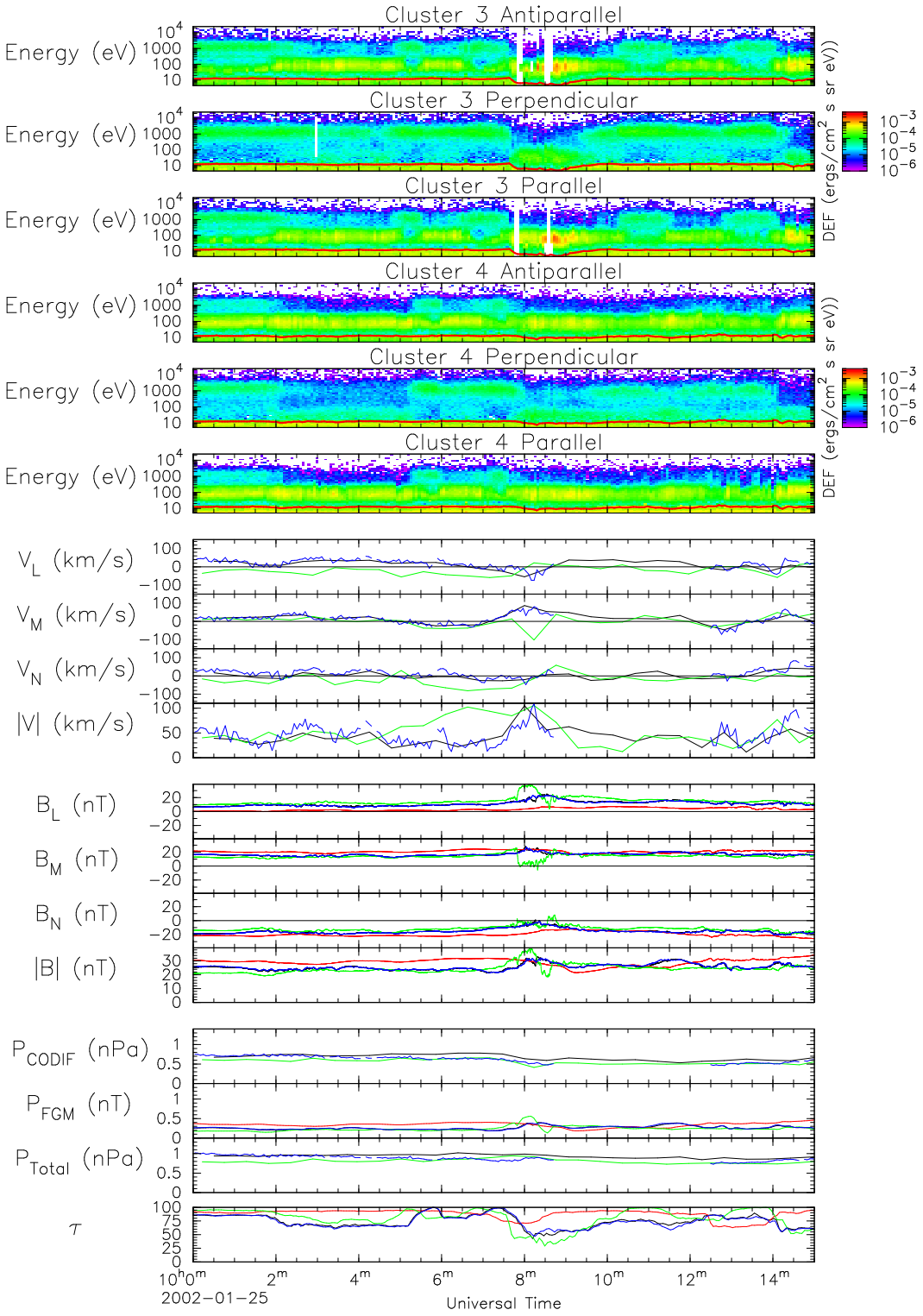

Figure 3.8: Plasma and magnetic field data from the 10:08 UT event. The top six panels show electron spectrograms from Cluster 3 (closest to the magnetopause) and Cluster 4 antiparallel, perpendicular and parallel to the magnetic field. The Cluster 4 spectrograms show data resulting from on-board binning of measured data into pitch angle bins, but the Cluster 3 data have been rebinned on the ground, which results in some data gaps. The next four panels show the proton ground moment velocities in boundary normal coordinates for Clusters 1 and 4 (corrected for dead-time effects) and Cluster 3. They are followed by the high resolution magnetic field observed on each spacecraft (also in boundary normal coordinates), and the gas, magnetic and total pressures. The final panel shows the transition parameter calculated for each spacecraft.

der 5×10^{-4} ergs $(\mathrm{cm}^2\,\mathrm{s}\,\mathrm{sr}\,\mathrm{eV})^{-1}$, of field-aligned plasma below 100 eV is evident in the spectrograms, and there was a drop-out of 1 keV plasma in the field-aligned directions. Similar spectra and values of τ were observed by Clusters 1, 3 and 4 at 10:12 UT and after 10:14 UT. These signatures are consistent with the behaviour in Figures 3.5, 3.6 and 3.7; at these values of τ, the spacecraft were well inside the inner boundary layer: no variation was observed in the magnetic field or bulk velocities, but bidirectional field-aligned plasma was observed.

At 10:08 UT, a deeper transient entry into the boundary layer structure was observed. τ dropped to 30 on Cluster 3 and 40 on Clusters 1 and 4. Cluster 3 observed an even higher DEF burst of low energy plasma in the field-aligned directions ($\sim 4 \times 10^{-3}$ ergs $(\mathrm{cm}^2\,\mathrm{s}\,\mathrm{sr}\,\mathrm{eV})^{-1}$). There was also an enhancement of plasma at this energy in the perpendicular direction, but only to a DEF of 10^{-4} ergs $(\mathrm{cm}^2\,\mathrm{s}\,\mathrm{sr}\,\mathrm{eV})^{-1}$, and a drop-out in electrons in all directions at ~ 1 keV. Cluster 4 observed a DEF of $\sim 5 \times 10^{-4}$ ergs $(\mathrm{cm}^2\,\mathrm{s}\,\mathrm{sr}\,\mathrm{eV})^{-1}$ in the field-aligned directions, with little enhancement in the perpendicular direction. At the same time, Clusters 1 and 4 observed an increase in B_L, B_M and $|\boldsymbol{B}|$, whilst B_N decreased to nearly zero. The Cluster 3 magnetic field followed this behaviour at edges of the signatures observed by Clusters 1 and 4 (before 10:07.45 and after 10:08.30 UT), but between these times B_M turned negative. There was an enhancement in the plasma velocity on these three spacecraft, which largely consisted of an increase in V_M, but within this enhancement V_M observed by Cluster 3 also reversed direction. There was also a brief V_L enhancement on Cluster 3. The proton gas pressure on all three spacecraft decreased, but this was approximately balanced by an enhancement of the magnetic pressure. The signature observed by Cluster 3 was preceded by a V_N flow of ~ -80 km/s and followed by a positive V_N flow of ~ 60 km/s; this bipolar flow pattern had a duration of 5 minutes.

Cluster 2 also observed a small increase in DEF below 100 eV at 10:08 UT (seen in Figure 3.3), and τ dropped to ~ 70. However, these signatures occurred slightly before those observed at Cluster 3. Since Cluster 3, the most Sunward spacecraft, observed the signatures before Clusters 1 and 4, this is believed to be a separate boundary layer entry. Furthermore, the variation of τ on Cluster 2 between 10:00 and 10:15 UT is not closely related to the variation observed by the other spacecraft. Cluster 2 was tailward of the other spacecraft, and was separated from Cluster 1 by 4400 km in $\hat{\boldsymbol{N}}$ and by 3300 km tangential to the magnetopause plane.

The B_L, B_M and magnetic pressure enhancements, along with the decrease in B_N and the gas pressure observed on all three spacecraft are consistent with the trends illustrated in Figures 3.6 and 3.7 associated with the observed decrease to $\tau \approx 40$. Although at this value of τ the mean value of V_L increased and V_M became

negative, there was a considerable spread and the observed values on Clusters 1 and 4 at 10:08 UT were not outliers in the distribution. The B_M and V_M reversals observed by Cluster 3 are also consistent with the slightly deeper penetration into the outer boundary layer made by Cluster 3, due to its position closer to the magnetopause than the other spacecraft.

3.7.2 10:52 UT Flux Transfer Event

After 10:30 UT the lagged IMF was generally southwards, although still dominated in the clock-angle plane by B_Y (Figure 3.3). Following their respective magnetopause crossings, all four spacecraft observed traditional magnetosheath FTE signatures (bipolar B_N signatures and an enhancement in the magnetic field strength; some exhibited a heating of magnetosheath electron plasma, proton velocity enhancements and an increase in the transition parameter). Four such FTEs, identified by their characteristic bipolar B_N variations, are shown in Figure 3.9, at 10:48.45, 10:49.40, 10:50.20 and 10:51.50 UT.

Figure 3.9, showing the period from 10:48 to 10:56 UT, adopts the same format as Figure 3.8 except that PEACE spectrograms from Clusters 4 and 2 are shown. On-board pitch-angle binning is again used for Cluster 4 PEACE data since the magnetic field did not change rapidly enough to affect the on-board pitch angle selection, but Cluster 2 data have been rebinned to the true pitch angles on the ground. By this time, Clusters 1, 3 and 4 had crossed into the magnetosheath; the Cluster 3 CODIF moments are not shown since they are unreliable in the magnetosheath without the dead-time correction. These three spacecraft observed a cool, dense, isotropic electron plasma distribution typical of the magnetosheath ($\sim 10^{-3}$ ergs $(\mathrm{cm}^2\,\mathrm{s}\,\mathrm{sr}\,\mathrm{eV})^{-1}$ between 10 and 100 eV), corresponding to a low transition parameter. The plasma flow direction was in $+V_L$ and $-V_M$, and the magnetosheath magnetic field was predominantly along B_M. Just before 10:52 UT, Clusters 1 and 4 observed a 'standard' polarity (outward then Earthward) bipolar B_N FTE signature in the terminology of Rijnbeek *et al.* (1984, see Chapter 1), which is shown in more detail in Figure 3.10. An enhancement in B_L, a decrease in B_M and a small velocity enhancement were also observed. There was a small increase in the total pressure observed by these spacecraft due to an increase in the magnetic pressure, and the PEACE instruments observed accelerated magnetosheath electrons in the direction parallel to the magnetic field (Cluster 1 spectrogram not shown).

By this time Cluster 3 (the leading spacecraft in the formation – see Figure 3.1) was too far from the magnetopause to observe a change in the electron spectra, but a small bipolar B_N signature was observed, which can be attributed to draping

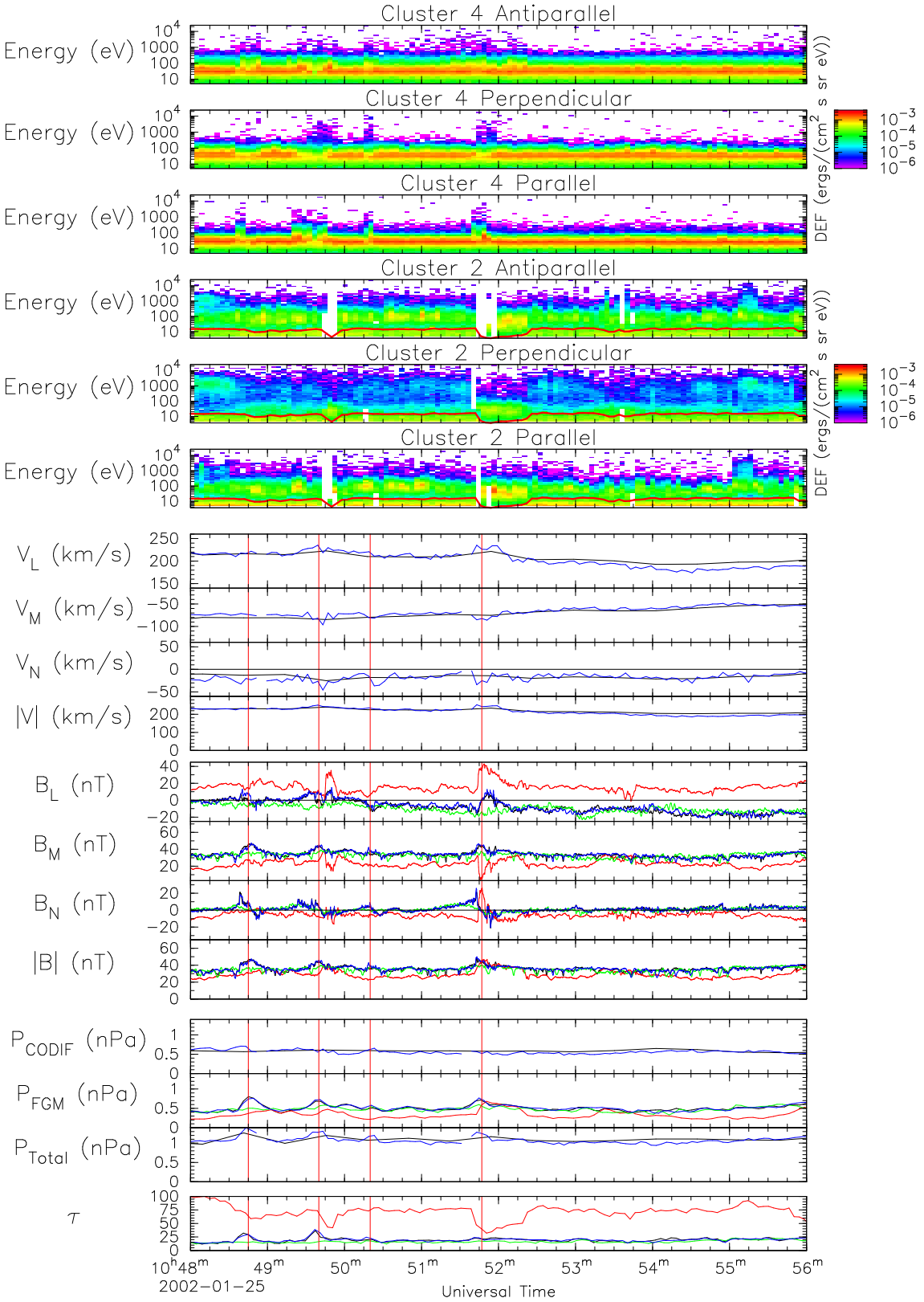

Figure 3.9: Plasma and magnetic field data from the 10:52 UT event. This figure follows the same layout as Figure 3.8, except that spectrograms for Clusters 4 and 2 are shown (Cluster 4 data use on-board pitch angle binning; Cluster 2 data have been rebinned on the ground). Cluster 3 CIS-CODIF moments are not shown as the lack of dead-time correction reduces their reliability in the magnetosheath. Four magnetosheath FTEs are identified by vertical red lines.

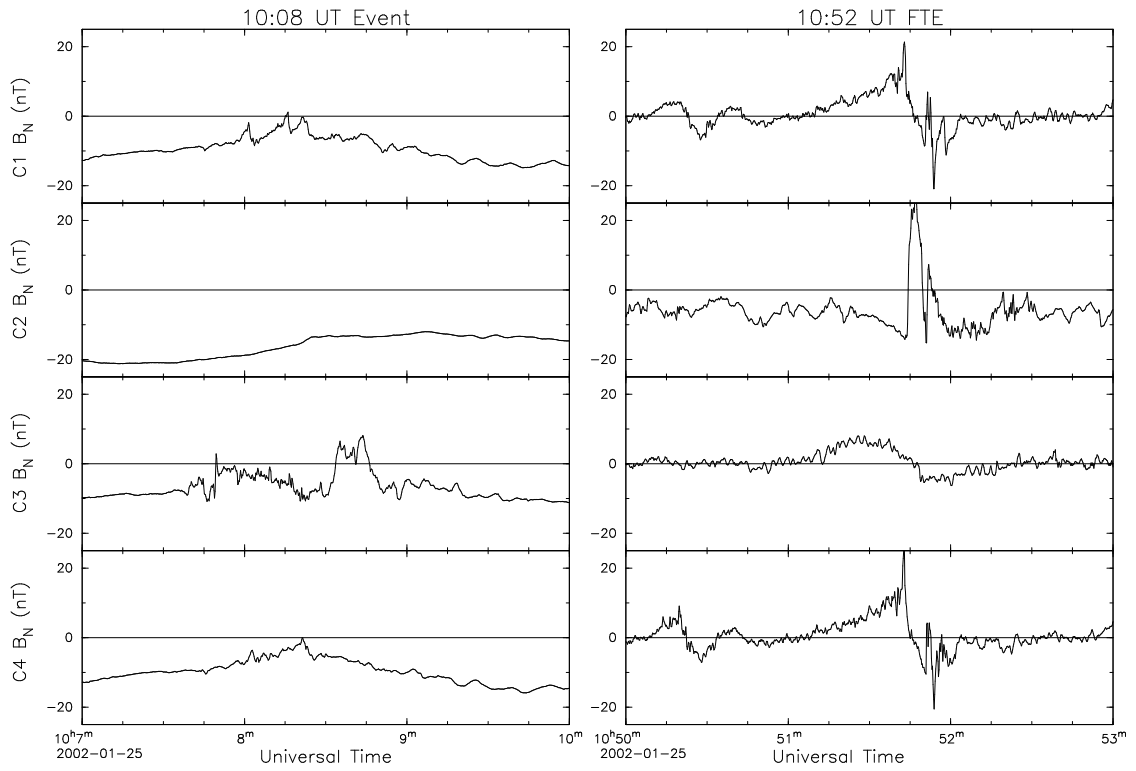

Figure 3.10: The B_N signatures observed by the four Cluster spacecraft at 10:08 and 10:52UT. The signature observed by Cluster 2 at 10:52 UT is similar to that observed by Cluster 3 at 10:08 UT, although the signature observed at 10:52 UT was shorter-lived. In both events, a B_L enhancement was observed along with reduction in B_M (see Figures 3.8 and 3.9), however at 10:52 UT Clusters 1, 3 and 4 were in the magnetosheath and observed bipolar B_N signatures.

of the magnetic field. On the magnetospheric side of the magnetopause, Cluster 2 observed similar signatures to those which had been observed by Cluster 3 at 10:08 UT (see Figure 3.10), although the signatures observed by Cluster 2 were shorter-lived. As the transition parameter dropped from around 80 to approximately 40, a burst of low energy field-aligned plasma was observed with a DEF of order 10^{-3} ergs $(\mathrm{cm}^2\,\mathrm{s}\,\mathrm{sr}\,\mathrm{eV})^{-1}$. The DEF of plasma in the perpendicular direction also rose to $\sim 10^{-4}$ ergs $(\mathrm{cm}^2\,\mathrm{s}\,\mathrm{sr}\,\mathrm{eV})^{-1}$. The magnetic field strength also increased, but this increase consisted of an enhancement in B_L, a decrease in B_M and a unipolar positive excursion in B_N.

3.8 Discussion

Using the transition parameter introduced by Hapgood and Bryant (1992), the basic characteristics of the cusp/magnetopause boundary layers observed by Cluster on the 25th January 2002 have been analysed. Cluster passed from within the magnetosphere near the rim of the cusp (i.e. where the magnetospheric magnetic field turns from positive to negative GSE B_Z) via a boundary layer to the magnetosheath.

This analysis revealed an inner boundary layer with bidirectional low-energy plasma and a similar magnetic field orientation to the magnetosphere, and an outer layer with lower anisotropy and higher fluxes than in the inner boundary layer, and with a different magnetic field orientation from the magnetosphere and magnetosheath. Details of the boundary layer structure are expected to relate to the age of the reconnected field lines. Further work on this topic is planned, but the presence of trapped electrons (90° pitch angle) in part of the inner boundary layer ($\tau >\sim 80$) suggests that this region was on closed magnetic field lines or field lines from which not all magnetospheric electrons had had time to escape. The electron distribution in the inner boundary layer, and the similarity of the inner boundary layer magnetic field to that of the magnetosphere-proper are consistent with being magnetically connected to the LLBL/cleft. The electron distribution of the outer boundary layer is consistent with the exterior cusp (heated bi-directional electrons at a lower DEF than in the magnetosheath, without a trapped population). Furthermore, the occurrence of plasma with bulk velocities greater than the magnetosheath (Figures 3.6 and 3.7) is suggestive of sub-solar reconnection occurring. This is consistent with the negative B_Z excursions which were occurring at the same time (Figure 3.3).

In this context, an example event at 10:08 UT was examined, where the Cluster spacecraft penetrated the boundary layers to three different depths: Cluster 3 entered deeper than Clusters 1 and 4 and observed a greater DEF enhancement in all directions, although largest in the field-aligned directions, between 10 and 100 eV. Cluster 4 (and Cluster 1) only observed a significant increase in DEF in the field-aligned directions at these energies. All three spacecraft observed a positive enhancement in V_M, B_L and B_M and a decrease in B_N (which became positive on Cluster 3); in addition, Cluster 3 observed reversals in V_M and B_M. These signatures were observed first by Cluster 3, then by Clusters 1 and 4, which is consistent with the cause of the signatures moving tailward. Cluster 2 made a shallower entry into the inner boundary layer around this time, but this entry occurred slightly before that observed by Cluster 3. Furthermore, the variations in τ observed by Cluster 2 do not relate closely to those observed by the other three spacecraft. Therefore, it is believed that this entry was unrelated. Thus the scale size of these events was smaller than the separation of Cluster 2 from Clusters 1 and 4 (4400 km in $\hat{\boldsymbol{N}}$, and 3300 km tangential to the magnetopause plane). The proton velocity components normal to the magnetopause observed by Cluster 3 before/after the magnetic field signatures show that there was an inward/outward bulk motion of the plasma with a duration of 5 minutes, but in the absence of observations in the magnetosheath and solar wind there is no conclusive evidence for whether this boundary layer entry was caused by a simple pressure pulse or if it had another cause, such as a passing FTE.

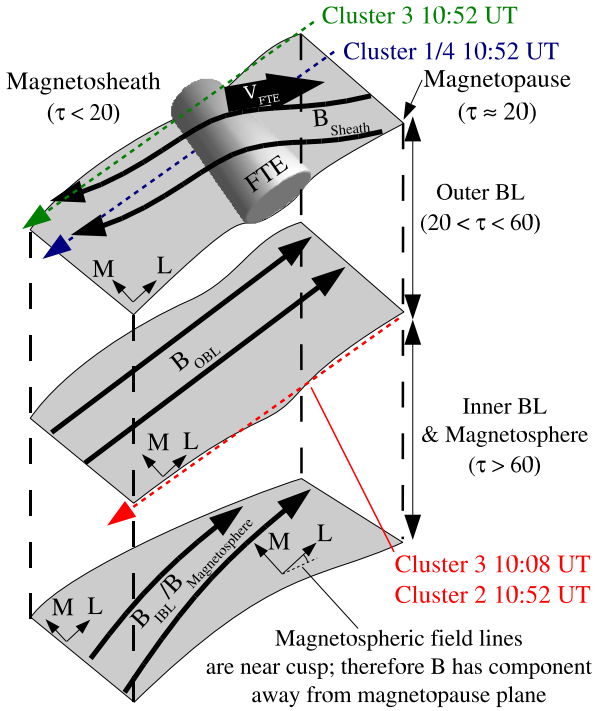

Figure 3.11: A sketch of the boundary layer structure, and the relative paths of the spacecraft at 10:52 UT. Clusters 1 and 4 were in the magnetosheath and passed through an FTE. Cluster 3 was also in the magnetosheath but further from the magnetopause and observed only field line draping. Cluster 2 was in the inner boundary layer, but entered the outer boundary layer as the FTE passed, leading to characteristic plasma and magnetic field signatures, but with no bipolar B_N signature. Cluster 2 observed similar signatures at 10:52 UT to those observed by Cluster 3 at 10:08 UT.

At 10:52 UT, the spacecraft in the magnetosheath (Clusters 1, 3 and 4) observed signatures which can be attributed to flux transfer events (bipolar B_N signatures, field-aligned acceleration of magnetosheath electrons, and an increase in the magnetic pressure). Clusters 1 and 4 observed an enhancement in the proton velocity, so it is likely that these spacecraft entered the FTE, whereas Cluster 3 only observed the effects on the surrounding plasma. Cluster 2 was already in the inner boundary layer, but unlike earlier simultaneous observations of FTEs either side of the low-latitude magnetopause (e.g. Farrugia *et al.*, 1987b), no bipolar B_N signature was observed. At the low-latitude magnetopause, there is usually a simple rotation directly between the magnetospheric and magnetosheath magnetic fields. In the 10:52 UT event, a range of characteristics were observed which were consistent with moving deeper into the temporally stable boundary layer structure as the FTEs passed by (sketched in Figure 3.11). In fact, few bipolar B_N signatures occurred in the magnetosphere or within the boundary layer during this interval; they were first observed just before the spacecraft crossed the magnetopause. One explanation for the observed signatures might be that the velocity of the FTE has a strong component antiparallel to the magnetosheath magnetic field, producing a clear standard-polarity bipolar signature through draping of the magnetic field lines, but only a weak component along the magnetic field directions observed by the spacecraft in the boundary

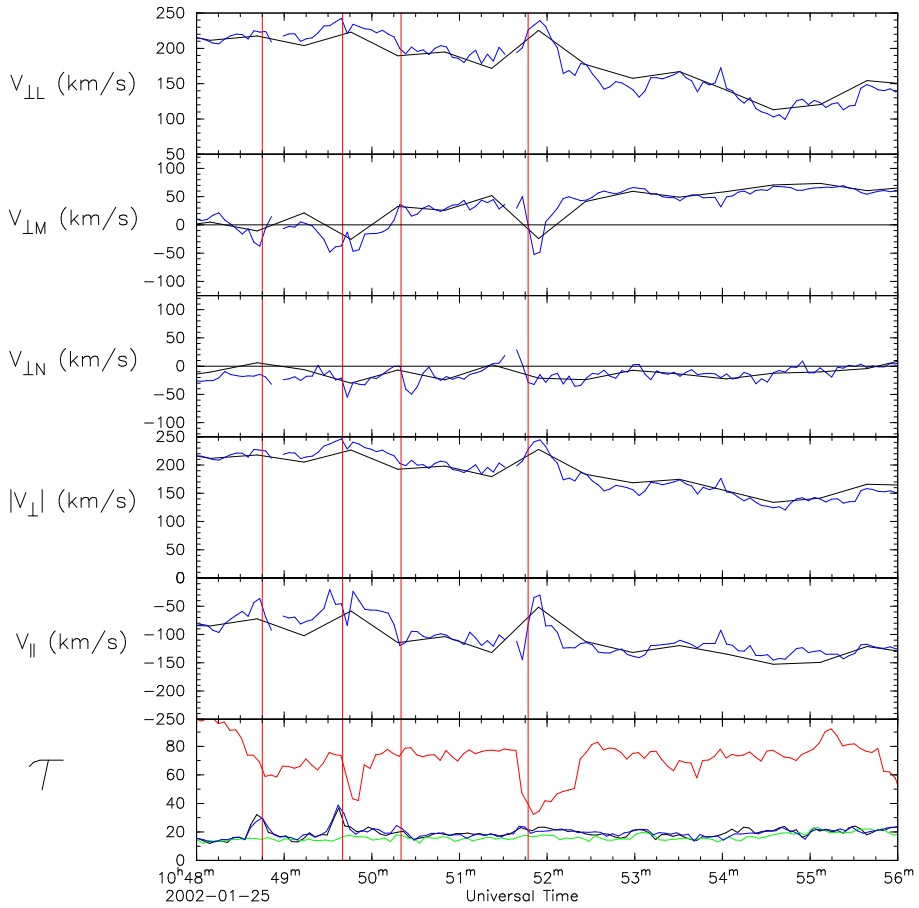

Figure 3.12: The perpendicular and parallel ion velocities at 10:52 UT. The top four panels show the components and magnitude of the ion velocities observed perpendicular to the magnetic field in boundary normal coordinates. Dead time corrected CODIF moments from Clusters 1 and 4 are used. The next panel shows the component of the ion velocity parallel to the magnetic field, and the bottom panel shows the transition parameter derived for all four spacecraft.

layer/magnetosphere. However the best measure we have of the velocity of the FTE is the peak perpendicular velocity, observed in the corrected CODIF moments at 10:51.55 UT, which is $(239, -48, -15)_{LMN}$ kms^{-1} (Figure 3.12). The background magnetosheath and inner boundary layer magnetic fields, observed by Clusters 4 and 2 respectively at 10:51.20 UT, are $(-7, 35, 3)_{LMN}$ nT and $(16, 21, -7)_{LMN}$ nT. These magnetic field vectors form angles with the peak perpendicular velocity of 113° and 64° respectively; consequently the FTE has a stronger component of velocity along the background magnetic field in the inner boundary layer observed at Cluster 2 (107 kms^{-1}) than along the magnetosheath field (–95 kms^{-1}). Hence the lack of a bipolar B_N signature at Cluster 2 does not appear to be due to a weaker component of velocity along the magnetic field. Therefore it appears likely that local compression of the magnetosphere as the FTE passes by is sufficient to force Cluster 2 deeper into the boundary layer structure, but not sufficient to produce a bipolar signature that can be observed as far from the magnetopause as Cluster 2.

As Clusters 3 and 2 both observed effects of the FTE without entering the

FTE itself, its diameter can be identified as less than the separation of the two spacecraft along $\hat{\boldsymbol{N}}$ (4800 km). This is consistent with low-latitude estimates of $\sim 1\ R_E$ (Saunders *et al.*, 1984). Other FTEs were observed in the magnetosheath by Clusters 1 and 4 just before the 10:52 UT event (also highlighted in Figure 3.9), for which Cluster 2 observed either no signature (10:48.45 and 10:50.20 UT) or a less significant signature (10:49.40 UT). These FTEs were presumably smaller than the 10:52 UT event. Cluster 3 did not observe a clear bipolar B_N signature in any of these cases.

Lockwood *et al.* (2001) concluded that a bipolar B_N signature was absent when an FTE was observed near the wall of the interior cusp ($B_Z < 0$). Our observations are similar to their first 'bipolar' signature; both were observed near the lip of the cusp, where $B_Z \approx 0$ (Fig. 14, Lockwood *et al.*, 2001). The magnetic signature observed by Lockwood *et al.* (2001) was closer to those observed in the present study at 10:08 and 10:52 UT than to a traditional bipolar FTE signature. Our 10:52 UT event, with direct measurement of traditional magnetosheath FTE signatures, confirms that these less orthodox boundary layer signatures are also caused by FTEs.

3.9 Conclusions

The magnetopause transition parameter was used to reorder plasma and magnetic field observations throughout this complicated interval. This procedure clarified the boundary layer structure. Although transitions within this structure were not generally sharp, the structure was split into four regions (magnetosphere, an inner boundary layer, an outer boundary layer and the magnetosheath) and the magnetopause was identified as the interface between the outer boundary layer and magnetosheath. After the outer three spacecraft had entered the magnetosheath, a series of FTEs was observed with clear plasma and bipolar B_N signatures. At the same time as one of these FTEs passed (10:52 UT), the spacecraft within the magnetopause observed signatures consistent with moving deeper into the boundary layer structure. Without the benefit of simultaneous magnetosheath observations, this signature would most likely not have been identified as being related to an FTE, as there was no bipolar B_N variation.

It is entirely possible that some of the earlier boundary layer entries (including 10:08 UT) observed by Clusters 1, 3 and 4 were due to passing FTEs forcing the boundary layer structure inwards, illustrating that it can be difficult to identify magnetospheric FTEs at high latitudes. Contrary to the low-latitude debate, which concentrated on alternative explanations for the magnetic field and plasma obser-

vations attributed to transient reconnection or pressure pulses, this difficulty arises from the presence of the observed boundary layer structure.

Chapter 4

A Survey of Flux Transfer Events

> He uses statistics as a drunken man uses lamp-posts – for support rather than illumination.
> *Andrew Lang (1844-1912)*

4.1 Introduction

The Cluster spacecraft cross the dayside magnetopause at high latitudes near local noon, and at lower latitudes along the flanks, between November and June each year. This period of time is referred to as the 'dayside crossing season'. In this chapter, the results of a survey of FTEs observed by Cluster in the 2002/3 dayside season are presented. General statistics are shown and compared with earlier surveys. The major difference between this survey and most previous work is that a significant number of FTEs were observed under strongly northward IMF. Since multi-spacecraft techniques enable more accurate velocities to be calculated than previously possible, the motion of these northward IMF FTEs was determined by four-spacecraft timing and compared with a model. The observed velocities are consistent with a long, component reconnection X-line emanating from the antiparallel reconnection site in the lobe; they are not consistent with a strictly antiparallel X-line as reconnection extends to regions of lower shear on the flank (Fear *et al.*, 2005b). The velocities observed at lower latitudes are also not consistent with a subsolar component X-line. The motion of the events which occur under southward and dawn-dusk dominated IMF will be discussed in Chapter 5. First, other survey work will be reviewed, which was discussed in some depth in Chapter 1.

4.2 A Review of Earlier Surveys

The polarity of the bipolar signature is determined by the motion of the FTE relative to the local, undisturbed magnetic field, which drapes around the FTE. In the magnetosheath, a 'standard' polarity signature in B_N (+/– relative to $\hat{\mathbf{N}}$, which is directed away from the Earth) is observed if the FTE velocity has a component antiparallel to the local magnetosheath magnetic field, whereas a 'reverse' signature (–/+) occurs if the FTE velocity has a component parallel to the local field. Within the magnetosphere, a standard signature is observed when the velocity has a component parallel to the geomagnetic field, and a reverse signature when antiparallel. Since FTEs are generated in regions of high magnetic shear, the polarities observed by two nearby spacecraft on either side of the magnetopause are the same (Farrugia *et al.*, 1987b).

Several statistical studies have shown that FTEs occur predominantly when IMF $B_Z < 0$ (e.g. Berchem and Russell, 1984; Rijnbeek *et al.*, 1984; Southwood *et al.*, 1986; Kuo *et al.*, 1995), although these surveys were restricted to observations in the pre-terminator region ($X_{GSM} > 0$). Standard polarity FTEs are generally observed in the northern hemisphere, and reverse events in the southern hemisphere, consistent with FTEs being generated by dayside low-latitude reconnection (i.e. equatorward of the cusps). Russell *et al.* (1985) and Kawano and Russell (1997a) have shown FTE polarity, and hence motion, to be consistent with low-latitude reconnection even when there is a dominant IMF B_Y component. This is the major piece of evidence for the component reconnection model (Gonzalez and Mozer, 1974), as opposed to strictly antiparallel reconnection (Crooker, 1979) which is supported by other observations (e.g. Newell *et al.*, 1995; Coleman *et al.*, 2001).

High-latitude reconnection may occur between magnetosheath and lobe magnetic fields when $B_Z > 0$ (Dungey, 1963). Freeman *et al.* (1993) examined ionospheric convection as a magnetic cloud passed the Earth, causing a long, steady rotation of the IMF. From the ionospheric convection patterns observed, these authors concluded that subsolar reconnection occurs for IMF clock angles $|\theta_{CA}| > 70°$, and lobe reconnection occurs when $|\theta_{CA}| < 70°$ ($\theta_{CA} = \arctan[B_Y/B_Z]$, where B_Y and B_Z are GSM components of the IMF). This conclusion has been supported by Senior *et al.* (2002). Observations of FTEs when IMF $B_Z > 0$ are few, but Kawano and Russell (1997b) examined 144 FTEs in the post-terminator region ($X_{GSM} < 0$, $|Z_{GSM}| < 15$ R_E), 79 of which occurred when $B_Z > 0$. They concluded from the polarities of the signatures that a tilted equatorial reconnection line (X-line), could explain most events when $|\theta_{CA}| < 90°$ if flux tubes in the subsolar region were prevented from being observed by 're-reconnection' (Nishida, 1989, illustrated in

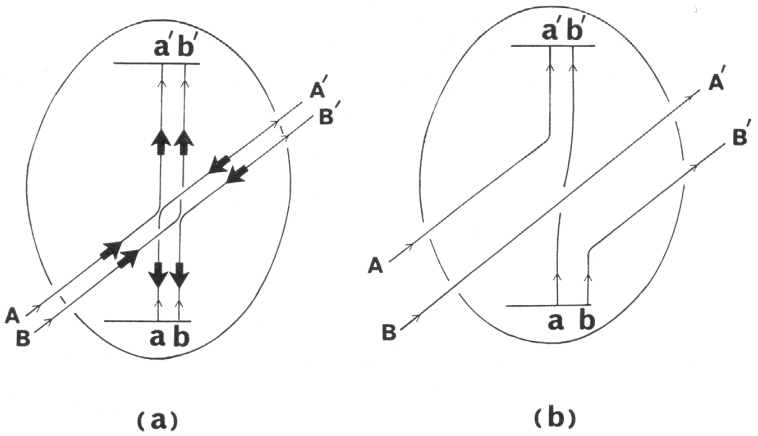

Figure 4.1: An illustration of 're-reconnection' (from Nishida, 1989). (a) Magnetosheath magnetic field lines AA′ and BB′ reconnect with magnetospheric magnetic field lines aa′ and bb′, forming open field lines Aa′, Bb′, aA′ and bB′. (b) If re-reconnection occurs, between Aa′ and aA′ and between Bb′ and bB′, the net result is two open magnetic field lines (Aa′ and bB′), one closed magnetospheric field line (ab′) and one magnetosheath field line with both ends in the solar wind (BA′).

Figure 4.1). When the IMF was more strongly northward, the polarities and B_Y dependency could also be explained by the FTEs being generated near the polar cusp at an antiparallel reconnection site, then moving somehow equatorward and tailward.

In this chapter, a survey of FTEs observed over one season of Cluster dayside magnetopause crossings (9th November 2002 – 28th June 2003) is presented. Some general statistics on the occurrence location, polarity and IMF dependence of the FTEs are discussed. A significant number of FTEs were observed whilst the lagged IMF was 'strongly northward' ($|\theta_{CA}| < 70°$). The velocities of these strongly northward events will be compared with a model of open field-line evolution. The velocities of those events which occurred when $|\theta_{CA}| > 70°$ will be discussed in Chapter 5.

4.3 Methodology and FTE Selection Criteria

The 2002/3 dayside season was selected as the separation of the four spacecraft in the vicinity of the magnetopause was comparable to the scale size of an FTE (∼5000 km) for most of the season, enabling determination of FTE motion from multi-spacecraft techniques. Six-hour periods of data from the Flux Gate Magnetometer (FGM), centred on each observed magnetopause crossing time, were examined in detail along with data from the Plasma Electron and Current Experiment (PEACE) where available (see Chapter 2 for more discussion of these instruments). The duration of the inspected interval was extended for crossings in the flank re-

gions, when Cluster skimmed the magnetopause for up to 18 hours. The magnetic field data were transformed into the boundary normal coordinate frame introduced by Russell and Elphic (1978) using a magnetopause normal derived from the Roelof and Sibeck (1993) model. Minimum variance analysis (MVA) was also carried out on each crossing.

The following events were selected:

1. A bipolar variation that was clear in relation to the background variation of the magnetic field was required in either B_N (where $\hat{\mathbf{N}}$ was derived from the model) or the minimum variance component of $\mathbf{B}$ (when MVA on the magnetopause crossing was successful).

2. An enhancement or decrease was also required in $|\mathbf{B}|$, which had to be centred close to the centre of the B_N signature.

3. Bipolar signatures centred on magnetopause crossings were excluded unless they were observed by at least one other spacecraft which did not cross the magnetopause. This criterion was chosen to reduce the possibility of FTE-like signals being caused by transient motion of the magnetopause across the spacecraft (e.g. Sibeck, 1990, 1992). This criterion was also applied by Kuo *et al.* (1995).

446 FTEs were identified which satisfied these criteria on one or more spacecraft. 286 FTEs were observed only in the magnetosheath, and 50 in the magnetosphere-proper. A further 32 were observed only in a boundary layer. A boundary layer was defined as having both a distinct electron distribution from the magnetosheath/magnetosphere-proper (where PEACE data were available), and a magnetic field orientation that was also different from either side or which was similar to the magnetosphere-proper but more turbulent. 78 events were observed when the tetrahedron straddled two of these regions. One reason for the dominance of magnetosheath events is that the dayside magnetosphere-proper was relatively rarely sampled. Near local noon, the orbit tended to pass from the cusp to the magnetosheath in the northern hemisphere, and from the magnetosheath to the lobe in the southern hemisphere. As shown in Chapter 3, magnetospheric/boundary layer FTE signatures may become more complicated at higher latitudes, possibly leading to an underestimation if a bipolar B_N is required.

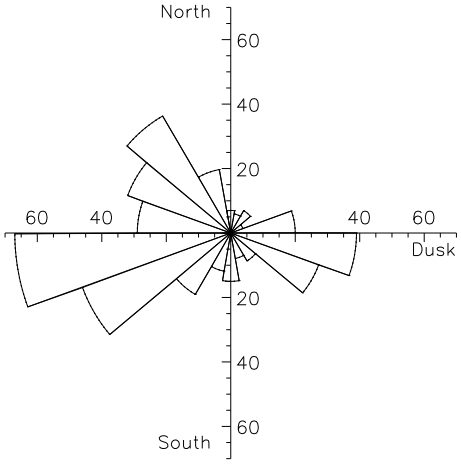

Figure 4.2: A polar histogram of the lagged IMF clock angle at the time of observation of each FTE. The angle clockwise from north is the IMF clock angle; hence the angles are those as viewed from the Sun. North and south ($\pm Z_{GSM}$) are at the top and bottom, and dusk & dawn ($\pm Y_{GSM}$) are right & left. Each bin is 20° wide.

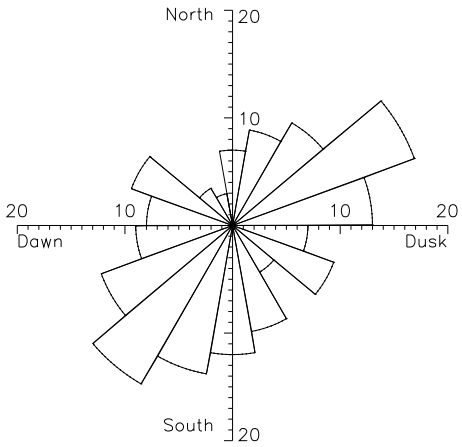

Figure 4.3: A polar histogram of the IMF clock angle at the time of each magnetopause crossing. The figure takes the same format as Figure 4.2.

4.4 Correlation with IMF

IMF and plasma data from the ACE MAG and SWEPAM instruments (Smith *et al.*, 1998; McComas *et al.*, 1998) were available for 421 of the FTEs, and at the time of 180 of the 192 magnetopause crossings included in the survey. A histogram of the lagged IMF clock angle at the time of each FTE observation is presented in Figure 4.2. This shows that most events were observed under strongly dawnward or duskward IMF, with a significant number of events when the IMF was northward and dawnward. However, this must be compared with the background IMF clock angle distribution; Figure 4.3 shows a histogram of the IMF clock angle at the time of each of the 180 magnetopause crossings for which solar wind data were available. During this season, there was a tendency for the IMF to be either southward and dawnward, or northward and duskward. Therefore, the dependency of FTE occurrence with IMF was normalised to the background IMF distribution using the following method, adopted by Kuo *et al.* (1995). For those magnetopause passes on which FTEs were observed, the lagged IMF at the time of each FTE was taken, and averaged for each pass. For those passes on which no FTEs were observed, the IMF was taken to be that at the magnetopause crossing time. Consequently, each magnetopause pass has one IMF clock angle associated with it. The number of passes on which FTEs were observed in each clock angle bin was then divided by the total number of passes to obtain an 'FTE occurrence probability', which is shown in Figure 4.4. For the purposes of this figure, the number of FTEs observed on a crossing is irrelevant; it shows the probability of one or more FTEs being observed.

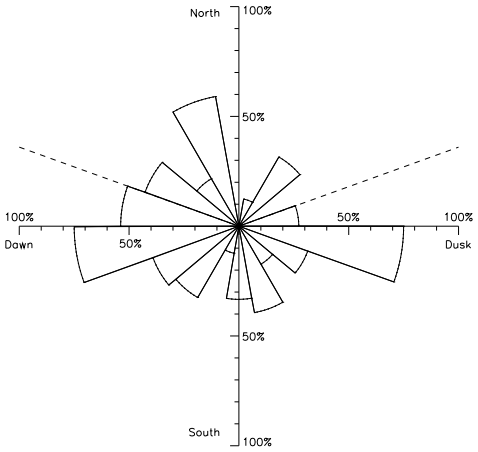

Figure 4.4: The FTE 'occurrence probability' (as defined by Kuo *et al.*, 1995) for the present survey as a function of clock angle. The dashed line marks a clock angle of ±70°.

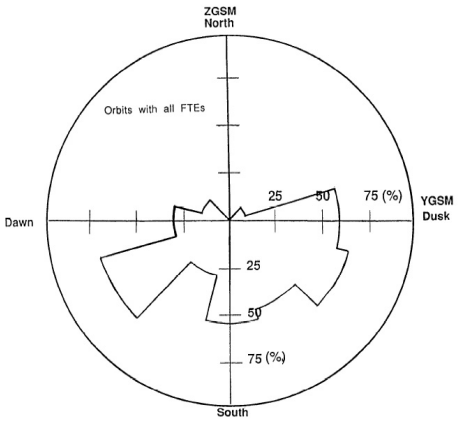

Figure 4.5: The FTE occurrence probability as reported by Kuo *et al.* (1995).

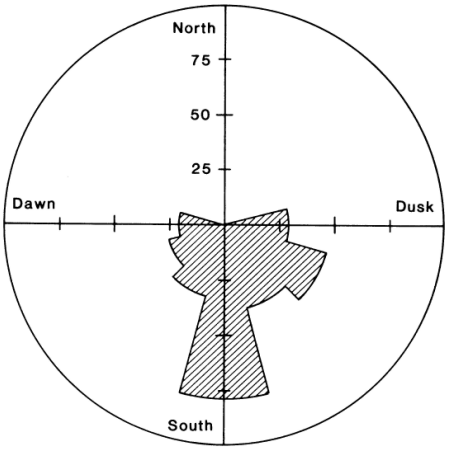

Figure 4.6: The number of FTEs reported by Berchem and Russell (1984) as a function of IMF clock angle, normalised by the number of magnetopause crossings in each clock angle bin.

Figure 4.4 can be compared with the equivalent figure from Kuo *et al.* (1995), which is shown in Figure 4.5. Kuo *et al.* (1995) studied 436 ISEE magnetopause crossings between 24th October 1977 and 30th August 1981, and identified 400 FTEs. Whereas Berchem and Russell (1984) found a strong peak in FTE occurrence when the IMF was close to due south (Figure 4.6), Kuo *et al.* (1995) found a broader distribution, although most FTEs occurred when IMF $B_Z < 0$. Kuo *et al.* (1995) attributed the strong southward peak reported by Berchem and Russell (1984) to a relatively small number of magnetopause crossings in that bin. Figure 4.4 also shows a broad spread of FTEs during southward IMF. Interestingly, the highest probability of observing FTEs occurred when the IMF was southward, but strongly dawn- or duskward. This is possibly because the apogee of the Cluster orbit extends into the solar wind near local noon, and so spends relatively little time near the magnetopause on high-latitude, near-noon crossings, but spends long periods near the low-latitude magnetopause on the flanks. One would expect FTEs formed during intervals of low IMF B_Y to move predominantly latitudinally, whereas

those formed under B_Y-dominated IMF would move more longitudinally. Thus, if the FTEs are generated at a component reconnection line in the subsolar region as previously postulated (Russell *et al.*, 1985), there is a higher probability of observing B_Y-dominated events on the flanks than at the high-latitude, near-noon magnetopause. Since more time is spent by the spacecraft at the low-latitude flank magnetopause, the probability of observing at least one FTE on a crossing is thus enhanced. Consequently, there are more observations of FTEs during B_Y-dominated IMF intervals than when B_Y is low.

121 FTEs were observed when the IMF was strongly northward ($|\theta_{CA}| < 70°$), 100 of which occurred at $X_{GSM} < 0$; therefore most of these FTEs would not have been included in earlier surveys (with the exception of Kawano and Russell, 1997a,b). Of these 121 events, 91 were observed only in the magnetosheath, 13 in a boundary layer, 6 in the magnetosphere-proper and 11 when the tetrahedron straddled two of these regions.

4.5 Location and Polarity

The locations and polarities of the FTEs which occurred when the lagged IMF was southward ($|\theta_{CA}| > 90°$) are shown in Figure 4.7. The location of Cluster 3 at the time of each FTE observation has been projected into the GSM Y-Z plane. There is a tendency for standard polarity events to be observed in the northern hemisphere, and reverse polarity events to be observed in the southern hemisphere, although this distribution has been rotated clockwise by the tendency of the IMF to be directed dawnward when southward (Figure 4.3). Most of the standard polarity events which were observed in the south/dusk quadrant ($Y_{GSM} > 0$, $Z_{GSM} < 0$) and most of the reverse polarity events in the north/dawn quadrant ($Y_{GSM} < 0$, $Z_{GSM} > 0$) were observed when the IMF B_Y component was negative (dawnward). Although no reverse polarity events were observed in the north/dusk quadrant ($Y_{GSM} > 0$, $Z_{GSM} > 0$), the majority of the standard polarity events observed in the south/dawn quadrant ($Y_{GSM} < 0$, $Z_{GSM} < 0$) occurred when the IMF B_Y component was positive (duskward). These observations are consistent with those reported in earlier surveys (e.g. Russell *et al.*, 1985), which concluded that the FTE polarity distribution is consistent with a tilted, subsolar reconnection line such as that proposed by Gonzalez and Mozer (1974).

The locations and polarities of all FTEs which occurred when $|\theta_{CA}| < 70°$ are shown in Figure 4.8, which adopts the same format as Figure 4.7. Events occurring under duskward IMF conditions were mostly observed on the dawn flank, and *vice*

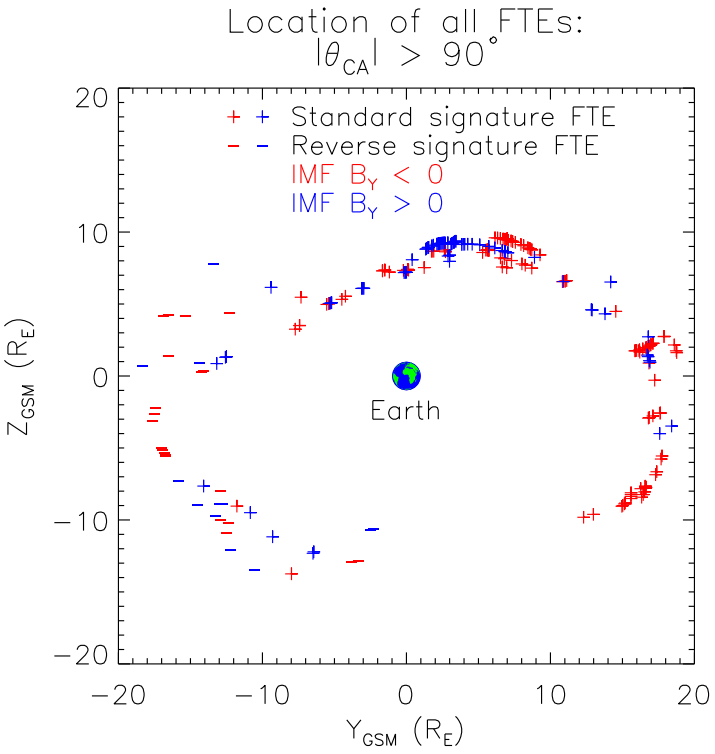

Figure 4.7: The locations and polarities of all FTEs which occurred when the lagged IMF was southward. The location of each FTE is projected into the GSM Y-Z plane. The plot symbols +/− denote the FTE polarities. FTEs which occurred when the lagged IMF was dawnward are plotted in red, and those which occurred when the IMF was duskward are plotted in blue.

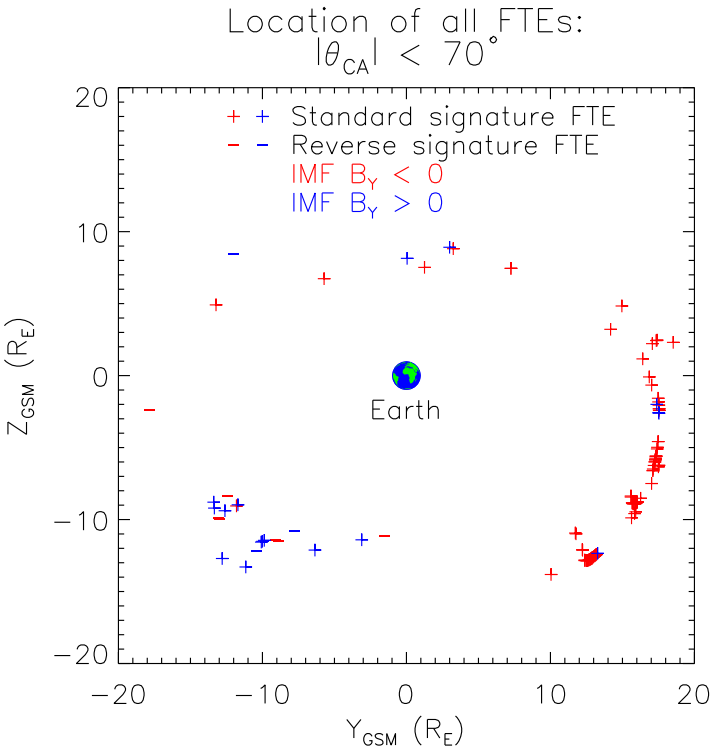

Figure 4.8: The locations of all FTEs which occurred when the lagged IMF was within ±70° of north. This figure adopts the same format as Figure 4.7.

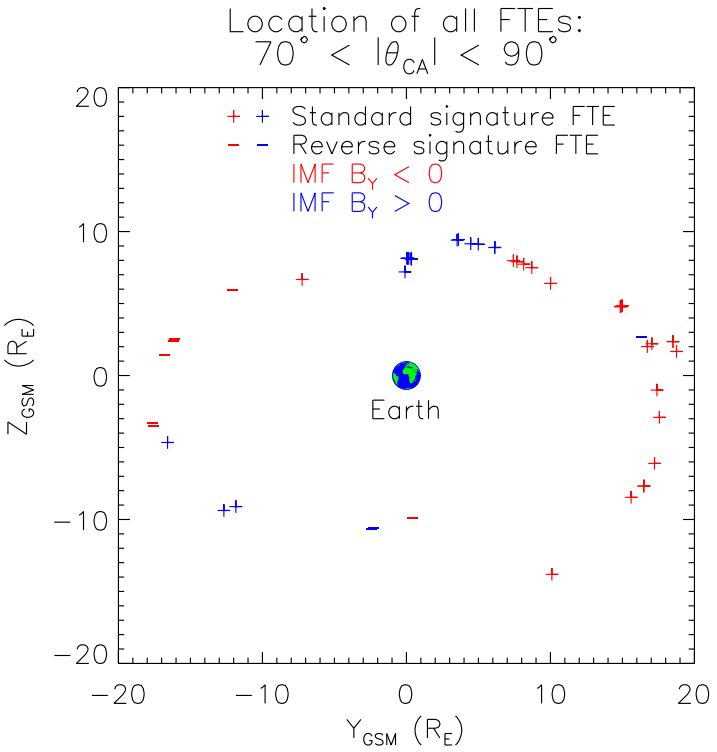

Figure 4.9: The locations and polarities of FTEs which occurred when the IMF was slightly northward, but dominated by the B_Y component ($70° < |\theta_{CA}| < 90°$). The figure adopts the same format as Figure 4.7.

versa. The FTEs were predominantly standard polarity, although 11 reverse events were observed. The division between standard and reverse polarities shown in Figure 4.8 appears to be consistent with the southward IMF event polarities: there is a dawn/dusk division, which is rotated clockwise when $B_Y < 0$, and anticlockwise when $B_Y > 0$. The origin and motion of these FTEs will be discussed further in the remainder of the chapter.

For completeness, the 49 FTEs which were observed when the IMF was slightly northward, but predominantly dawn- or duskward (i.e. $70\ ° < |\theta_{CA}| < 90°$), is shown in Figure 4.9. Given that the polarity distribution of the strongly northward IMF events is the same as the distribution of the southward IMF events, it is not surprising that in the case of the marginally northward IMF events there is also a division between standard and reverse polarity, which rotates with B_Y.

4.6 Multi-spacecraft timing analysis: Strongly northward IMF events

Multi-spacecraft timing analysis was applied to the 51 strongly northward IMF FTEs which were observed with a clear bipolar B_N signature on all four spacecraft prior to the 10th June 2003, when an orbital manoeuvre rearranged the Cluster quartet into two pairs. The time difference was determined by maximising the cross-correlation function between the B_N signature observed by Cluster 3 and each of the other three spacecraft. This was combined with the spacecraft separations to calculate a velocity vector for each event, using the following method described by Harvey (1998, p309). The time differences were formed into a 1×3 matrix:

$$\mathbf{T} = \begin{pmatrix} t_1 - t_3 \\ t_2 - t_3 \\ t_4 - t_3 \end{pmatrix} \tag{4.1}$$

where t_α is the time of observation at Cluster α. The distance between Cluster 3 and each of the other spacecraft was formed into a 3×3 matrix:

$$\mathbf{D} = (\mathbf{r}_1 - \mathbf{r}_3, \mathbf{r}_2 - \mathbf{r}_3, \mathbf{r}_4 - \mathbf{r}_3) \tag{4.2}$$

where $\mathbf{r}_\alpha$ is the position vector of Cluster α. These matrices were used to find the vector $\mathbf{m}$:

$$\mathbf{m} = \mathbf{D}^{-1}\mathbf{T} \tag{4.3}$$

which uniquely defines the both the speed (V) and direction of motion ($\hat{\mathbf{v}}$) of the FTE:

$$\mathbf{m} = \frac{\hat{\mathbf{v}}}{V} \tag{4.4}$$

This method assumes that the differences in time between the signatures observed at the four spacecraft (i.e. the matrix $\mathbf{T}$) is due to the passage of a structure that can be assumed to be planar on the scale size of the Cluster tetrahedron. In the case of an FTE, it is therefore assumed that maximising the cross correlation coefficient aligns the mid-point of the bipolar B_N signature, which in turn forms a planar surface. This point will be discussed further in Chapter 5.

The velocities ($\mathbf{V} = V\hat{\mathbf{v}}$) are shown in Figure 4.10. The majority of the 51 events occurred on the dusk flank; most occurred in the post-terminator region and in the southern hemisphere. All of the dusk-flank FTEs moved anti-Sunward; most which occurred at Z_{GSM} < -10 R_E had a negative V_Z (13 out of 17 FTEs), but 17 of the 30 FTEs at Z_{GSM} > -10 R_E had a small, positive V_Z component. Few

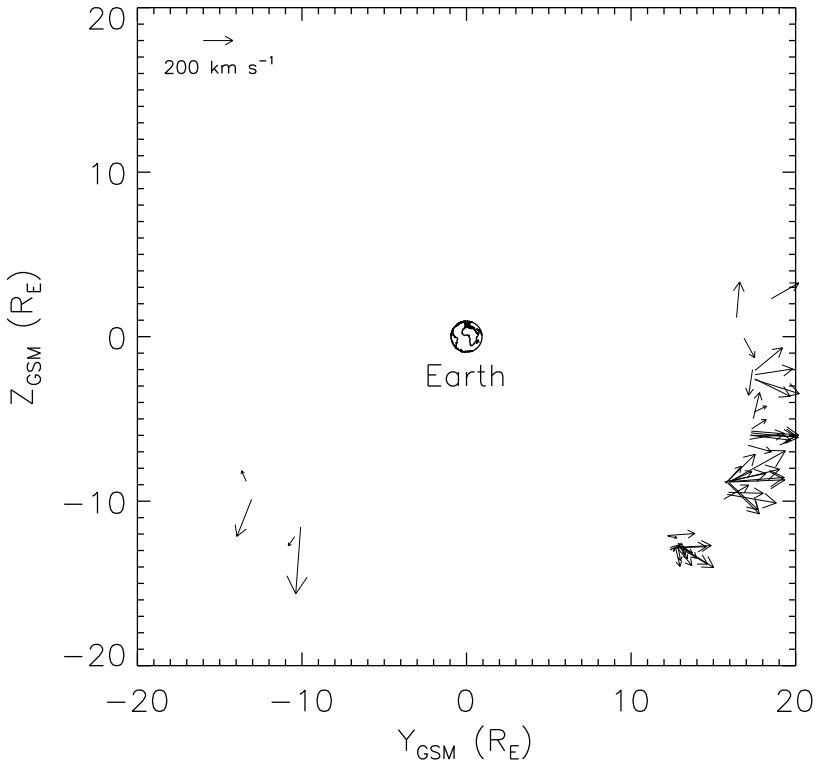

Figure 4.10: Velocities of 'strongly northward IMF' FTEs ($|\theta_{CA}| < 70°$), calculated by multi-spacecraft timing analysis, projected into the GSM Y-Z plane. The length of the arrow is proportional to the magnitude of the velocity within the Y-Z plane.

velocities were determined on the dawn flank, so it is difficult to draw generalisations about the motion of these FTEs. However, the behaviour of the examples we do have appears to be similar to that observed on the dusk flank: there were three southward-moving FTEs where $Z_{GSM} <$ -10 R_E, and one lower-latitude FTE which moved equatorward.

4.7 Comparison with model

The model developed by Cooling *et al.* (2001) calculates the motion of reconnected flux tubes over the surface of a model magnetopause for specified magnetosheath and solar wind conditions. The instantaneous velocity of an FTE is the velocity of the de Hoffmann-Teller frame ($\mathbf{V}_{HT}$): the frame in which the electric field transforms to zero (de Hoffmann and Teller, 1950). Cowley and Owen (1989) derived the following relationships between the de Hoffmann-Teller velocities and the magnetosheath

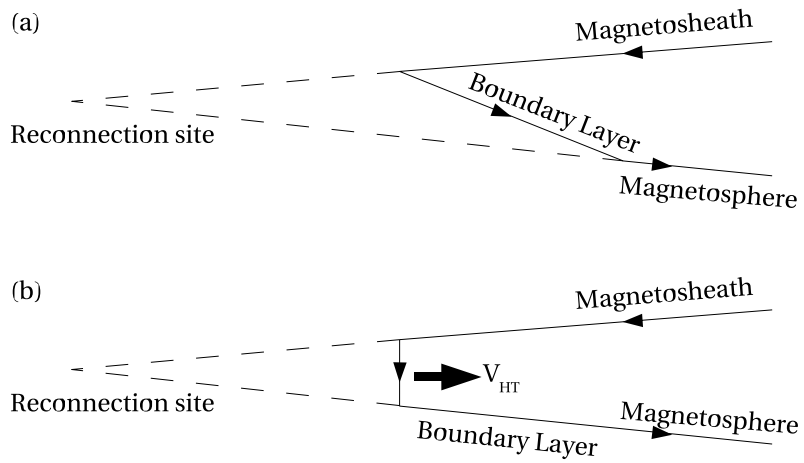

Figure 4.11: When magnetosheath and magnetospheric magnetic field lines reconnect, the 'kink' travels along the magnetic field line as an Alfvén wave. (a) (after Lockwood and Hapgood, 1997) shows the case where the Alfvén speed in the magnetosphere is greater than that in the magnetosheath, which leads to separate interior and exterior waves. The field rotation at the exterior wave is generally greater than that at the interior wave. The region between the two kinks is the boundary layer – the magnetic field takes a different orientation from the magnetosheath and magnetospheric fields. (b) Note that Cowley and Owen (1989) and Cooling *et al.* (2001) make the simplifying assumption that the boundary layer is thin, the discontinuity is purely rotational and that the thermodynamic properties of the magnetosheath plasma are unaffected as the plasma passes across the open magnetopause. Hence the interior and exterior Alfvén speeds are the same. In this assumption, the boundary layer magnetic field direction is the same as that of the magnetospheric magnetic field.

velocity, magnetic field and Alfvén speed:

$$\mathbf{V}_{HTN} = \mathbf{V}_{SH} - V_A \hat{\mathbf{b}}_{SH} \tag{4.5}$$

$$\mathbf{V}_{HTS} = \mathbf{V}_{SH} + V_A \hat{\mathbf{b}}_{SH} \tag{4.6}$$

where $\mathbf{V}_{HTN}$ and $\mathbf{V}_{HTS}$ are the velocities of the flux tubes connected to the northern and southern hemispheres, $\mathbf{V}_{SH}$ is the magnetosheath velocity, V_A is the Alfvén speed, and $\hat{\mathbf{b}}_{SH}$ is the magnetosheath magnetic field unit vector. The distinction between $\mathbf{V}_{HTN}$ and $\mathbf{V}_{HTS}$ arises from the plasma flow crossing the magnetopause, which is parallel and antiparallel to the magnetic field respectively. Therefore, these vectors will be unaffected if reconnection takes place with open magnetospheric field lines in the lobe, even though the flux tube will not be connected to the corresponding hemisphere. In deriving these equations, Cowley and Owen (1989) assumed that the plasma flow along the reconnected flux tube is purely inward across the magnetopause (neglecting outward flow of magnetospheric plasma, reflection of magnetosheath plasma at the kink in the reconnected field line and mirroring of magnetosheath plasma at lower altitudes). They also assumed that, whilst the velocity of the plasma is changed as it crosses the magnetopause, its thermodynamic properties are unaffected and the plasma pressure just inside the magnetopause is

the same as that in the magnetosheath. This region is referred to as the boundary layer (Figure 4.11). The boundary layer magnetic field direction is the same as the local magnetospheric field orientation, but to maintain the stress balance normal to the magnetopause, the boundary layer magnetic pressure is assumed to be the same as that in the magnetosheath. Therefore the magnetic field strengths in the boundary layer and magnetosheath are taken to be the same. Consequently, the boundary layer magnetic field strength is suppressed compared with the magnetospheric field. The Alfvén speeds in the magnetosheath and boundary layer are therefore taken to be equal.

The Cooling *et al.* (2001) model calculates the magnetosheath magnetic field from a model ($\mathbf{B}_{ms}$) developed by Kobel and Flückiger (1994). The Kobel and Flückiger (1994) model takes three inputs: the stand-off distances of the bow shock and magnetopause (R_{bs} and R_{mp}) and the IMF. The magnetopause is modelled as a paraboloid.

Since Cowley and Owen (1989) and Cooling *et al.* (2001) assume that the magnetic field magnitude is the same either side of the current sheet, only the direction of the magnetospheric (geomagnetic) field ($\mathbf{B}_{gm}$) is required. The geomagnetic field direction is derived from a simple model which assumes two point cusps on the paraboloid magnetopause at the locations $(\frac{1}{2}R_{mp}, 0, \pm R_{mp})_{GSM}$. All field lines are mapped from the southern to the northern cusp over the surface of the magnetopause.

An initial reconnection site is specified by the user; if the magnetic shear $|\mathbf{B}_{ms} - \mathbf{B}_{gm}|$ is above a threshold (which is also user-specified), reconnection is permitted. This formulation allows reconnection to take place in regions of lower angular shear if the magnitudes of $\mathbf{B}_{ms}$ and $\mathbf{B}_{gm}$ are large enough. A component reconnection X-line with an arbitrary length is traced along the direction of the local magnetopause current, i.e. perpendicular to the vector $(\mathbf{B}_{ms} - \mathbf{B}_{gm})$. Several pairs of reconnected flux tubes are placed along the X-line, and their velocities ($\mathbf{V}_{HTN}$ and $\mathbf{V}_{HTS}$) are calculated. The positions of the flux tubes are then incremented by $\mathbf{V}_{HT}\Delta T$, where ΔT is a short time interval (ΔT is set to be one thousandth of the time for which the flux tube velocities are integrated. In this thesis, integration times of 500 and 750 s are used, so ΔT=0.5 or 0.75 s).

Runs of this model were conducted using typical conditions from the 10th, 12th and 17th November, when the majority of the $\theta_{CA} < 70°$ events occurred. The results are shown in Figures 4.12 to 4.17. The figures are shown in reverse chronological order, as this corresponds to FTE observations at increasing southern latitudes. Each figure shows the result of a model run. The parameters used for each run (the

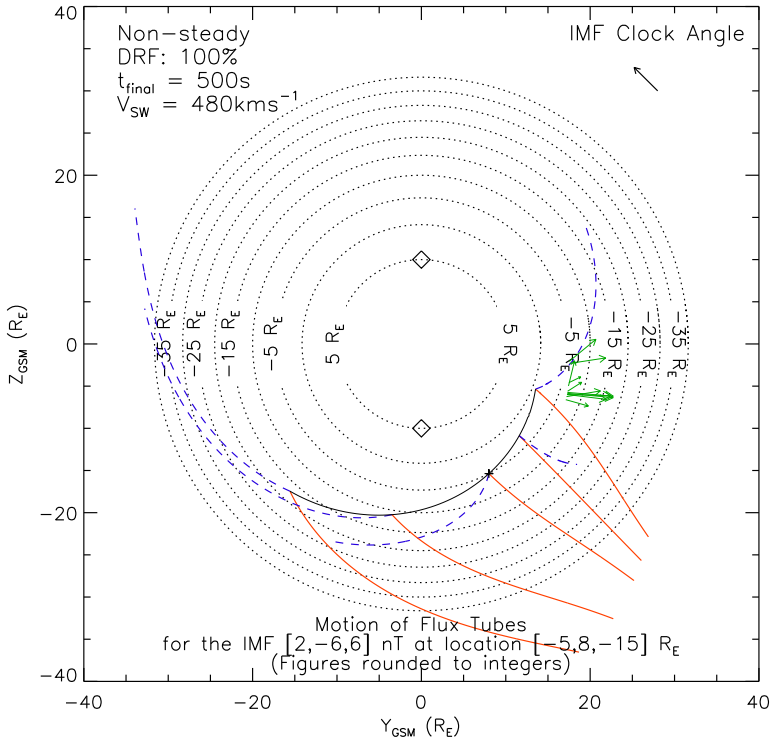

Figure 4.12: Evolution of flux tubes predicted by the model of Cooling *et al.* (2001), using solar wind parameters from the 17th November 2002. The figure shows a view in the GSM Y-Z plane of the magnetopause. Concentric circles represent contours of X_{GSM}. The diamonds are the positions of the cusps. Solid red and dashed blue lines denote model flux tube paths, and green arrows show the location and velocities of the FTEs observed on the 17th November. A component X-line (black solid line), emanating from a region of 180° magnetic shear to lower shears, has been assumed.

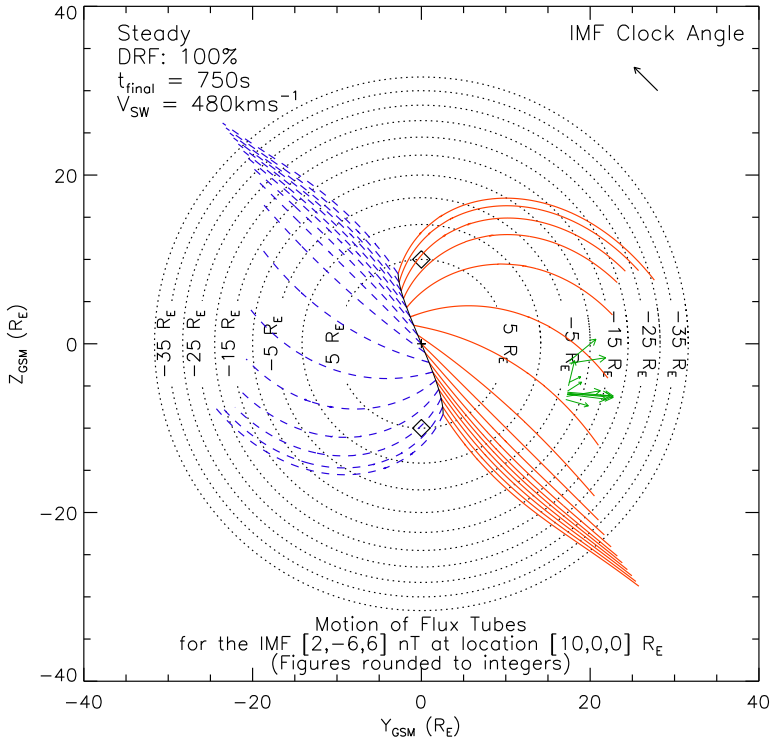

Figure 4.13: As Figure 4.12, but with a subsolar reconnection line. The magnetic shear threshold required for reconnection to occur at the initial reconnection site has been set to zero to illustrate the paths of flux tubes if subsolar reconnection did occur.

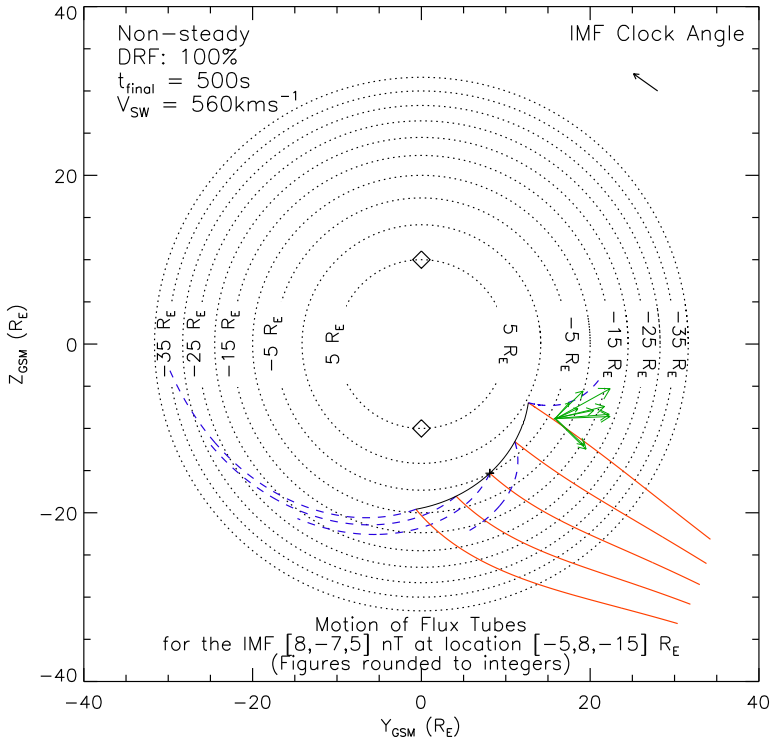

Figure 4.14: As Figure 4.12, but with IMF conditions and FTE velocities from the 12th November.

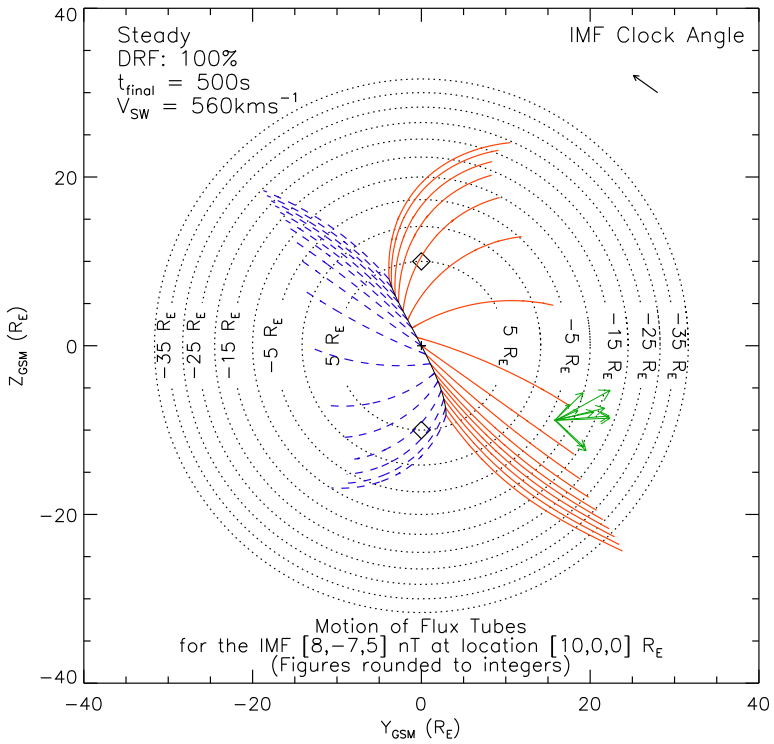

Figure 4.15: As Figure 4.13, but with IMF conditions and FTE velocities from the 12th November.

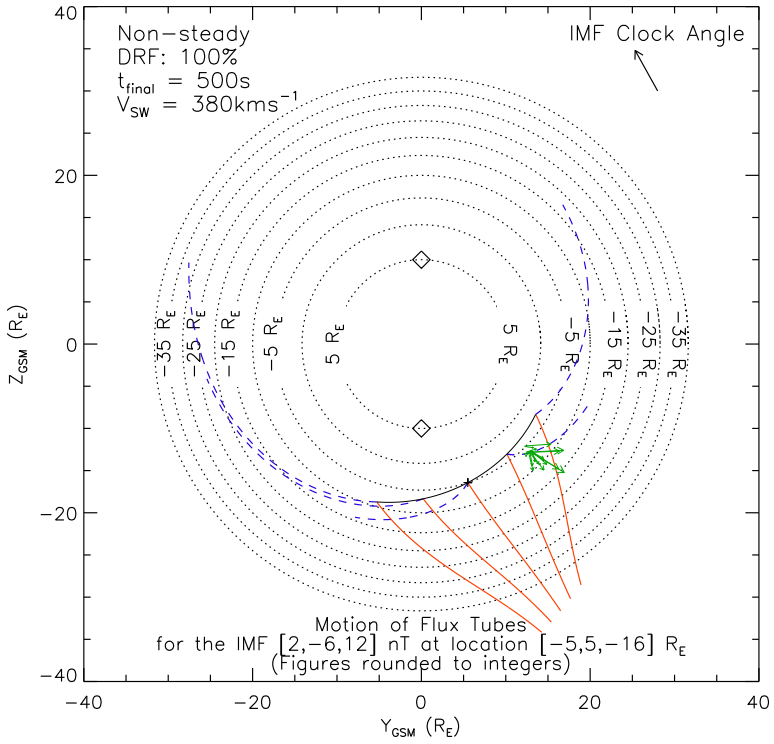

Figure 4.16: As Figure 4.12, but with IMF conditions and FTE velocities from the 10th November.

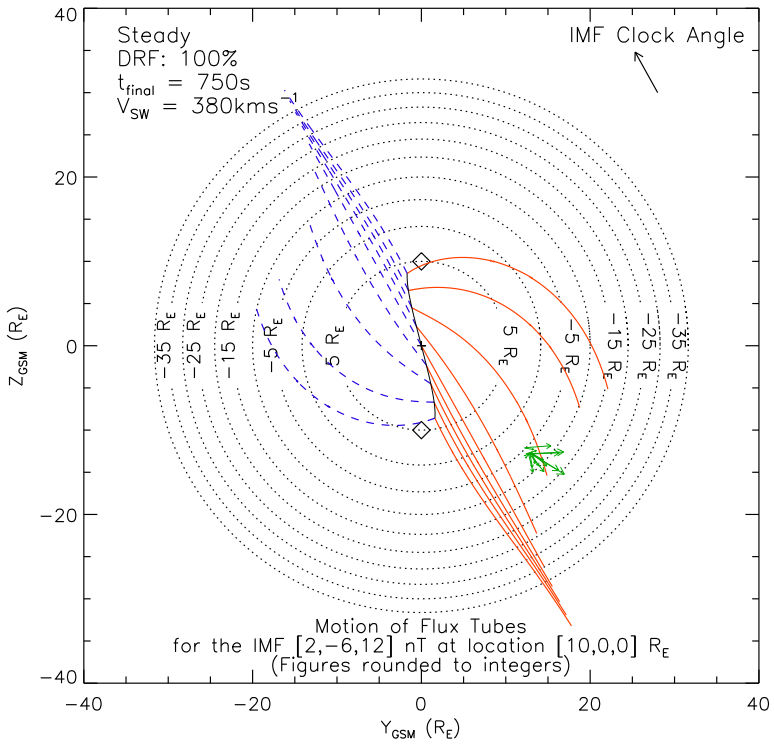

Figure 4.17: As Figure 4.13, but with IMF conditions and FTE velocities from the 10th November.

IMF, solar wind speed and solar wind density) were calculated separately for each day by taking one value of each lagged quantity for each FTE on that day (the value that is nearest in time to each FTE), and then calculating the mean of the resulting set of values of each parameter.

In each of these three cases, the mean lagged IMF was northward, dawnward and Sunward: (2, -6, 12)$_{GSM}$ nT, (8, -7, 8)$_{GSM}$ nT and (2, -6, 6)$_{GSM}$ nT on the 10th, 12th and 17th November respectively. The solar wind speeds were 380, 560 and 480 kms^{-1} and the solar wind plasma densities were 12, 7 and 8 cm^{-3}. Under such conditions, the antiparallel reconnection hypothesis predicts a reconnection site in each hemisphere. Each site has one end at the cusp in that hemisphere; the northern hemisphere X-line extends dawnward, and the southern hemisphere line extends duskward. The fact that IMF $B_X > 0$, combined with the Earth's dipole tilt in the northern hemisphere summer, implies that reconnection is likely to occur preferentially in the southern hemisphere (Crooker, 1992). Furthermore, if the model reconnection site is placed in the north/dawn quadrant, the model flux tubes are swept tailward and therefore not observed at the location of Cluster, unless the solar wind density entered into the model is set at a value much lower than that observed ($\sim$1 cm^{-3}). In this case the magnetosheath flow becomes sub-Alfvénic allowing the flux tubes connected to the southern hemisphere to move southward toward Cluster, but their motion is strongly southward.

Therefore, we can assume that the reconnection site which generated the FTEs is more likely to have occurred in the southern hemisphere. When reconnection in this model is restricted to regions of 180° shear, the model flux tube paths do not move past the observed locations of the FTEs. Therefore, an initial reconnection site was selected that lay on the locus of 180° shear and on the $X_{GSM} = -5$ R$_E$ contour. A component reconnection line was then extended from this point along the local model magnetopause current direction [i.e. perpendicular to the vector $(\mathbf{B}_{ms} - \mathbf{B}_{gm})$] until its equatorward end formed flux tubes which passed the location of Cluster. Thus the magnetic shear was not equal to 180° at most points on the reconnection line. In the case of the 17th November, which included the most equatorward of observations out of these three days, the X-line had to be extended until the shear between the model magnetic fields was 70°. These results are shown in Figures 4.12, 4.14 and 4.16.

Two sets of flux tubes are generated at each X-line; one set are generated on the southward side and move southward and tailward (red lines). These flux tubes are either connected to the northern hemisphere, or they are connected to lobe field lines and therefore have both ends in the solar wind. The other set are generated on the northward side, but are also swept tailward (blue lines) as the model mag-

netosheath flow is super-Alfvénic. These flux tubes are connected to the southern hemisphere. The FTEs on the 17th November were observed between 02:50 and 05:50 UT; between these times the Alfvén Mach numbers generally observed in the magnetosheath ($1.5 < M_A < 2.5$) compare well with the values predicted by the model at the location of Cluster ($1.8 < M_A < 2.2$).

Also shown in Figures 4.12-4.17 are the locations and velocities of the FTEs observed on the each day (green arrows). The equatorward and duskward motion of the FTEs observed nearer the equator in Figures 4.12 and 4.14 is consistent with the most northward dashed model FTE path. Figure 4.18 shows some of the PEACE electron signatures observed between 04:20 and 05:00 UT on the 17th November. The top three panels show re-ordered PAD data from Cluster 2, and the bottom four panels show the high resolution magnetic field data observed by all four spacecraft. In this interval, many smaller FTEs can be identified, but only three fulfilled the identification criteria, which are marked by vertical dashed lines. The observed background magnetosheath electron distribution was anisotropic; the antiparallel electron distribution was more energetic. However, the clearest electron signature at the time of most of these events was an energization of the parallel-moving electron population. Whilst there was no net anisotropy in these events (the background antiparallel anisotropy was reduced), an acceleration of parallel-moving electrons observed in the magnetosheath is consistent with being on magnetic field lines that are connected to the southern hemisphere.

Two FTEs observed on the 12th November (Figure 4.14) had a more southerly velocity, and appear to compare well with one of the solid model FTE paths. These model paths are either connected to the lobe magnetic field, or the northern hemisphere ionosphere. These two events were also observed when the spacecraft were in a boundary layer. The first, at 13:53 UT exhibited a bidirectional electron signature (not shown). At the time of the second southward-moving FTE (14:20 UT), the PEACE instruments on Cluster 4 observed a signature of magnetosheath-energy electrons moving parallel to the magnetic field (Figure 4.19). This is consistent with a northern hemisphere or lobe connection if the boundary layer lies within the magnetopause. The bidirectional signature observed at 13:53 UT and the large magnetic field rotation observed by the spacecraft as they cross from the boundary layer to the magnetosheath between 14:24 and 14:27 UT are both evidence for this assumption. Once the Cluster spacecraft re-entered the magnetosheath, further FTE signatures were accompanied by accelerated parallel electrons (such as at 14:29 UT, also shown in Figure 4.19), consistent with the southern hemisphere connection that is more generally observed in the model run shown in Figure 4.14.

For the FTEs originating further south on the X-lines, the dashed model FTE

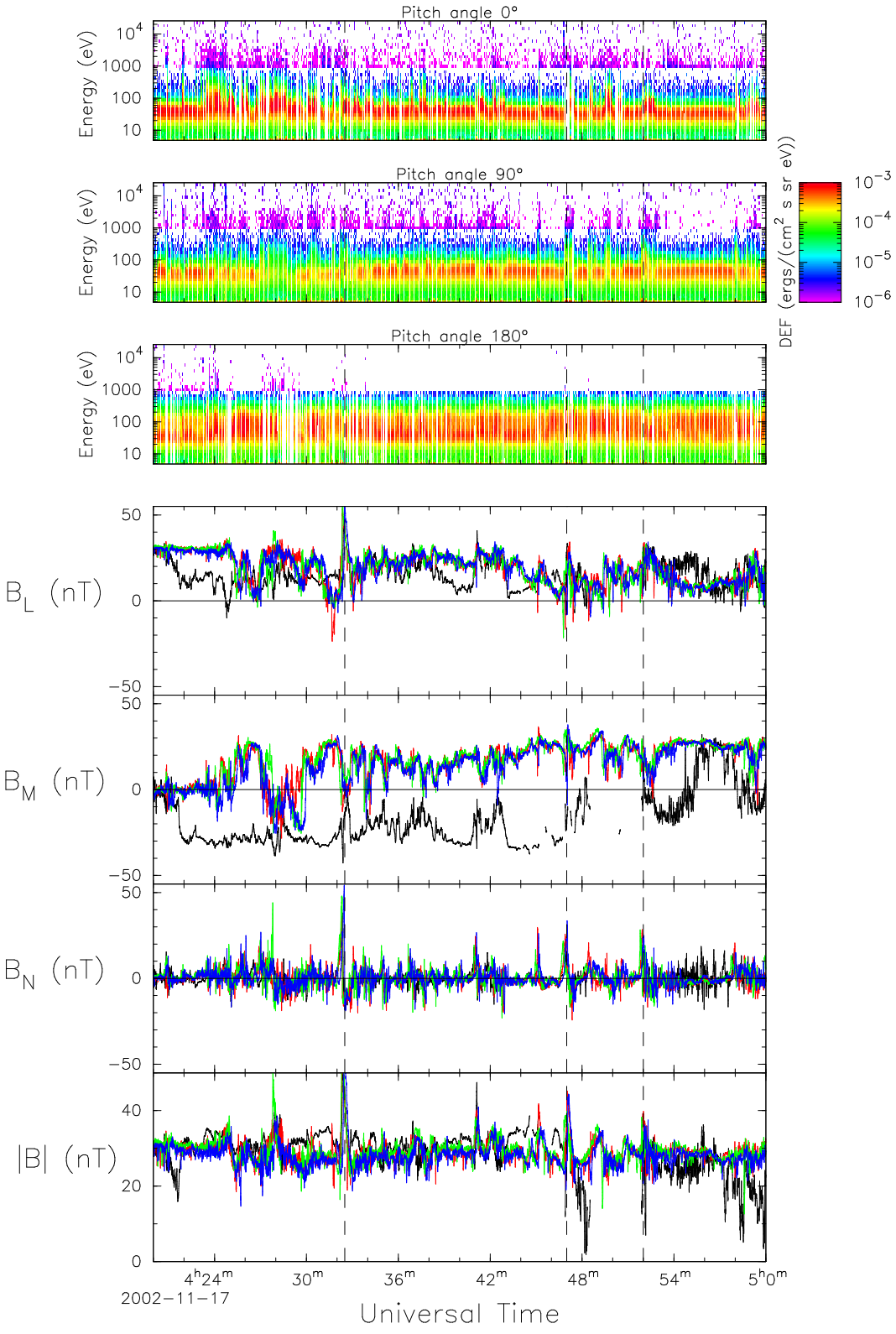

Figure 4.18: An FTE train on the 17th November 2002. The top three panels show electron data from the PEACE LEEA and HEEA instruments on Cluster 2. Re-ordered PAD data have been used. The spacecraft potential remained below the bottom of the LEEA energy range throughout this interval. The bottom four panels show the components and magnitude of the magnetic field in boundary normal coordinates. During this interval, there was generally an antiparallel anisotropy in the magnetosheath, but when many of the FTEs were observed, accelerated magnetosheath electrons were also observed streaming parallel to the magnetic field (some of which are marked by vertical dashed lines). Although there was no clear net anisotropy in these events, the parallel-moving electron bursts are consistent with a magnetic connection to the southern hemisphere.

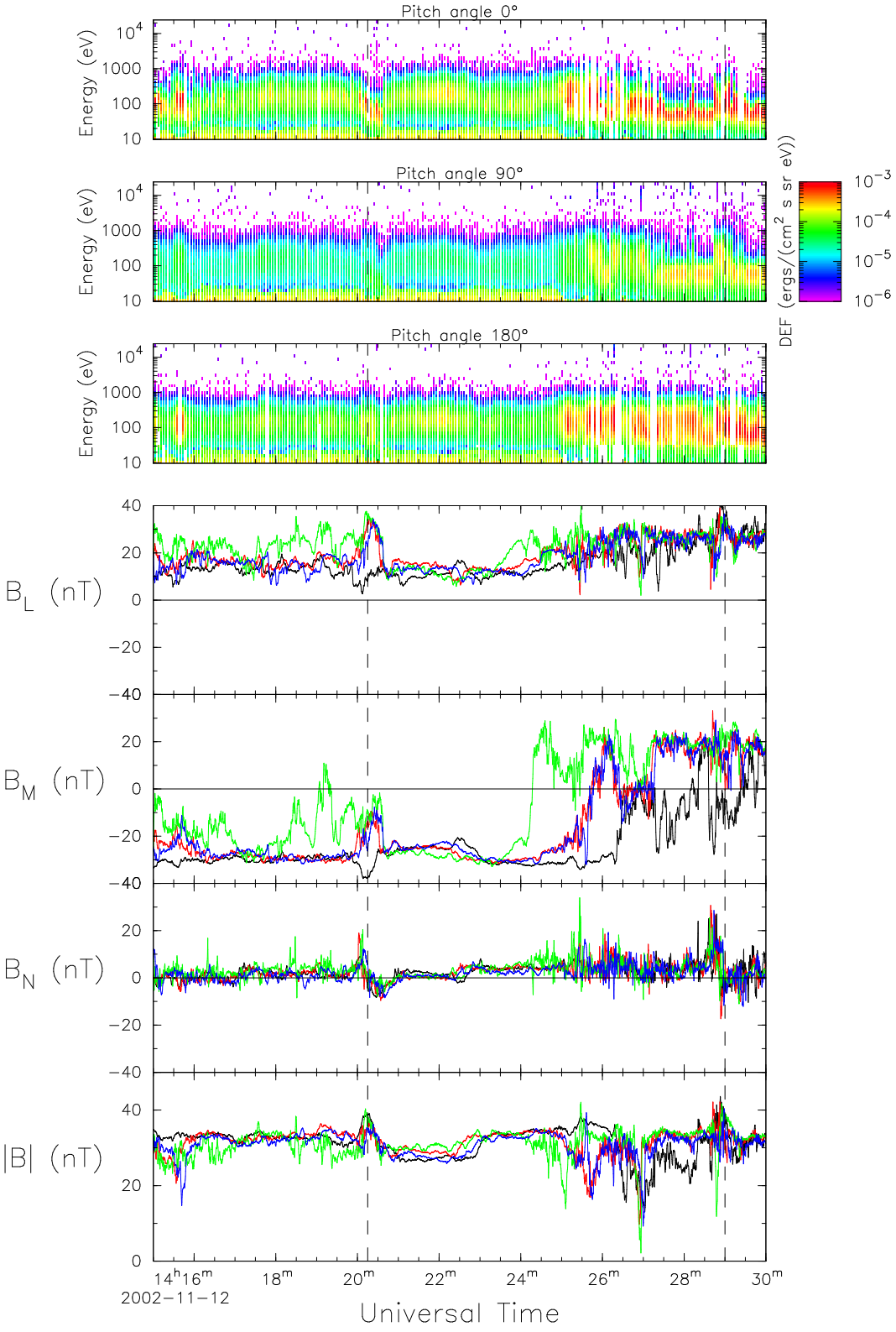

Figure 4.19: Two FTEs on the 12th November 2002. This figure takes the same format as Figure 4.18, except that rebinned PAD spectrograms from Cluster 4 are shown. For most of this interval, the spacecraft were in a boundary layer; they re-entered the magnetosheath between 14:24 and 14:27 UT. At 14:20 UT, a standard polarity FTE was observed (marked by a dashed line). The electron signature consisted of magnetosheath energy electrons moving parallel to the magnetic field. The velocity determined for this FTE was consistent with a flux tube connected to the lobe or northern hemisphere; therefore the parallel anisotropy of the FTE signature is consistent with the model velocity if the boundary layer lies inside the magnetopause. Note that there is a significant magnetic field rotation as the spacecraft cross back into the magnetosheath. FTE signatures similar to those observed in Figure 4.18 are observed in the magnetosheath, such as the event at 14:29 UT (also marked by a dashed line). In this case, parallel-streaming accelerated magnetosheath electrons were observed, implying a connection to the southern hemisphere, which was consistent with the velocity observed.

paths turn southward. This can explain the absence of equatorward-moving FTEs on the 10th November (Figure 4.16). The observed velocity vectors of all of the magnetosheath FTEs on these three days have components antiparallel to the observed magnetosheath magnetic field, whilst those observed in the magnetosphere/boundary layer have velocity components parallel to the local magnetic field. This is consistent with the standard polarity signatures observed in all cases.

The other interpretation proposed by Kawano and Russell (1997b) to explain the northward IMF post-terminator events was a tilted equatorial X-line. This interpretation also invoked 're-reconnection' (Nishida, 1989) to explain the absence of strongly northward IMF FTEs in the subsolar region. For this reason, model runs assuming a subsolar X-line are shown in Figures 4.13, 4.15 and 4.17. In these examples, the magnetic shear threshold ($|\mathbf{B}_{ms} - \mathbf{B}_{gm}|$) required for reconnection to occur has been set to zero. The dashed model FTE paths do not move duskward, and so only southward-moving model paths occur in the vicinity of the Cluster spacecraft.

4.8 Discussion

As noted earlier, Kawano and Russell (1997b) concluded that there were two possible mechanisms for post-terminator FTEs under strongly northward IMF conditions: a tilted equatorial X-line, and near-cusp reconnection where the FTEs moved equatorward. Their interpretations are shown in Figure 4.20, which is an adaptation of Figures 9, 10 and 11 of Kawano and Russell (1997b). The observations presented in this chapter show that the FTEs in Figures 4.10 and 4.12 are more consistent with high-latitude (near cusp) and flank reconnection, but not quite in the same way as Kawano and Russell (1997b) envisaged.

The directions of the FTE velocities studied in detail are similar to those derived from the Cooling *et al.* (2001) model for a near-cusp reconnection line and their polarities are consistent with the FTE velocities relative to the local magnetic field. In the interpretation of Kawano and Russell (1997b), lower latitude observations of cusp reconnection are a consequence of observing the lower-latitude portion of the reconnected field line (Figure 4.20c). The equatorward motion in the Cooling *et al.* (2001) model is a consequence of super-Alfvénic flow at the X-line, and the electron signatures of the equatorward moving events on the 12th and 17th November are consistent with this interpretation.

A further consequence of the super-Alfvénic magnetosheath flow at the recon-

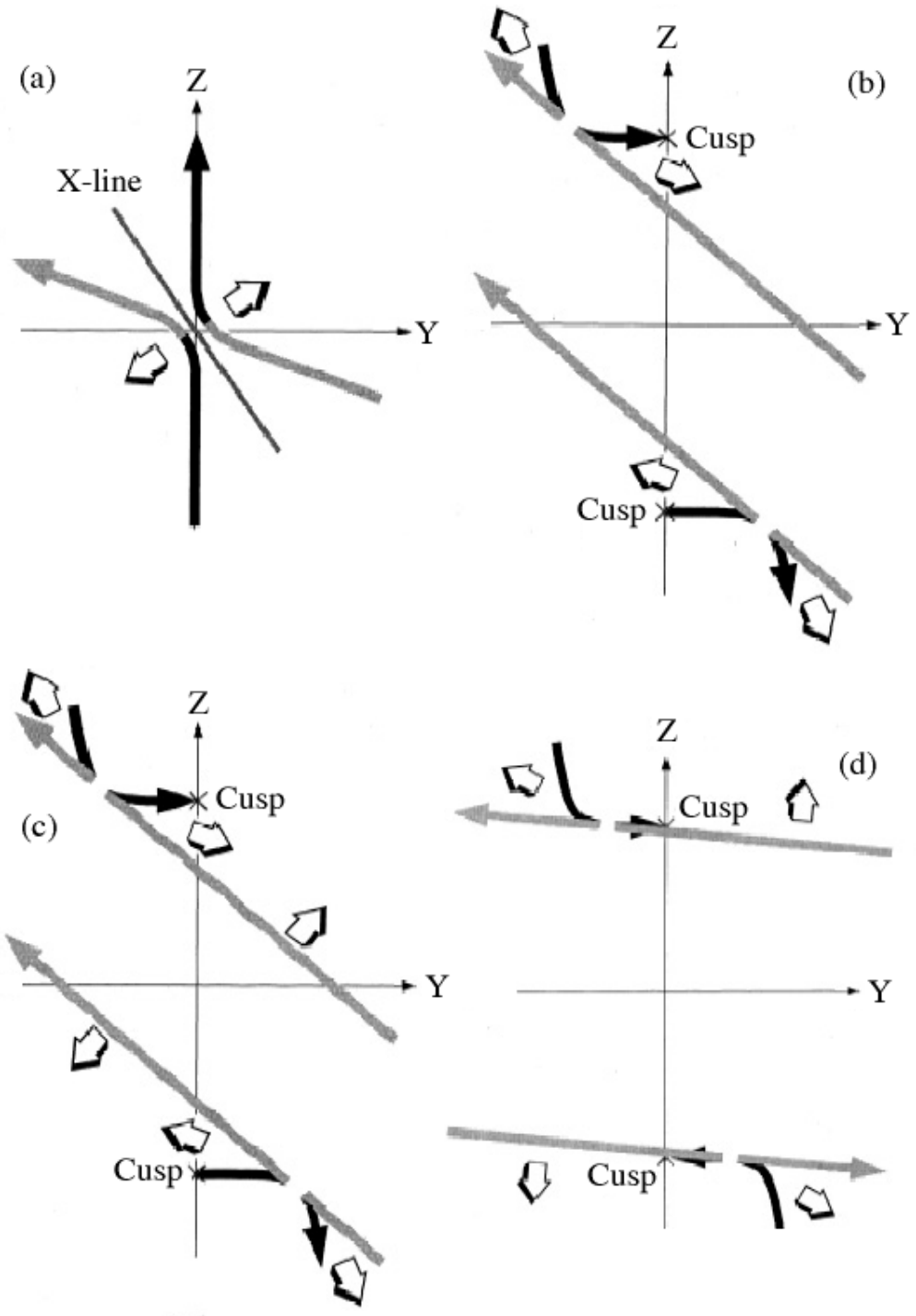

Figure 4.20: The interpretation of northward IMF FTEs by Kawano and Russell (1997b), adapted for the case of IMF $B_Y < 0$. (a) Subsolar reconnection: The authors proposed that the polarities of the FTEs they observed under northward IMF conditions could be explained by a tilted subsolar X-line. (b) If the IMF was strongly northward, then cusp reconnection could also lead to FTE signatures if the lower latitude FTE observations were caused by the lower-latitude extent of the field line that was reconnected at high latitude (c). (d) This explanation does not explain those FTEs which were observed when the IMF was slightly northward, but predominantly dawn- or duskward.

nection site is that steady state reconnection cannot be supported: if reconnection does occur, it must be transient. This is because the reconnected magnetic field lines must flow away from the reconnection line in opposite directions in the rest frame of the X-line, in order that more unreconnected field lines can move in toward the reconnection site (Cowley and Owen, 1989). This criterion is satisfied in the sub-Alfvénic flow region if the X-line is stationary, but in the super-Alfvénic region the X-line must move for reconnection to continue. Therefore the X-line will soon move to another region which is less suitable for reconnection and reconnection will cease.

Furthermore, the southern hemisphere equatorward velocities observed in Figures 4.13 and 4.15 are not consistent with a tilted X-line originating at the subsolar point for two reasons. First, if subsolar reconnection is forced in the model, only southward flux tube motion is predicted in the vicinity of Cluster (Figures 4.13, 4.15 and 4.17). Second, Kawano and Russell (1997b) suggested that the reason that strongly northward IMF FTEs were not observed near the subsolar region was that although random reconnection might occur near the subsolar point, open field lines generated near the subsolar point would be re-closed by 're-reconnection' (Nishida, 1989) and FTEs would only be observed from the ends of the X-line away from this region. The model flux tube paths which pass nearest Cluster in Figures 4.13, 4.15 and 4.17 originate within 5 R_E of the subsolar point, which is not consistent with the lack of observed northward IMF FTEs in earlier surveys (e.g. Berchem and Russell, 1984; Rijnbeek *et al.*, 1984; Southwood *et al.*, 1986; Kuo *et al.*, 1995). Since 71 FTEs were observed under strongly northward IMF conditions on these three separate days, and a further 50 events were observed in the rest of the season, there is no reason to believe that strongly northward IMF events are a rare occurrence, and it most likely that they are generated on the post-terminator magnetopause.

Although the initial reconnection point used in the model runs was selected by requiring a 180° magnetic shear, the fitting of predicted FTE paths to the observations did require the inclusion of a long X-line which extends into regions on the flank where the local shear drops down to the 70° threshold of Freeman *et al.* (1993), implying that the FTEs were generated at a component reconnection site. Recently, Trattner *et al.* (2004, 2005) examined cusp ion signatures observed by the Polar satellite during intervals of northward IMF. From the low-velocity cut-offs of precipitating and mirrored ion signatures, they estimated the distance from the satellite to the reconnection site causing the precipitation and hence the position of the site, and also concluded that reconnection lines formed in regions of high magnetic shear at high latitudes often extend into regions of lower magnetic shear. Although the reconnection lines in Figures 4.12, 4.14 and 4.16 of this chapter were shown as continuous X-lines extending from the antiparallel reconnection region, there is

no evidence that reconnection occurred along the whole length of each X-line simultaneously (or even that reconnection did occur at the antiparallel reconnection site). Thus, a less ordered theory of the location of magnetic reconnection (such as fractal reconnection, e.g. Coleman and Freeman, 2005) might also be compatible with these results. It is also worth noting that in the flank region, the simple model magnetospheric field used by Cooling *et al.* (2001) is less reliable than in subsolar regions and so the magnetic shear would therefore be better calculated from a more advanced geomagnetic field model.

The choice of X_{GSM} for the initial reconnection point was arbitrary, but it was deliberately selected so that the X-line remained tailward of the terminator and in a region of super-Alfvénic magnetosheath flow. Since the instantaneous velocity calculated by the Cooling *et al.* (2001) model does not depend upon any time history or momentum of the flux tube, the same motion would be derived if the reconnection site were moved Sunward or tailward. The important factor is that the magnetosheath flow must remain super-Alfvénic at the region of X-line generating the FTEs and the X-line must remain Sunward of the observed FTEs. However, if the X-line is moved tailward, the X-line would be required to extend further equatorward, and hence to a region of lower magnetic shear.

A northern hemisphere reconnection site is also possible for the observed IMF (shown in Figure 4.20b, c and d). Although this site is less likely to occur due to the combined effect of the Earth's dipole tilt and the IMF B_X component corresponding to each FTE on these three days (Crooker, 1992), Cluster is not in a suitable location to determine whether this site is active in November. In May/June, when Cluster crosses the magnetopause on the dawn flank, northern hemisphere reconnection is more likely, and FTEs will move tailward and predominantly northward. However, as can be seen from the FTE locations in Figure 4.8, FTEs in the northern hemisphere were observed at lower latitudes than in the southern hemisphere, as the spacecraft crossed the magnetopause at lower latitudes in the north than in the south. Consequently the latitude of the Cluster spacecraft will generally be too low and too far upstream in the northern hemisphere to observe most of the FTEs which move directly down the tail, or those FTEs which do move equatorward.

If the IMF B_Y component is positive and $B_Z > 0$, reconnection sites in the northern/dusk and southern/dawn quadrants are likely. Once again, Cluster's location at the northern hemisphere magnetopause makes observation of FTEs from site the northern/dusk site less likely. However, although reconnection is less likely to occur in the southern hemisphere in May/June, Cluster is in a better position to observe the FTEs when it does. Any FTEs generated at the southern/dawn site should move either strongly southward and dawnward, or dawnward with a slight

equatorward component. Such motion should generally result in a standard polarity signature. All four FTE velocities in the dawn sector of Figure 4.10 are consistent with this motion, and 11 out of the 13 FTEs in Figure 4.8 in the southern dawn quadrant which occurred when IMF $B_Y > 0$ were standard polarity events.

4.9 Conclusions

A catalogue of 446 high-latitude and flank FTEs observed by Cluster during the 2002/3 dayside magnetopause crossing season has been compiled; this is the first survey of FTE velocities using four-spacecraft timing. Upstream IMF data were available for 421 of these FTEs. 121 FTEs were observed when the absolute clock angle was less than 70°. The locations, polarities and velocities of these FTEs are generally consistent with a long, component reconnection X-line originating from a region of high magnetic shear in the lobe. The strict antiparallel reconnection hypothesis is not sufficient to explain the locations or velocities of many of the events; reconnection must occur in regions of lower shear. The equatorward velocities observed at lower southern latitudes (a consequence of super-Alfvénic flow at the reconnection site) are not consistent with an X-line centred on the subsolar point.

Chapter 5

FTE Motion: Southward and Dawn/Dusk-Dominated IMF

> All models are wrong. Some are useful.
> *Professor George Box (1919-), alumnus of University College London*

5.1 Introduction

In the final study of this thesis, the database of FTEs identified in Chapter 4 is used to investigate those events which occurred when the IMF was either southward or dominated by the dawn/dusk component (B_Y). Only those events which occurred when the magnitude of the IMF clock angle θ_{CA} was greater than 70° are considered. Thus, the study is restricted to clock angles for which Freeman *et al.* (1993) and Senior *et al.* (2002) concluded dayside, low-latitude reconnection (i.e. reconnection between the cusps) may occur.

The purpose of this study is twofold: to test the Cooling *et al.* (2001) model, and to investigate the antiparallel and component reconnection hypotheses. The Cooling *et al.* (2001) model often predicts the FTE motion reasonably well: 43 out of 81 events had velocities that were within 20° of the model de Hoffmann–Teller velocity with a magnitude between 50% and 150% of the model value. A further 15 events were within 30° and satisfied the same magnitude criterion. Seven further cases were within 30° of the model magnetosheath velocity and satisfied the magnitude criterion. This implies that either some of the signatures are of structures that are embedded into the magnetosheath flow (e.g. boundary waves, Sibeck, 1990, 1992), or that they suffer from a violation of the assumption made

by Cowley and Owen (1989), and hence Cooling *et al.* (2001), that the plasma flow across the reconnection kink is dominated by magnetosheath plasma which has not had time to mirror, and is therefore unidirectional. In general, this assumption should be valid. The magnetosheath density is regularly observed to be as low as 10 cm^{-3}, and the magnetosheath magnetic field strength often reaches 30 nT. Therefore Alfvén speeds of order 200 kms^{-1} are quite feasible. This is the speed by which a magnetosheath particle will be accelerated as it crosses the magnetopause when travelling along a reconnected field line. If it is also assumed (e.g. Lockwood and Hapgood, 1997) that the distance from a low-latitude reconnection site along the magnetospheric field line to the ionosphere is of order 20 R_E, the return journey should take approximately 1300 s, which is a longer time interval than the period for which the model flux tube paths are traced in this chapter (750 s). If reconnection takes place nearer the cusp, the field-aligned distance to the ionosphere may be nearer 10 R_E, and the Alfvén travel time will also be halved; therefore in a small number of cases it may be feasible that mirrored particles are observed. In this case the plasma density in the boundary layer will be up to double that assumed by Cowley and Owen (1989) and the Alfvén speed will correspondingly drop to a minimum value of $\frac{1}{\sqrt{2}}$ times the model value. The flux tube velocity vector will then rotate toward the magnetosheath velocity vector.

Some inconsistencies between the observed and model velocities are caused by the method used to determine the inter-spacecraft timings of the B_N signatures. The delay between FTE signatures on a pair of spacecraft was initially determined by maximising the cross-correlation coefficient between the B_N signatures for each spacecraft pair. Sometimes this failed to align the central point of each signature, and hence the true velocity vector is not returned unless the signatures are aligned by eye.

Four FTEs were found to be inconsistent with the predictions of the Cooling *et al.* (2001) model, but consistent with the velocities of the open flux tubes calculated using the original formulae derived by Cowley and Owen (1989) if the observed magnetosheath parameters are used. The discrepancies between the model vectors predicted by Cooling *et al.* (2001) and those calculated from the observed parameters were due to a combination of factors, but in three of the four events the observed magnetosheath density differed significantly from the model values (in one case, the observed density was almost double the model density). In the fourth case, the observed magnetic field strength was only 35% of the model value. In these four cases, the directions of the observed magnetosheath velocity and magnetic field vectors were close to their model values, differing only by up to 20°. A further two FTEs, whose velocity vectors were directed by more than 35° out of the plane containing the observed magnetosheath velocity and magnetic field vectors (and hence the two

possible de Hoffmann–Teller velocities), were 'consistent' with the de Hoffmann–Teller velocity calculated from the observed magnetosheath parameters (1 event) or consistent with the observed magnetosheath flow (1 event) if projected into the plane defined by the magnetosheath velocity and magnetic field.

The second object of this chapter is to see whether it is possible to identify whether individual FTEs have been generated by an antiparallel reconnection site, or a component reconnection line which originates near the subsolar point, but which may extend to higher latitudes. If the IMF B_Y component is small, these reconnection sites coincide (see Chapter 1). At other times the sites are separate, but the model flux tube paths can be traced back to both reconnection sites so it is not possible to distinguish from which site the observed flux tube originated. Earlier surveys (e.g. Russell *et al.*, 1985) concluded that only component reconnection could explain the occurrence of FTEs at low latitudes when the IMF B_Y component was strong. Whilst this does appear to be the case in this survey, a small number of FTEs were observed at high latitudes which were clearly only consistent with a model flux tube path which passed through regions of high magnetic shear, but did not cross the model subsolar component reconnection line. A further three events, observed on the 31st January 2003, appear from the model to have been generated at a reconnection site at low magnetic shear, at least 8 R_E from the model component subsolar X-line. However, the observed ion signatures are inconsistent with this interpretation, and the inconsistency has not yet been resolved.

5.2 Multi-Spacecraft Timing Analysis: A More Advanced Approach

In order to make a more detailed case-by-case comparison with the Cooling *et al.* (2001) model, a more advanced method was used to calculate the FTE velocities than that used in Chapter 4. Unfortunately it is not possible to derive a separate angular and magnitude error on the FTE velocities using standard error analysis; however this advanced method, also described by Harvey (1998, p311), uses the relative time differences between the signature observations at each of the six possible pairs of Cluster spacecraft, reducing the effect of an error on a single timing measurement on the outcome, and provides a measure of the mutual consistency of the six timings.

Since there are four Cluster spacecraft, there are six possible time delays:

$$t_{\alpha\beta} = t_\alpha - t_\beta \tag{5.1}$$

where t_α and t_β are the observation times at Clusters α and β, $1 \leq \alpha \leq 4$, and $1 \leq \beta < \alpha$.

$t_{\alpha\beta}$ was obtained by maximising the cross-correlation functions between the B_N signatures on each spacecraft pair – the same technique as was used in Chapter 4.

The direction of motion $\hat{\mathbf{v}}$ and speed V were determined by minimising the function:

$$S = \sum_{\alpha=1}^{4} \sum_{\beta=1}^{4} [\hat{\mathbf{v}} \cdot (\mathbf{R}_\alpha - \mathbf{R}_\beta) - V t_{\alpha\beta}]^2 \tag{5.2}$$

Again defining the vector $\mathbf{m}$ as a vector with the direction of the FTE velocity but the magnitude of the reciprocal of the speed ($\mathbf{m} = \frac{\hat{\mathbf{v}}}{V}$); this becomes, in tensor notation:

$$S = \sum_{\alpha=1}^{4} \sum_{\beta=1}^{4} [m_l(r_{\alpha l} - r_{\beta l}) - t_{\alpha\beta}]^2 \tag{5.3}$$

Seeking to minimise S ($\frac{\partial S}{\partial m_k} = 0$):

$$\sum_{\alpha=1}^{4} \sum_{\beta=1}^{4} [m_l(r_{\alpha l} - r_{\beta l}) - t_{\alpha\beta}][r_{\alpha k} - r_{\beta k}] = 0 \tag{5.4}$$

which can be written:

$$m_l \sum_{\alpha=1}^{4} \sum_{\beta=1}^{4} (r_{\alpha l} - r_{\beta l})(r_{\alpha k} - r_{\beta k}) = \sum_{\alpha=1}^{4} \sum_{\beta=1}^{4} t_{\alpha\beta}(r_{\alpha k} - r_{\beta k}) \tag{5.5}$$

so:

$$2N^2 m_j R_{jk} = \sum_{\alpha=1}^{4} \sum_{\beta=1}^{4} t_{\alpha\beta}(r_{\alpha k} - r_{\beta k}) \tag{5.6}$$

where:

$$R_{jk} = \frac{1}{N} \sum_{\alpha=1}^{4} r_{\alpha j} r_{\alpha k} \tag{5.7}$$

The spacecraft position vectors used to construct the tensor R_{jk} must be measured relative to the tetrahedron mesocentre (Harvey, 1998, p310), which means that

$$\sum_{\alpha=1}^{N} \boldsymbol{r}_\alpha = \mathbf{0} \tag{5.8}$$

$\mathbf{m}$ is then given by:

$$m_l = \frac{1}{N^2} \left[\sum_{\alpha \neq \beta} t_{\alpha\beta}(r_{\alpha k} - r_{\beta k}) \right] R_{kl}^{-1} \tag{5.9}$$

The value S (Equation 5.2), which was minimised for each event, gives a measure of the mutual consistency of each of the six inter-spacecraft timings deduced for each event. S represents the sum of the squares of the differences (for each spacecraft

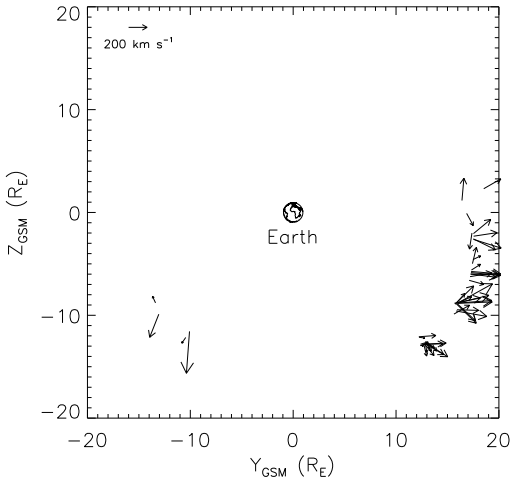

Figure 5.1: The velocities derived in Chapter 4 from the FTEs which occurred under strongly northward IMF (this figure is a reproduction of Figure 4.10)

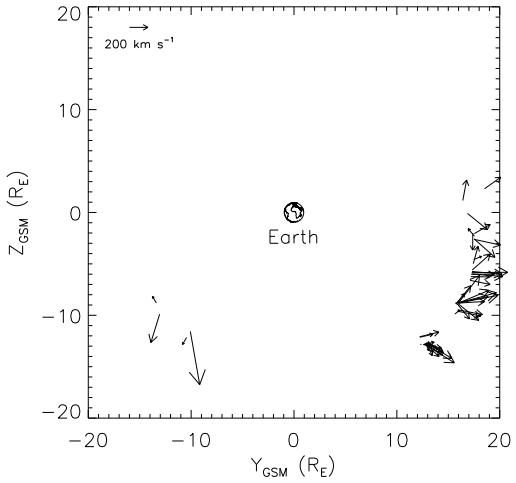

Figure 5.2: The results of applying the more advanced multi-spacecraft timing analysis to the same events

pair) between: (a) the distance between the two spacecraft in the direction of motion of the FTE, and (b) the distance travelled by the FTE in the time between the B_N signature being observed at each spacecraft if it moves steadily at speed V. Hence, if:

$$t_{\alpha\beta} = t_{\beta\gamma} + t_{\gamma\alpha} \tag{5.10}$$

for each α, β and γ, then $S = 0$. In this case, the method is identical to that described in Section 4.6. Whilst the six inter-spacecraft timing measurements are then perfectly consistent, this does not mean that $\mathbf{V}$ has been determined perfectly; if the cross correlation procedure consistently lines up a feature that is not at the centre of the FTE signature, the resulting planar surface may not be oriented perpendicular to the actual velocity vector of the FTE. If the same feature has consistently been selected, the corresponding S value might still be small.

A comparison of the results from this technique with the results from the simpler approach used in Chapter 4 is shown in Figures 5.1 and 5.2. Although there are slight differences between the calculated velocities of some vectors (such as the strongly southward-moving FTE at (-10,-12)R_E in the GSM Y-Z plane), the general characteristics are the same, and it can be seen that there is sometimes less variation in the velocities derived for individual events that are contained in a train of FTEs, such as those observed on the 10th November (discussed in Chapter 4 and located at (13,-13)R_E in the plane of the plots).

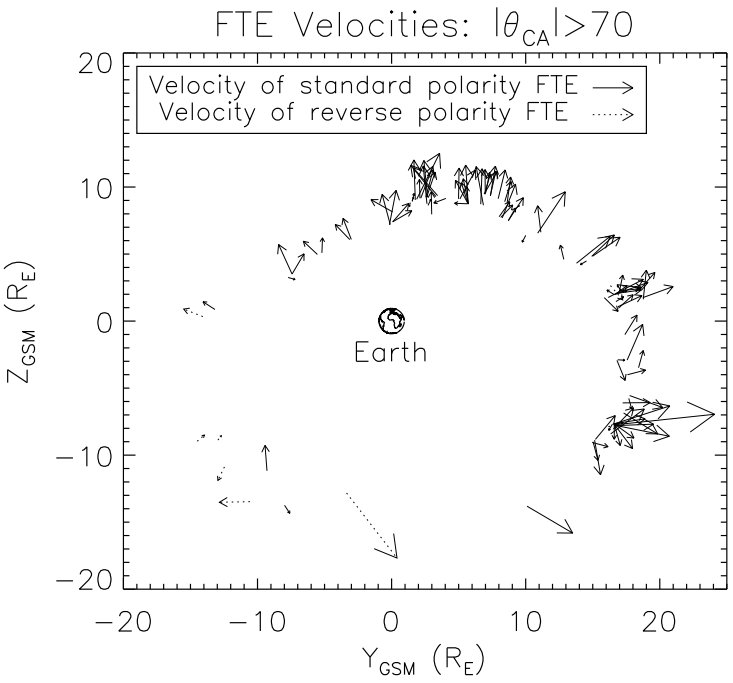

Figure 5.3: Velocities of FTEs which occurred when $|\theta_{CA}| > 70°$, calculated by the more advanced multi-spacecraft timing analysis method described in Section 5.2. The vectors have been projected into the GSM Y-Z plane. The length of the arrow is proportional to the magnitude of the projection of the velocity onto the Y-Z plane.

5.3 Results

Of the 300 FTEs which occurred when the lagged IMF clock angle, θ_{CA}, was greater than 70°, 118 events had a bipolar signature on all four spacecraft and occurred before the spacecraft manoeuvre on the 10th June 2003 which reduced the tetrahedron quality (see Chapter 4). The multi-spacecraft timing technique described in Section 5.2 was applied to these 118 events, and the results are shown in Figure 5.3.

A histogram of the observed distribution of S is shown in Figure 5.4. After an initial examination of the velocities in Figure 5.3, an arbitrary threshold of S was set at 30, and events with a greater S value were discarded. One further event was discarded as its speed was particularly low (only 22 kms^{-1}) compared with the other 81 FTEs, all of which had a speed of greater than 100 kms^{-1}. The velocities of the 81 FTEs are shown in Figure 5.5.

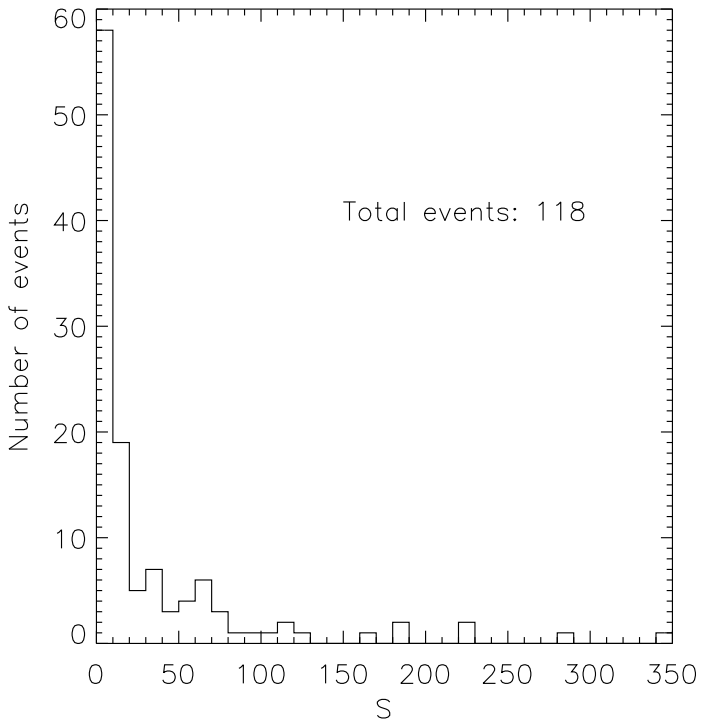

Figure 5.4: A histogram of the observed distribution of S. One value of S (Equation 5.2) was calculated for each of the 118 FTEs which occurred when $\theta_{CA} > 70°$. The 81 FTEs which had a corresponding S value less than 30 and a velocity greater than 22 kms^{-1} were used for more detailed study in this chapter.

5.4 Comparison with Cooling Model

As discussed in Chapter 4, the model developed by Cooling *et al.* (2001) uses a model magnetosheath magnetic field and a very simple geomagnetic field model to calculate the path of a reconnected flux tube according to the expressions presented by Cowley and Owen (1989). The velocity of the reconnected flux tube (specifically the velocity of the kink in the reconnected flux tube at the magnetopause, as shown in Figure 4.11b) depends only upon the local magnetosheath magnetic field, plasma flow and plasma density (see Equations 4.5 and 4.6). For a more detailed comparison of the 81 individual FTE velocities shown in Figure 5.5 with the Cooling *et al.* (2001) model, the Cooling model code was modified so that the flux tube paths were calculated in reverse:

- The position of the FTE observation was projected onto the model magnetopause
- Equations 4.5 and 4.6 were evaluated at this point to provide $\mathbf{V}_{HTN}$ and $\mathbf{V}_{HTS}$
- A small step backward was evaluated for both the flux tube connected to the northern hemisphere ($-\mathbf{V}_{HTN}\Delta T$) and the tube connected to the southern

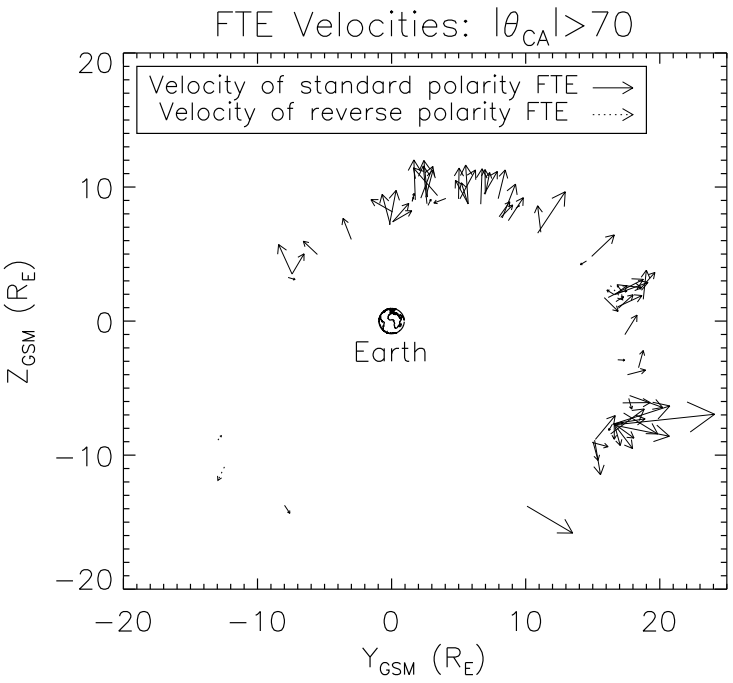

Figure 5.5: The velocities of the 81 FTEs which occurred when $|\theta_{CA}| > 70°$, S was less than an arbitrary threshold of 30 and excluding one event which had a speed of 22 kms^{-1}. These short-listed events are used for more detailed study in the rest of this chapter. The figure takes the same format as Figure 5.3.

hemisphere ($-\mathbf{V}_{HTS}\Delta T$), where $\Delta T = 0.75$ s.

- Equations 4.5 and 4.6 were re-evaluated, and the steps traced back for 750 s. This time was chosen as it was generally long enough for the paths to be traced back to the point at which they 'stall' – i.e., where the magnetosheath flow and Alfvén velocity are equal and opposite.

A separate model run was carried out for each of the 81 FTEs, using the lagged IMF, solar wind velocity and solar wind density for each event. Another model input, the magnetopause stand-off distance (R_{mp}), was calculated separately for each event:

$$R_{mp} = \left(\frac{B_E^2}{\mu_0 n_{sw} m_i v_{sw}^2} \right)^{\frac{1}{6}} \tag{5.11}$$

(Baumjohann and Treumann, 1997, p188), where n_{sw} is the solar wind ion density and v_{sw} is the solar wind speed, both of which were taken from the lagged ACE data, B_E is the equatorial magnetic field strength at the Earth's surface (taken to be 3.1×10^4 nT), μ_0 is the permeability of free space and m_i is the proton mass. The possible presence of heavier ions in the solar wind was neglected. Each model run is shown in chronological order in Appendix 1 (each FTE is numbered at the

top of the plot for reference). The observed FTE velocity ($\mathbf{V}_{FTE}$) should lie on the magnetopause surface, but in order to compare $\mathbf{V}_{FTE}$ with the model FTE velocities $\mathbf{V}_{HTN}$ and $\mathbf{V}_{HTS}$, and neglect angular differences between the observed and model vectors due to differences between the actual and magnetopause surfaces, $\mathbf{V}_{FTE}$ was projected onto the model magnetopause surface. The Kobel and Flückiger (1994) model magnetopause surface is described by:

$$\psi = Y_{GSM}^2 + Z_{GSM}^2 - 2R_{mp}(R_{mp} - X_{GSM}) = 0 \tag{5.12}$$

so the model normal is obtained by normalising the gradient:

$$\hat{\mathbf{n}} = \frac{\nabla\psi}{|\nabla\psi|} = \frac{(R_{mp}, Y, Z)_{GSM}}{|(R_{mp}, Y, Z)_{GSM}|} \tag{5.13}$$

The projection of $\mathbf{V}_{FTE}$ onto the surface defined locally by $\hat{\mathbf{n}}$ is therefore derived from the triple vector product:

$$\mathbf{V}_{plane} = \hat{\mathbf{n}} \times (\mathbf{V}_{FTE} \times \hat{\mathbf{n}}) \tag{5.14}$$

An example run is shown in Figure 5.6, which takes a similar format to Figure 4.12; the figure shows a view of the model magnetopause projected into the GSM Y–Z plane. Concentric circles mark contours of X_{GSM}, and the locations of the cusps $[(\frac{1}{2}R_{mp}, 0, \pm R_{mp})_{GSM}]$ are marked by diamonds. However, the figure differs from those in Chapter 4 in a few respects. The boundary between sub- and super-Alfvénic model magnetosheath flow is marked by a purple contour. In this example, two regions of sub-Alfvénic model magnetosheath flow also exist at $X_{GSM} < -35\ R_E$ as the model plasma density decreases down-tail (increasing the Alfvén speed) whilst the flow speed increases; in these two regions the strength of the model draped magnetosheath magnetic field is high enough to raise the model Alfvén speed above the model magnetosheath flow speed.

The model component reconnection line was initiated at the subsolar point, which was assumed to lie at the point where the model magnetopause surface intersects with the X_{GSM} axis. This assumption is a simple one, which neglects any effect of dipole tilt on the location at which reconnection might be initiated, but will be used as an initial test of the subsolar component reconnection hypothesis (Gonzalez and Mozer, 1974). The position of observation of the FTE has been projected onto the model magnetopause; $\mathbf{V}_{HTN}$, $\mathbf{V}_{HTS}$ and $\mathbf{V}_{sheath}$ have been evaluated at this point and are marked by black arrows. $\mathbf{V}_{plane}$ is shown in green. The paths of the corresponding flux tubes have been traced backwards in steps of 0.75 s for 750 s. The subsolar point, and closest approach of each path to the model reconnection line, have been marked by a '+', and as both flux tube paths crossed a region where

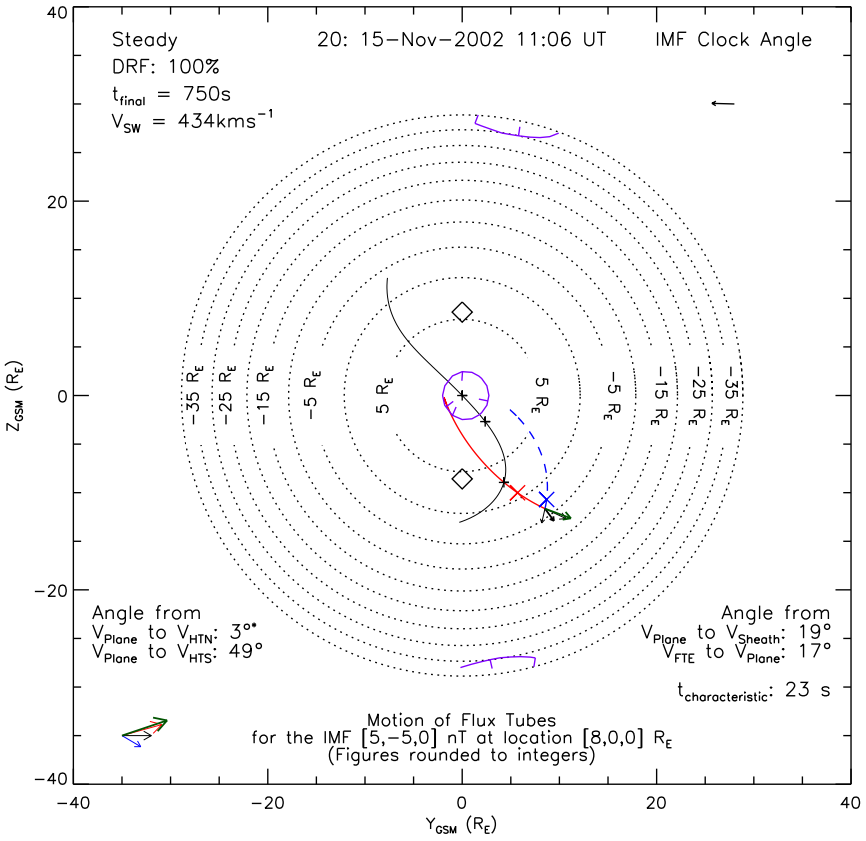

Figure 5.6: An example model run: 15th November 2002, 11:06 UT (FTE 20). The figure shows a view of the model magnetopause in the GSM Y-Z plane, with concentric circles marking contours of X_{GSM}; the cusps are considered to be point singularities marked by diamonds. The point at which the model magnetosheath flow becomes super-Alfvénic is marked by a purple contour, with tick marks pointing to the direction in which the flow is sub-Alfvénic. A model subsolar component reconnection line has been initiated at $(R_{mp}, 0, 0)_{GSM}$ (marked by the central '+') and traced in each direction for 20 R_E.

The position and velocity of the observed FTE have been projected onto the model magnetopause. The projected observed FTE velocity ($\mathbf{V}_{plane}$) is shown as a green arrow. The model velocities for flux tubes connected to the northern and southern hemispheres ($\mathbf{V}_{HTN}$ and $\mathbf{V}_{HTS}$) have also been calculated using the model magnetosheath magnetic field and flow speed at the projected position (black arrows). The model flux tube paths have been traced backward for 750 s. A black '+' the closest approach of each FTE path to the model component reconnection line. If either model FTE path passes through a region where the shear between the model magnetosheath and geomagnetic fields is greater than 150° then the position of maximum shear is denoted by a blue or red '×'. Also shown as a black arrow is the model magnetosheath flow; this is radial, and lies between $\mathbf{V}_{HTN}$ and $\mathbf{V}_{HTS}$.

The model and observed vectors are shown in an inset in the bottom left corner ($\mathbf{V}_{HTN}$ in red, $\mathbf{V}_{HTS}$ in blue, $\mathbf{V}_{sheath}$ in black and $\mathbf{V}_{plane}$ in green). They are magnified and plotted in plane of the magnetopause. A radial and tailward vector points to the right (e.g. $\mathbf{V}_{sheath}$), and a tangential component is shown by a clockwise/anticlockwise rotation. The angle between $\mathbf{V}_{plane}$ and the three model vectors is noted, along with the angle between $\mathbf{V}_{FTE}$ and its projection into the model magnetopause plane ($\mathbf{V}_{plane}$). In this example, the observed $\mathbf{V}_{FTE}$ lies 17° from the model magnetopause surface, and its projection $\mathbf{V}_{plane}$ is very close in magnitude and direction to the model $\mathbf{V}_{HTN}$. $\mathbf{V}_{HTN}$ can be traced back to a region of high magnetic shear (marked by the red '×') and the model component reconnection line. However, the FTE could have been reconnected anywhere on the red path, which traces back to where the model magnetosheath flow becomes super-Alfvénic.

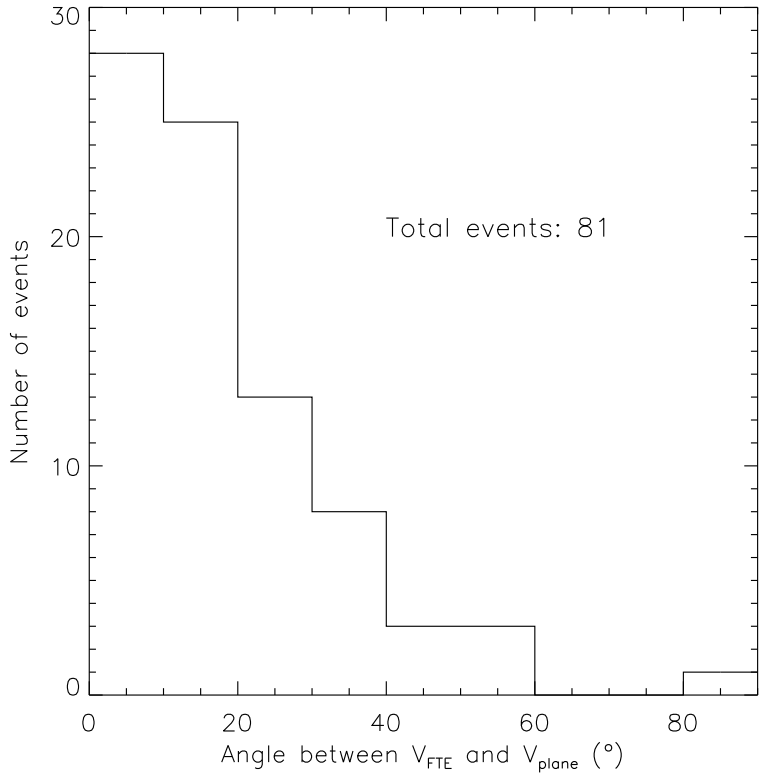

Figure 5.7: A histogram of the angles between $\mathbf{V}_{FTE}$ and $\mathbf{V}_{plane}$ for each of the 81 FTEs in Figure 5.5.

the shear between the model magnetic fields either side of the magnetopause was greater than 150°, the point of highest shear has been marked on each path by an '×'. The figure also shows the angle between $\mathbf{V}_{FTE}$ and the surface defined by $\hat{\mathbf{n}}$ (which contains $\mathbf{V}_{plane}$), and the angles between $\mathbf{V}_{plane}$ and $\mathbf{V}_{HTN}$, $\mathbf{V}_{HTS}$ and $\mathbf{V}_{sheath}$. In the bottom-left corner of the figure, $\mathbf{V}_{HTN}$ (red), $\mathbf{V}_{HTS}$ (blue), $\mathbf{V}_{sheath}$ (black) and $\mathbf{V}_{plane}$ (green) have been shown as they appear in the plane of the magnetopause. Finally, the 'characteristic time' (t_{char}) defined by Kawano *et al.* (1992) has been noted; this is the time between the positive and negative peaks of the bipolar B_N signature. The maximum characteristic time was 80 s, so all 81 events were within the category that Kawano *et al.* (1992) ascribed to reconnection.

By multiplying the magnitude of $\mathbf{V}_{FTE}$ by t_{char}, the spatial distance between the peaks in B_N can be evaluated. The peak-to-peak scale size of the 80 s event was 58,000 km (9 R_E). This is nine times larger than the low-latitude scale size estimate of Saunders *et al.* (1984). However, this event was an isolated one; the other 80 peak-to-peak scale sizes were between 2000 km and 22,000 km. Although there is not a direct comparison between the spatial separation of the peak B_N values and the total spatial scale estimated by Saunders *et al.* (1984), 58 of the remaining 80 values were greater than 1 R_E.

A histogram of the angles between $\mathbf{V}_{FTE}$ and $\mathbf{V}_{plane}$ is shown in Figure 5.7. For the majority of events (53 FTEs), $\mathbf{V}_{FTE}$ lay within 20° of the model magnetopause, but there were 27 events where the angle was between 20° and 60°, and one event where the angle was 81°.

Each $\mathbf{V}_{plane}$ vector was compared with the three model vectors which were evaluated at the projection of the FTE location onto the model magnetopause: the model flux tube velocities $\mathbf{V}_{HTN}$ and $\mathbf{V}_{HTS}$, and the model magnetosheath velocity $\mathbf{V}_{sheath}$. In order to evaluate the accuracy to which the observed velocities fitted the model, three thresholds were used in each comparison: $\mathbf{V}_{plane}$ was classified as 'consistent' with these vectors if the magnitude of $\mathbf{V}_{plane}$ was between 50% and 150% of the magnitude of $\mathbf{V}_{HTN}$, $\mathbf{V}_{HTS}$ or $\mathbf{V}_{sheath}$, and the angle between $\mathbf{V}_{plane}$ and the model vector was less than (a) 20°, (b) 25° or (c) 30°.

48 of the 81 FTEs were consistent with one or more of the possible model velocity vectors if the angular threshold was chosen to be 20°. A further 11 events were within 30° of one or more of these velocities. Whilst increasing the angular threshold to a higher value will naturally 'catch' more events, and makes it harder to distinguish between the three possible model velocities since more events are 'consistent' with two or three of the model velocities, note that 28 of the 81 events had an angle between $\mathbf{V}_{FTE}$ and the model magnetopause plane that was greater than 20° (Figure 5.7), implying that a discrepancy of this order may be due to errors in the multi-spacecraft timing analysis.

Unfortunately, there is no satisfactory straightforward analytical method of calculating the error on the velocities due to multi-spacecraft timing. 22 events had $\mathbf{V}_{plane}$ vectors which were more than 30° from each of the three model vectors. The cross-correlations of these 22 events were re-examined, but rather than taking the time delay which maximised the cross-correlation function, the B_N signatures were shifted in time until the delay looked correct. In each case, if the resulting S value, which quantifies the mutual consistency of the six inter-spacecraft timings, was greater than 30, the process was repeated until a selection of inter-spacecraft timings were found which both matched the features of the B_N signature well, and produced a value of S that was lower than 30.

In six cases, use of this method resulted in $\mathbf{V}_{FTE}$ vectors which, when projected onto the model magnetopause plane, were consistent with the value of either $\mathbf{V}_{HTN}$, $\mathbf{V}_{HTS}$ or $\mathbf{V}_{sheath}$ calculated in the Cooling *et al.* (2001) model. These events are listed in Table 5.1.

Whilst this is a subjective method, reasons for cross-correlation producing an incorrect lag did become apparent. An assumption made in multi-spacecraft timing

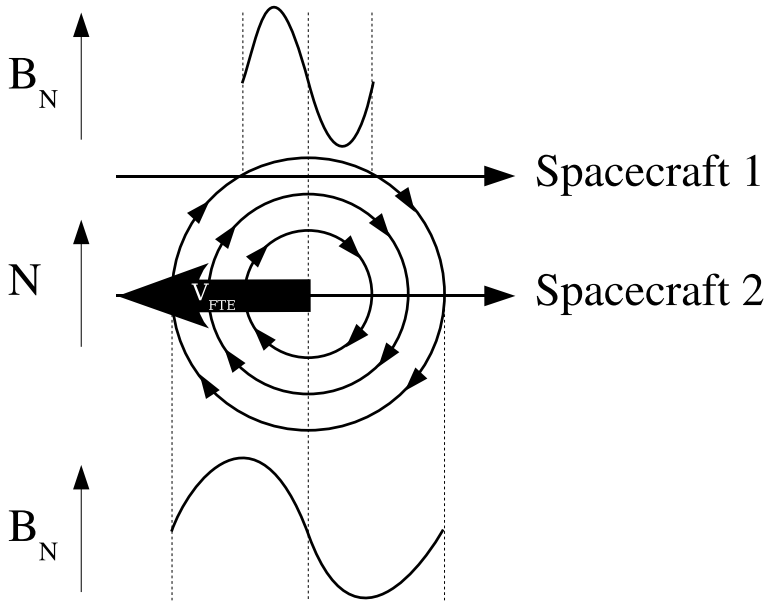

Figure 5.8: An illustration of the B_N signature observed by two spacecraft intersecting the FTE at different positions. An assumption made in the multi-spacecraft timing analysis is that the delay between the observed signatures on each spacecraft is due to the passage of a planar surface. In this figure, spacecraft 1 observes a briefer signature than spacecraft 2, but the planar surface is that which passes through the points in the FTE where B_N is zero.

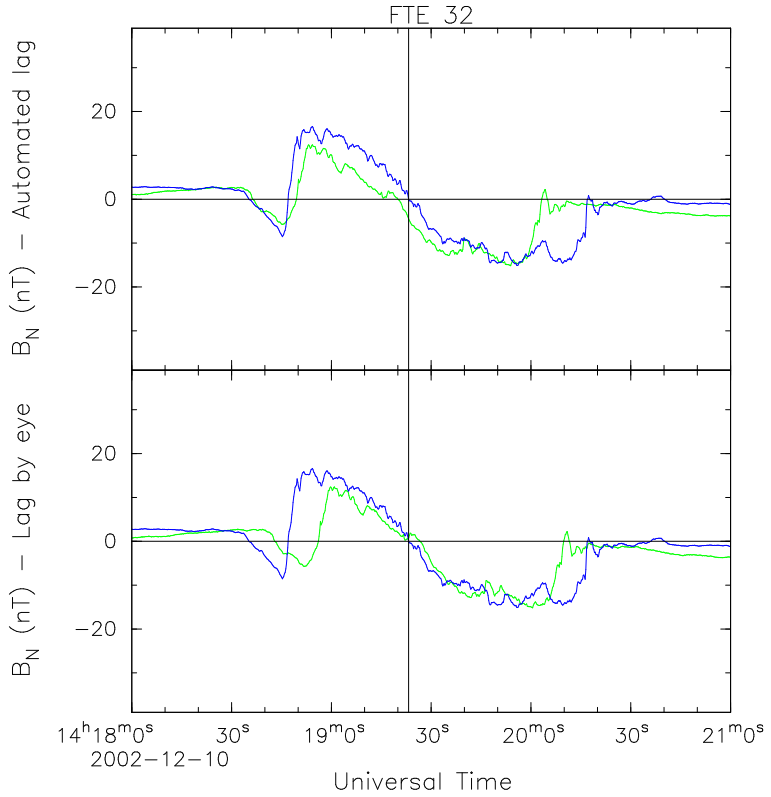

Figure 5.9: An example of an event where judging the lag by eye is an improvement over maximising the cross-correlation coefficient. Both panels show the Cluster 3 and Cluster 4 B_N signatures of FTE 32 (10th December 2002, 14:19 UT). In the top panel, the Cluster 3 signature has lagged by the time derived by maximising the cross-correlation function ($\delta t_{43} = 10.8$ s), and in the bottom panel the lag has determined by eye ($\delta t_{43} = 17.4$ s)

Event no.	Time (UT)	Angle between $\mathbf{V}_{plane}$ and $\mathbf{V}_{FTE}$	$\mathbf{V}_{HTN}$	$\mathbf{V}_{HTS}$	$\mathbf{V}_{sheath}$	$\frac{\lvert\mathbf{V}_{plane}\rvert}{\lvert\mathbf{V}_{HTN}\rvert}$	$\frac{\lvert\mathbf{V}_{plane}\rvert}{\lvert\mathbf{V}_{HTS}\rvert}$	$\frac{\lvert\mathbf{V}_{plane}\rvert}{\lvert\mathbf{V}_{sheath}\rvert}$
1	12-Nov-2002 16:26	10°	**6°** (37°)	63° (94°)	**20°** (51°)	**0.54** (0.55)	1.5 (1.6)	**0.88** (0.90)
12	13-Nov-2002 00:04	12°	**15°** (31°)	75° (92°)	31° (47°)	**0.57** (0.52)	1.4 (1.32)	0.92 (0.84)
25	28-Nov-2002 18:46	17°	36° (51°)	27° (43°)	**30°** (45°)	0.86 (0.75)	0.38 (0.34)	**0.53** (0.47)
30	08-Dec-2002 03:54	42°	4° (8.3°)	**3°** (1.4°)	1° (5.7°)	0.32 (0.28)	**0.52** (0.46)	0.40 (0.35)
32	10-Dec-2002 14:19	5°	11° (33°)	**14°** (36°)	12° (34°)	0.39 (0.55)	**0.64** (0.92)	0.49 (0.69)
40	10-Dec-2002 23:40	24°	**27°** (49°)	30° (52°)	**28°** (50°)	**0.61** (0.75)	1.8 (2.2)	**0.90** (1.1)

Table 5.1: Improvements in the timing analysis. The events for which $\mathbf{V}_{plane}$ is consistent with the Cooling *et al.* (2001) values of $\mathbf{V}_{HTN}$, $\mathbf{V}_{HTS}$ and/or $\mathbf{V}_{sheath}$ when $\mathbf{V}_{FTE}$ is determined from time lags that were judged by eye are shown, alongside results using the original lags (determined by maximising the cross-correlation function) which are shown in parentheses. The model values which are consistent with the observed $\mathbf{V}_{plane}$ vector are marked in bold. (For consistency, the angle between the two vectors is required to be less than 30°, and the magnitude of $\mathbf{V}_{plane}$ to be within 50% of the model value).

analysis is that the time delays are caused by the motion of a planar surface. In the case of an FTE signature, this is assumed to be valid for the mid-point in the B_N signature (Figure 5.8). In some cases, the cross-correlation function was not maximised when the centres overlapped. An example is shown in Figure 5.9, which shows the lag originally calculated between the signatures observed by Cluster 3 and Cluster 4 for FTE 32 (10th December 2002, 14:19 UT), and the lag decided by eye. In this example, the cross-correlation function was dominated by the effect of a short negative B_N excursion prior to the bipolar signature. This feature was observed on all four spacecraft; the combined effect on the automated lag was an error of 22° with respect to the values determined by eye. In other cases, the peak in the cross-correlation function was broad, and the lag at which the maximum correlation coefficient occurred was dominated by smaller-scale structure observed in the magnetic field.

A Venn diagram illustrating the proportion of $\mathbf{V}_{plane}$ vectors that were consistent with $\mathbf{V}_{HTN}$, $\mathbf{V}_{HTS}$ and/or $\mathbf{V}_{sheath}$ using each of the three angular thresholds is shown in Figure 5.10. In this figure and subsequent discussion, the velocities derived from the lags determined by eye have been used for the events which were re-examined. The velocities derived from the automated lags are used for the remainder of the events. Only 16 events remain which do not fulfil the magnitude and 30° criteria for at least one of the model velocities. However, 43 events are consistent with more than one model vector, making it difficult to distinguish between them. These are often cases where the magnetosheath flow speed dominates over the Alfvén speed, and there is therefore not a significant difference between the three model vectors.

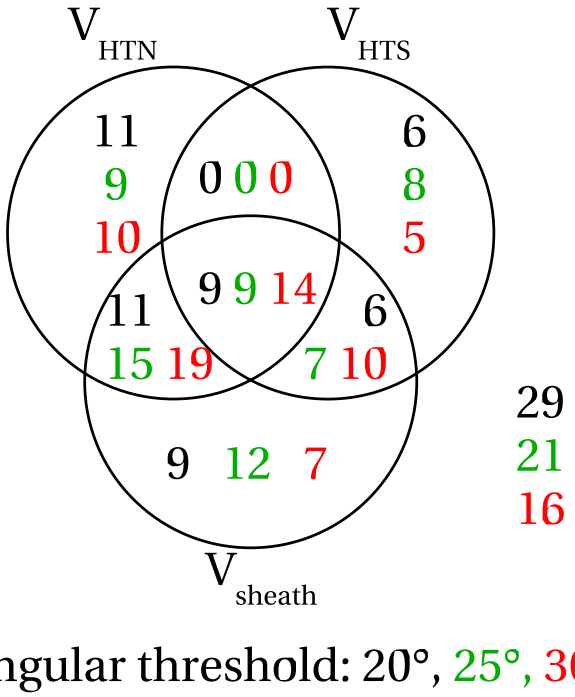

Figure 5.10: A Venn diagram showing the number of events where $\mathbf{V}_{plane}$ was consistent with $\mathbf{V}_{HTN}$, $\mathbf{V}_{HTS}$ & $\mathbf{V}_{sheath}$. $\mathbf{V}_{plane}$ was deemed to be consistent if its magnitude was within 50% of the magnitude of $\mathbf{V}_{HTN}/\mathbf{V}_{HTS}/\mathbf{V}_{sheath}$, and the angle between the two vectors was below a defined threshold. The results are shown for three angular thresholds: 20° (numbers in black), 25° (green) and 30° (red). Even when the angular threshold was 30°, 16 events did not appear to be consistent with any of the three model vectors.

Figure 5.11 divides the same data into those events where $\mathbf{V}_{FTE}$ is greater than 20° from the model magnetopause, and those events where $\mathbf{V}_{FTE}$ is within 20° of the magnetopause. Of those events which are within 20° of the magnetopause, only 14% are inconsistent with all three model vectors, compared with 30% if the events that are more than 20° from the magnetopause are considered. Similar proportions in these two categories are only consistent with $\mathbf{V}_{sheath}$ (7% and 10%), and similar proportions are consistent with both $\mathbf{V}_{sheath}$ and $\mathbf{V}_{HTN}$ or $\mathbf{V}_{HTS}$ (50% and 55%). However, significantly more events are only consistent with $\mathbf{V}_{HTN}$ or $\mathbf{V}_{HTS}$ if the events within 20° of the magnetopause are taken (22%) than if those events which are more than 20° from the magnetopause are considered (13%).

Taking the 65 events which were within 30° of one or more of the model velocities, and which satisfied the criterion that the magnitude of $\mathbf{V}_{plane}$ must be between 50% and 150% of the model vector magnitude, the relative proportions that are consistent a subsolar component reconnection line (i.e. a component reconnection line which originates at the subsolar point, but which may extend to higher latitudes) and antiparallel reconnection (for which a maximum model magnetic field shear of at least 150° is required) will now be investigated.

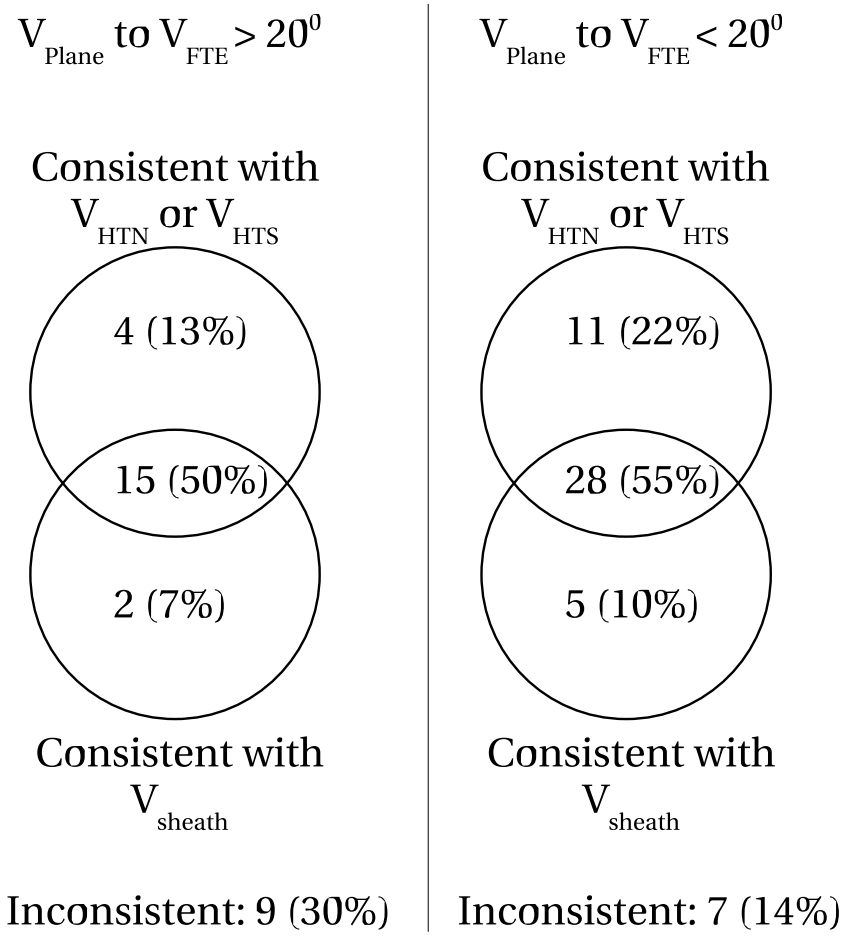

Figure 5.11: A Venn diagram showing the data in Figure 5.10, split between those events for which $\mathbf{V}_{FTE}$ was less than and greater than 20° out of the model magnetopause plane. The events which are consistent with $\mathbf{V}_{HTN}$ and $\mathbf{V}_{HTS}$ have been merged. Of the events which were more than 20° from the plane, 30% were inconsistent with all three model vectors (taking the 30° threshold) , compared with 14% if only those within 20° of the plane are considered. In these two categories, similar proportions were consistent only with $\mathbf{V}_{sheath}$ (7% and 10%), and with both $\mathbf{V}_{sheath}$ and $\mathbf{V}_{HTN}$ or $\mathbf{V}_{HTS}$ (50% and 55%), but significantly more events were consistent with only $\mathbf{V}_{HTN}$ or $\mathbf{V}_{HTS}$ when $\mathbf{V}_{FTE}$ was within 20° of the plane (22%) than when it was more than 20° from the plane (13%).

5.4.1 Subsolar Component Reconnection Events

38 of the FTEs were consistent with model de Hoffmann–Teller velocities which could be traced back to the model subsolar component reconnection line which passed through the subsolar point. Many of these events occurred in regions on the flanks where the model Alfvén Mach number was high, and consequently the magnetosheath flow term in Equations 4.5 and 4.6 dominated over the term containing V_A. As a result, there was not a significant difference between the three model vectors. However, nine events, listed in Table 5.2, were inconsistent with the model $\mathbf{V}_{sheath}$ vector; three were also inconsistent with an antiparallel site if a magnetic shear of 150° is required (FTEs 69, 70 and 74).

FTE 69 (22nd February 2003, 01:23 UT) is shown in Figures 5.12 and 5.13. At

Event	Time (UT)	Maximum model magnetic shear
4	12-Nov-2002 19:19	152°
8	12-Nov-2002 19:58	173°
12	13-Nov-2002 00:04	161°
20	15-Nov-2002 11:06	180°
56	22-Jan-2003 04:33	174°
66	03-Feb-2003 00:50	180°
69	22-Feb-2003 01:23	83°
70	08-Mar-2003 07:03	125°
74	08-Apr-2003 03:45	116°

Table 5.2: Events which were consistent with either $\mathbf{V}_{HTN}$ or $\mathbf{V}_{HTS}$, but not $\mathbf{V}_{sheath}$, and whose paths passed through the Cooling *et al.* (2001) model reconnection line.

this time the Cluster spacecraft were located at the near-noon dayside magnetopause in the northern hemisphere. Figure 5.12 shows PEACE pitch-angle spectrograms from Cluster 2 parallel, antiparallel and perpendicular to the magnetic field. The PAD data have been rebinned to the magnetic field on the ground. The figure also shows a spectrogram of anisotropy, which shall be defined as:

$$Anisotropy = \frac{(DEF_{Parallel} - DEF_{Antiparallel})}{(DEF_{Parallel} + DEF_{Antiparallel})} \tag{5.15}$$

which was calculated for every energy/time bin for which there was a non-zero DEF in the parallel and antiparallel directions. Therefore, if the pitch-angle binning fails to select the parallel or antiparallel pitch angle data for telemetry, no anisotropy is calculated. There is evidence of an electron signature in all three pitch-angle spectrograms, but the anisotropy spectrogram shows that the accelerated magnetosheath electrons have a stronger DEF antiparallel to the magnetic field than parallel. This compares with a generally parallel anisotropy at energies just over 100 eV in the surrounding magnetosheath, and implies a connection to the northern hemisphere magnetosphere. The bottom two panels show the magnetic field normal component and magnitude observed by FGM on all four spacecraft.

Figure 5.13 shows the model run for the same event. The lagged IMF was slightly northward, but strongly duskward. The measured $\mathbf{V}_{FTE}$ vector was 4° from the magnetopause plane, and $\mathbf{V}_{plane}$ was 24° from $\mathbf{V}_{HTN}$. $\mathbf{V}_{plane}$ matched the magnitude of $\mathbf{V}_{HTN}$ well; this is consistent with the antiparallel anisotropy that is observed. $\mathbf{V}_{HTN}$ can be traced back past the model component reconnection line, so this event is consistent with an FTE that was generated at the model X-line. However, it is also consistent with being generated either side of the X-line, so long as it was generated on the red path in Figure 5.13. The model does not allow specific determination of the reconnection site without complementary observations from another spacecraft of the flux tube that is connected to the southern hemisphere

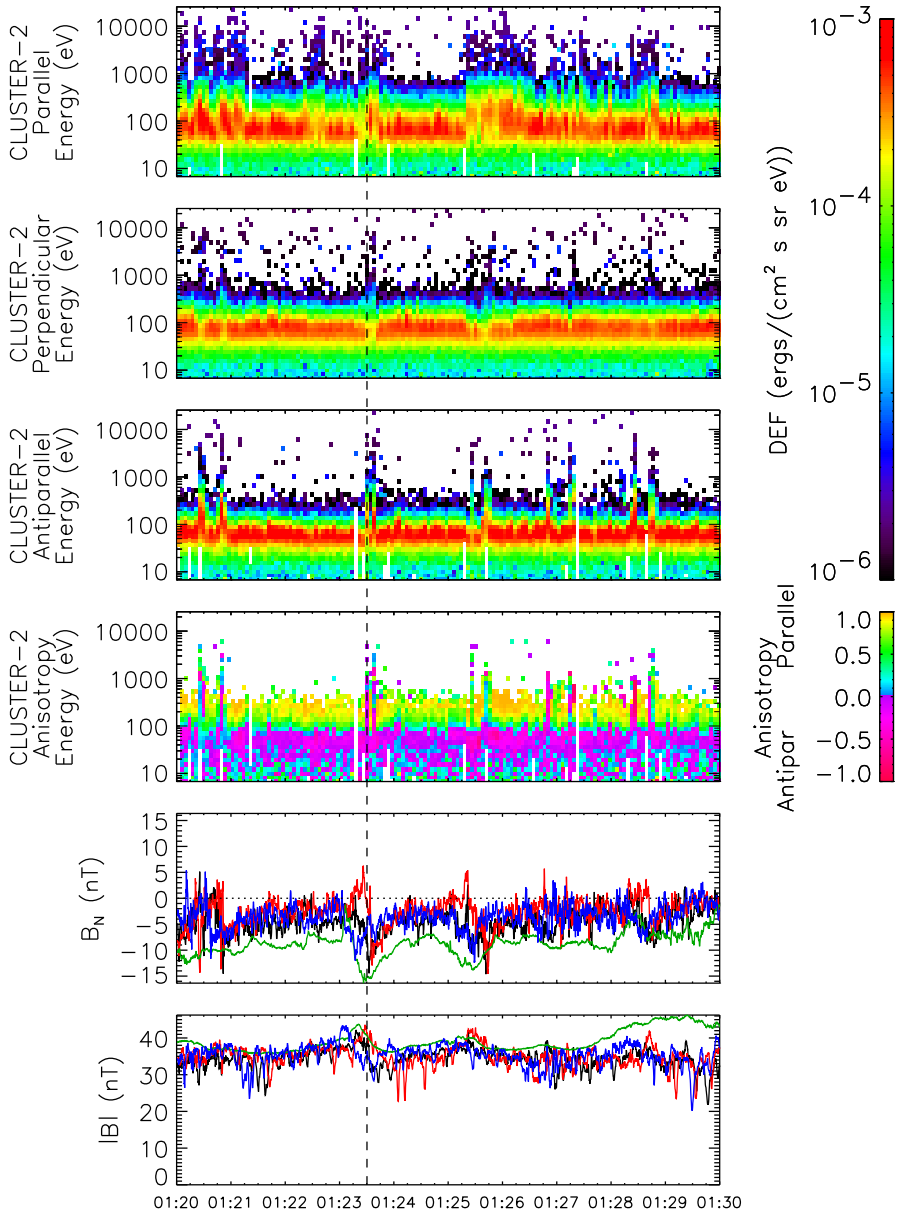

Figure 5.12: PEACE and FGM signatures of FTE 69 (22nd February 2003, 01:23 UT). Spectrograms from Cluster 2 are shown.

and which was generated at the same reconnection site. In this case, it would be possible to triangulate the observations and find a specific reconnection site, but no such conjunctions will be examined in this thesis.

The maximum magnetic shear between the model magnetic fields either side of the magnetopause along the path followed by $\mathbf{V}_{HTN}$ was 83°, so this event does not appear to be consistent with an antiparallel reconnection site. The FTE is located relatively close to the model cusp positions, which has the capability of significantly altering the magnetic shear relative to the model. Since the tetrahedron straddled the magnetopause at the time when the FTE was observed, the position of the spacecraft relative to the cusp can be checked. Cluster 3 observed a magnetospheric magnetic field of

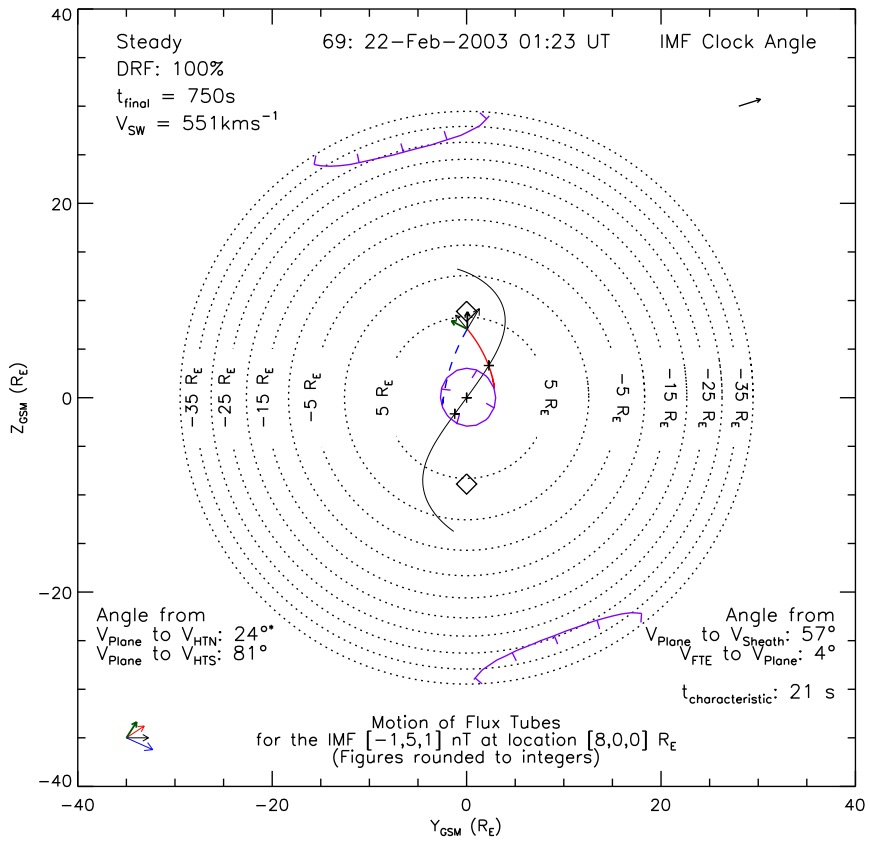

Figure 5.13: Model run: FTE 69 (22nd February 2003, 01:23 UT). This is an example of an event which was *only* consistent with a subsolar component reconnection line.

(-28,0,23)$_{GSM}$ nT; since the field is northward and tailward, it is consistent with the spacecraft being on dayside magnetic field lines near local noon. The other three spacecraft all observed a magnetosheath magnetic field of (-15,27,15)$_{GSM}$ nT, therefore the magnetic shear across the magnetopause is 52°, and the observations confirm that this event is not consistent with an antiparallel reconnection site.

5.4.2 Antiparallel Reconnection Events

28 FTEs were consistent with a model flux tube velocity that passed through a region of high magnetic shear (greater than 150°), but only one event (FTE 13: 13th November 2002, 00:08 UT) was also inconsistent with both a subsolar reconnection line and radial sheath-like motion. This is partly because any model flux tube that is generated at an antiparallel reconnection site and connected to: (a) the northern hemisphere if observed on the northern side of the subsolar X-line, or (b) the southern hemisphere if observed southward of the subsolar X-line, can be traced back to a subsolar component reconnection line if enough time is allowed. The model run for FTE 13 is shown in Figure 5.14. $\mathbf{V}_{FTE}$ was 17° from the model

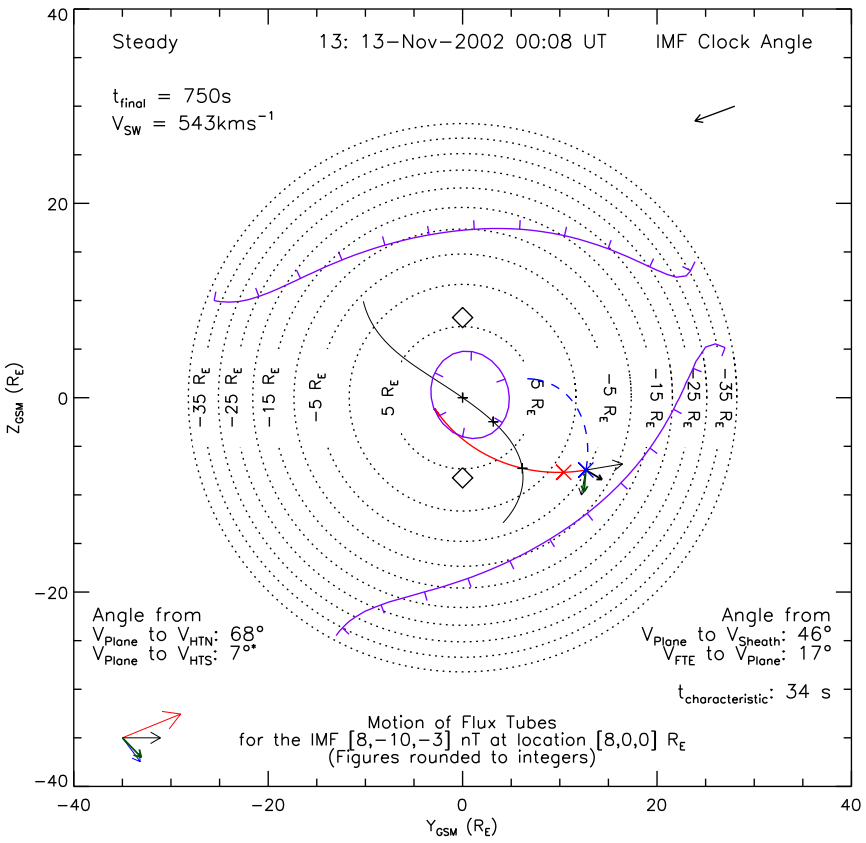

Figure 5.14: Model run: FTE 13 (13th November 2002, 00:08 UT)

magnetopause plane, and $\mathbf{V}_{plane}$ was 7° from $\mathbf{V}_{HTS}$, 46° from the model $\mathbf{V}_{sheath}$ vector and 68° from $\mathbf{V}_{HTN}$. $\mathbf{V}_{HTS}$ did not trace back to the model component reconnection line in the previous 750 s; even if the integration time of the model is extended, the closest approach the path can make to the component X-line is approximately 5 R_E from the subsolar point, where the model magnetosheath flow becomes super-Alfvénic. At the point of observation of this event, the model magnetic shear was 172°. Although all four spacecraft were in the magnetosheath at this time, the FTE occurred fifteen minutes after a magnetopause crossing. Comparing the observed magnetosheath magnetic field with the magnetospheric magnetic field observed just before the magnetopause crossing, the shear is slightly lower (158°). Whilst it is possible that this event was created by a dayside component reconnection line, such a line would have to be displaced significantly northward and/or duskward from the line shown in Figure 5.14. It therefore appears likely that this event was a consequence of 'antiparallel' reconnection.

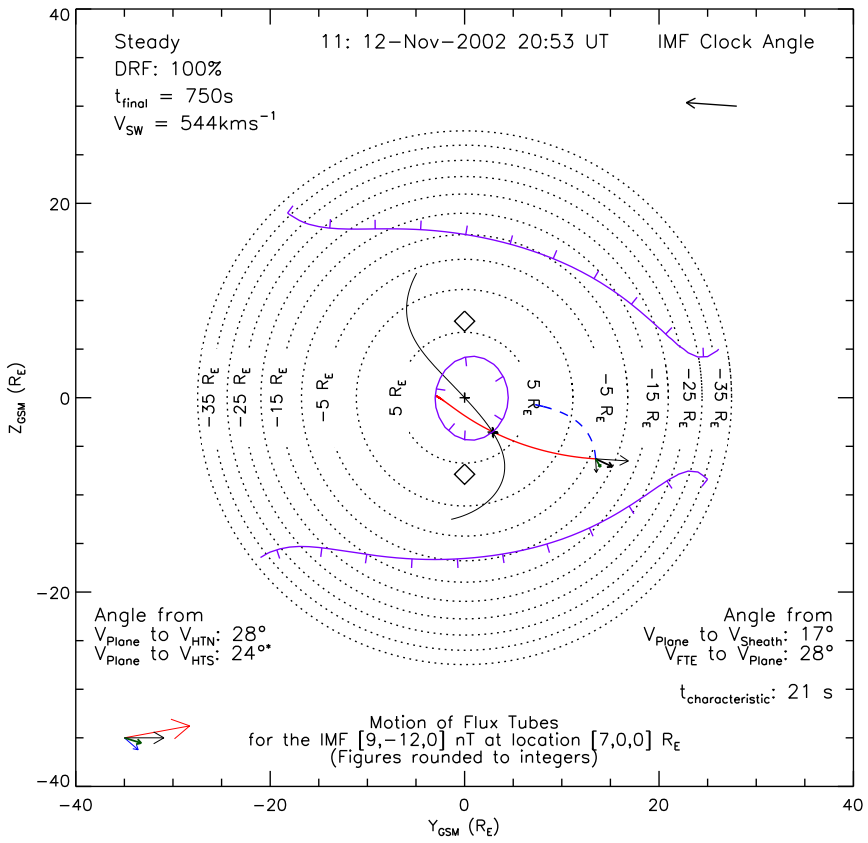

Figure 5.15: Model run: FTE 11 (12th November 2002, 20:53 UT)

5.4.3 Other Events

Event	Time (UT)	Closest approach to X-line	Maximum shear
11	12-Nov-2002 20:53	$4.9R_E$	144°
30	08-Dec-2002 03:54	$0.7R_E$	137°
32	10-Dec-2002 14:19	$2.5R_E$	92°
38	10-Dec-2002 17:19	$2.4R_E$	94°
76	24-Apr-2003 22:00	$1.3R_E$	147°

Table 5.3: Events which were consistent with either $\mathbf{V}_{HTN}$ or $\mathbf{V}_{HTS}$, but not $\mathbf{V}_{sheath}$, whose paths did not pass through the Cooling *et al.* (2001) model subsolar component reconnection line or through a region with greater than 150° magnetic shear.

There were five other events which were consistent with $\mathbf{V}_{HTN}$ or $\mathbf{V}_{HTS}$, but not $\mathbf{V}_{sheath}$, which are listed in Table 5.3. FTE 11 (which occurred on the same magnetopause crossing as FTE 13 and is shown in Figure 5.15) was consistent with a model flux tube path which passed through a region of relatively high model magnetic shear (144°), but which could not be traced back to the model subsolar component reconnection line. Unfortunately all four spacecraft were in the magnetosheath when this FTE was observed, and the nearest magnetopause crossing was over an hour later. However, the model magnetosheath magnetic field was only 8°

from the observed value, and the observed field magnitude was 31 nT compared with an observed value of 34 nT.

FTEs 30, 32 and 38 all had $\mathbf{V}_{plane}$ vectors which were close in angle to $\mathbf{V}_{HTN}$, $\mathbf{V}_{HTS}$ and $\mathbf{V}_{sheath}$, but were only consistent in magnitude with $\mathbf{V}_{HTS}$. Despite the fact that the closest model vector was connected to the southern hemisphere, all three were observed on the northward side of the model component reconnection line. The CIS CODIF detectors on Cluster spacecraft in the magnetosphere observed parallel-streaming ions at the same time as FTEs 32 and 38 (not shown), indicating that the FTEs must have been connected to the northern hemisphere, as one might expect from component reconnection given their position on the north side of the X-line. On the other hand, all four spacecraft were in the magnetosheath when FTE 30 occurred, and parallel-streaming ions were observed (Figure 5.16) indicating that this FTE was connected to the southern hemisphere, despite being reconnected on the northern side of the model X-line. In the model run for this event, the magnetosheath flow became super-Alfvénic very close to the subsolar point, so the FTE could still have been generated extremely close to the model reconnection line, but was swept northward and duskward (Figure 5.17).

The final event in this section, FTE 76, occurred within 1.3 R_E of the model reconnection line (Figure 5.18), but also occurred in a region of relatively high model magnetic shear (147°). It may be that a component reconnection line is displaced slightly relative to the model line assumed to pass through $(R_{mp}, 0, 0)_{GSM}$. Alternatively, this event could be explained by either hypothesis if the component or antiparallel reconnection sites are slightly broader than assumed in this model, or if the actual magnetic fields differ significantly from the model values. The observed magnetosheath magnetic field differs from the model value by 19°, and the observed magnitude is more than double the model value. The magnetospheric magnetic field was observed half an hour before the FTE; the observed value differs from the model value by 32°, and the observed field magnitude was almost double the model value.

5.4.4 Inconsistent events

A possible cause of inaccuracy is that the model magnetosheath magnetic field, plasma velocity and/or density used by the Cooling *et al.* (2001) model in the Cowley and Owen (1989) calculation (Equations 4.5 and 4.6) could be inaccurate. There are two possible reasons for this inaccuracy. First, there is a limitation to the reliability of the IMF lag. Four minute resolution data were used, as the error on the delay calculation is of the order of two minutes even if the error on the solar wind speed measured at ACE is assumed to be as low as 10 kms^{-1}. Second, no

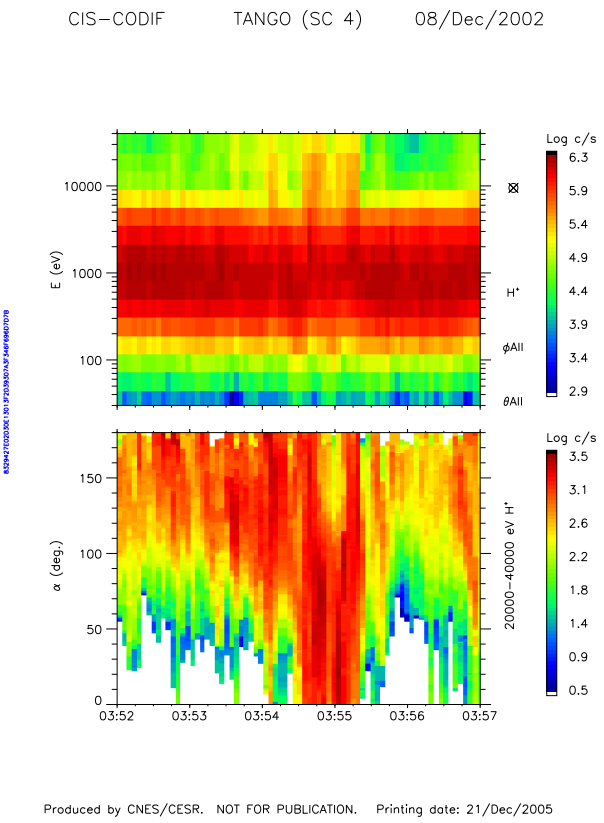

Figure 5.16: CODIF ion signatures for FTE 30, observed by Cluster 4. The top panel shows an omnidirectional energy/time spectrogram of counts per second, and the bottom panel shows an pitch-angle spectrogram for energies between 20 and 40 keV. Cluster 4 observed FTE 30 at 03:54:45 UT; at this time there was a burst of high energy ions moving parallel to the magnetic field, indicative of a connection to the southern hemisphere.

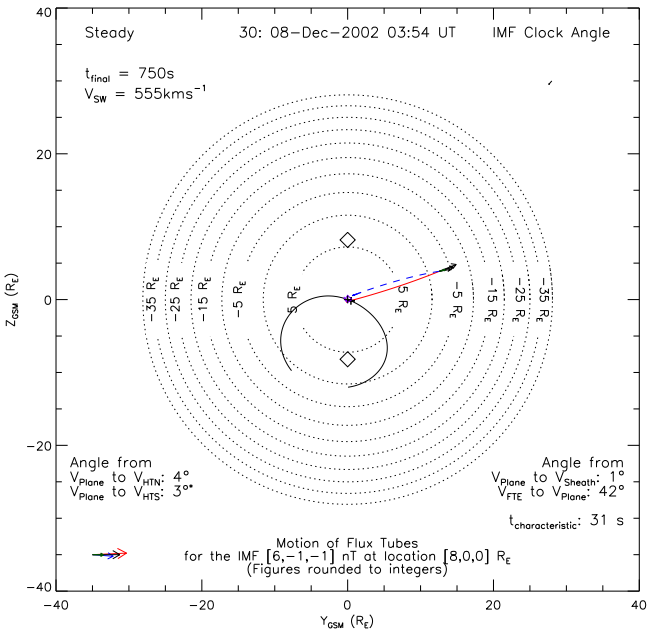

Figure 5.17: Model run: FTE 30 (8th December 2002, 03:54 UT)

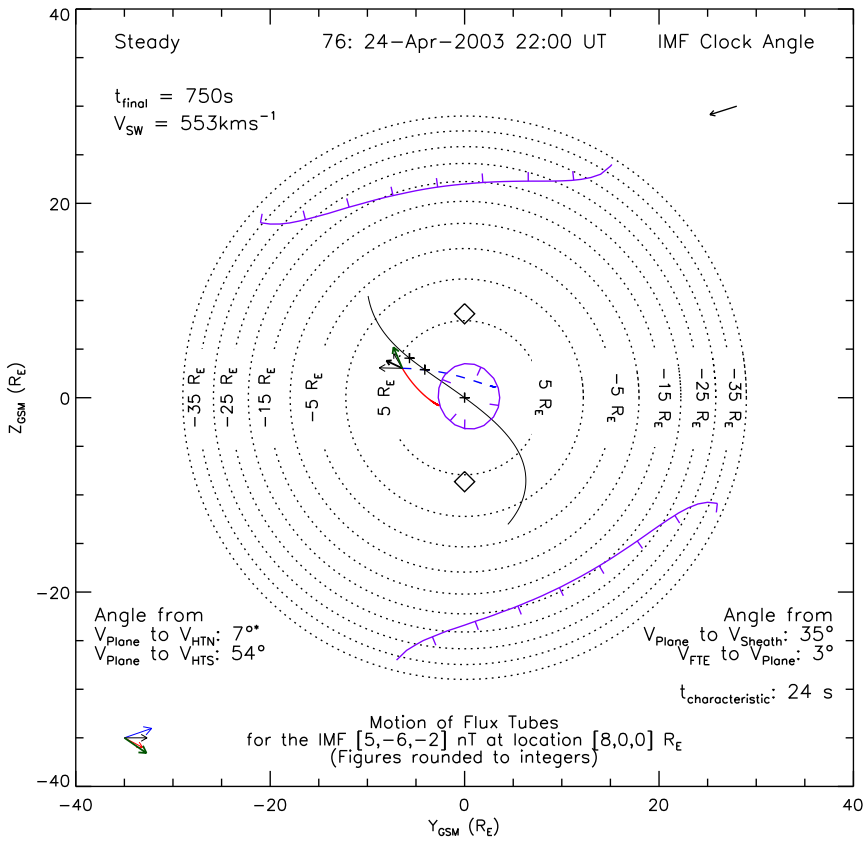

Figure 5.18: Model run: FTE 76 (24th April 2003, 22:00 UT)

model is more accurate than reality, so although the lags were adjusted by eye where necessary, a more realistic result should be obtained by using the observed magnetosheath magnetic fields for those events where one or more spacecraft were in the magnetosheath rather than the model values used by Cooling *et al.* (2001).

Therefore, taking the remaining 16 FTEs, $\mathbf{V}_{FTE}$ (as calculated using the multi-spacecraft timing analysis with the timings determined by eye) was compared with with the observed magnetosheath plasma velocity, and with values of $\mathbf{V}_{HTN}$ and $\mathbf{V}_{HTS}$ calculated from the observed magnetosheath magnetic field, plasma flow and density using Equations 4.5 and 4.6. Since no model magnetopause surface is assumed when using the observed magnetosheath data, the comparison was made with $\mathbf{V}_{FTE}$, rather than $\mathbf{V}_{plane}$ which was used to compare with the results of the Cooling *et al.* (2001) model. Four of the remaining 16 FTEs, shown in Table 5.4, were consistent with $\mathbf{V}_{HTN}$ or $\mathbf{V}_{HTS}$ when calculated using the observed magnetosheath values. No further events were consistent with the observed $\mathbf{V}_{sheath}$ vector.

The causes of the deviation from the Cooling *et al.* (2001) model for these events were varied:

Event no.	Time (UT)	Angle between $\mathbf{V}_{FTE}$ and MP	$\mathbf{V}_{HTN}$	$\mathbf{V}_{HTS}$	$\mathbf{V}_{sheath}$	$\frac{\lvert\mathbf{V}_{FTE}\rvert}{\lvert\mathbf{V}_{HTN}\rvert}$	$\frac{\lvert\mathbf{V}_{FTE}\rvert}{\lvert\mathbf{V}_{HTS}\rvert}$	$\frac{\lvert\mathbf{V}_{FTE}\rvert}{\lvert\mathbf{V}_{sheath}\rvert}$
7	12-Nov-2002 19:55	6°	51° (58°)	**7°** (31°)	39° (33°)	0.29 (0.21)	**0.88** (0.45)	0.47 (0.38)
57	26-Jan-2003 21:10	25°	**29°** (31°)	79° (76°)	50° (57°)	**0.57** (0.78)	0.63 (0.60)	0.71 (0.74)
60	31-Jan-2003 19:55	24°	86° (83°)	**29°** (41°)	67° (65°)	0.37 (0.39)	**1.0** (1.2)	0.74 (0.90)
77	24-Apr-2003 22:02	18°	**21°** (70°)	115° (106°)	78° (91°)	**0.73** (0.95)	0.50 (0.69)	1.0 (0.84)

Table 5.4: The events for which $\mathbf{V}_{FTE}$ is consistent with the values of $\mathbf{V}_{HTN}/\mathbf{V}_{HTS}$ calculated from observed magnetosheath data. $\mathbf{V}_{FTE}$ was determined from time lags that were judged by eye. 'MP' refers to the magnetopause plane, which is taken to be the plane containing $\mathbf{V}_{HTN}$ and $\mathbf{V}_{HTS}$.

- FTE 7 (12-Nov-2002 19:55): Whilst the model and observed magnetosheath velocities were close (separated by an angle of 4° and a magnitude ratio of 1.2), the angle between the observed and model magnetosheath magnetic fields was 19° and the model field strength was 30% too high. Furthermore, the observed magnetosheath density was 60% of the model value. This caused a 30° discrepancy in $\mathbf{V}_{HTS}$.

- FTE 57 (26-Jan-2003 21:10): The observed and model values of the magnetosheath plasma velocity and magnetic field differed by 16° and 13° respectively. This time, the observed magnetosheath density was 160% of the model value. These factors combined to produce a 20° discrepancy in $\mathbf{V}_{HTN}$.

- FTE 60 (31-Jan-2003 19:55): The observed and model values of the magnetosheath plasma velocity and magnetic field differed by 10° and 7° respectively, and the observed magnetosheath density was 195% of the model value, producing a 29° discrepancy in $\mathbf{V}_{HTS}$.

- FTE 77 (24-Apr-2003 22:02): The observed and model values of the magnetosheath plasma velocity and magnetic field both differed by 16°, and the model magnetic field strength was only 35% of the observed value. This time the ratio of observed to model values of density was relatively good (81%), but the net result was a discrepancy in $\mathbf{V}_{HTN}$ of 68°.

In all four cases, the magnetosheath magnetic field was relatively steady.

FTE 60, which is consistent with the velocity of the flux tube connected to the southern hemisphere when $\mathbf{V}_{HTS}$ is calculated from the observed values (see Table 5.4), was one of three events on the 31st January 2003 (19:44, 19:53 and 19:55 UT). The other two values of $\mathbf{V}_{FTE}$ are directed further tailward; all three lie between $\mathbf{V}_{HTS}$ and $\mathbf{V}_{sheath}$ (except for an angle out of the plane, which is below 17° in

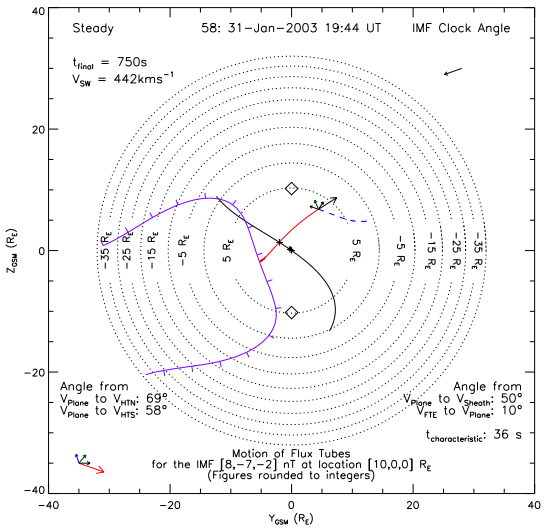

Figure 5.19: Model run: FTE 58 (31st January 2003 19:44 UT)

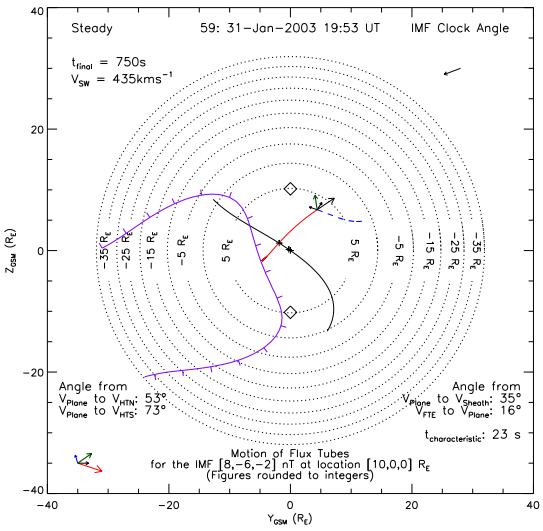

Figure 5.20: Model run: FTE 59

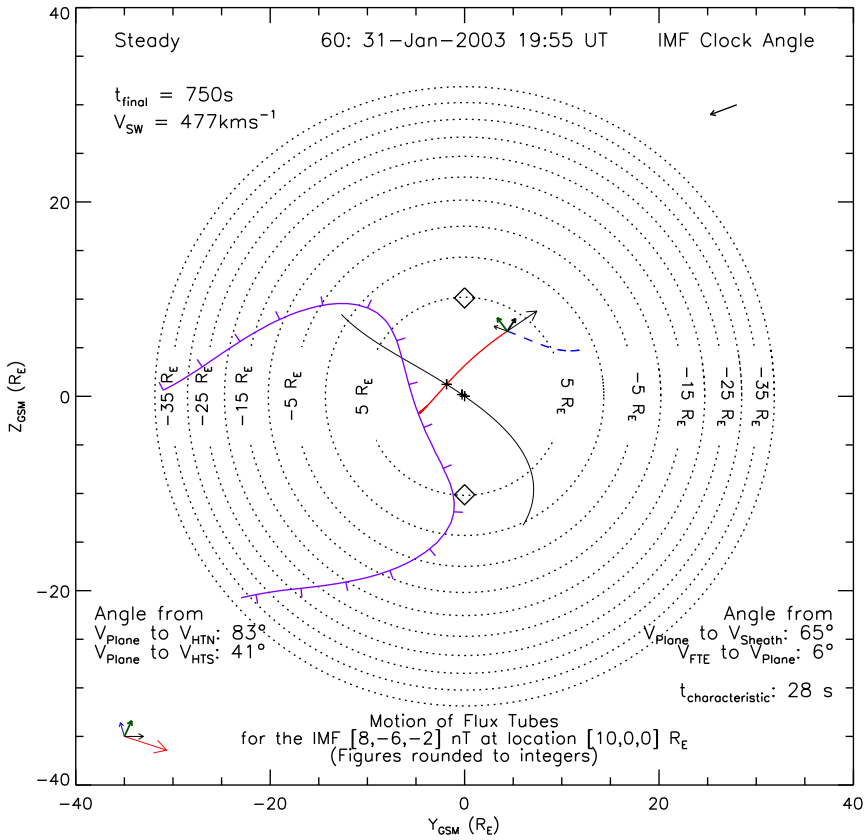

Figure 5.21: Model run: FTE 60

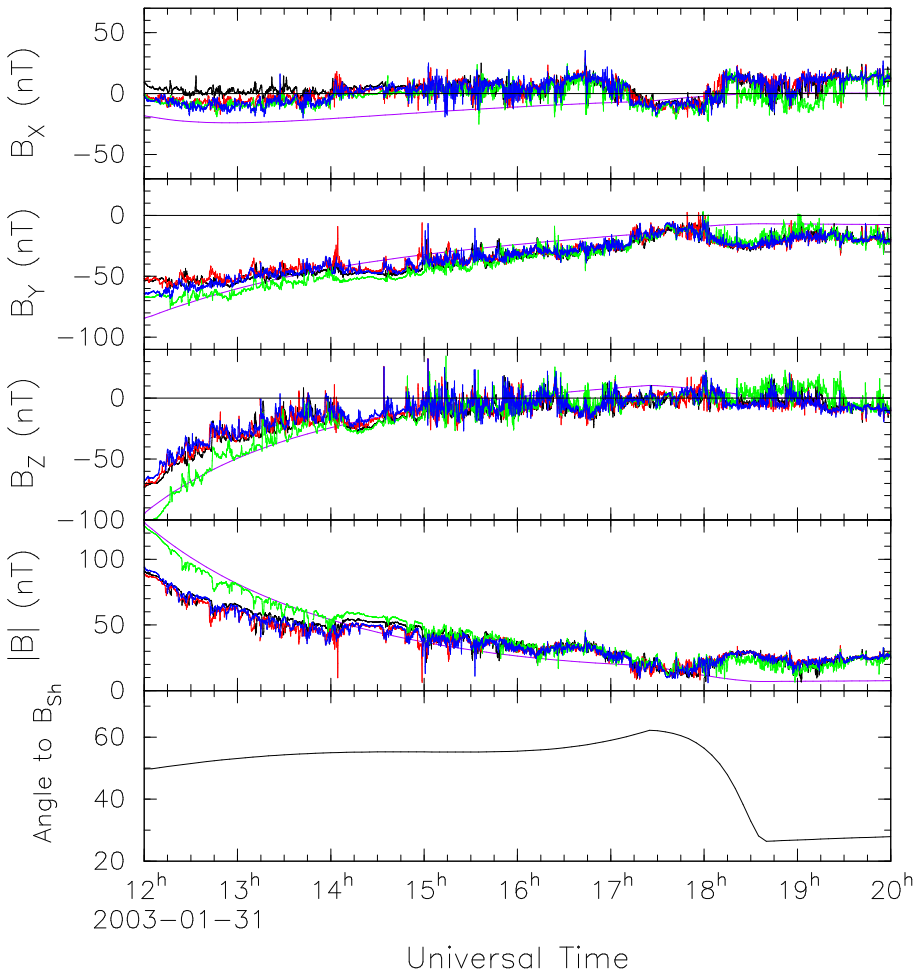

Figure 5.22: The GSM magnetic field observed by Cluster leading up to FTEs 58-60 (31st January 2003), and the model Tsyganenko 1996 (T96) magnetic field evaluated at the position of Cluster 3 (purple). The bottom panel shows the angle between the model magnetic field, as a function of time, and the magnetosheath magnetic field observed in the vicinity of the FTE signatures (B_{sh}). The spacecraft cross the model magnetopause used by T96 between 17:00 and 18:00 UT; however the magnetic shear angle remains below 60° whilst the spacecraft were in the magnetosphere.

all three cases). All three are magnetosheath events and are shown in Figures 5.19 to 5.21. The magnetosheath conditions at the location of Cluster at these times were slightly unusual for the distance from the subsolar point; the observed magnetosheath density was relatively low (∼3 cm^{-3}), and the observed magnetic field magnitude was 24 nT. Consequently, the magnetosheath flow was sub-Alfvénic, and $\mathbf{V}_{HTS}$ had a Sunward velocity component. The corresponding model path did not cross either the model subsolar component reconnection X-line, or a region of high magnetic shear (the largest shear on the path was 83°), so it is not possible to estimate a potential elapsed time since reconnection occurred by assuming the location of a reconnection site. However, if sufficient time had elapsed to allow the accelerated magnetosheath particles that have crossed the magnetopause to mirror and return, the boundary layer density would be enhanced, and the Alfvén speed would therefore decrease. This may explain why the observed $\mathbf{V}_{plane}$ and $\mathbf{V}_{FTE}$ vectors lie between the model $\mathbf{V}_{HTS}$ and $\mathbf{V}_{sheath}$ values. Given the magnetosheath parameters observed ($|\mathbf{B}|$=24 nT, n=3 cm^{-3}), the Alfvén speed is 300 kms^{-1}. If

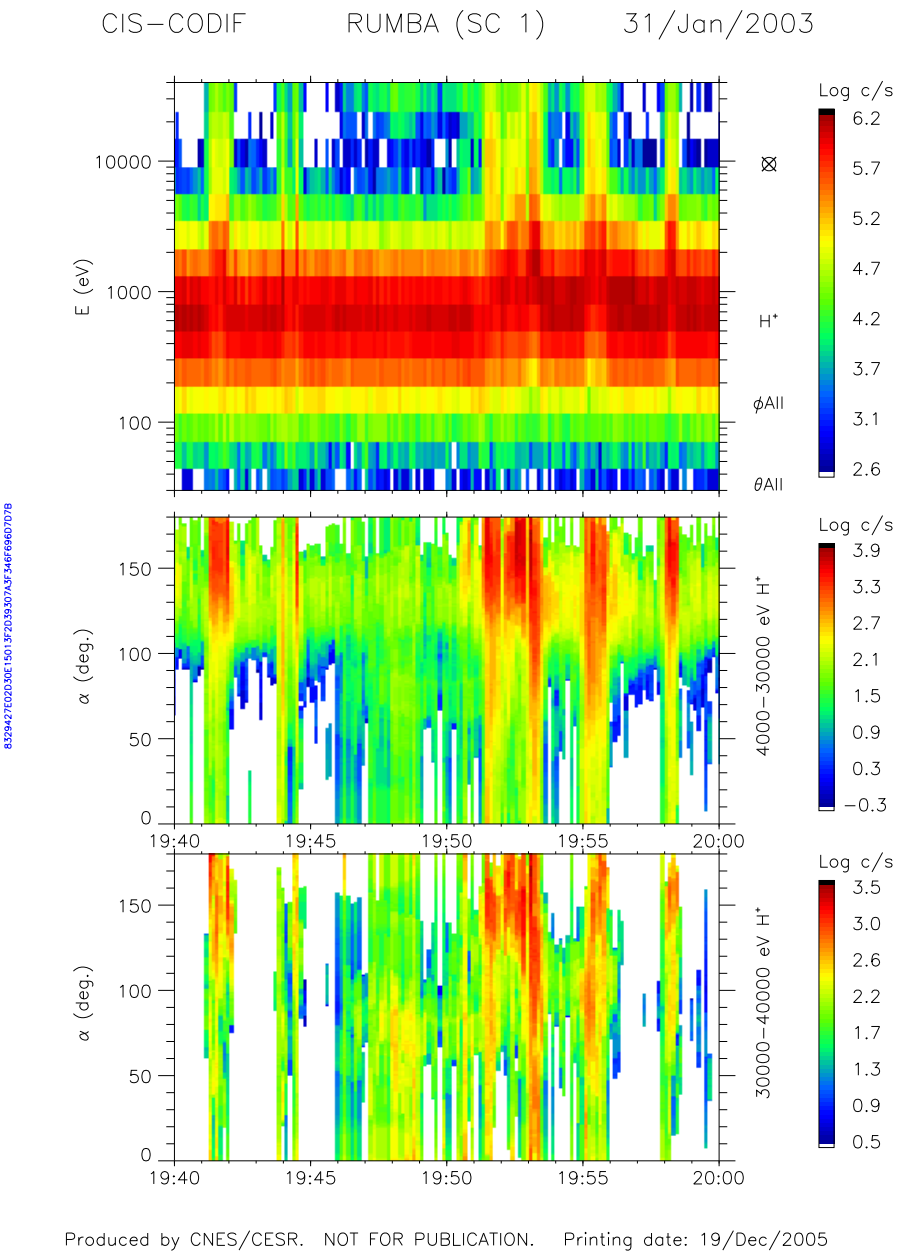

Figure 5.23: CODIF ion signatures for FTEs on the 31st January 2003. The top panel shows an omnidirectional energy/time spectrogram of counts per second. The middle and bottom panels show pitch-angle spectrograms for energies between 4 – 30 keV, and 30 – 40 keV respectively. FTEs 58, 59 and 60 occurred at 19:44, 19:53 and 19:55 UT; at these times there appears to be some acceleration of magnetosheath plasma, but it is predominantly directed antiparallel to the magnetic field.

it is assumed that the field-aligned distance to the ionosphere is shorter than the estimate in Section 5.1 since the spacecraft were located at higher latitudes, and take a value of $15R_E$, the Alfvén travel time to the ionosphere and back is 640 s, which is shorter than the time taken for the model flux tubes to follow the blue dashed paths in Figures 5.19 to 5.21.

Since the model magnetosheath flow is sub-Alfvénic for all values of

$Y_{GSM} > 0$ at least as far as 40 R_E down-tail, if the model run-time is extended then the path of $\mathbf{V}_{HTS}$ will be traced further tailward and the time elapsed since reconnection would be higher than 750 s. If this is so, the implication is that these three FTEs were generated in a region that was far from the subsolar reconnection line. Furthermore, unless they are able to map back to the southern hemisphere, they appear to have been generated in a region of low magnetic shear; the maximum angle between the model magnetic fields at the magnetopause along the path of $\mathbf{V}_{HTS}$ in the previous 750 s was between 83° for the three events. Unfortunately, none of the Cluster spacecraft observed the magnetospheric magnetic field around the time of the FTE observations, but if the Tsyganenko 1996 model magnetic field (Tsyganenko, 1995) is plotted for the period up to the the magnetopause crossing (Figure 5.22), the angle between this field and the unperturbed magnetosheath magnetic field observed around the time of the three FTEs rises to a maximum value of about 60°.

Accelerated magnetosheath ions were observed at the times of these FTEs by the CIS CODIF detector on Cluster 1, (Figure 5.23). Unfortunately, these signatures are inconsistent with the interpretation of a flux tube connected to the southern hemisphere in one major respect: the majority of the ion population in the energy range 30–40 keV at the times the FTEs were observed was moving antiparallel to the magnetic field. This is indicative of a magnetic connection to the northern hemisphere, but the calculated $\mathbf{V}_{plane}$ vectors for these three events differ from the model $\mathbf{V}_{HTN}$ vectors by between 53° and 83°. Although the bulk magnetosheath plasma flow has a component antiparallel to the magnetosheath magnetic field, the discrepancy between the observed ion distribution and the comparison of the observed FTE velocity with the model vector is currently unresolved.

A further two events, listed in Table 5.5, had $\mathbf{V}_{FTE}$ vectors which were directed further out of the magnetopause plane (i.e. the plane which contains the $\mathbf{V}_{HTN}$ and $\mathbf{V}_{HTS}$ vectors calculated from the magnetosheath parameters), but which were consistent with either the observed $\mathbf{V}_{sheath}$, or $\mathbf{V}_{HTN}/\mathbf{V}_{HTS}$ when projected onto that plane. In these two cases, $\mathbf{V}_{FTE}$ was at an angle of 27° and 44° to the $\mathbf{V}_{HTN}/\mathbf{V}_{HTS}$ plane.

Therefore, 8 events (shown in Figure 5.24) out of the original 81 are left, which do not appear to be consistent with the predictions of the Cowley and Owen (1989) or Cooling *et al.* (2001) models. Whilst there is not yet a satisfactory explanation for these events, it should be noted this group includes five of the seven events where $\mathbf{V}_{FTE}$ was directed out of the model magnetopause plane by more than 40°. Three of the eight FTEs have $\mathbf{V}_{plane}$ vectors which are within 30° of one of the model vectors, but fail the criterion that the magnitude of $\mathbf{V}_{plane}$ must be within 50% and

Event no.	Time (UT)	Angle between $\mathbf{V}_{plane}$ and $\mathbf{V}_{FTE}$	$\mathbf{V}_{HTN}$	$\mathbf{V}_{HTS}$	$\mathbf{V}_{sheath}$	$\frac{\lvert\mathbf{V}_{plane}\rvert}{\lvert\mathbf{V}_{HTN}\rvert}$	$\frac{\lvert\mathbf{V}_{plane}\rvert}{\lvert\mathbf{V}_{HTS}\rvert}$	$\frac{\lvert\mathbf{V}_{plane}\rvert}{\lvert\mathbf{V}_{sheath}\rvert}$
9	12-Nov-2002 20:04	37°	36° (39°)	**30°** (51°)	16° (13°)	0.28 (0.21)	**0.57** (0.42)	0.44 (0.37)
50	15-Jan-2003 01:51	43°	42° (47°)	46° (32°)	**26°** (42°)	0.56 (0.53)	1.53 (1.16)	**1.0** (0.73)

Table 5.5: The events for which $\mathbf{V}_{FTE}$ is consistent with the observed values of $\mathbf{V}_{sheath}$, or the values of $\mathbf{V}_{HTN}/\mathbf{V}_{HTS}$ calculated from observed magnetosheath data, when projected into the plane defined by $\mathbf{V}_{HTN}$ and $\mathbf{V}_{HTS}$. $\mathbf{V}_{FTE}$ was determined from time lags that were judged by eye. The angles between $\mathbf{V}_{FTE}$ and the plane defined by $\mathbf{V}_{HTN}/\mathbf{V}_{HTS}$ were 37° and 44° for these two events.

150% of the model value. FTEs 24 and 53 both have three spacecraft with similar B_N signatures, and one which differs, making the alignment of the signatures more complicated. In the case of FTE 24, the trace of the B_N signature observed by Cluster 1 is followed by an extended region of negative B_N, whilst the Cluster 3 trace of FTE 53 is offset in B_N with respect to the others. Since all four spacecraft were in the magnetosphere for this last event, it is not possible to carry out the Cowley and Owen (1989) calculation with observed magnetosheath parameters.

5.5 Discussion

In this chapter, the velocities of 81 FTEs which occurred under southward IMF conditions, or an IMF that was slightly northward but dominated in the dawn-dusk direction, have been compared with the predictions of the model developed by Cooling *et al.* (2001) and used in Chapter 4. More than half of the events (43) had velocities which, when projected into the model magnetopause plane, were within 20° of either $\mathbf{V}_{HTN}$ or $\mathbf{V}_{HTS}$ and which had a magnitude that was within ±50% of the model value. However, since many of the FTEs were observed on the magnetopause flanks, where the magnetosheath flow is faster, there was often not a large difference between the model $\mathbf{V}_{HTN}/\mathbf{V}_{HTS}$ vector and the model magnetosheath flow, $\mathbf{V}_{sheath}$. Consequently, 26 of these 43 events were also within 20° of the model magnetosheath flow and satisfied the magnitude criterion. Naturally, if the angular threshold is broadened to 30° more events are consistent with $\mathbf{V}_{HTN}$ or $\mathbf{V}_{HTS}$, but it becomes harder to discriminate between events that are consistent with reconnected flux tube velocities and those which are consistent with the magnetosheath flow.

The equations that were derived by Cowley and Owen (1989) for the motion of a reconnected flux tube are purely dependent upon the local magnetosheath velocity, magnetic field and density. Therefore, it is possible to calculate these vectors at the point of observation of an FTE and run the Cooling *et al.* (2001) model in

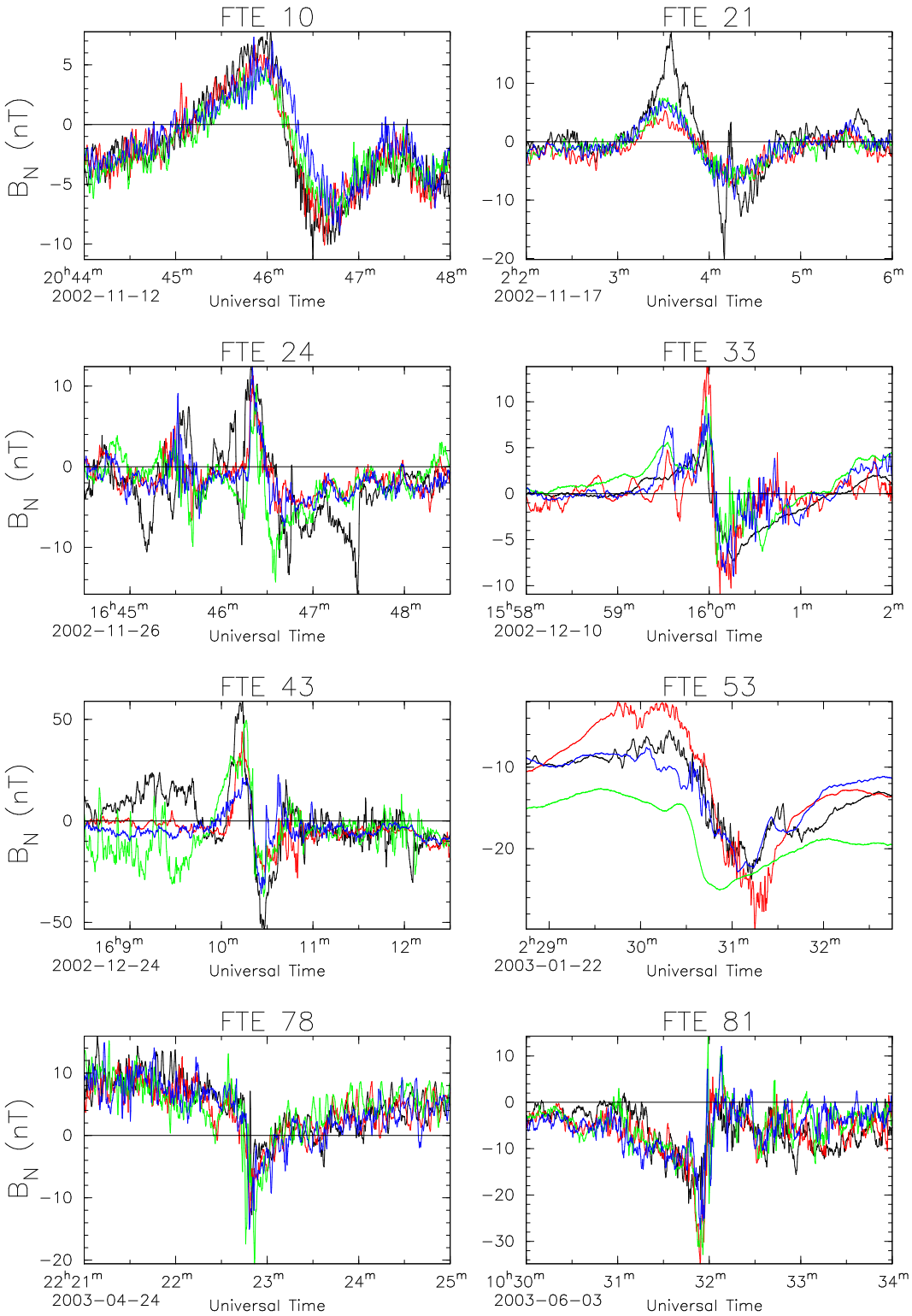

Figure 5.24: B_N signatures of events which did not fit the Cooling *et al.* (2001) model or Cowley and Owen (1989) calculations. The Cluster 1, 2 and 4 traces have been lagged relative to Cluster 3.

reverse. When the model is run in its usual format (moving forwards in time from a reconnection event), it is possible to set a magnetic shear threshold to decide whether the model permits reconnection. However, the selection of this threshold is arbitrary. Therefore, when the model is run in reverse it is not possible to conclude exactly where the tube reconnected, although reconnection must occur on the path of the model flux tube. Nonetheless, there are some examples of events which are only consistent with a subsolar component reconnection line (e.g. Figure 5.13), and one which is only only consistent with an antiparallel reconnection site, which is shown in Figure 5.14[1]. To emphasise the point, although the model component reconnection line selected passes through $(R_{mp}, 0, 0)_{GSM}$, which is taken to be the subsolar point, the model flux tube path in Figure 5.13 (and many other model runs) can be traced past the model X-line until the forces exerted by the magnetosheath flow and magnetic tension are equal and opposite. Hence the observed FTE velocity is still consistent with a component reconnection line if the X-line is either rotated or translated for some reason. For example, the variation of the Earth's magnetic dipole in the GSM X-direction is ignored in this model. This seasonal effect causes the nose of the magnetopause to 'nod' up and down with respect to the GSM X-axis, which may have an effect on the position of the reconnection line. It is also likely that a subsolar component reconnection line has a finite breadth perpendicular to its length, rather than the thin line that is used in the model; thus the FTE may be generated slightly away from the model X-line. Furthermore, the location of active reconnection sites may be slightly more random even if an X-line with large-scale structure is present (e.g. Coleman and Freeman, 2005). A more random reconnection site that is between the model component site and the location of the spacecraft cannot be distinguished from more traditional component reconnection (Gonzalez and Mozer, 1974) if both sites lie on the model path followed by the FTE.

Several events were observed which had velocities that were close to radial, and not consistent with the model $\mathbf{V}_{HTN}/\mathbf{V}_{HTS}$ velocities. A preliminary examination of the lagged solar wind dynamic pressure for some events which were closest to the model $\mathbf{V}_{sheath}$ vector (five events which were within 10° of the model $\mathbf{V}_{sheath}$ and more than 20° from $\mathbf{V}_{HTN}$ and $\mathbf{V}_{HTS}$) does not reveal any significant pressure pulses at the time of these events (not shown), but further study into these events is warranted.

The Cooling *et al.* (2001) model makes several simplifications. First, the Cowley

[1]Further events which are not discussed in this chapter are more likely to be consistent with an antiparallel reconnection site than a subsolar component X-line, but the event shown is the only one in which $\mathbf{V}_{FTE}$ was consistent with one model flux tube velocity which could be traced back to a region of high shear but not to the model subsolar component reconnection line, *and* which was more than 30° from both the model magnetosheath velocity and the second model flux tube velocity. All events are shown in Appendix 1.

and Owen (1989) calculations assume that no ions have mirrored; from an approximate calculation of the Alfvén travel time to the ionosphere, this appears to be a reasonable assumption in general. However, the parameters used in the Cooling *et al.* (2001) model are in turn based on several simplifications. It is assumed that the magnetosheath flow increases uniformly from a subsolar stagnation point (which is naturally fed by the solar wind crossing the bow shock). Possible local time asymmetries are neglected (such as a potentially elongated stagnation point, as suggested by Pudovkin and Semenov, 1977; Sonnerup, 1979). Furthermore, a relatively simple model of the magnetospheric field is used, which is likely to be inaccurate near the cusps as precession of the cusps with the Earth's dipole has been ignored. The model field is also likely to be inaccurate on the flanks, where more advanced models of the geomagnetic field (e.g. Tsyganenko, 1995) incorporate an increased GSM B_X component compared with a simple dipole projected onto the magnetopause surface.

Recently, Kawano and Russell (2005) have re-examined the database of 1246 FTEs observed by the ISEE satellite and compiled by Kawano and Russell (1996), and investigated the dependency between the time delay between those signatures observed by both ISEE-1 and -2 and the longitudinal and latitudinal separation of the two spacecraft. They found a much stronger correlation between the time delays and longitudinal separation than with latitudinal separation. However, the velocities derived in this study from four-spacecraft techniques often do have a significant latitudinal motion (particularly at high latitudes near local noon, which were not sampled by ISEE), which is consistent with the trade-off between the $\boldsymbol{j} \times \boldsymbol{B}$ force and the force exerted by the magnetosheath flow. However, a factor that has not been considered in this study is the error on the multi-spacecraft timing analysis. Whilst it is possible to check the mutual consistency of the six inter-spacecraft timings used to calculate each FTE velocity vector by using the technique described in Section 5.2, there is not a standard analytical method of calculating the error on the resulting vector. Given that even when $\mathbf{V}_{HTN}$ and $\mathbf{V}_{HTS}$ are calculated from the observed magnetosheath parameters, there is still sometimes a significant discrepancy between the observed and calculated vectors, this is certainly a point which needs to be addressed.

5.6 Conclusions

From an analysis of 81 FTEs which occurred when $|\theta_{CA}| > 70°$, it can be concluded that the Cooling *et al.* (2001) model generally describes reconnected flux tube motion reasonably well. Although some cases are very well explained, the motion of

some events was closer to the model magnetosheath flow. It is possible that some of the signatures are caused by structures embedded into the magnetosheath flow (such as magnetosheath pressure pulses, as suggested by Sibeck, 1990, 1992), and further study into these events is warranted. However, the fact that a significant number of events match one of the model de Hoffmann–Teller velocities well, and are inconsistent with the model magnetosheath flow velocity, is further evidence that many FTE signatures cannot be explained by the (Sibeck, 1990, 1992) model, but are consistent with transient reconnection as originally proposed by Russell and Elphic (1978, 1979)

In some cases, cross-correlation fails to align the centre of the B_N signatures, so it is more accurate to use a subjective method of aligning the signatures by eye. Furthermore, it is also worthwhile comparing the result with the original equations derived by Cowley and Owen (1989) if accurate magnetosheath data are available.

Although many events were observed at low latitudes when the IMF B_Y component was strong, consistent with earlier conclusions that FTEs can be generated at a low-latitude component reconnection X-line (e.g. Russell *et al.*, 1985), they tended to be observed on the magnetopause flanks, where the magnetosheath velocity was strong enough to dominate the Alfvén velocity term in the expressions for the de Hoffmann–Teller velocities. Furthermore, even when there was a clear distinction between the model de Hoffmann–Teller velocities and the model magnetosheath flow, the model flux tube paths often crossed both the model subsolar component reconnection line and regions of high magnetic shear. However, one event was highlighted which appears to be most consistent with a subsolar component reconnection line, along with one event which was not consistent with the model subsolar component reconnection line, but was consistent with a high-latitude antiparallel reconnection site.

Chapter 6

Summary and Conclusions

> Quotation, n: The act of repeating erroneously the words of another.
> *Ambrose Bierce, "The Devil's Dictionary", 1911*

In this thesis, new research into flux transfer events has been presented. All three studies used the previously unavailable potential of four-spacecraft plasma measurements.

In Chapter 3 (Fear *et al.*, 2005a), it was shown that some high-latitude magnetospheric FTEs may have untraditional B_N signatures, making identification more difficult. Over a two-hour period on the 25th January 2002, all four spacecraft in the Cluster quartet observed a transition from the dayside magnetosphere, through a boundary layer, into the magnetosheath. The magnetosphere was characterised by a hot, rare electron distribution with the highest fluxes in the direction perpendicular to the magnetic field (typical of a trapped population). The magnetosheath was identified by a cooler, denser electron distribution, and a magnetic field orientation that was consistent with being draped over the magnetopause. The structure of the boundary layer was revealed by plotting the data as a function of the magnetopause transition parameter, which is a proxy for distance through such layers derived from an observed anticorrelation between plasma temperature and density as spacecraft move from the magnetosphere to the magnetosheath.

There were no sharp divisions with the boundary layer, but for discussion it was split into two sections. The inner boundary layer had a magnetospheric magnetic field and electron distribution (including the presence of trapped electrons), but was distinguished by a field-aligned population of magnetosheath energy ($\sim$ 10–100 eV) electrons with differential electron fluxes that were lower than those observed in the magnetosheath. The outer boundary layer exhibited higher fluxes of the field-aligned distribution than observed in the inner boundary layer, but there were also

weaker fluxes of electrons at magnetosheath energy perpendicular to the magnetic field. There were no trapped magnetospheric electrons in the outer boundary layer, suggesting that it was on open magnetic field lines. Two specific events were studied, which were consistent with the spacecraft passing, to different extents, through the boundary layer structure. There is no conclusive evidence for the cause of entry into the boundary layer for the first event; when the second event occurred, three of the spacecraft were in the magnetosheath and observed the passage of a standard polarity FTE. Considering the unusual signature observed by the spacecraft which was in the magnetosphere immediately before and after the event, it is unlikely that the plasma and magnetic field characteristics would have been identified as a magnetospheric FTE were it not for the observations made in the magnetosheath. Thus it is probable that the occurrence of magnetospheric FTEs may be underestimated in this region.

In Chapter 4, the results of a survey of FTEs observed by Cluster during an entire dayside magnetopause season were presented. During the season (November 2002 – June 2003), the orbit of the spacecraft precessed with respect to the Sun-Earth line as the Earth orbited the Sun. The orbit crossed the magnetopause at relatively low latitudes on the dusk flank in November/December, moving to higher latitudes closer to local noon, before crossing the low-latitude dawn flank magnetopause in May/June. Most events were observed when the lagged IMF was directed southward, which is consistent with the results of previous surveys carried out at the pre-terminator magnetopause ($X_{GSM} > 0$). The dependence on location and IMF of the polarities of the FTEs which occurred when the IMF was southward was also consistent with earlier surveys. Standard polarity FTEs tended to be observed in the northern hemisphere, and reverse polarity FTEs tended to be observed in the southern hemisphere. When the IMF B_Y component was directed dawnward, the division between standard and reverse polarities was rotated clockwise in the GSM Y-Z plane, as viewed from the Sun. When the IMF B_Y component was duskward, the rotation of this division was reversed. This rotation is consistent with the conclusion of Russell *et al.* (1985) that FTEs are generated by component reconnection, which may take place on the dayside magnetopause at low latitudes (equatorward of the cusps). Since Cluster does not yet sample the low-latitude, near-noon magnetopause it is not possible to exclude the possibility of antiparallel reconnection on the basis of polarity alone.

The survey in Chapter 4 included observations of the post-terminator magnetopause ($X_{GSM} < 0$); the only previous FTE survey to have done so was published by Kawano and Russell (1997a,b). In both surveys, significant numbers of FTEs were observed whilst the lagged IMF was strongly northward, which was defined in Chapter 4 as cases for which the magnitude of the IMF clock angle was less than

70°. The majority of these events were observed at the post-terminator magnetopause. Kawano and Russell (1997a,b) proposed two alternative explanations for their northward IMF events. Their first explanation was that reconnection could possibly occur under northward IMF at the dayside magnetopause as a random process, but that the signatures of such reconnection could not normally be observed at the dayside magnetopause if a process of 're-reconnection' (Nishida, 1989) occurred at the central section of a subsolar reconnection line. If the ends of the reconnection line did not undergo the re-reconnection process, FTEs could be generated under northward IMF conditions and observed away from the subsolar point as they propagated tailward. Their second explanation was that the FTEs were generated at a high-shear (antiparallel) reconnection site near the cusp, but that they somehow moved equatorward. Combining the ability of four spacecraft to determine the velocity of a structure which passes them with the model of reconnected flux tube evolution developed by Cooling *et al.* (2001), it was shown in Chapter 4 that the observed FTEs were not consistent with a subsolar reconnection line that was inhibited by re-reconnection, since the observed FTEs would have been generated near the subsolar point and therefore should often be observed at the subsolar magnetopause. However, it was also shown that equatorward motion from a near-cusp reconnection site could be explained by the fact that the magnetosheath flow (model and observed) was super-Alfvénic (Fear *et al.*, 2005b). If this is also the case at the reconnection site (as it is in the model), one set of FTEs would be generated at the reconnection line and swept tailward and poleward as the magnetosheath flow and kink Alfvén wave would be aligned. However, the FTEs generated on the equatorward edge of the reconnection line would be swept back across the reconnection line by the super-Alfvénic flow. These FTEs could also be swept equatorward. In order to produce model FTE paths that were consistent with the velocities observed by Cluster, the reconnection line had to be extended from an antiparallel reconnection site to a region of lower shear, implying that component reconnection also occurred in this scenario. The shear between the model magnetic fields at the equatorward edge of the reconnection line was 70°, but it was noted that the simple geomagnetic field model employed by Cooling *et al.* (2001) is not as accurate on the flanks, or near the cusps, as it is in the subsolar region. Therefore a more accurate estimation of the magnetic shear would be determined by incorporating a more realistic terrestrial magnetic field model, such as the Tsyganenko 1996 model (Tsyganenko, 1995).

In Chapter 5, the database of FTEs compiled in Chapter 4 was used to evaluate the effectiveness of the Cooling *et al.* (2001) model. The FTEs which occurred when the magnitude of the lagged IMF clock angle was greater than 70° were used (i.e. FTEs which occurred when the IMF was either southward, or dominated by the dawn-dusk component). In this chapter, a more advanced technique was used

to determine the FTE velocities. Velocities were calculated for 81 FTEs which exhibited bipolar B_N signatures on all four spacecraft and passed a criterion on the mutual consistency of the inter-spacecraft timings. The model results generally compared well with the observed velocities, confirming that the model is a useful illustrative tool when considering flux tube motion. 52 events matched the model flux tube velocities or the model magnetosheath flow to within 20° in angle, and ±50% in magnitude. A further 13 events were within 30° of one of the model vectors. Many events were observed on the magnetopause flank, where the magnetosheath flow dominated the Alfvénic term in the model FTE velocity; hence many results were consistent with both a model FTE velocity and the model magnetosheath flow. Of the events which were consistent with a model FTE velocity and inconsistent with the model magnetosheath flow (i.e. where the observed and model FTE velocities were similar and both differed significantly from the model magnetosheath flow), many apparently crossed regions of high magnetic shear (greater than 150°). Most of these events could also be traced back to the model subsolar component reconnection line, as the model cannot be used in its present form to distinguish between different feasible reconnection sites found along a model flux tube path. However, of the events which were only consistent with one of the model FTE velocities (and not $\mathbf{V}_{sheath}$), three events appear only to be consistent with a component reconnection line (probably originating near the subsolar point); one event was observed which was inconsistent with the model subsolar component X-line, but consistent with a high-latitude antiparallel reconnection site. It would not have been possible to distinguish the antiparallel reconnection event using *in situ* observations without the use of four spacecraft to determine the velocity.

Whilst the Cooling *et al.* (2001) model serves as a useful tool to illustrate the motion of reconnected flux tubes, differences between the observed and model magnetosheath/magnetospheric magnetic fields and the observed & model magnetosheath flow can be significant enough to affect the calculated de Hoffmann–Teller velocities. Therefore it is worthwhile comparing the observations and Cooling *et al.* (2001) model results with the velocities calculated from observed magnetosheath parameters (where available) using the equations derived by Cowley and Owen (1989).

6.1 Further work

There are three obvious avenues for further work. The first is to try and remove some of the simplifications made by the Cooling *et al.* (2001) model. It would be relatively straightforward to incorporate a more advanced magnetic field model (e.g. Tsyganenko, 1995); whilst this does not have an effect on the calculation of the flux

tube velocities derived by Cowley and Owen (1989), it would enable a more accurate determination of the magnetic shear at the magnetopause, and hence antiparallel and component reconnection sites. Another consequence would be a more accurate determination of the location and characteristics of the cusps, which would give a better indication of where the model magnetopause surface is reliable, and which would introduce the effects of seasonal dipole tilt on the model reconnection lines. There is a scarcity of more advanced magnetosheath models; hopefully current and future studies will enable this to be addressed (Longmore, 2005).

A second area which could be developed is a form of error analysis for the multi-spacecraft timing technique. Some forms of error have been discussed in this thesis. The technique described in Chapter 5 combines the timing differences of the signatures observed at all six possible pairs of the four spacecraft. Since only three timings are required to determine the 3D velocity, it is possible to minimise the effects of error on a simple timing measurement, and to exclude events which incorporate a relatively high degree of inconsistency. Furthermore, the sensitivity of the calculated velocity vectors to the timings was emphasised by a small number of events where the cross-correlation function failed to align the key features of the signatures. In the absence of a more rigorous technique, it would be possible to define a confidence interval by determining an estimated error on each timing, and calculating the effect on the velocity caused by different combinations of the error on the six measurements.

Little has been done since the launch of Cluster to discriminate between the different models of FTE structure. It is still not clear whether FTEs take the form of a flux tube that is created with a small latitudinal extent (Russell and Elphic, 1978, 1979), a reconnection 'bubble' (Southwood *et al.*, 1988; Scholer, 1988a) or long flux tubes generated parallel to multiple X-lines (Lee and Fu, 1985). It is possible that investigation of the internal current/magnetic field structure may help address this issue, particularly in years to come as the Cluster satellites start to cross the northern hemisphere dayside magnetosphere at lower latitudes.

Appendix 1:
Model results from Chapter 5

This appendix contains the Cooling *et al.* (2001) model run for each FTE which was examined in Chapter 5. Each figure takes the same format as Figure 5.6. Each figure shows a view of the model magnetopause projected into the GSM Y–Z plane. Concentric circles mark contours of X_{GSM}, and the locations of the cusps $[(\frac{1}{2}R_{mp}, 0, \pm R_{mp})_{GSM}]$ are marked by diamonds. The boundary between sub- and super-Alfvénic model magnetosheath flow is marked by a purple contour with tick marks pointing towards the sub-Alfvénic region.

The model component reconnection line has been initiated at the subsolar point, which is assumed to lie at the point where the model magnetopause surface intersects with the X_{GSM} axis, and extended for $20R_E$ in both directions. The reconnection line is traced perpendicular to the vector field $(\mathbf{B}_{ms} - \mathbf{B}_{gm})$, where $\mathbf{B}_{ms}$ and $\mathbf{B}_{gm}$ are the model magnetosheath and geomagnetic fields respectively. The position of observation of the FTE has been projected onto the model magnetopause; $\mathbf{V}_{HTN}$, $\mathbf{V}_{HTS}$ and $\mathbf{V}_{sheath}$ have been evaluated at this point and are marked by black arrows. $\mathbf{V}_{plane}$ is shown in green. The paths of the corresponding flux tubes have been traced backwards in steps of 0.75 s for 750 s. The subsolar point, and closest approach of each path to the model reconnection line, have been marked by a '+'. If a model flux tube paths crossed a region where the shear between the model magnetic fields either side of the magnetopause was greater than 150°, the point of highest shear is marked on each path by a red or blue '×'. The figure also shows the angle between $\mathbf{V}_{FTE}$ and the surface defined by $\hat{\mathbf{n}}$ (which contains $\mathbf{V}_{plane}$), and the angles between $\mathbf{V}_{plane}$ and $\mathbf{V}_{HTN}$, $\mathbf{V}_{HTS}$ and $\mathbf{V}_{sheath}$. In the bottom-left corner of the figure, $\mathbf{V}_{HTN}$ (red), $\mathbf{V}_{HTS}$ (blue), $\mathbf{V}_{sheath}$ (black) and $\mathbf{V}_{plane}$ (green) have been shown as they appear in the plane of the magnetopause. The 'characteristic time' (t_{char}) defined by Kawano *et al.* (1992) has been noted; this is the time between the positive and negative peaks of the bipolar B_N signature.

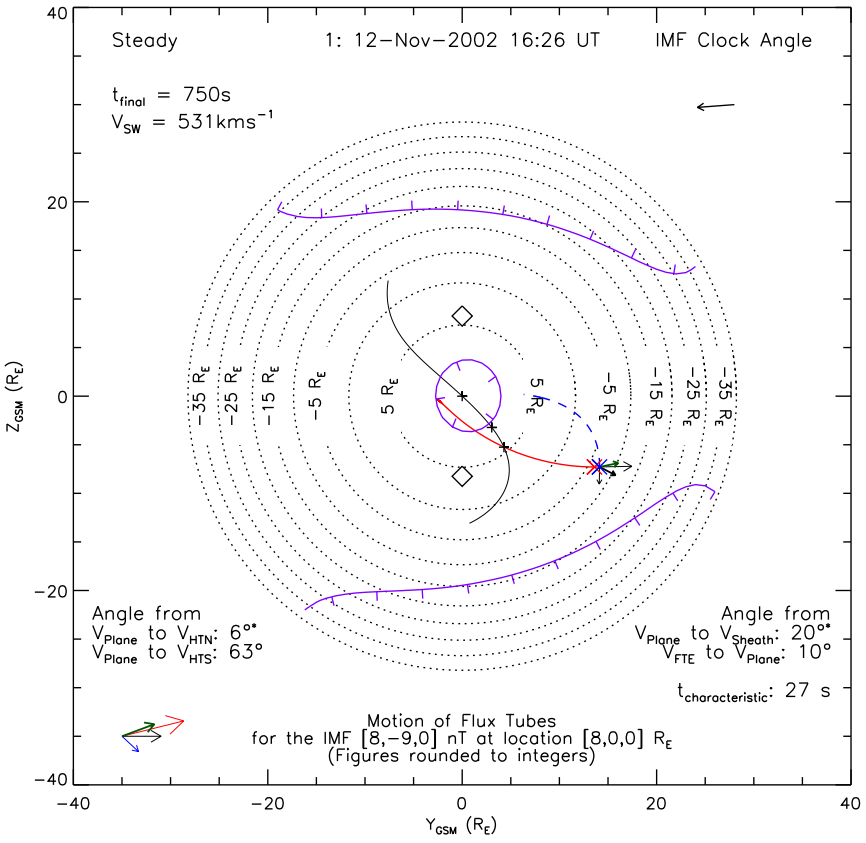
Steady
1: 12−Nov−2002 16:26 UT
IMF Clock Angle
t_{final} = 750s
V_{SW} = 531kms^{-1}
Angle from
V_{Plane} to V_{HTN}: 6°
V_{Plane} to V_{HTS}: 63°
Angle from
V_{Plane} to V_{Sheath}: 20°
V_{FTE} to V_{Plane}: 10°
$t_{characteristic}$: 27 s
Motion of Flux Tubes
for the IMF [8,−9,0] nT at location [8,0,0] R_E
(Figures rounded to integers)
Z_{GSM} (R_E)
Y_{GSM} (R_E)

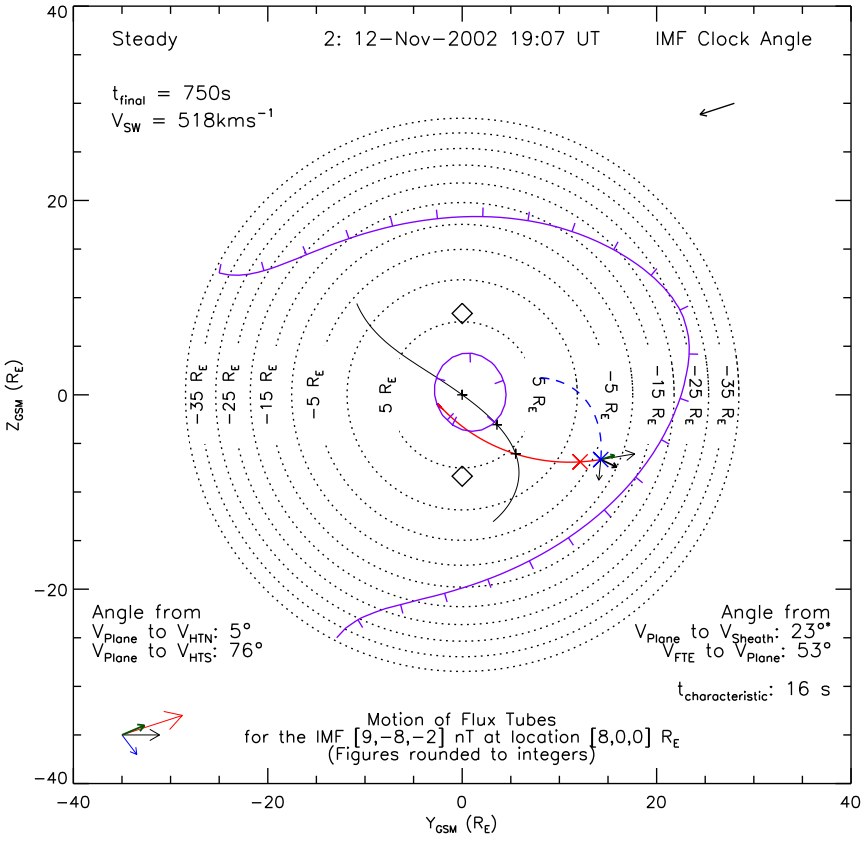
Steady
2: 12−Nov−2002 19:07 UT
IMF Clock Angle
t_{final} = 750s
V_{SW} = 518kms^{-1}
Angle from
V_{Plane} to V_{HTN}: 5°
V_{Plane} to V_{HTS}: 76°
Angle from
V_{Plane} to V_{Sheath}: 23°
V_{FTE} to V_{Plane}: 53°
$t_{characteristic}$: 16 s
Motion of Flux Tubes
for the IMF [9,−8,−2] nT at location [8,0,0] R_E
(Figures rounded to integers)
Z_{GSM} (R_E)
Y_{GSM} (R_E)

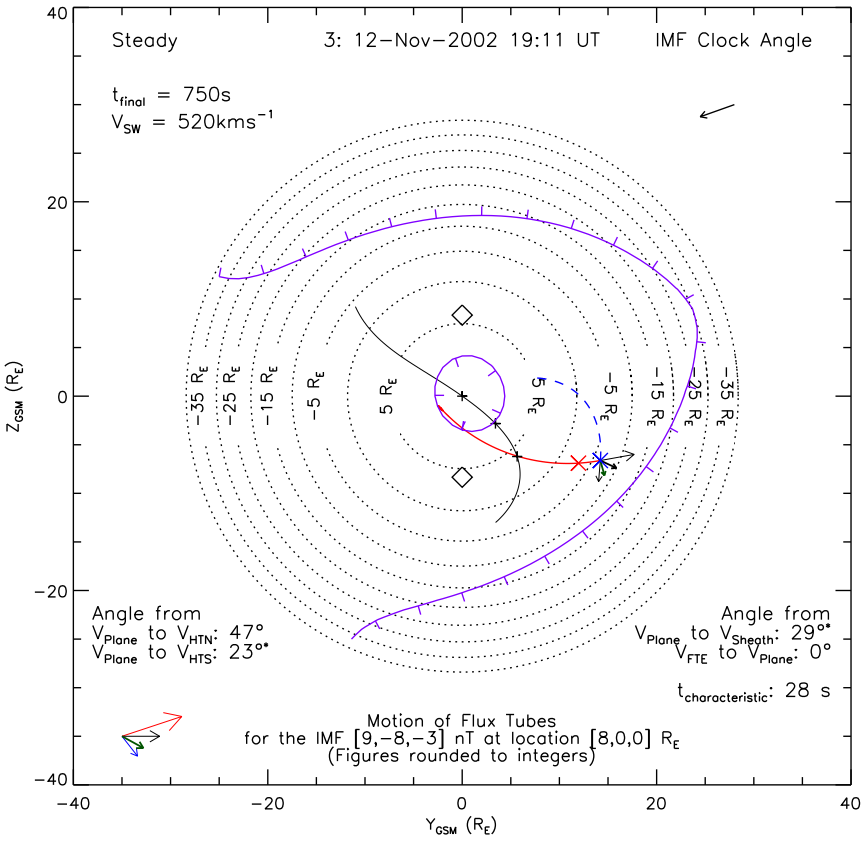
Steady
3: 12−Nov−2002 19:11 UT
IMF Clock Angle
t_{final} = 750s
V_{SW} = 520kms^{-1}
−35 R_E
−25 R_E
−15 R_E
−5 R_E
5 R_E
Angle from
V_{Plane} to V_{HTN}: 47°
V_{Plane} to V_{HTS}: 23°
Angle from
V_{Plane} to V_{Sheath}: 29°
V_{FTE} to V_{Plane}: 0°
$t_{characteristic}$: 28 s
Motion of Flux Tubes
for the IMF [9,−8,−3] nT at location [8,0,0] R_E
(Figures rounded to integers)
Z_{GSM} (R_E)
Y_{GSM} (R_E)

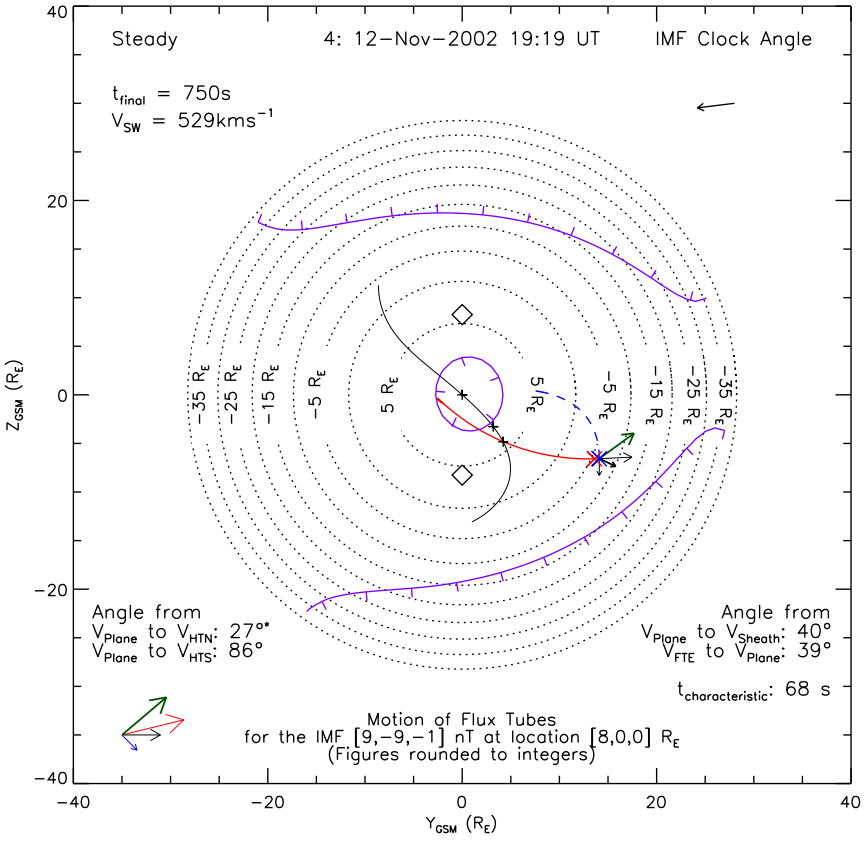
Steady
4: 12−Nov−2002 19:19 UT
IMF Clock Angle
t_{final} = 750s
V_{SW} = 529kms^{-1}
−35 R_E
−25 R_E
−15 R_E
−5 R_E
5 R_E
Angle from
V_{Plane} to V_{HTN}: 27°
V_{Plane} to V_{HTS}: 86°
Angle from
V_{Plane} to V_{Sheath}: 40°
V_{FTE} to V_{Plane}: 39°
$t_{characteristic}$: 68 s
Motion of Flux Tubes
for the IMF [9,−9,−1] nT at location [8,0,0] R_E
(Figures rounded to integers)
Z_{GSM} (R_E)
Y_{GSM} (R_E)

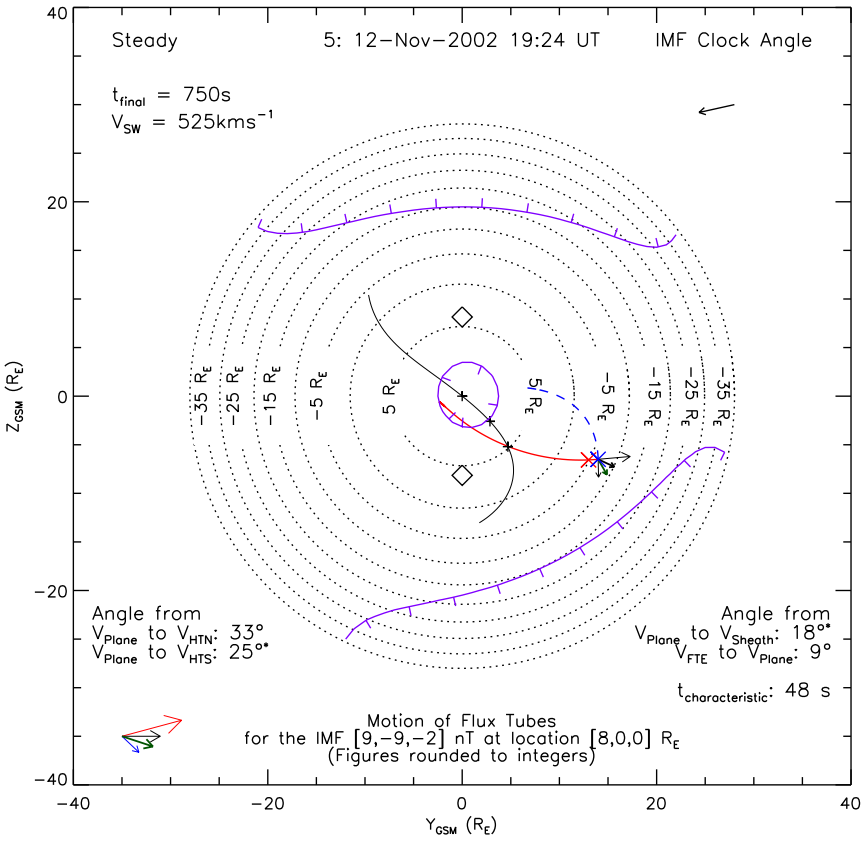
Steady
5: 12−Nov−2002 19:24 UT
IMF Clock Angle
t_{final} = 750s
V_{SW} = 525kms^{-1}
−35 R_E
−25 R_E
−15 R_E
−5 R_E
5 R_E
5 R_E
−5 R_E
−15 R_E
−25 R_E
−35 R_E
Angle from
V_{Plane} to V_{HTN}: 33°
V_{Plane} to V_{HTS}: 25°
Angle from
V_{Plane} to V_{Sheath}: 18°
V_{FTE} to V_{Plane}: 9°
$t_{characteristic}$: 48 s
Motion of Flux Tubes
for the IMF [9,−9,−2] nT at location [8,0,0] R_E
(Figures rounded to integers)
40
20
0
−20
−40
Z_{GSM} (R_E)
−40
−20
0
20
40
Y_{GSM} (R_E)

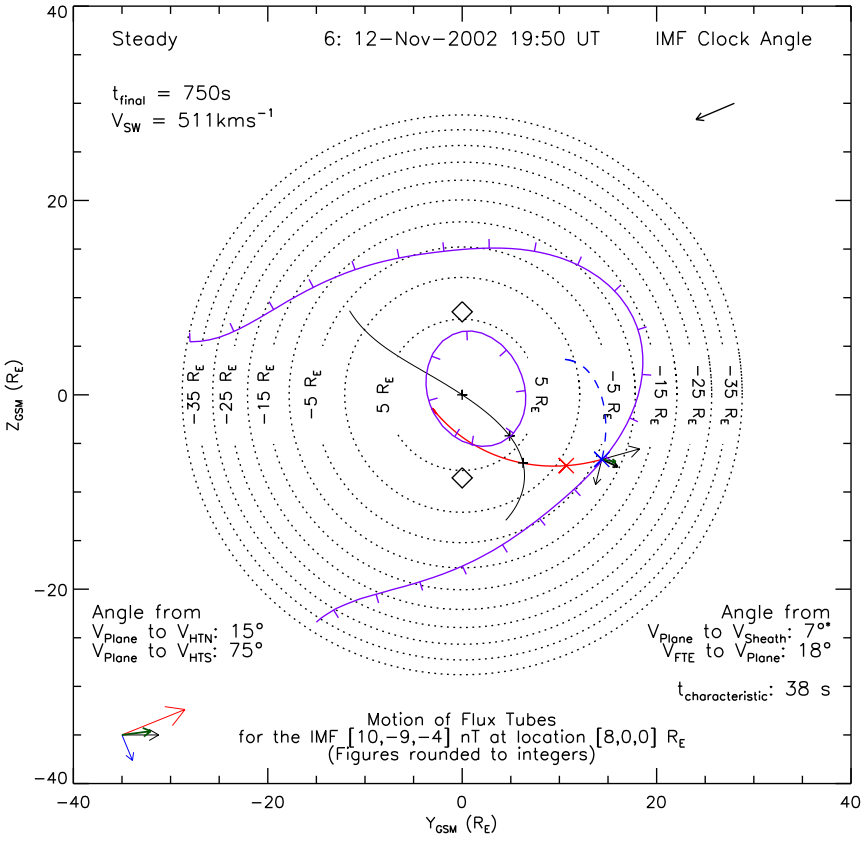
Steady
6: 12−Nov−2002 19:50 UT
IMF Clock Angle
t_{final} = 750s
V_{SW} = 511kms^{-1}
−35 R_E
−25 R_E
−15 R_E
−5 R_E
5 R_E
5 R_E
−5 R_E
−15 R_E
−25 R_E
−35 R_E
Angle from
V_{Plane} to V_{HTN}: 15°
V_{Plane} to V_{HTS}: 75°
Angle from
V_{Plane} to V_{Sheath}: 7°
V_{FTE} to V_{Plane}: 18°
$t_{characteristic}$: 38 s
Motion of Flux Tubes
for the IMF [10,−9,−4] nT at location [8,0,0] R_E
(Figures rounded to integers)
40
20
0
−20
−40
Z_{GSM} (R_E)
−40
−20
0
20
40
Y_{GSM} (R_E)

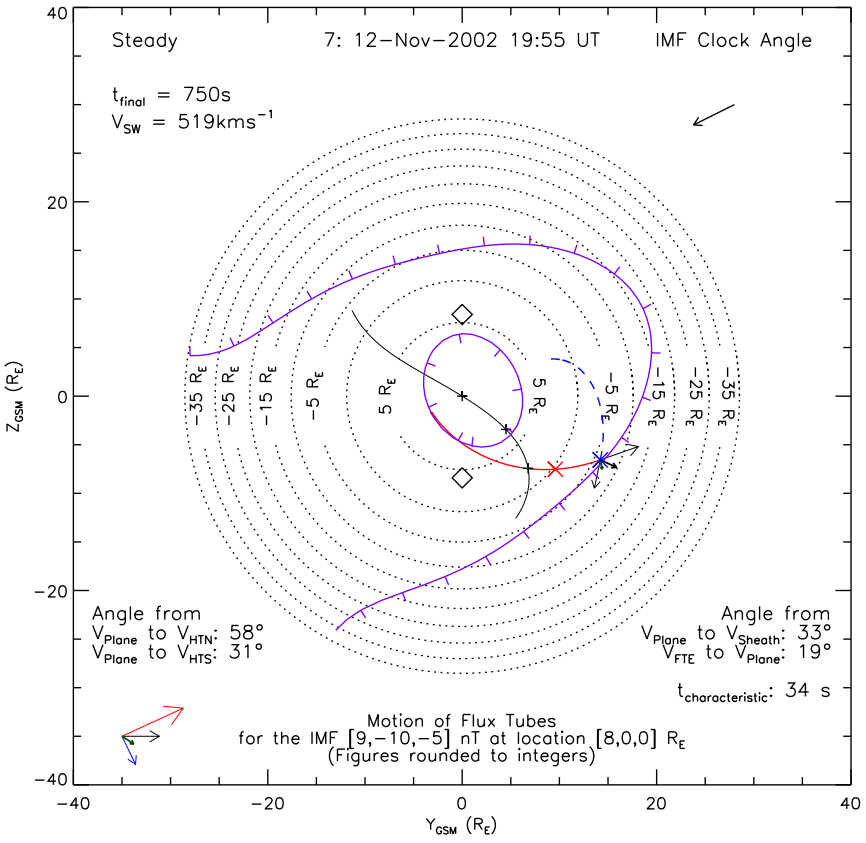
Steady
7: 12−Nov−2002 19:55 UT
IMF Clock Angle
t_{final} = 750s
V_{SW} = 519kms^{-1}
Angle from
V_{Plane} to V_{HTN}: 58°
V_{Plane} to V_{HTS}: 31°
Angle from
V_{Plane} to V_{Sheath}: 33°
V_{FTE} to V_{Plane}: 19°
$t_{characteristic}$: 34 s
Motion of Flux Tubes
for the IMF [9,−10,−5] nT at location [8,0,0] R_E
(Figures rounded to integers)
Z_{GSM} (R_E)
Y_{GSM} (R_E)

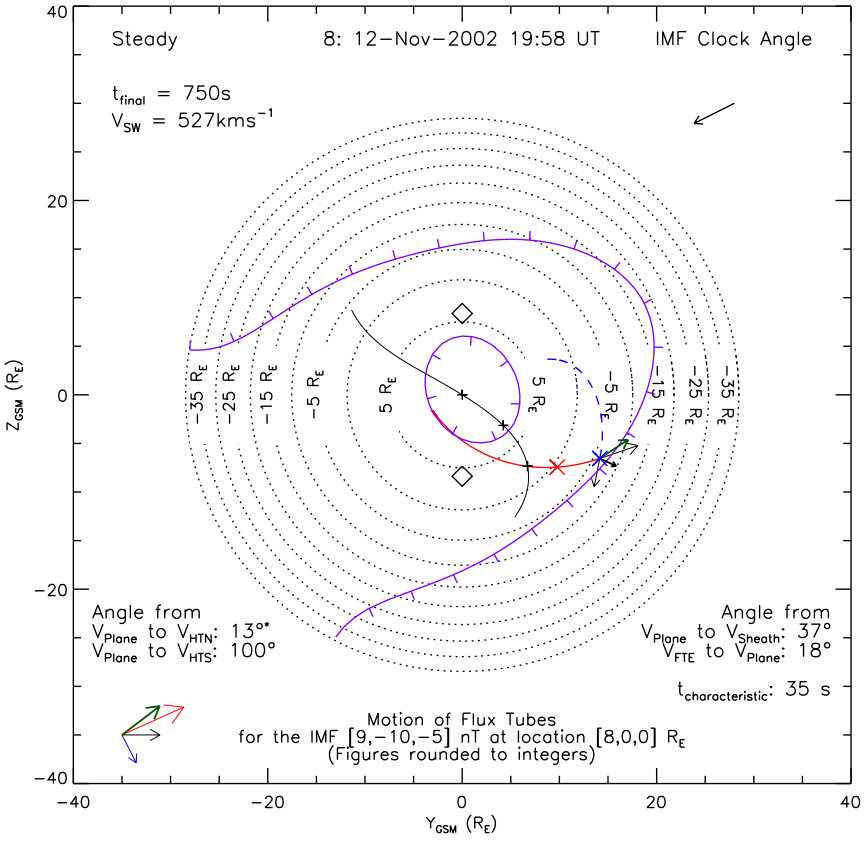
Steady
8: 12−Nov−2002 19:58 UT
IMF Clock Angle
t_{final} = 750s
V_{SW} = 527kms^{-1}
Angle from
V_{Plane} to V_{HTN}: 13°
V_{Plane} to V_{HTS}: 100°
Angle from
V_{Plane} to V_{Sheath}: 37°
V_{FTE} to V_{Plane}: 18°
$t_{characteristic}$: 35 s
Motion of Flux Tubes
for the IMF [9,−10,−5] nT at location [8,0,0] R_E
(Figures rounded to integers)
Z_{GSM} (R_E)
Y_{GSM} (R_E)

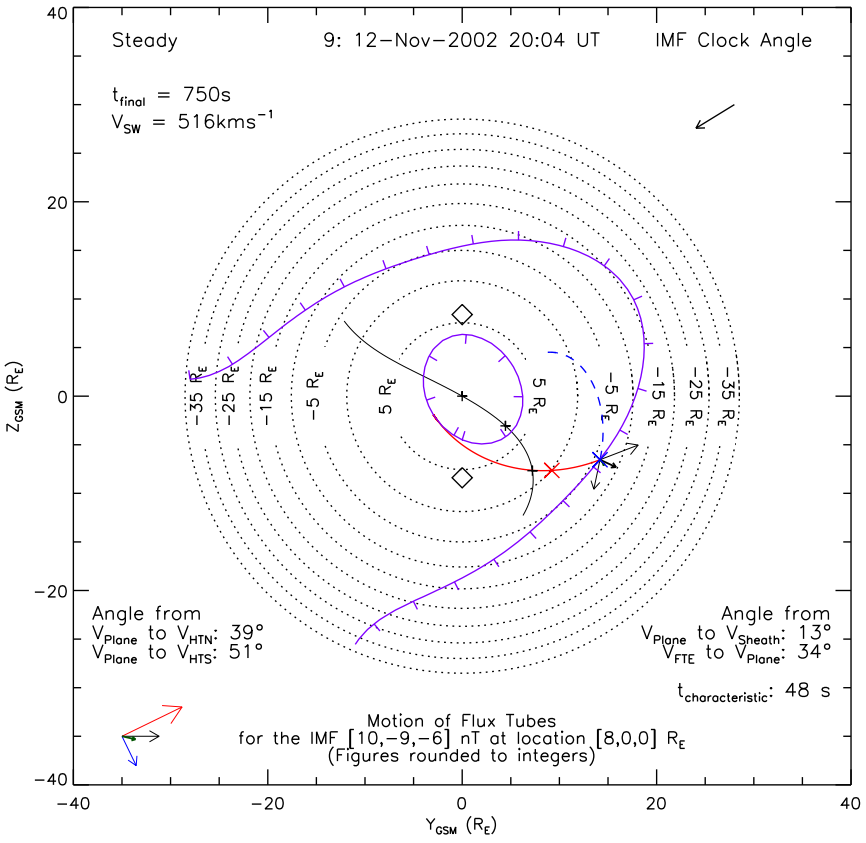
Steady
9: 12−Nov−2002 20:04 UT
IMF Clock Angle
t_{final} = 750s
V_{SW} = 516kms^{-1}
Angle from
V_{Plane} to V_{HTN}: 39°
V_{Plane} to V_{HTS}: 51°
Angle from
V_{Plane} to V_{Sheath}: 13°
V_{FTE} to V_{Plane}: 34°
$t_{characteristic}$: 48 s
Motion of Flux Tubes
for the IMF [10,−9,−6] nT at location [8,0,0] R_E
(Figures rounded to integers)
Z_{GSM} (R_E)
Y_{GSM} (R_E)

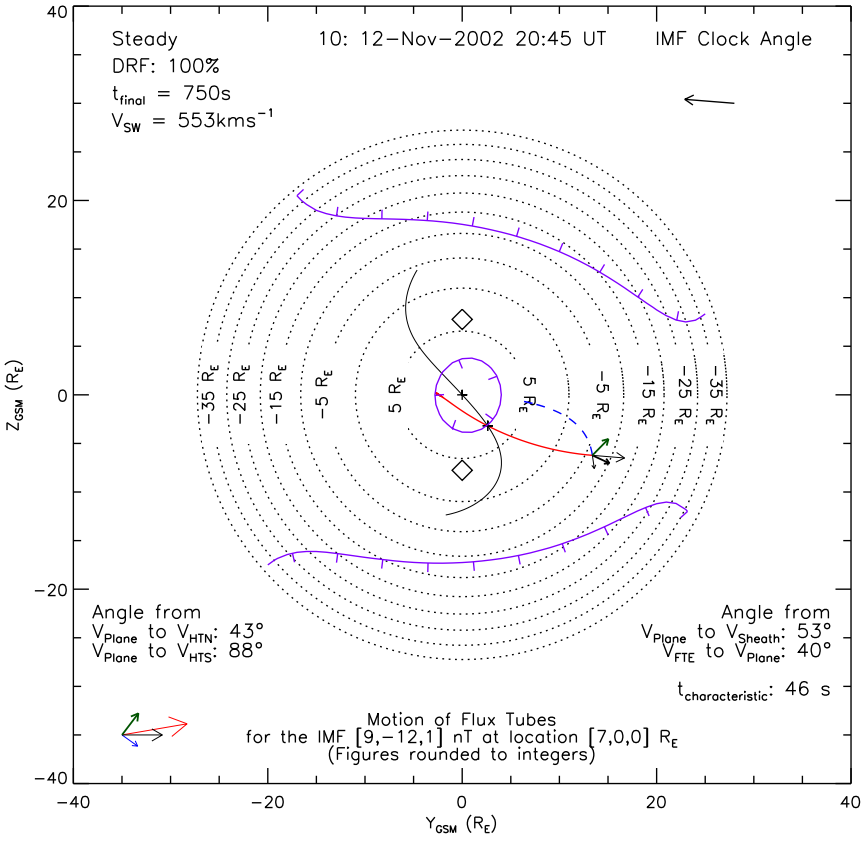
Steady
10: 12−Nov−2002 20:45 UT
IMF Clock Angle
DRF: 100%
t_{final} = 750s
V_{SW} = 553kms^{-1}
Angle from
V_{Plane} to V_{HTN}: 43°
V_{Plane} to V_{HTS}: 88°
Angle from
V_{Plane} to V_{Sheath}: 53°
V_{FTE} to V_{Plane}: 40°
$t_{characteristic}$: 46 s
Motion of Flux Tubes
for the IMF [9,−12,1] nT at location [7,0,0] R_E
(Figures rounded to integers)
Z_{GSM} (R_E)
Y_{GSM} (R_E)

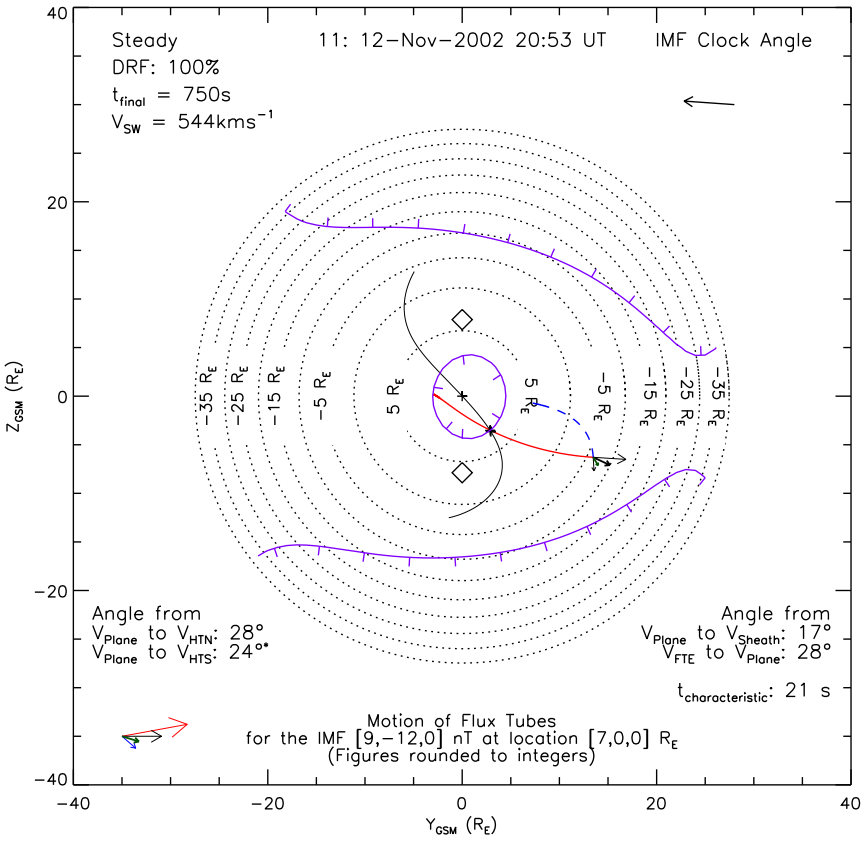
Steady
11: 12−Nov−2002 20:53 UT
IMF Clock Angle
DRF: 100%
t_{final} = 750s
V_{SW} = 544kms^{-1}
Angle from
V_{Plane} to V_{HTN}: 28°
V_{Plane} to V_{HTS}: 24°
Angle from
V_{Plane} to V_{Sheath}: 17°
V_{FTE} to V_{Plane}: 28°
$t_{characteristic}$: 21 s
Motion of Flux Tubes
for the IMF [9,−12,0] nT at location [7,0,0] R_E
(Figures rounded to integers)
Z_{GSM} (R_E)
Y_{GSM} (R_E)

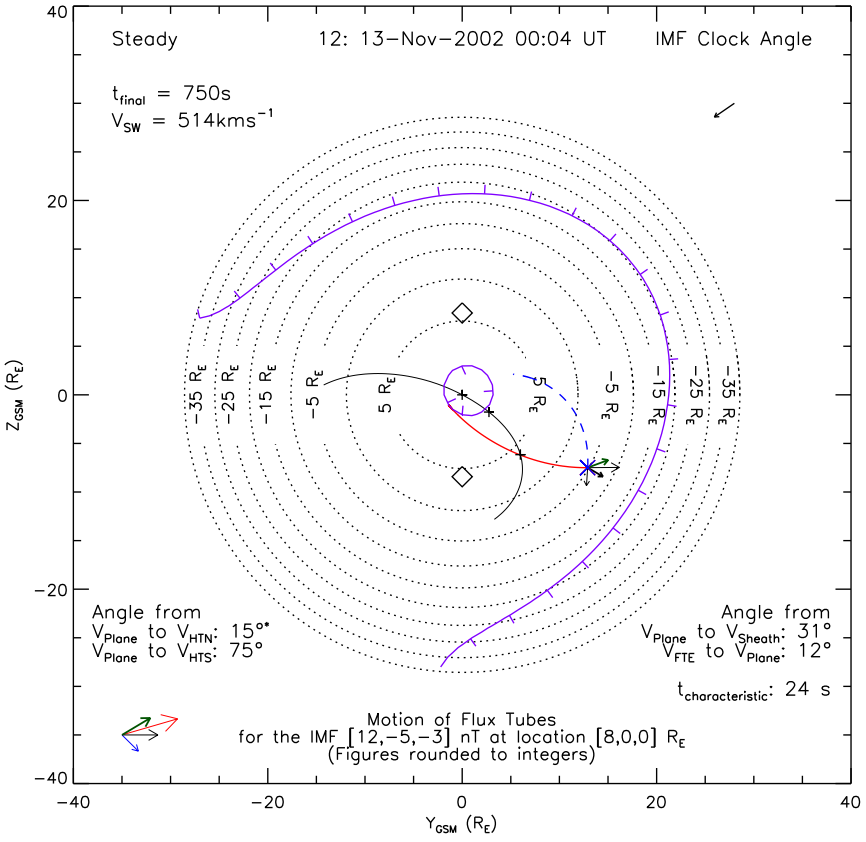
Steady
12: 13−Nov−2002 00:04 UT
IMF Clock Angle
t_{final} = 750s
V_{SW} = 514kms^{-1}
Angle from
V_{Plane} to V_{HTN}: 15°
V_{Plane} to V_{HTS}: 75°
Angle from
V_{Plane} to V_{Sheath}: 31°
V_{FTE} to V_{Plane}: 12°
$t_{characteristic}$: 24 s
Motion of Flux Tubes
for the IMF [12,−5,−3] nT at location [8,0,0] R_E
(Figures rounded to integers)
Z_{GSM} (R_E)
Y_{GSM} (R_E)

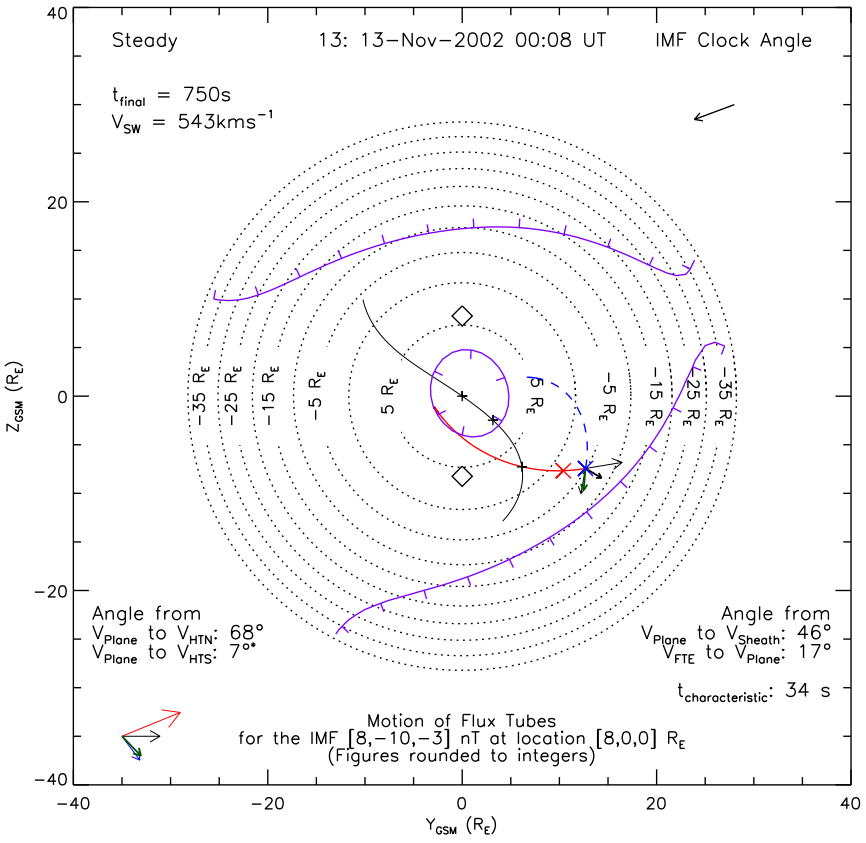
Steady
13: 13–Nov–2002 00:08 UT
IMF Clock Angle
t_{final} = 750s
V_{SW} = 543kms^{-1}
Angle from
V_{Plane} to V_{HTN}: 68°
V_{Plane} to V_{HTS}: 7°
Angle from
V_{Plane} to V_{Sheath}: 46°
V_{FTE} to V_{Plane}: 17°
$t_{characteristic}$: 34 s
Motion of Flux Tubes
for the IMF [8,–10,–3] nT at location [8,0,0] R_E
(Figures rounded to integers)
Z_{GSM} (R_E)
Y_{GSM} (R_E)

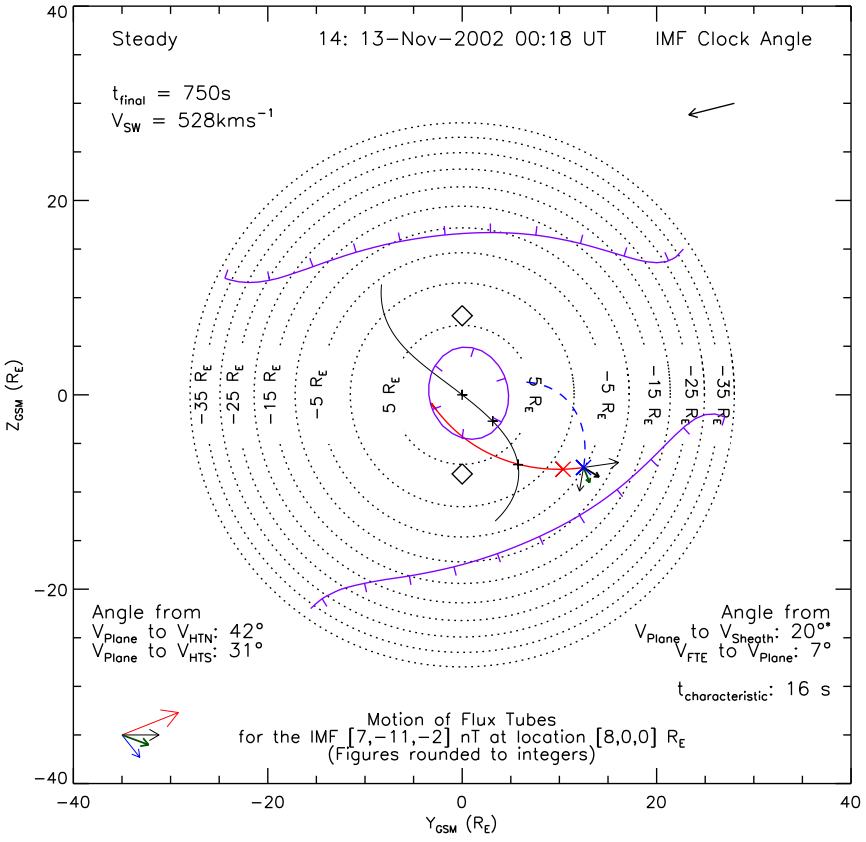
Steady
14: 13–Nov–2002 00:18 UT
IMF Clock Angle
t_{final} = 750s
V_{SW} = 528kms^{-1}
Angle from
V_{Plane} to V_{HTN}: 42°
V_{Plane} to V_{HTS}: 31°
Angle from
V_{Plane} to V_{Sheath}: 20°
V_{FTE} to V_{Plane}: 7°
$t_{characteristic}$: 16 s
Motion of Flux Tubes
for the IMF [7,–11,–2] nT at location [8,0,0] R_E
(Figures rounded to integers)
Z_{GSM} (R_E)
Y_{GSM} (R_E)

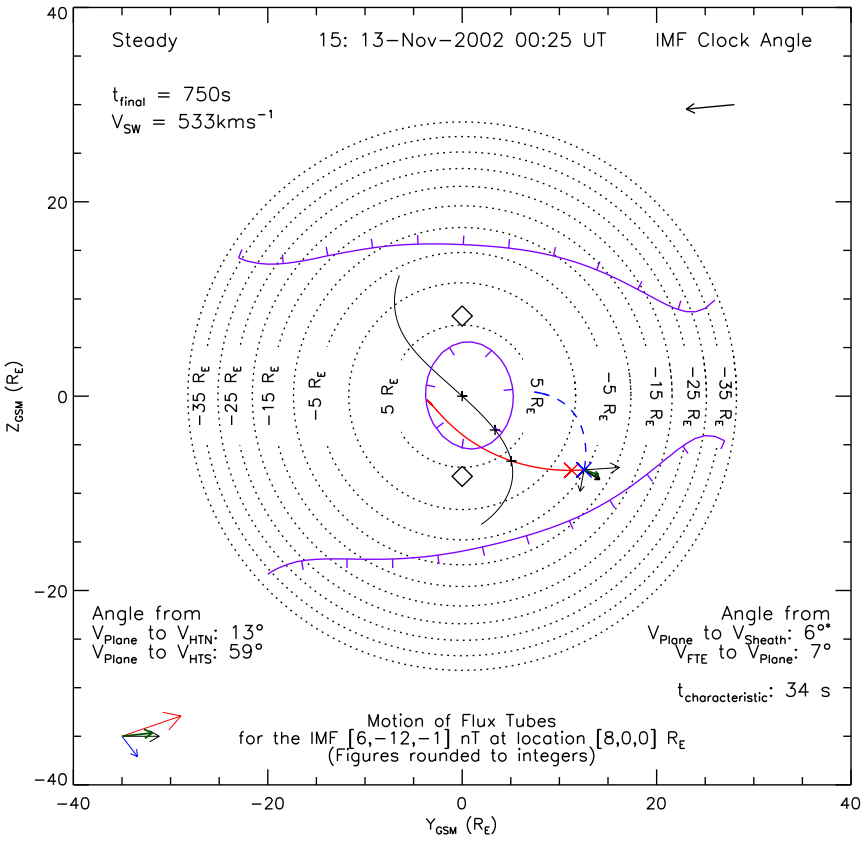
Steady
15: 13−Nov−2002 00:25 UT
IMF Clock Angle
t_{final} = 750s
V_{SW} = 533kms^{-1}
Angle from
V_{Plane} to V_{HTN}: 13°
V_{Plane} to V_{HTS}: 59°
Angle from
V_{Plane} to V_{Sheath}: 6°
V_{FTE} to V_{Plane}: 7°
$t_{characteristic}$: 34 s
Motion of Flux Tubes
for the IMF [6,−12,−1] nT at location [8,0,0] R_E
(Figures rounded to integers)
Z_{GSM} (R_E)
Y_{GSM} (R_E)

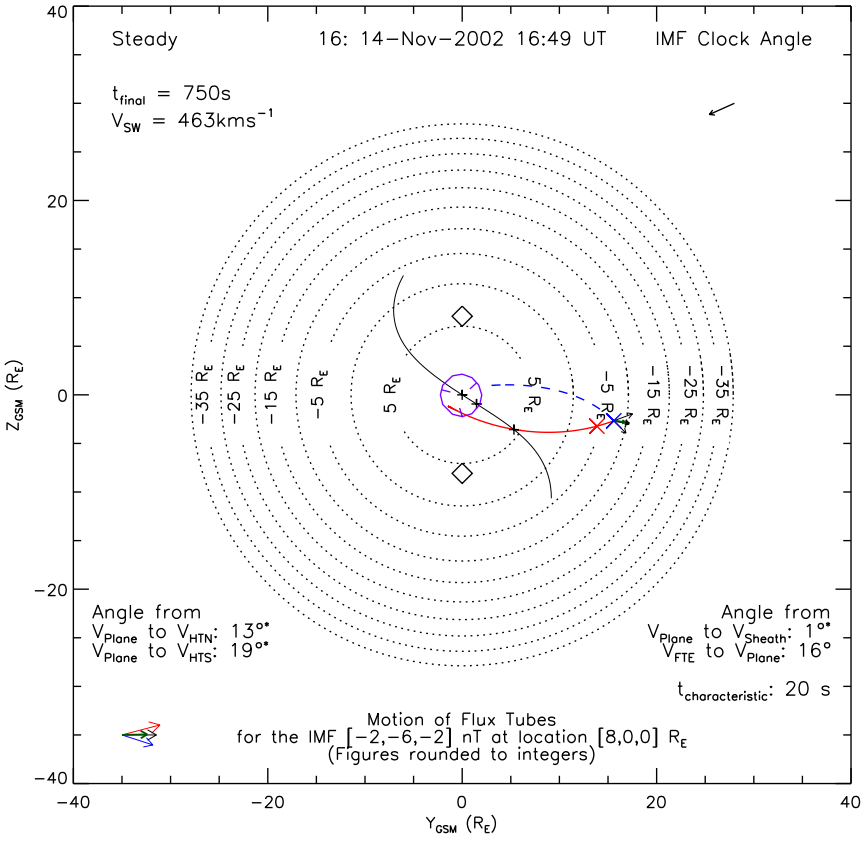
Steady
16: 14−Nov−2002 16:49 UT
IMF Clock Angle
t_{final} = 750s
V_{SW} = 463kms^{-1}
Angle from
V_{Plane} to V_{HTN}: 13°
V_{Plane} to V_{HTS}: 19°
Angle from
V_{Plane} to V_{Sheath}: 1°
V_{FTE} to V_{Plane}: 16°
$t_{characteristic}$: 20 s
Motion of Flux Tubes
for the IMF [−2,−6,−2] nT at location [8,0,0] R_E
(Figures rounded to integers)
Z_{GSM} (R_E)
Y_{GSM} (R_E)

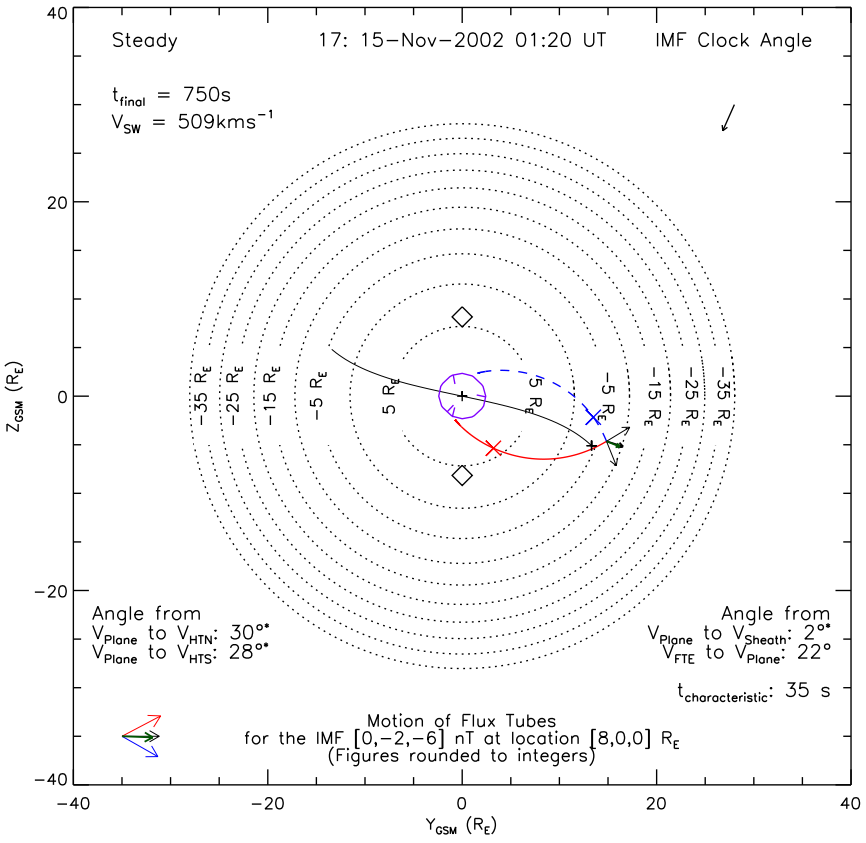
Steady
17: 15−Nov−2002 01:20 UT
IMF Clock Angle
t_{final} = 750s
V_{SW} = 509kms^{-1}
−35 R_E
−25 R_E
−15 R_E
−5 R_E
5 R_E
−5 R_E
−15 R_E
−25 R_E
−35 R_E
Angle from
V_{Plane} to V_{HTN}: 30°
V_{Plane} to V_{HTS}: 28°
Angle from
V_{Plane} to V_{Sheath}: 2°
V_{FTE} to V_{Plane}: 22°
$t_{characteristic}$: 35 s
Motion of Flux Tubes
for the IMF [0,−2,−6] nT at location [8,0,0] R_E
(Figures rounded to integers)
Z_{GSM} (R_E)
Y_{GSM} (R_E)
40
20
0
−20
−40

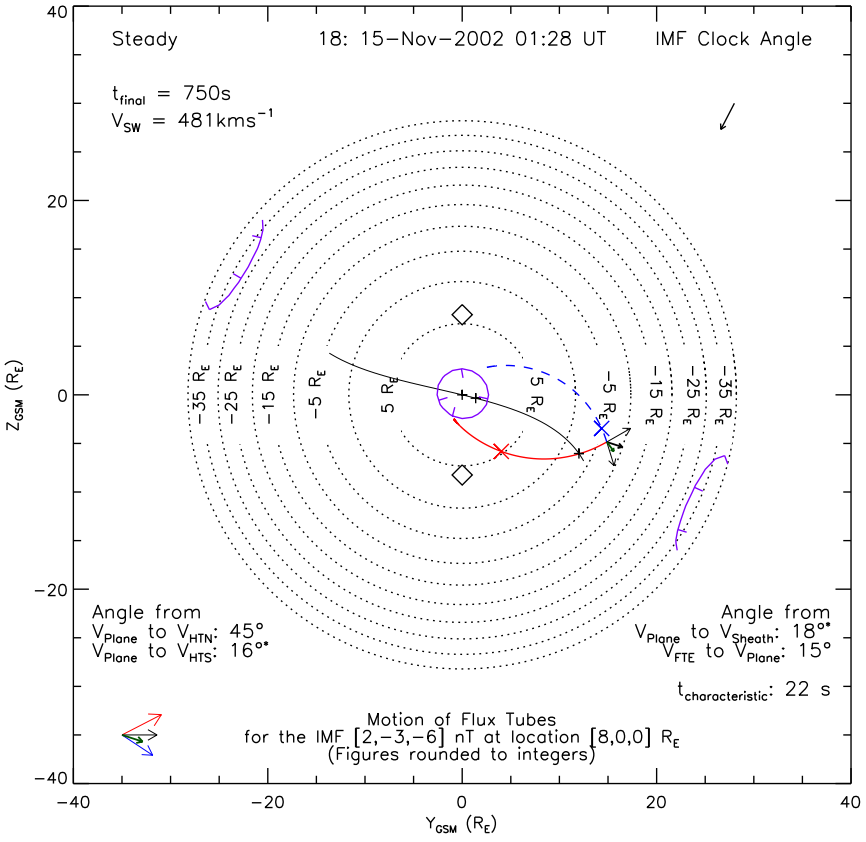
Steady
18: 15−Nov−2002 01:28 UT
IMF Clock Angle
t_{final} = 750s
V_{SW} = 481kms^{-1}
−35 R_E
−25 R_E
−15 R_E
−5 R_E
5 R_E
−5 R_E
−15 R_E
−25 R_E
−35 R_E
Angle from
V_{Plane} to V_{HTN}: 45°
V_{Plane} to V_{HTS}: 16°
Angle from
V_{Plane} to V_{Sheath}: 18°
V_{FTE} to V_{Plane}: 15°
$t_{characteristic}$: 22 s
Motion of Flux Tubes
for the IMF [2,−3,−6] nT at location [8,0,0] R_E
(Figures rounded to integers)
Z_{GSM} (R_E)
Y_{GSM} (R_E)
40
20
0
−20
−40

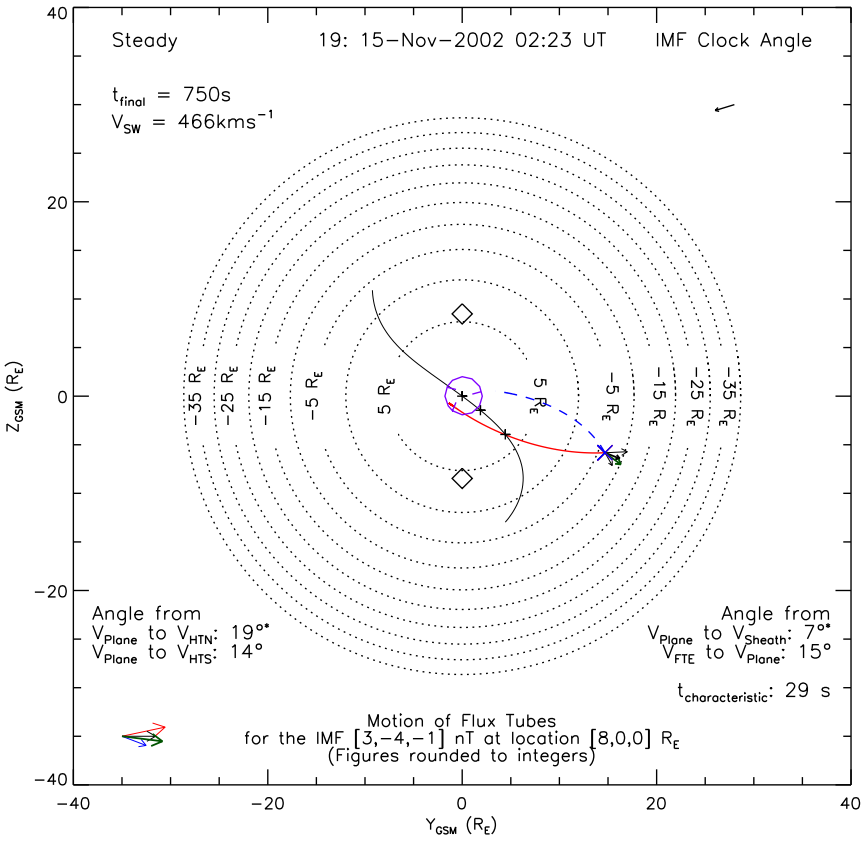
Steady
19: 15−Nov−2002 02:23 UT
IMF Clock Angle
t_{final} = 750s
V_{SW} = 466kms^{-1}
Angle from
V_{Plane} to V_{HTN}: 19°
V_{Plane} to V_{HTS}: 14°
Angle from
V_{Plane} to V_{Sheath}: 7°
V_{FTE} to V_{Plane}: 15°
$t_{characteristic}$: 29 s
Motion of Flux Tubes
for the IMF [3,−4,−1] nT at location [8,0,0] R_E
(Figures rounded to integers)
Z_{GSM} (R_E)
Y_{GSM} (R_E)

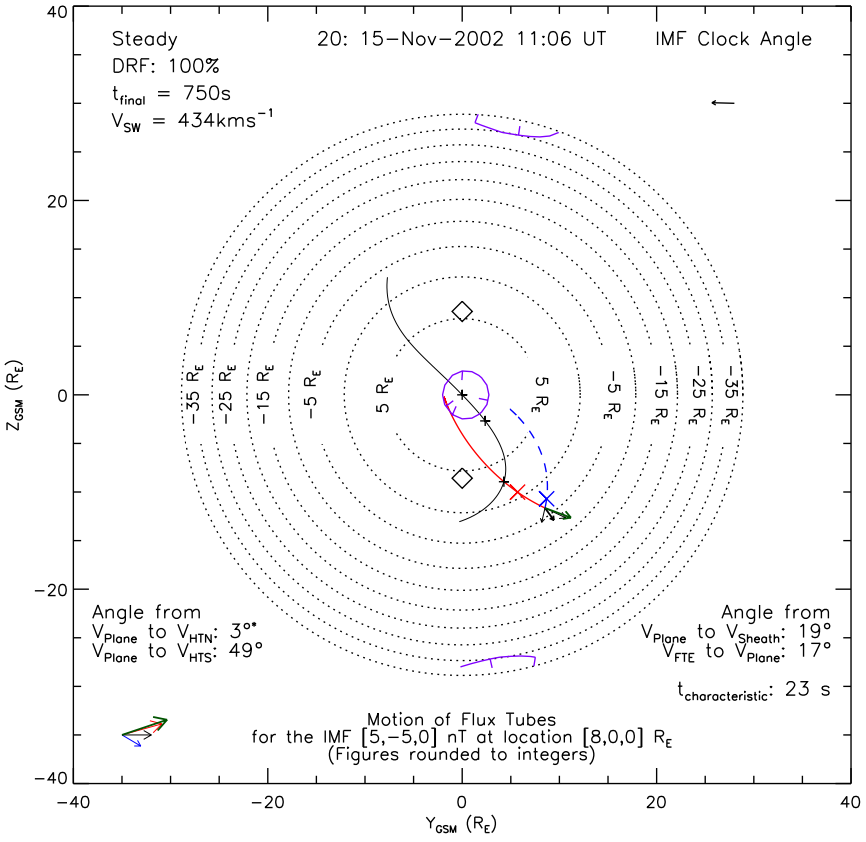
Steady
20: 15−Nov−2002 11:06 UT
IMF Clock Angle
DRF: 100%
t_{final} = 750s
V_{SW} = 434kms^{-1}
Angle from
V_{Plane} to V_{HTN}: 3°
V_{Plane} to V_{HTS}: 49°
Angle from
V_{Plane} to V_{Sheath}: 19°
V_{FTE} to V_{Plane}: 17°
$t_{characteristic}$: 23 s
Motion of Flux Tubes
for the IMF [5,−5,0] nT at location [8,0,0] R_E
(Figures rounded to integers)
Z_{GSM} (R_E)
Y_{GSM} (R_E)

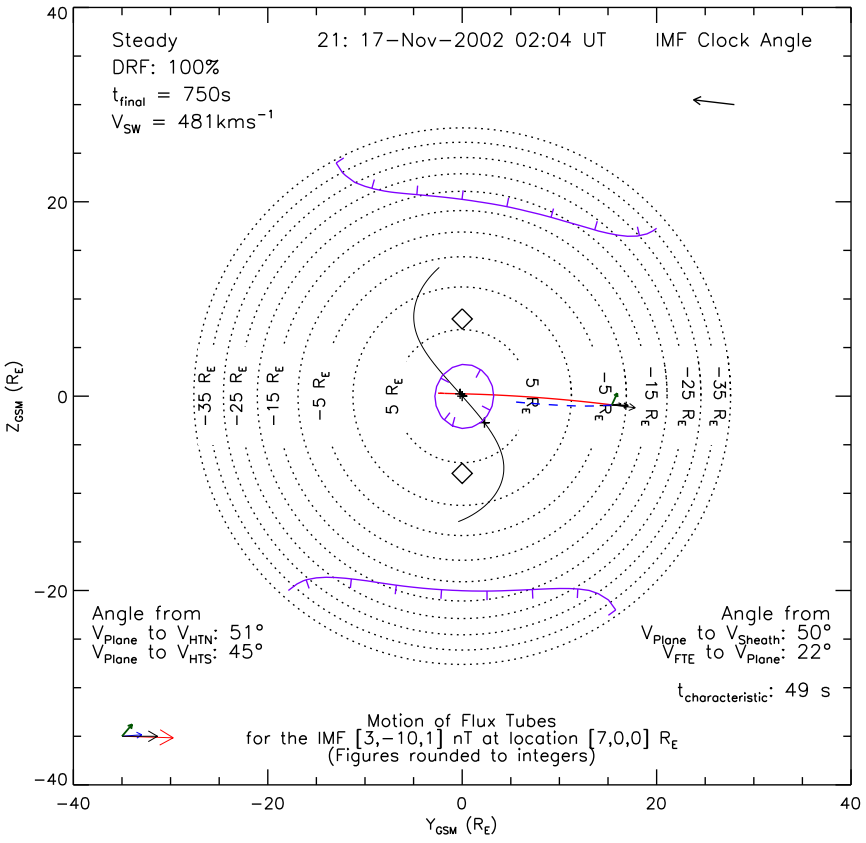
Steady
DRF: 100%
t_{final} = 750s
V_{SW} = 481kms^{-1}
21: 17−Nov−2002 02:04 UT
IMF Clock Angle
Angle from
V_{Plane} to V_{HTN}: 51°
V_{Plane} to V_{HTS}: 45°
Angle from
V_{Plane} to V_{Sheath}: 50°
V_{FTE} to V_{Plane}: 22°
$t_{characteristic}$: 49 s
Motion of Flux Tubes
for the IMF [3,−10,1] nT at location [7,0,0] R_E
(Figures rounded to integers)
Z_{GSM} (R_E)
Y_{GSM} (R_E)

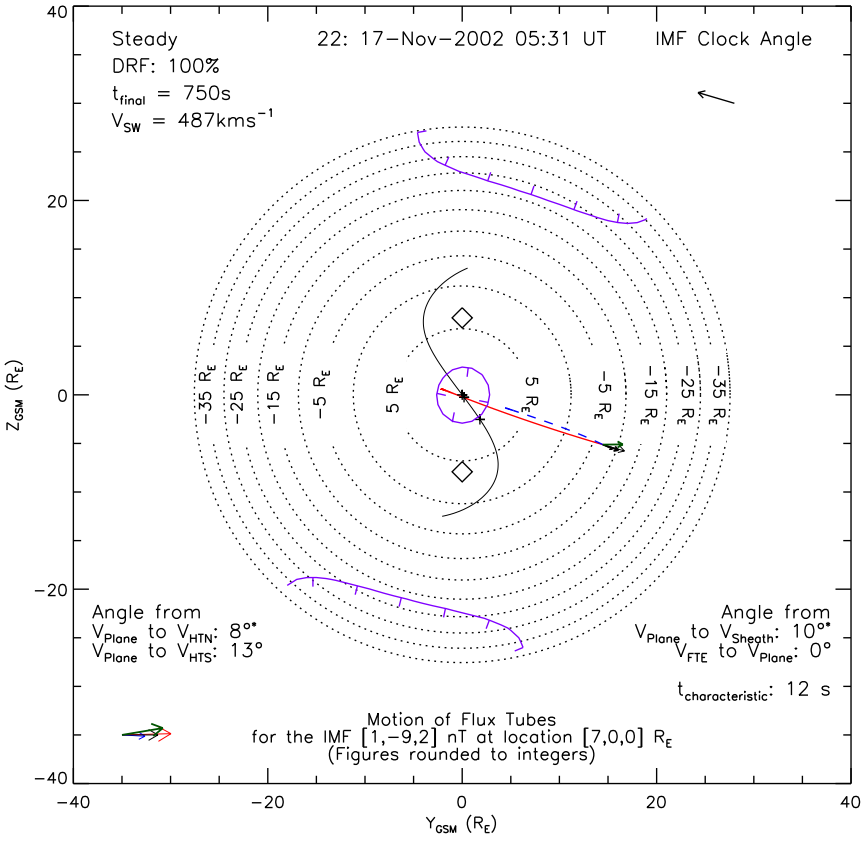
Steady
DRF: 100%
t_{final} = 750s
V_{SW} = 487kms^{-1}
22: 17−Nov−2002 05:31 UT
IMF Clock Angle
Angle from
V_{Plane} to V_{HTN}: 8°
V_{Plane} to V_{HTS}: 13°
Angle from
V_{Plane} to V_{Sheath}: 10°
V_{FTE} to V_{Plane}: 0°
$t_{characteristic}$: 12 s
Motion of Flux Tubes
for the IMF [1,−9,2] nT at location [7,0,0] R_E
(Figures rounded to integers)
Z_{GSM} (R_E)
Y_{GSM} (R_E)

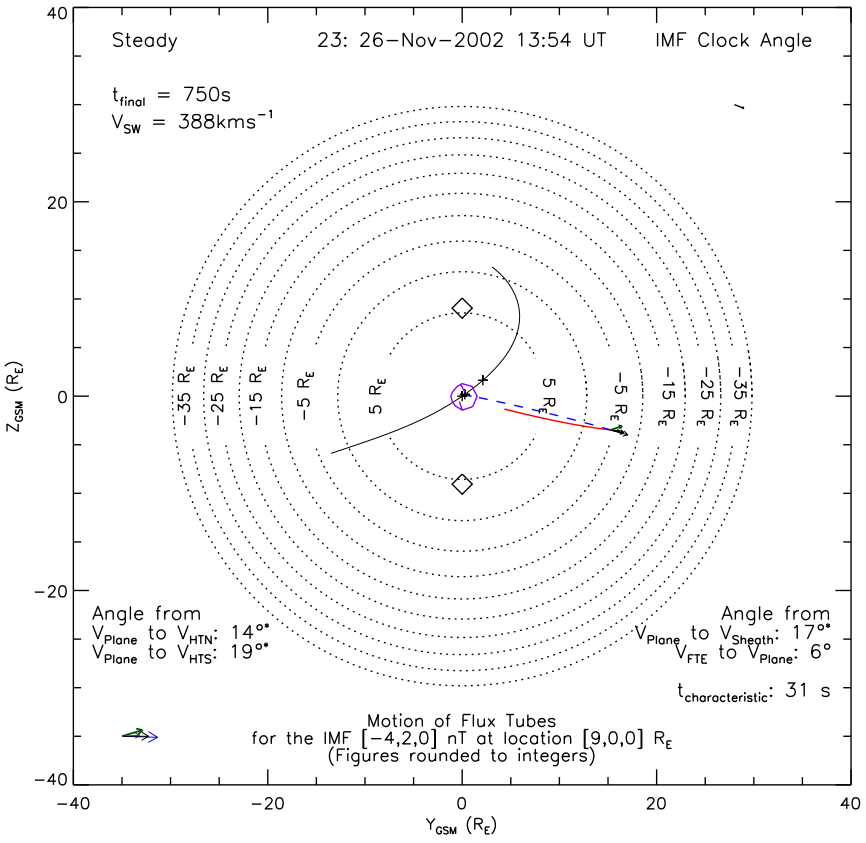
Steady
23: 26−Nov−2002 13:54 UT
IMF Clock Angle
t_{final} = 750s
V_{SW} = 388kms^{-1}
Angle from
V_{Plane} to V_{HTN}: 14°
V_{Plane} to V_{HTS}: 19°
Angle from
V_{Plane} to V_{Sheath}: 17°
V_{FTE} to V_{Plane}: 6°
$t_{characteristic}$: 31 s
Motion of Flux Tubes
for the IMF [−4,2,0] nT at location [9,0,0] R_E
(Figures rounded to integers)
Z_{GSM} (R_E)
Y_{GSM} (R_E)

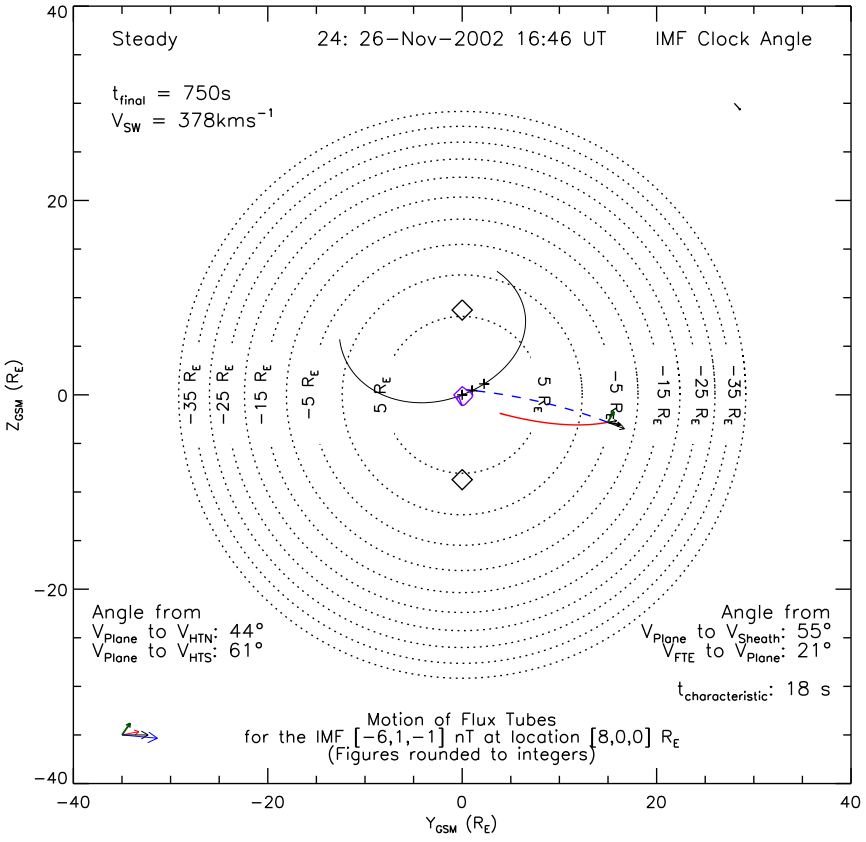
Steady
24: 26−Nov−2002 16:46 UT
IMF Clock Angle
t_{final} = 750s
V_{SW} = 378kms^{-1}
Angle from
V_{Plane} to V_{HTN}: 44°
V_{Plane} to V_{HTS}: 61°
Angle from
V_{Plane} to V_{Sheath}: 55°
V_{FTE} to V_{Plane}: 21°
$t_{characteristic}$: 18 s
Motion of Flux Tubes
for the IMF [−6,1,−1] nT at location [8,0,0] R_E
(Figures rounded to integers)
Z_{GSM} (R_E)
Y_{GSM} (R_E)

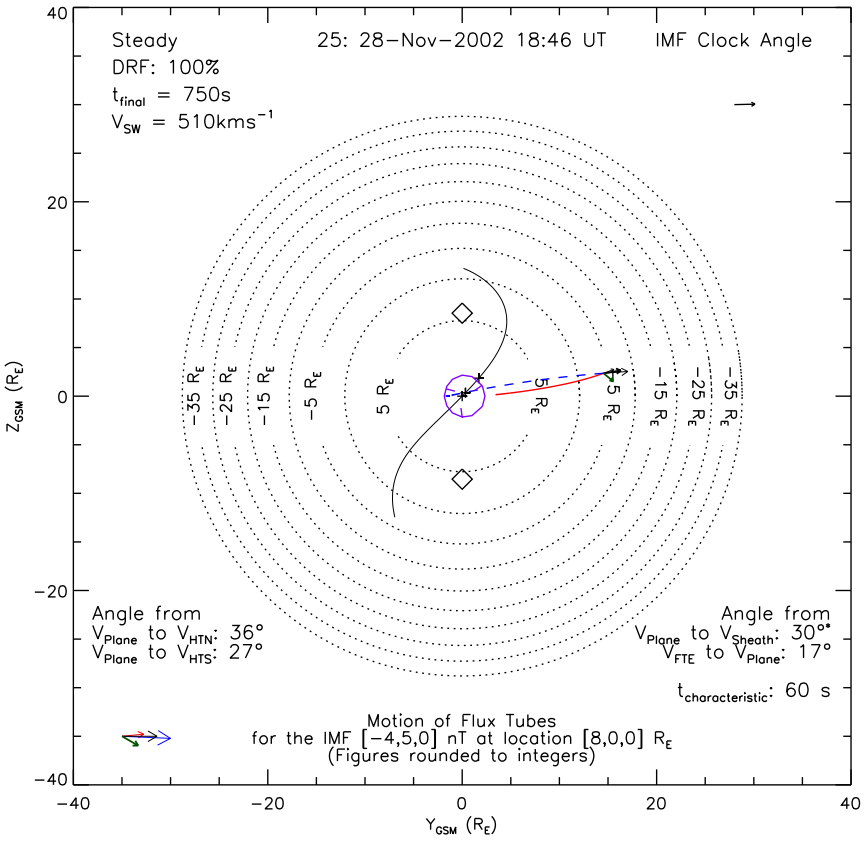
Steady
DRF: 100%
t_{final} = 750s
V_{SW} = 510kms^{-1}
25: 28−Nov−2002 18:46 UT
IMF Clock Angle
Angle from
V_{Plane} to V_{HTN}: 36°
V_{Plane} to V_{HTS}: 27°
Angle from
V_{Plane} to V_{Sheath}: 30°
V_{FTE} to V_{Plane}: 17°
$t_{characteristic}$: 60 s
Motion of Flux Tubes
for the IMF [−4,5,0] nT at location [8,0,0] R_E
(Figures rounded to integers)
Z_{GSM} (R_E)
Y_{GSM} (R_E)

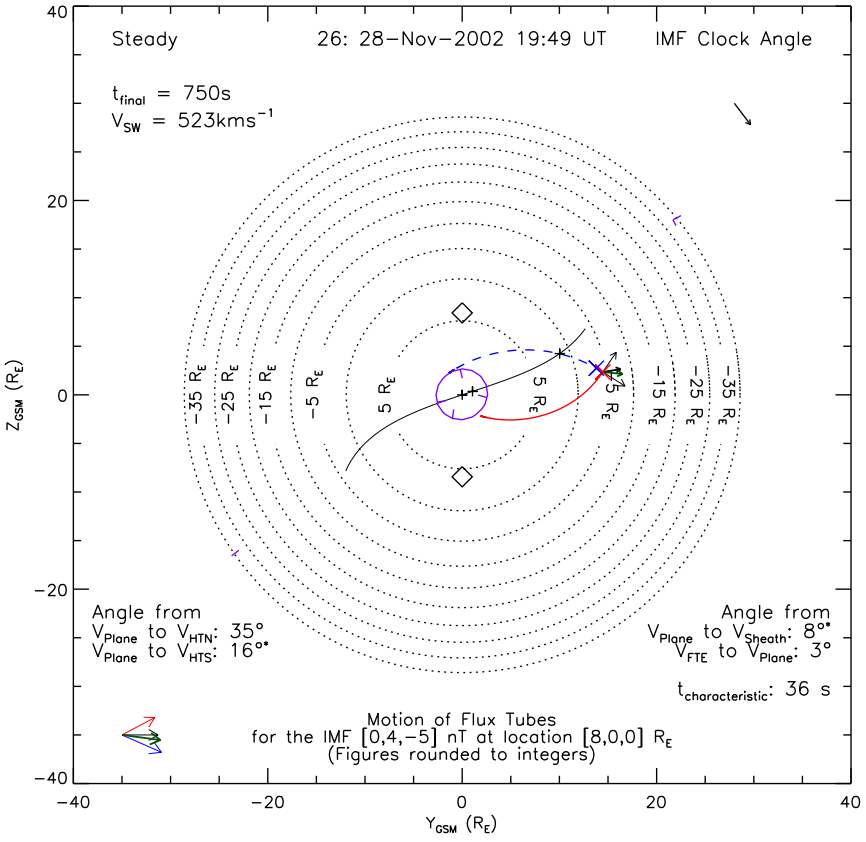
Steady
t_{final} = 750s
V_{SW} = 523kms^{-1}
26: 28−Nov−2002 19:49 UT
IMF Clock Angle
Angle from
V_{Plane} to V_{HTN}: 35°
V_{Plane} to V_{HTS}: 16°
Angle from
V_{Plane} to V_{Sheath}: 8°
V_{FTE} to V_{Plane}: 3°
$t_{characteristic}$: 36 s
Motion of Flux Tubes
for the IMF [0,4,−5] nT at location [8,0,0] R_E
(Figures rounded to integers)
Z_{GSM} (R_E)
Y_{GSM} (R_E)

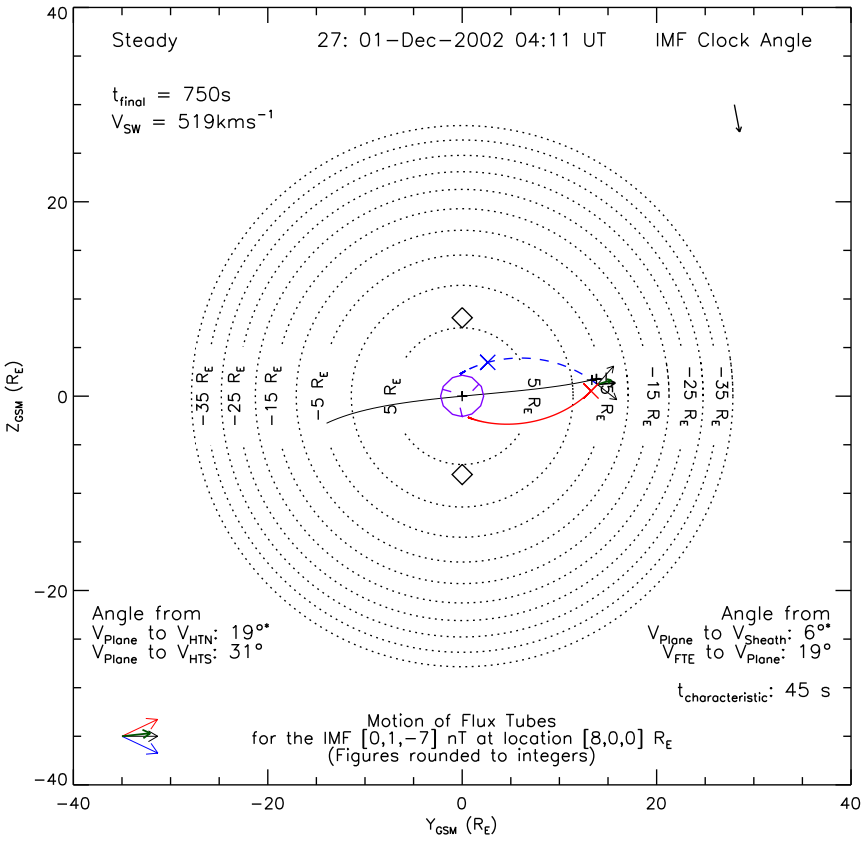
Steady
27: 01−Dec−2002 04:11 UT
IMF Clock Angle
t_{final} = 750s
V_{SW} = 519kms^{-1}
Angle from
V_{Plane} to V_{HTN}: 19°
V_{Plane} to V_{HTS}: 31°
Angle from
V_{Plane} to V_{Sheath}: 6°
V_{FTE} to V_{Plane}: 19°
$t_{characteristic}$: 45 s
Motion of Flux Tubes
for the IMF [0,1,−7] nT at location [8,0,0] R_E
(Figures rounded to integers)
Z_{GSM} (R_E)
Y_{GSM} (R_E)

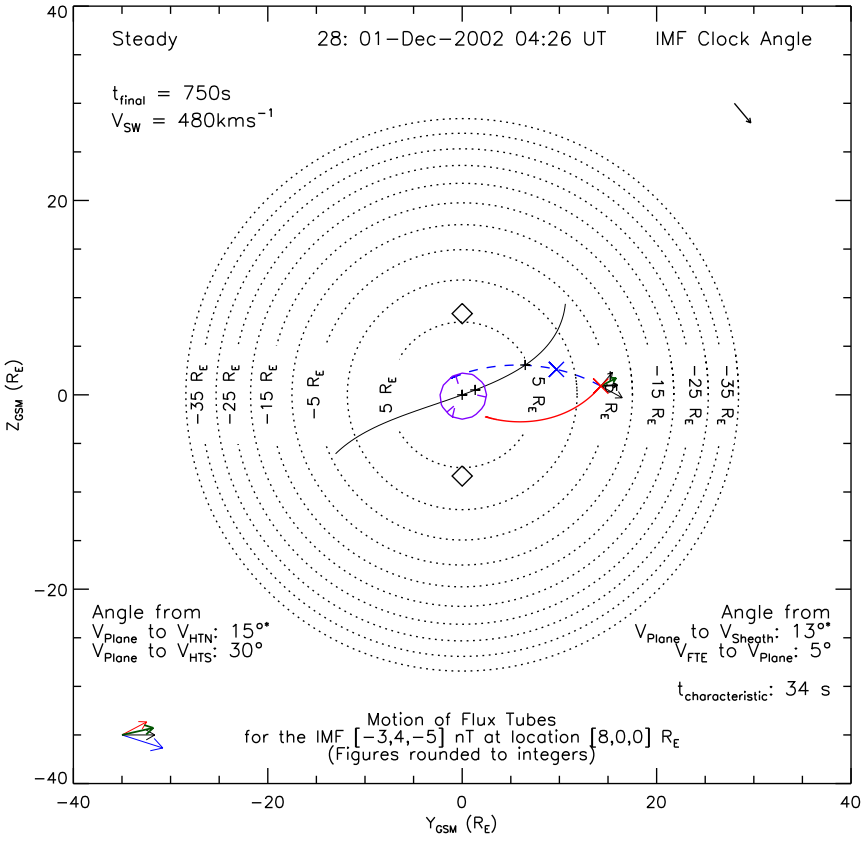
Steady
28: 01−Dec−2002 04:26 UT
IMF Clock Angle
t_{final} = 750s
V_{SW} = 480kms^{-1}
Angle from
V_{Plane} to V_{HTN}: 15°
V_{Plane} to V_{HTS}: 30°
Angle from
V_{Plane} to V_{Sheath}: 13°
V_{FTE} to V_{Plane}: 5°
$t_{characteristic}$: 34 s
Motion of Flux Tubes
for the IMF [−3,4,−5] nT at location [8,0,0] R_E
(Figures rounded to integers)
Z_{GSM} (R_E)
Y_{GSM} (R_E)

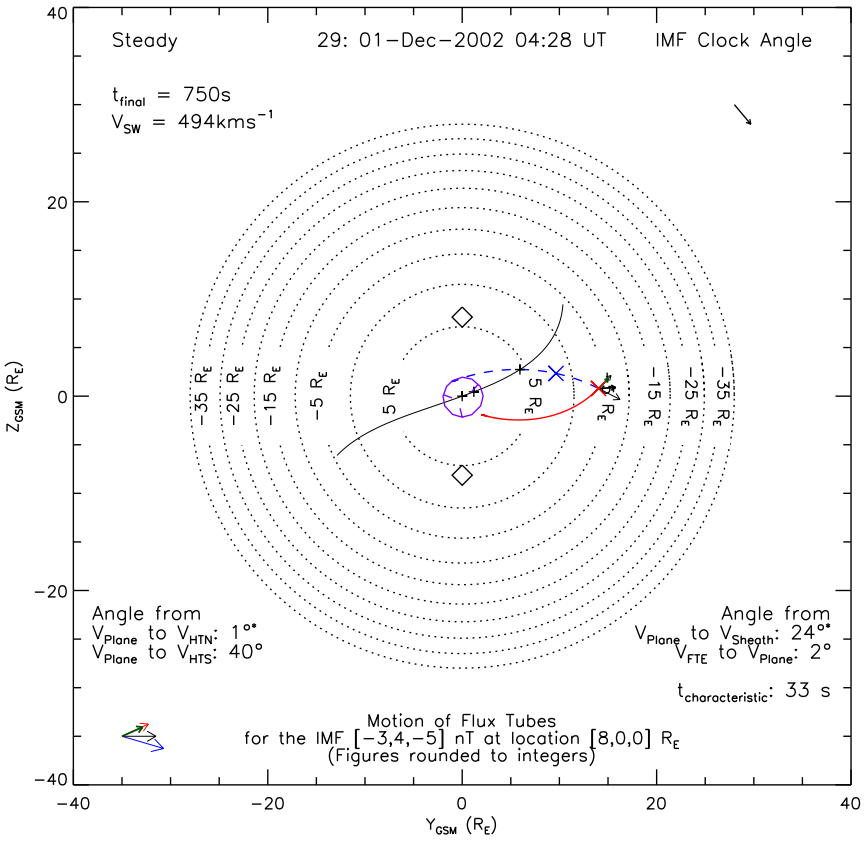
Steady
29: 01−Dec−2002 04:28 UT
IMF Clock Angle
t_{final} = 750s
V_{SW} = 494kms^{-1}
Angle from
V_{Plane} to V_{HTN}: 1°
V_{Plane} to V_{HTS}: 40°
Angle from
V_{Plane} to V_{Sheath}: 24°
V_{FTE} to V_{Plane}: 2°
$t_{characteristic}$: 33 s
Motion of Flux Tubes
for the IMF [−3,4,−5] nT at location [8,0,0] R_E
(Figures rounded to integers)
Z_{GSM} (R_E)
Y_{GSM} (R_E)

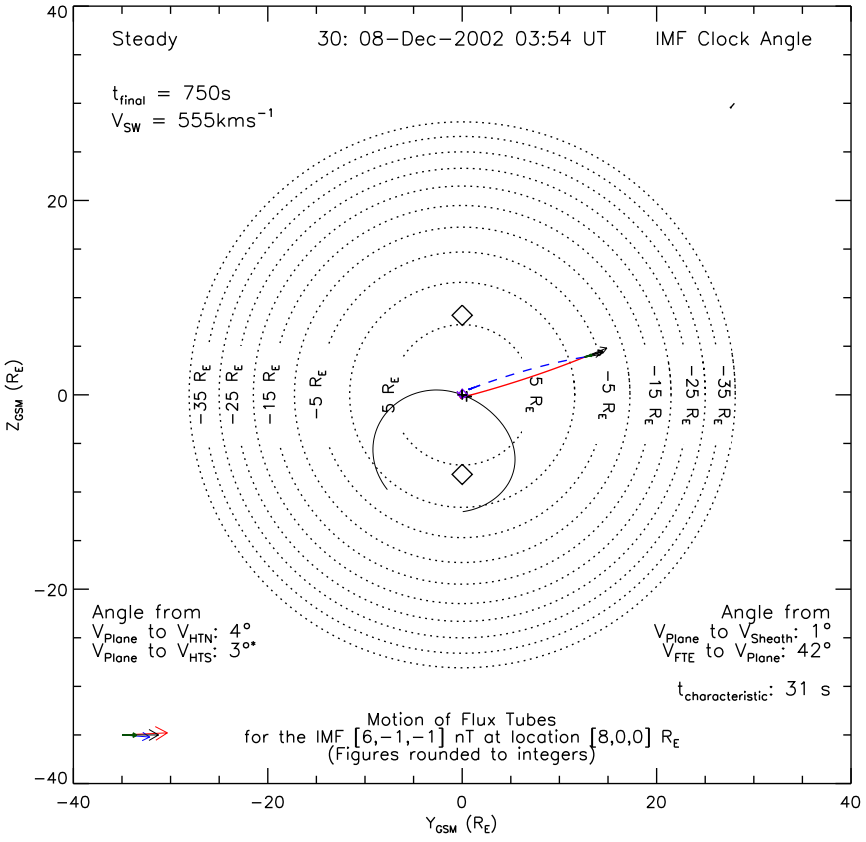
Steady
30: 08−Dec−2002 03:54 UT
IMF Clock Angle
t_{final} = 750s
V_{SW} = 555kms^{-1}
Angle from
V_{Plane} to V_{HTN}: 4°
V_{Plane} to V_{HTS}: 3°
Angle from
V_{Plane} to V_{Sheath}: 1°
V_{FTE} to V_{Plane}: 42°
$t_{characteristic}$: 31 s
Motion of Flux Tubes
for the IMF [6,−1,−1] nT at location [8,0,0] R_E
(Figures rounded to integers)
Z_{GSM} (R_E)
Y_{GSM} (R_E)

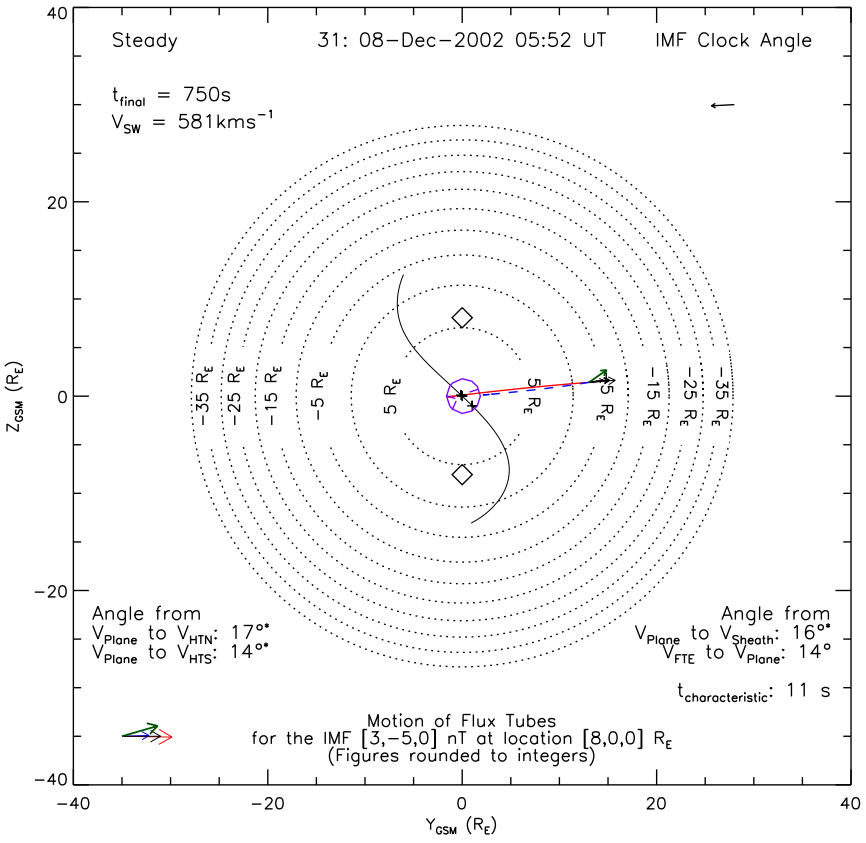
Steady
31: 08−Dec−2002 05:52 UT
IMF Clock Angle
t_{final} = 750s
V_{SW} = 581kms^{-1}
Angle from
V_{Plane} to V_{HTN}: 17°
V_{Plane} to V_{HTS}: 14°
Angle from
V_{Plane} to V_{Sheath}: 16°
V_{FTE} to V_{Plane}: 14°
$t_{characteristic}$: 11 s
Motion of Flux Tubes
for the IMF [3,−5,0] nT at location [8,0,0] R_E
(Figures rounded to integers)
Z_{GSM} (R_E)
Y_{GSM} (R_E)

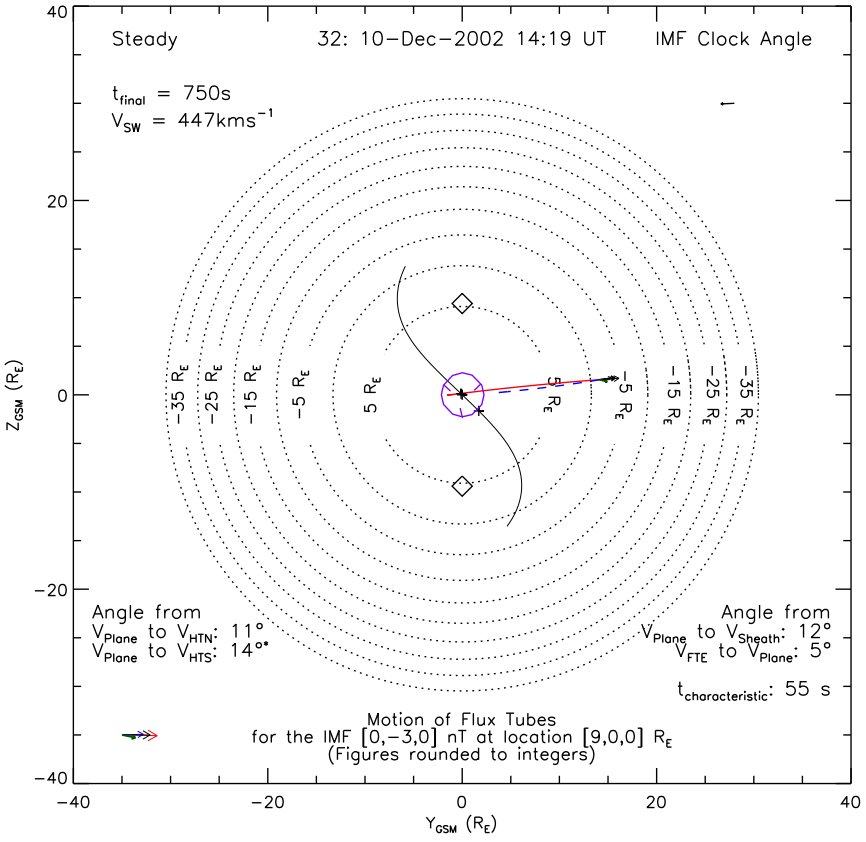
Steady
32: 10−Dec−2002 14:19 UT
IMF Clock Angle
t_{final} = 750s
V_{SW} = 447kms^{-1}
Angle from
V_{Plane} to V_{HTN}: 11°
V_{Plane} to V_{HTS}: 14°
Angle from
V_{Plane} to V_{Sheath}: 12°
V_{FTE} to V_{Plane}: 5°
$t_{characteristic}$: 55 s
Motion of Flux Tubes
for the IMF [0,−3,0] nT at location [9,0,0] R_E
(Figures rounded to integers)
Z_{GSM} (R_E)
Y_{GSM} (R_E)

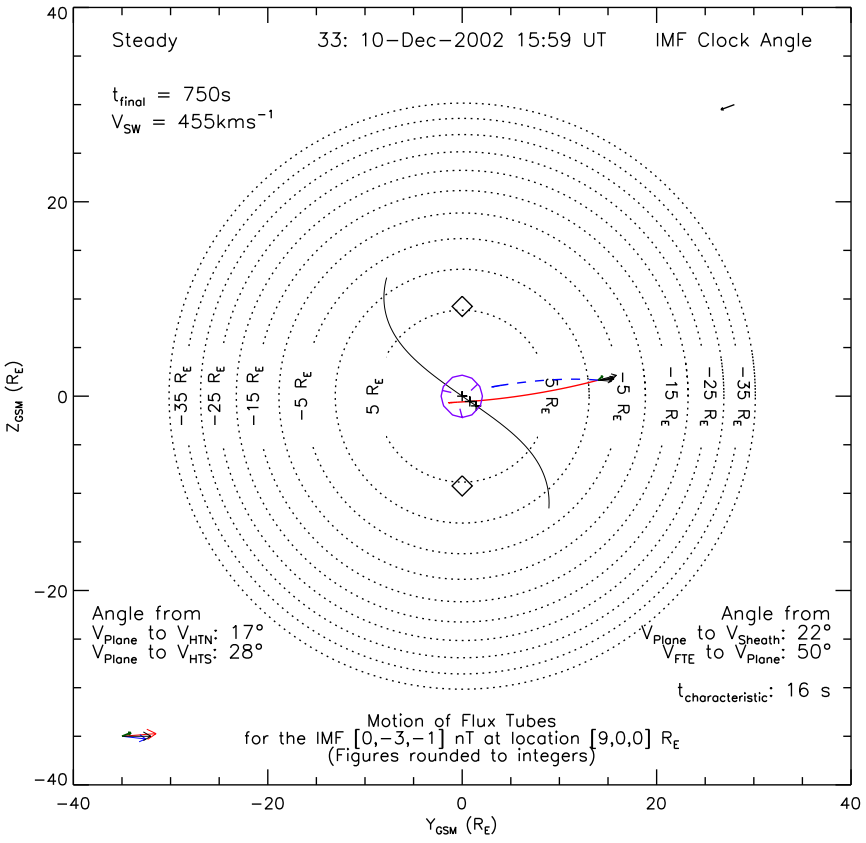
Steady
33: 10−Dec−2002 15:59 UT
IMF Clock Angle
t_{final} = 750s
V_{SW} = 455kms^{-1}
Angle from
V_{Plane} to V_{HTN}: 17°
V_{Plane} to V_{HTS}: 28°
Angle from
V_{Plane} to V_{Sheath}: 22°
V_{FTE} to V_{Plane}: 50°
$t_{characteristic}$: 16 s
Motion of Flux Tubes
for the IMF [0,−3,−1] nT at location [9,0,0] R_E
(Figures rounded to integers)
Z_{GSM} (R_E)
Y_{GSM} (R_E)

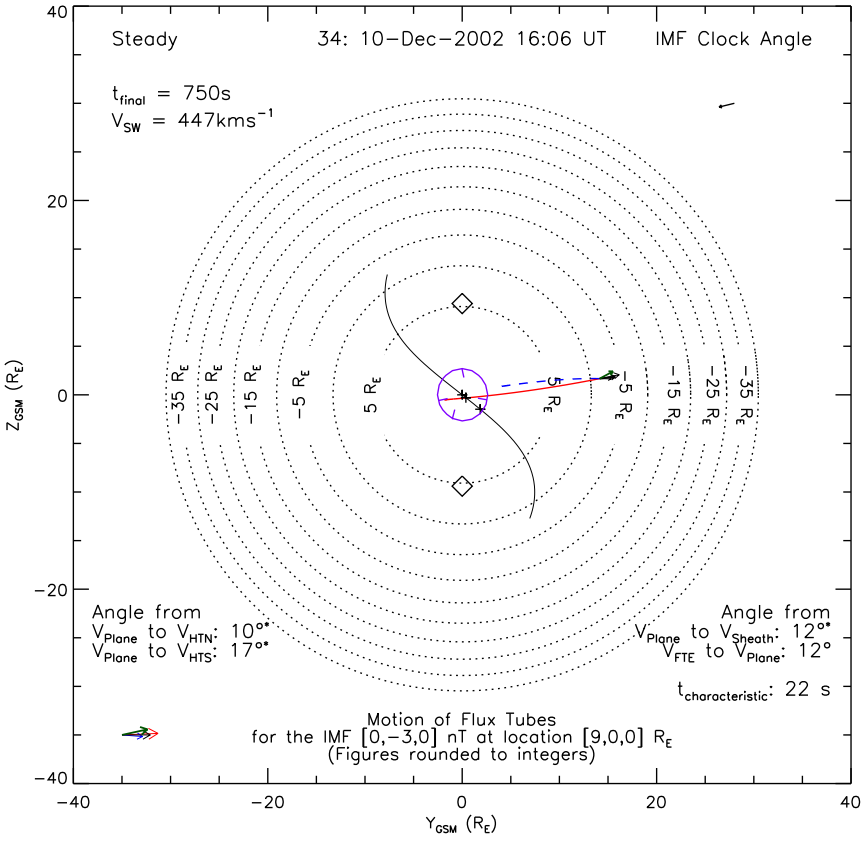
Steady
34: 10−Dec−2002 16:06 UT
IMF Clock Angle
t_{final} = 750s
V_{SW} = 447kms^{-1}
Angle from
V_{Plane} to V_{HTN}: 10°
V_{Plane} to V_{HTS}: 17°
Angle from
V_{Plane} to V_{Sheath}: 12°
V_{FTE} to V_{Plane}: 12°
$t_{characteristic}$: 22 s
Motion of Flux Tubes
for the IMF [0,−3,0] nT at location [9,0,0] R_E
(Figures rounded to integers)
Z_{GSM} (R_E)
Y_{GSM} (R_E)

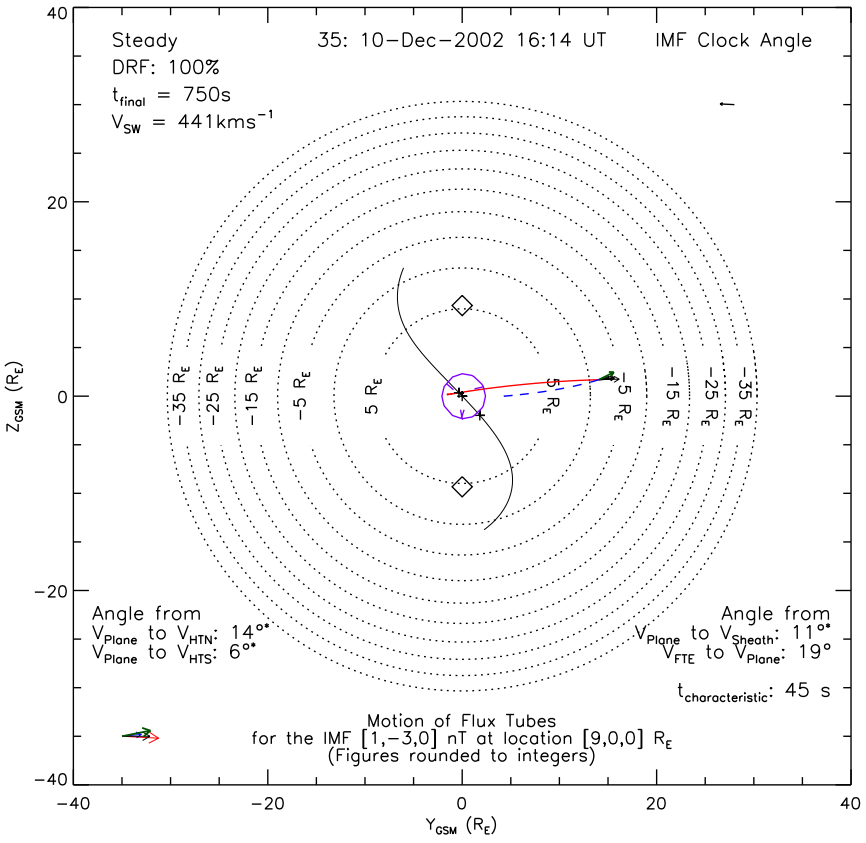
Steady
DRF: 100%
t_{final} = 750s
V_{SW} = 441kms^{-1}
35: 10−Dec−2002 16:14 UT
IMF Clock Angle
Angle from
V_{Plane} to V_{HTN}: 14°
V_{Plane} to V_{HTS}: 6°
Angle from
V_{Plane} to V_{Sheath}: 11°
V_{FTE} to V_{Plane}: 19°
$t_{characteristic}$: 45 s
Motion of Flux Tubes
for the IMF [1,−3,0] nT at location [9,0,0] R_E
(Figures rounded to integers)
Z_{GSM} (R_E)
Y_{GSM} (R_E)

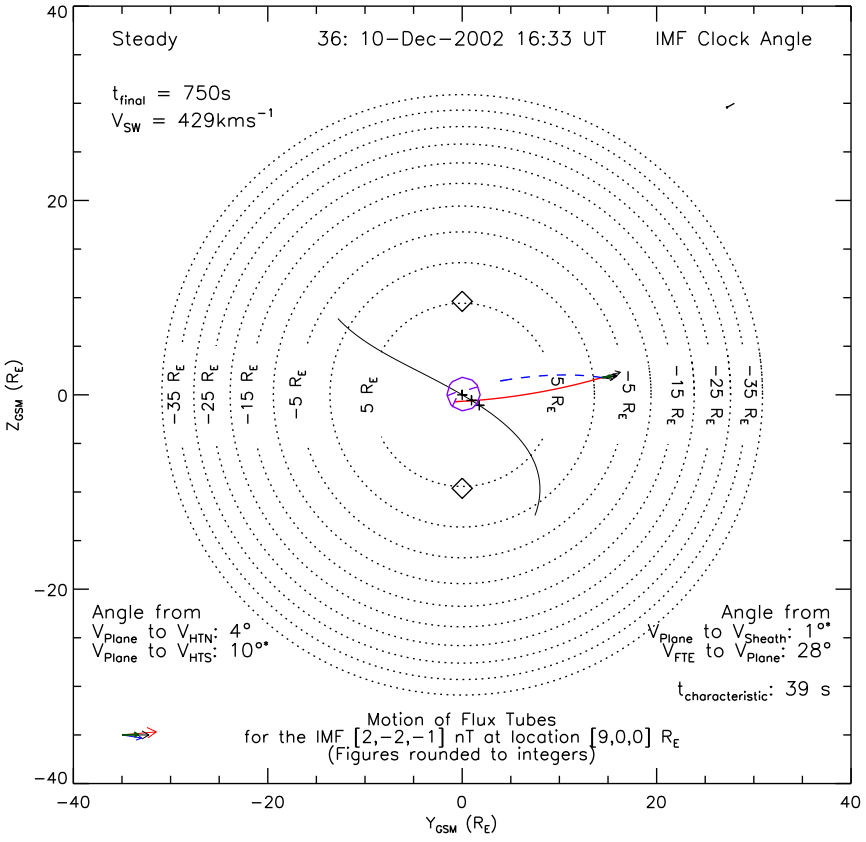
Steady
t_{final} = 750s
V_{SW} = 429kms^{-1}
36: 10−Dec−2002 16:33 UT
IMF Clock Angle
Angle from
V_{Plane} to V_{HTN}: 4°
V_{Plane} to V_{HTS}: 10°
Angle from
V_{Plane} to V_{Sheath}: 1°
V_{FTE} to V_{Plane}: 28°
$t_{characteristic}$: 39 s
Motion of Flux Tubes
for the IMF [2,−2,−1] nT at location [9,0,0] R_E
(Figures rounded to integers)
Z_{GSM} (R_E)
Y_{GSM} (R_E)

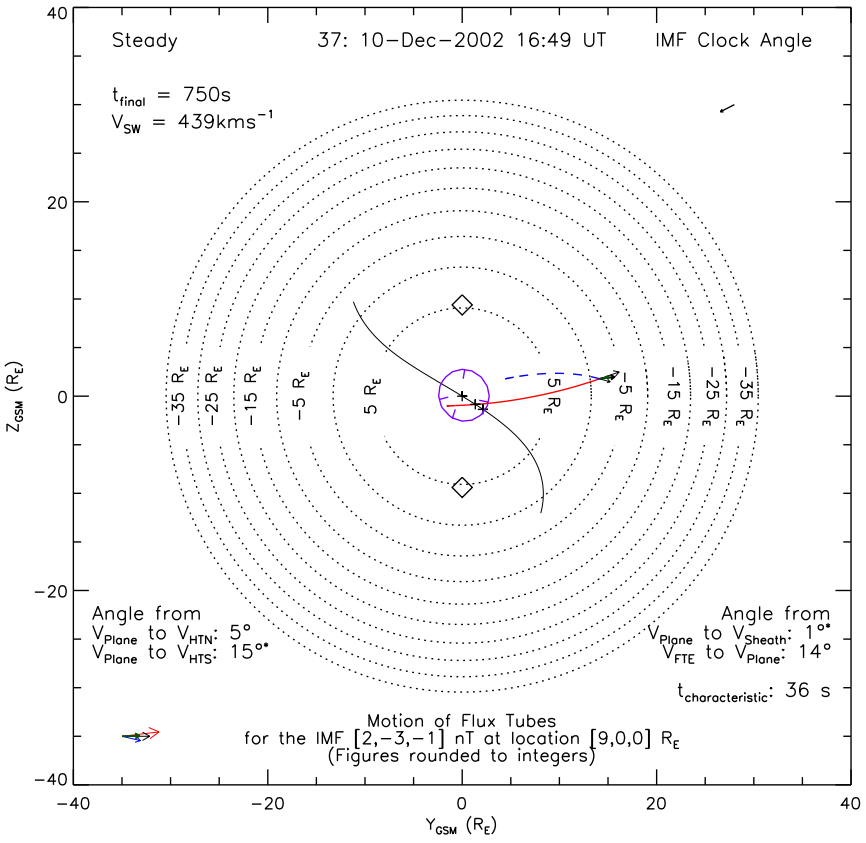
Steady
37: 10−Dec−2002 16:49 UT
IMF Clock Angle
t_{final} = 750s
V_{SW} = 439kms^{-1}
Angle from
V_{Plane} to V_{HTN}: 5°
V_{Plane} to V_{HTS}: 15°
Angle from
V_{Plane} to V_{Sheath}: 1°
V_{FTE} to V_{Plane}: 14°
$t_{characteristic}$: 36 s
Motion of Flux Tubes
for the IMF [2,−3,−1] nT at location [9,0,0] R_E
(Figures rounded to integers)
Z_{GSM} (R_E)
Y_{GSM} (R_E)

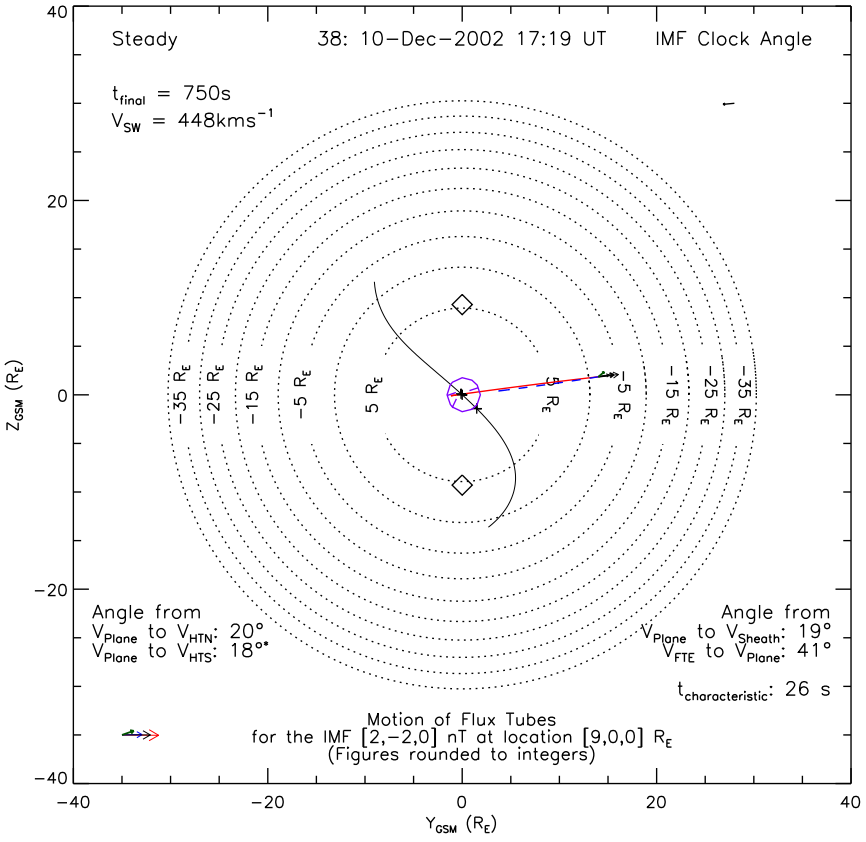
Steady
38: 10−Dec−2002 17:19 UT
IMF Clock Angle
t_{final} = 750s
V_{SW} = 448kms^{-1}
Angle from
V_{Plane} to V_{HTN}: 20°
V_{Plane} to V_{HTS}: 18°
Angle from
V_{Plane} to V_{Sheath}: 19°
V_{FTE} to V_{Plane}: 41°
$t_{characteristic}$: 26 s
Motion of Flux Tubes
for the IMF [2,−2,0] nT at location [9,0,0] R_E
(Figures rounded to integers)
Z_{GSM} (R_E)
Y_{GSM} (R_E)

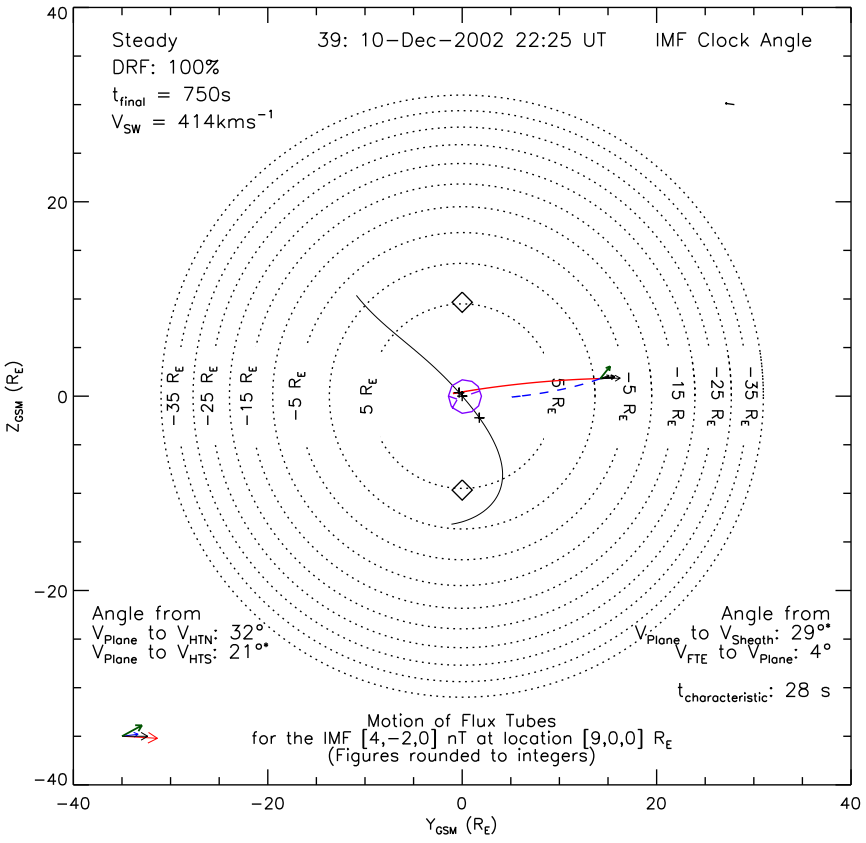
Steady
39: 10−Dec−2002 22:25 UT
IMF Clock Angle
DRF: 100%
t_{final} = 750s
V_{SW} = 414kms^{-1}
Angle from
V_{Plane} to V_{HTN}: 32°
V_{Plane} to V_{HTS}: 21°
Angle from
V_{Plane} to V_{Sheath}: 29°
V_{FTE} to V_{Plane}: 4°
$t_{characteristic}$: 28 s
Motion of Flux Tubes
for the IMF [4,−2,0] nT at location [9,0,0] R_E
(Figures rounded to integers)
Z_{GSM} (R_E)
Y_{GSM} (R_E)

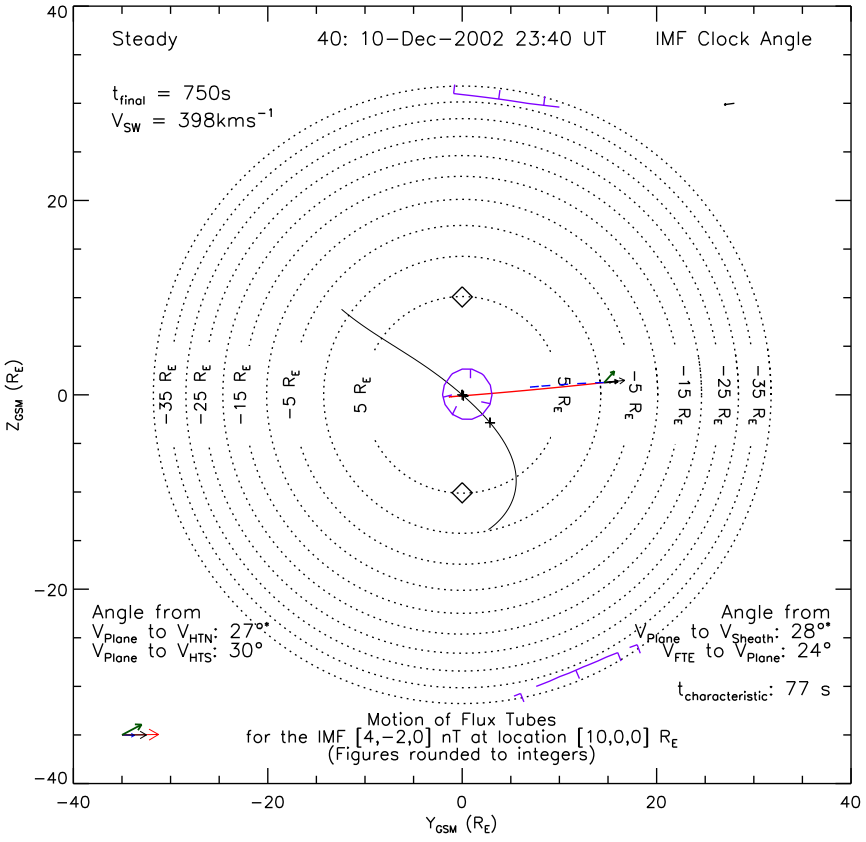
Steady
40: 10−Dec−2002 23:40 UT
IMF Clock Angle
t_{final} = 750s
V_{SW} = 398kms^{-1}
Angle from
V_{Plane} to V_{HTN}: 27°
V_{Plane} to V_{HTS}: 30°
Angle from
V_{Plane} to V_{Sheath}: 28°
V_{FTE} to V_{Plane}: 24°
$t_{characteristic}$: 77 s
Motion of Flux Tubes
for the IMF [4,−2,0] nT at location [10,0,0] R_E
(Figures rounded to integers)
Z_{GSM} (R_E)
Y_{GSM} (R_E)

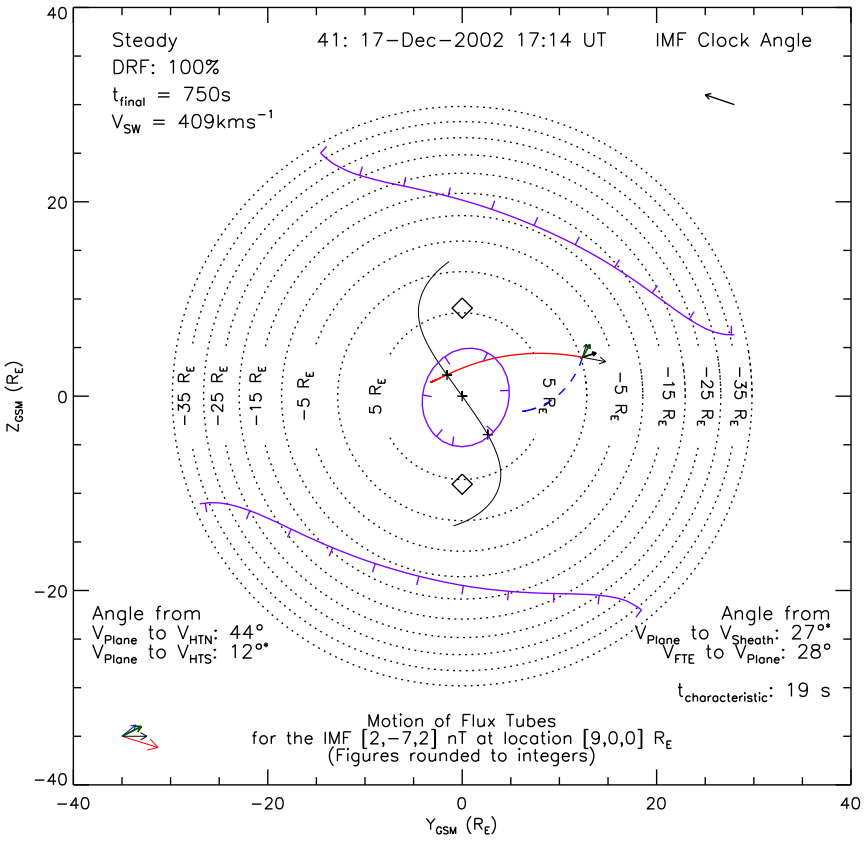
Steady
41: 17−Dec−2002 17:14 UT
IMF Clock Angle
DRF: 100%
t_{final} = 750s
V_{SW} = 409kms^{-1}
Angle from
V_{Plane} to V_{HTN}: 44°
V_{Plane} to V_{HTS}: 12°
Angle from
V_{Plane} to V_{Sheath}: 27°
V_{FTE} to V_{Plane}: 28°
$t_{characteristic}$: 19 s
Motion of Flux Tubes
for the IMF [2,−7,2] nT at location [9,0,0] R_E
(Figures rounded to integers)
Z_{GSM} (R_E)
Y_{GSM} (R_E)

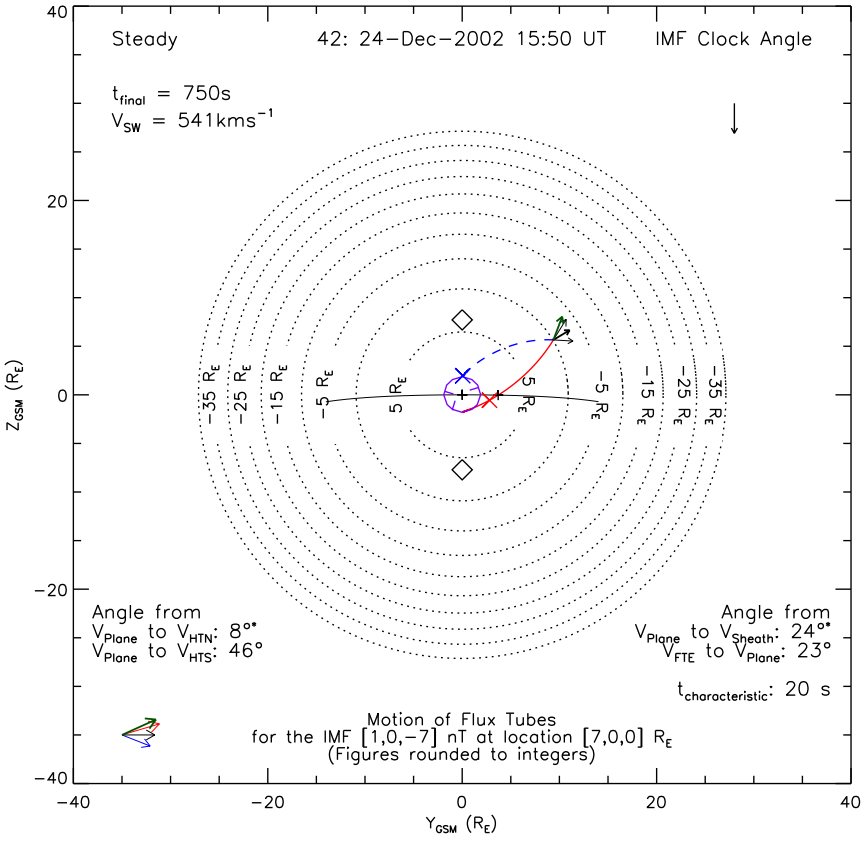
Steady
42: 24−Dec−2002 15:50 UT
IMF Clock Angle
t_{final} = 750s
V_{SW} = 541kms^{-1}
Angle from
V_{Plane} to V_{HTN}: 8°
V_{Plane} to V_{HTS}: 46°
Angle from
V_{Plane} to V_{Sheath}: 24°
V_{FTE} to V_{Plane}: 23°
$t_{characteristic}$: 20 s
Motion of Flux Tubes
for the IMF [1,0,−7] nT at location [7,0,0] R_E
(Figures rounded to integers)
Z_{GSM} (R_E)
Y_{GSM} (R_E)

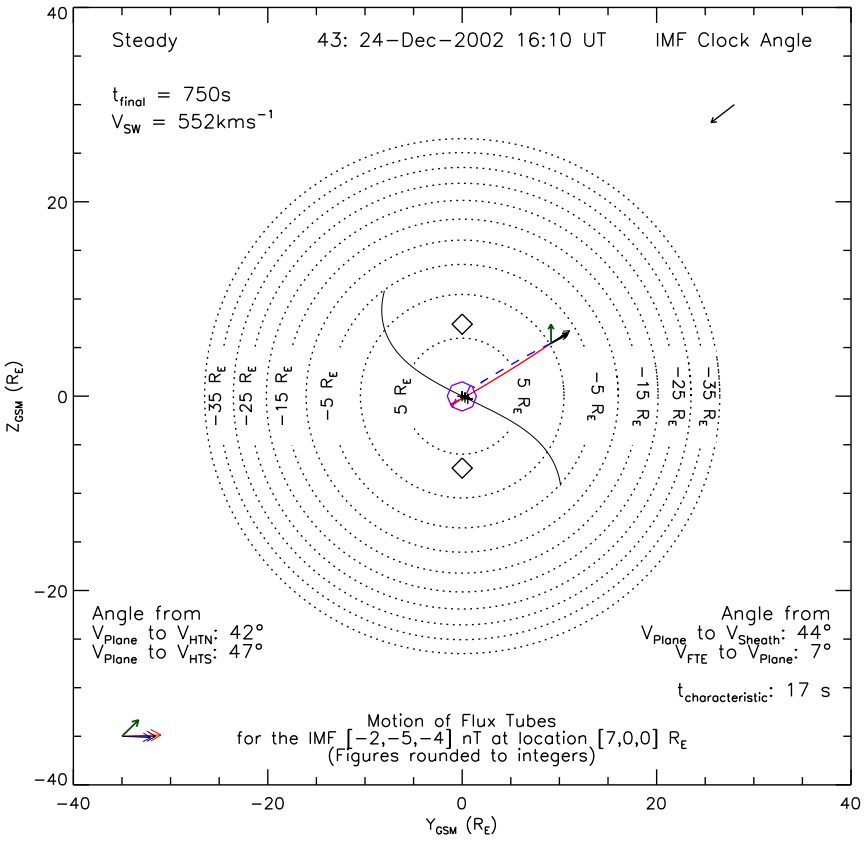
Steady
43: 24−Dec−2002 16:10 UT
IMF Clock Angle
t_{final} = 750s
V_{SW} = 552kms^{-1}
Angle from
V_{Plane} to V_{HTN}: 42°
V_{Plane} to V_{HTS}: 47°
Angle from
V_{Plane} to V_{Sheath}: 44°
V_{FTE} to V_{Plane}: 7°
$t_{characteristic}$: 17 s
Motion of Flux Tubes
for the IMF [−2,−5,−4] nT at location [7,0,0] R_E
(Figures rounded to integers)
Z_{GSM} (R_E)
Y_{GSM} (R_E)

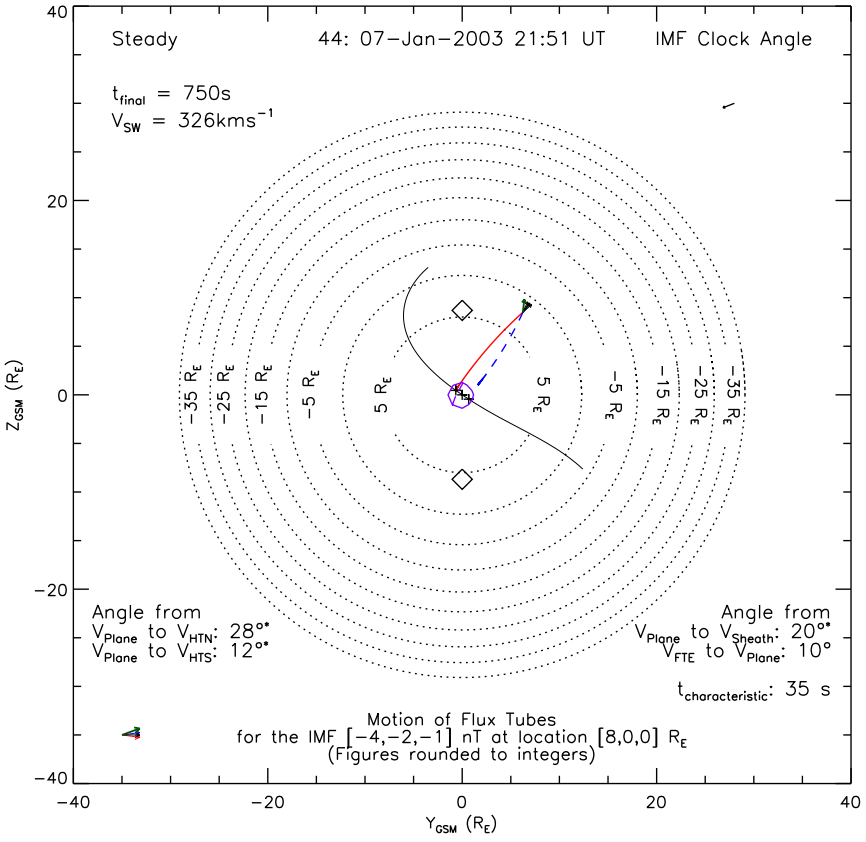
Steady
44: 07−Jan−2003 21:51 UT
IMF Clock Angle
t_{final} = 750s
V_{SW} = 326kms^{-1}
Angle from
V_{Plane} to V_{HTN}: 28°
V_{Plane} to V_{HTS}: 12°
Angle from
V_{Plane} to V_{Sheath}: 20°
V_{FTE} to V_{Plane}: 10°
$t_{characteristic}$: 35 s
Motion of Flux Tubes
for the IMF [−4,−2,−1] nT at location [8,0,0] R_E
(Figures rounded to integers)
Z_{GSM} (R_E)
Y_{GSM} (R_E)

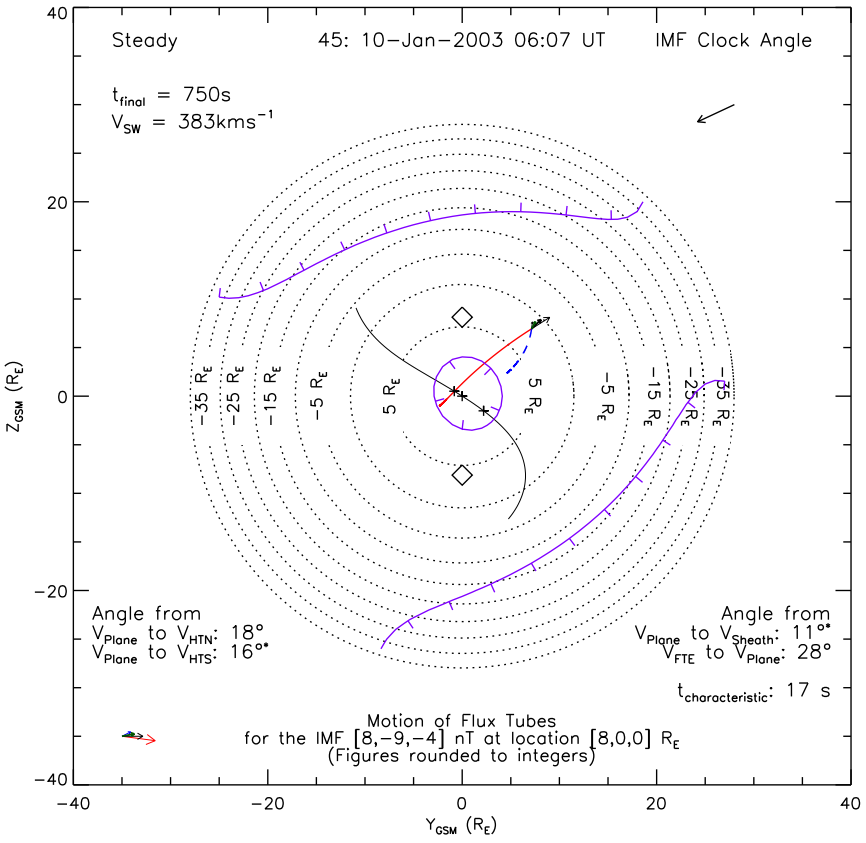
Steady
45: 10−Jan−2003 06:07 UT
IMF Clock Angle
t_{final} = 750s
V_{SW} = 383kms^{-1}
Angle from
V_{Plane} to V_{HTN}: 18°
V_{Plane} to V_{HTS}: 16°
Angle from
V_{Plane} to V_{Sheath}: 11°
V_{FTE} to V_{Plane}: 28°
$t_{characteristic}$: 17 s
Motion of Flux Tubes
for the IMF [8,−9,−4] nT at location [8,0,0] R_E
(Figures rounded to integers)
Z_{GSM} (R_E)
Y_{GSM} (R_E)

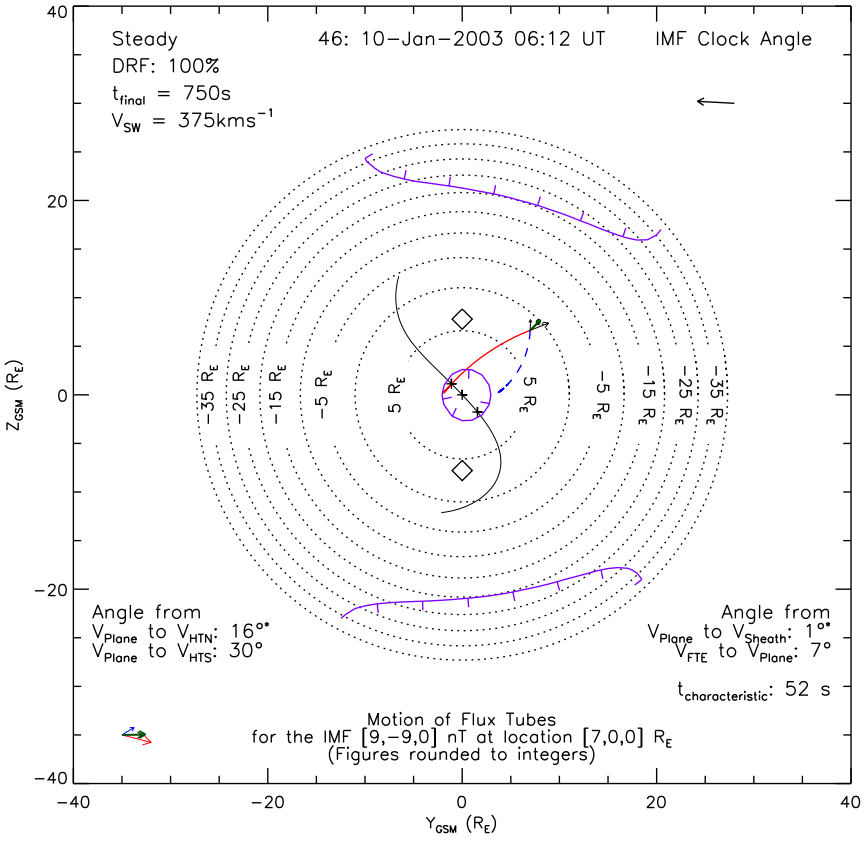
Steady
46: 10−Jan−2003 06:12 UT
IMF Clock Angle
DRF: 100%
t_{final} = 750s
V_{SW} = 375kms^{-1}
Angle from
V_{Plane} to V_{HTN}: 16°
V_{Plane} to V_{HTS}: 30°
Angle from
V_{Plane} to V_{Sheath}: 1°
V_{FTE} to V_{Plane}: 7°
$t_{characteristic}$: 52 s
Motion of Flux Tubes
for the IMF [9,−9,0] nT at location [7,0,0] R_E
(Figures rounded to integers)
Z_{GSM} (R_E)
Y_{GSM} (R_E)

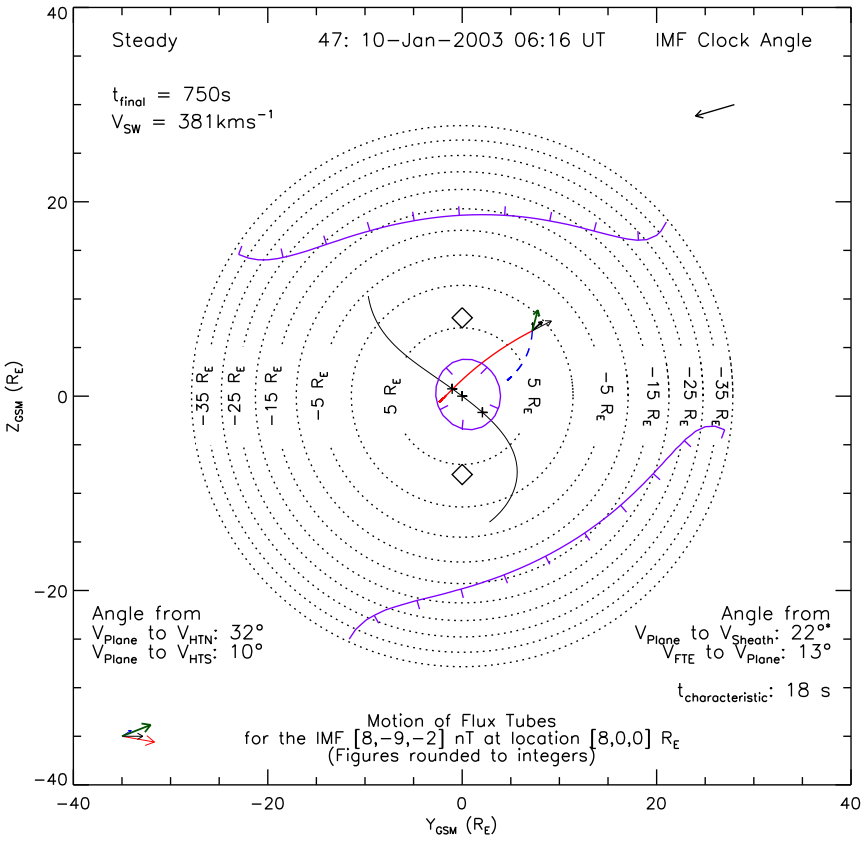
Steady
47: 10−Jan−2003 06:16 UT
IMF Clock Angle
t_{final} = 750s
V_{SW} = 381kms^{-1}
Angle from
V_{Plane} to V_{HTN}: 32°
V_{Plane} to V_{HTS}: 10°
Angle from
V_{Plane} to V_{Sheath}: 22°
V_{FTE} to V_{Plane}: 13°
$t_{characteristic}$: 18 s
Motion of Flux Tubes
for the IMF [8,−9,−2] nT at location [8,0,0] R_E
(Figures rounded to integers)
Z_{GSM} (R_E)
Y_{GSM} (R_E)

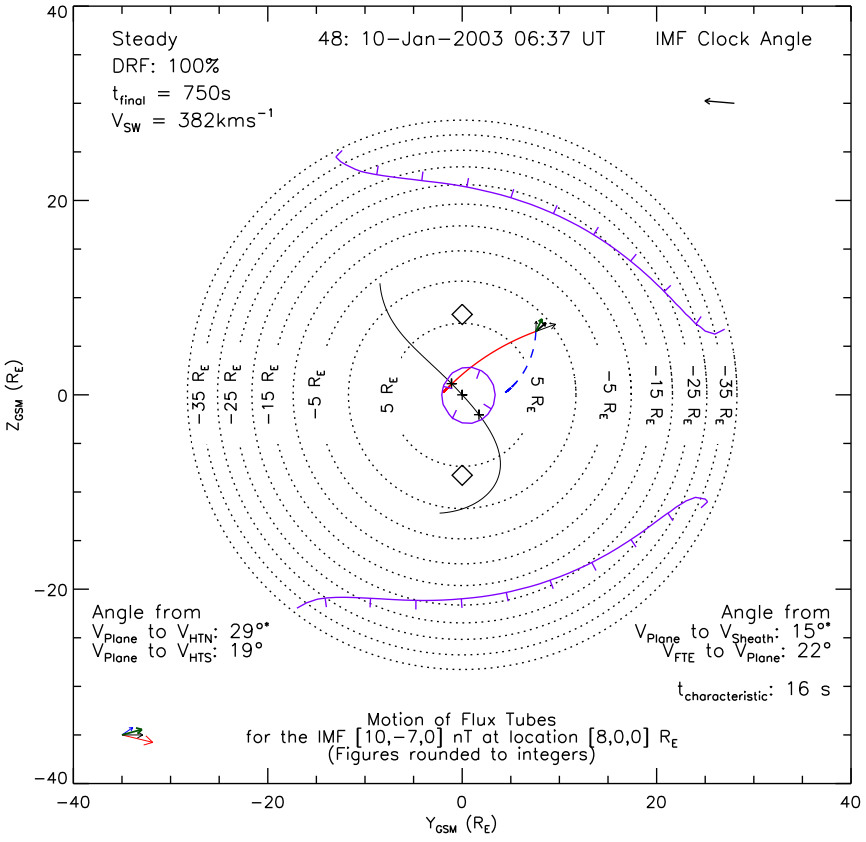
Steady
48: 10−Jan−2003 06:37 UT
IMF Clock Angle
DRF: 100%
t_{final} = 750s
V_{SW} = 382kms^{-1}
Angle from
V_{Plane} to V_{HTN}: 29°
V_{Plane} to V_{HTS}: 19°
Angle from
V_{Plane} to V_{Sheath}: 15°
V_{FTE} to V_{Plane}: 22°
$t_{characteristic}$: 16 s
Motion of Flux Tubes
for the IMF [10,−7,0] nT at location [8,0,0] R_E
(Figures rounded to integers)
Z_{GSM} (R_E)
Y_{GSM} (R_E)

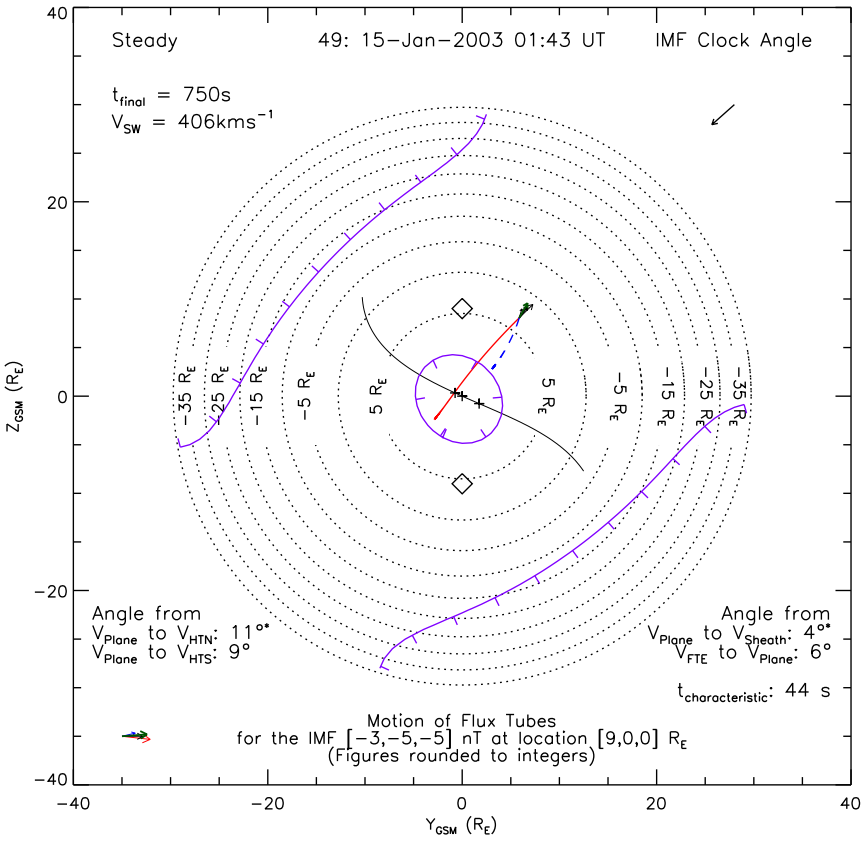
Steady
49: 15–Jan–2003 01:43 UT
IMF Clock Angle
t_{final} = 750s
V_{SW} = 406kms^{-1}
Angle from
V_{Plane} to V_{HTN}: 11°
V_{Plane} to V_{HTS}: 9°
Angle from
V_{Plane} to V_{Sheath}: 4°
V_{FTE} to V_{Plane}: 6°
$t_{characteristic}$: 44 s
Motion of Flux Tubes
for the IMF [−3,−5,−5] nT at location [9,0,0] R_E
(Figures rounded to integers)
Z_{GSM} (R_E)
Y_{GSM} (R_E)

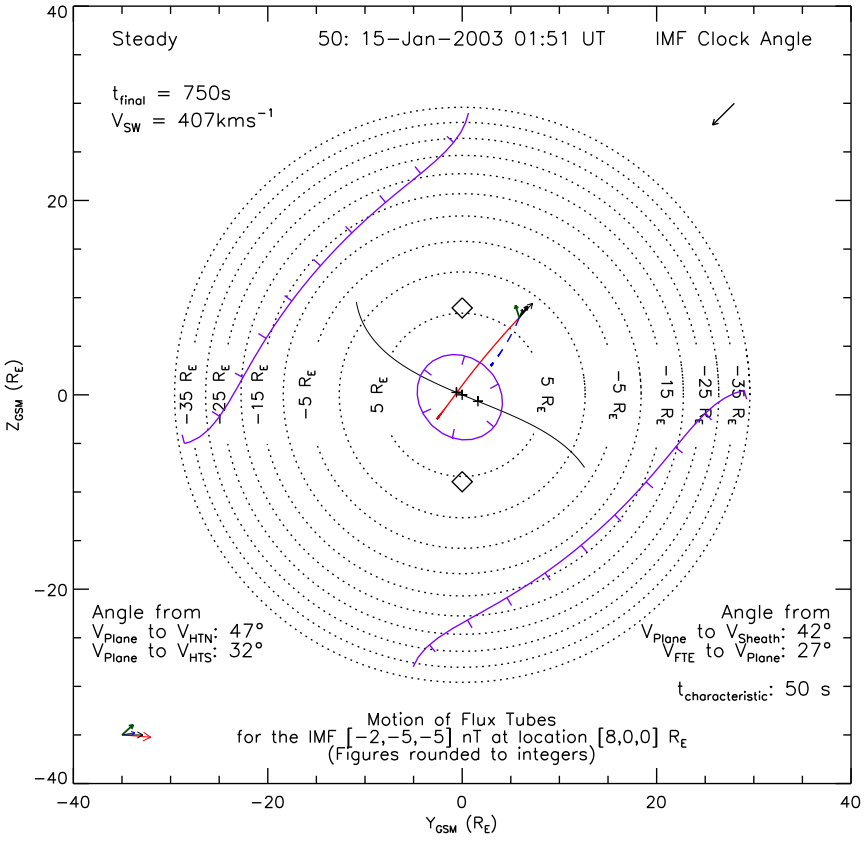
Steady
50: 15–Jan–2003 01:51 UT
IMF Clock Angle
t_{final} = 750s
V_{SW} = 407kms^{-1}
Angle from
V_{Plane} to V_{HTN}: 47°
V_{Plane} to V_{HTS}: 32°
Angle from
V_{Plane} to V_{Sheath}: 42°
V_{FTE} to V_{Plane}: 27°
$t_{characteristic}$: 50 s
Motion of Flux Tubes
for the IMF [−2,−5,−5] nT at location [8,0,0] R_E
(Figures rounded to integers)
Z_{GSM} (R_E)
Y_{GSM} (R_E)

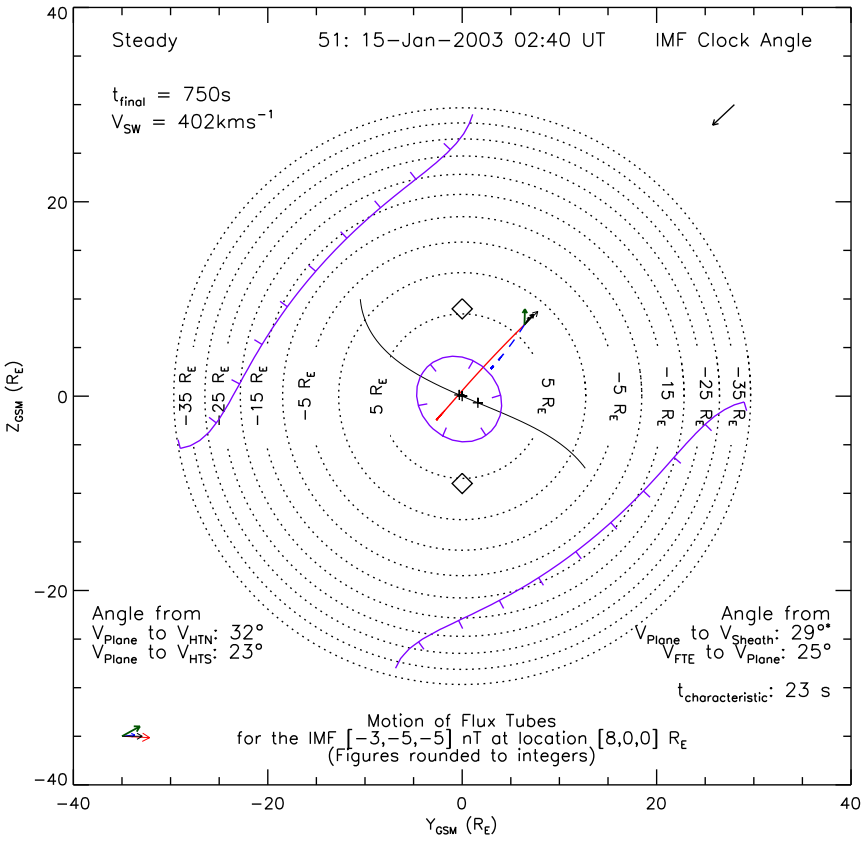
Steady
51: 15–Jan–2003 02:40 UT
IMF Clock Angle
t_{final} = 750s
V_{SW} = 402kms^{-1}
Angle from
V_{Plane} to V_{HTN}: 32°
V_{Plane} to V_{HTS}: 23°
Angle from
V_{Plane} to V_{Sheath}: 29°
V_{FTE} to V_{Plane}: 25°
$t_{characteristic}$: 23 s
Motion of Flux Tubes
for the IMF [−3,−5,−5] nT at location [8,0,0] R_E
(Figures rounded to integers)
Z_{GSM} (R_E)
Y_{GSM} (R_E)

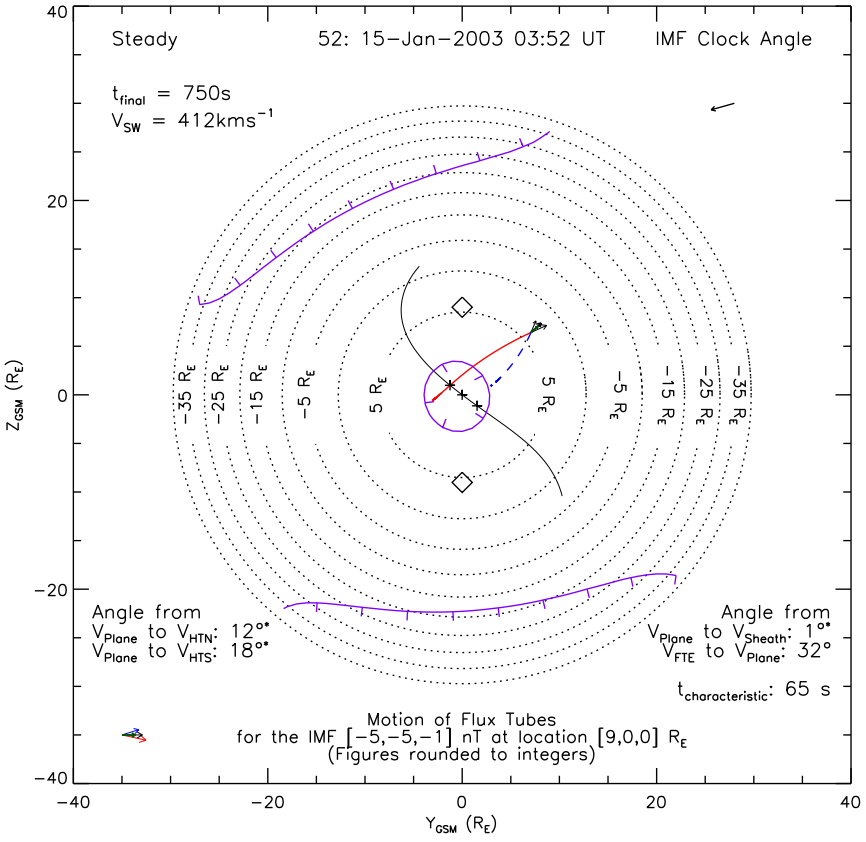
Steady
52: 15–Jan–2003 03:52 UT
IMF Clock Angle
t_{final} = 750s
V_{SW} = 412kms^{-1}
Angle from
V_{Plane} to V_{HTN}: 12°
V_{Plane} to V_{HTS}: 18°
Angle from
V_{Plane} to V_{Sheath}: 1°
V_{FTE} to V_{Plane}: 32°
$t_{characteristic}$: 65 s
Motion of Flux Tubes
for the IMF [−5,−5,−1] nT at location [9,0,0] R_E
(Figures rounded to integers)
Z_{GSM} (R_E)
Y_{GSM} (R_E)

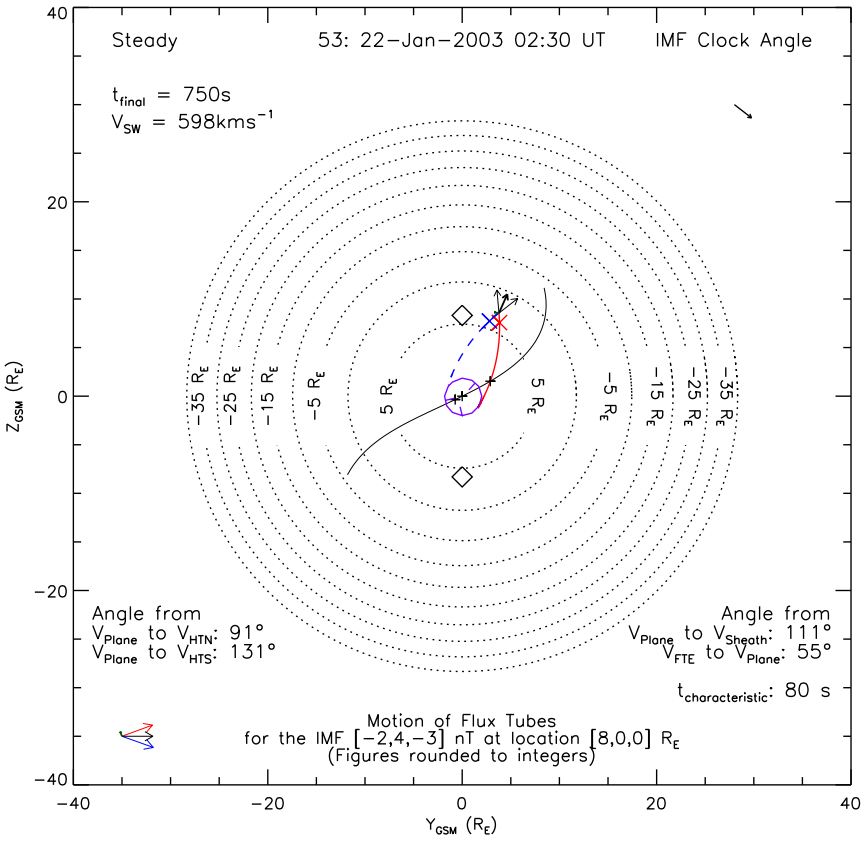
Steady
53: 22–Jan–2003 02:30 UT
IMF Clock Angle
t_{final} = 750s
V_{SW} = 598kms^{-1}
Angle from
V_{Plane} to V_{HTN}: 91°
V_{Plane} to V_{HTS}: 131°
Angle from
V_{Plane} to V_{Sheath}: 111°
V_{FTE} to V_{Plane}: 55°
$t_{characteristic}$: 80 s
Motion of Flux Tubes
for the IMF [−2,4,−3] nT at location [8,0,0] R_E
(Figures rounded to integers)
Z_{GSM} (R_E)
Y_{GSM} (R_E)

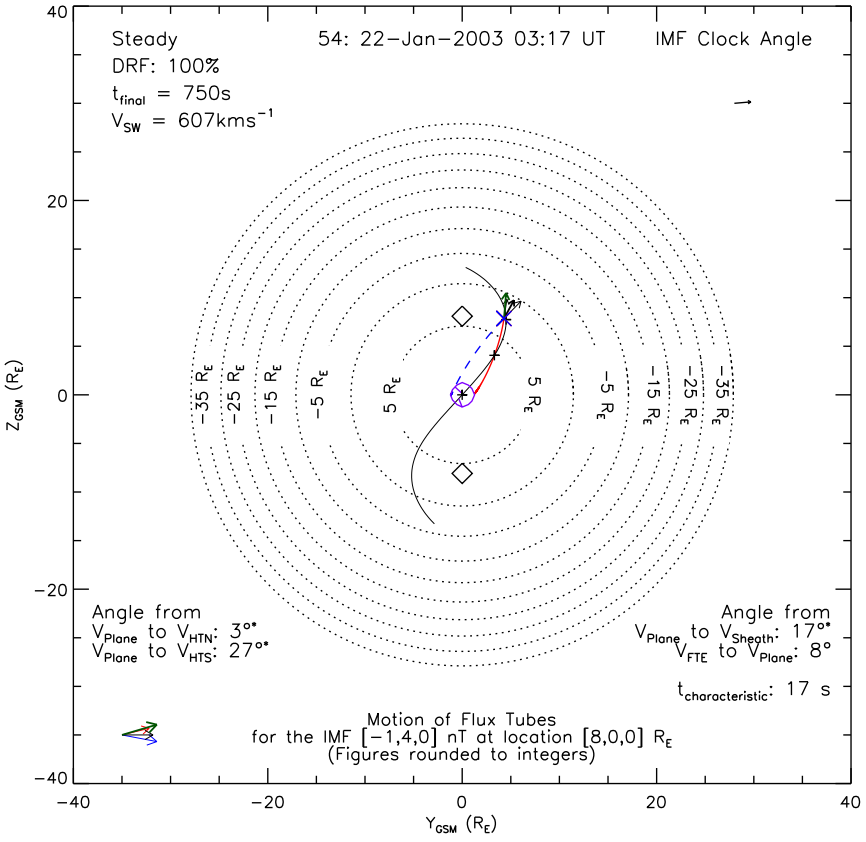
Steady
54: 22–Jan–2003 03:17 UT
IMF Clock Angle
DRF: 100%
t_{final} = 750s
V_{SW} = 607kms^{-1}
Angle from
V_{Plane} to V_{HTN}: 3°
V_{Plane} to V_{HTS}: 27°
Angle from
V_{Plane} to V_{Sheath}: 17°
V_{FTE} to V_{Plane}: 8°
$t_{characteristic}$: 17 s
Motion of Flux Tubes
for the IMF [−1,4,0] nT at location [8,0,0] R_E
(Figures rounded to integers)
Z_{GSM} (R_E)
Y_{GSM} (R_E)

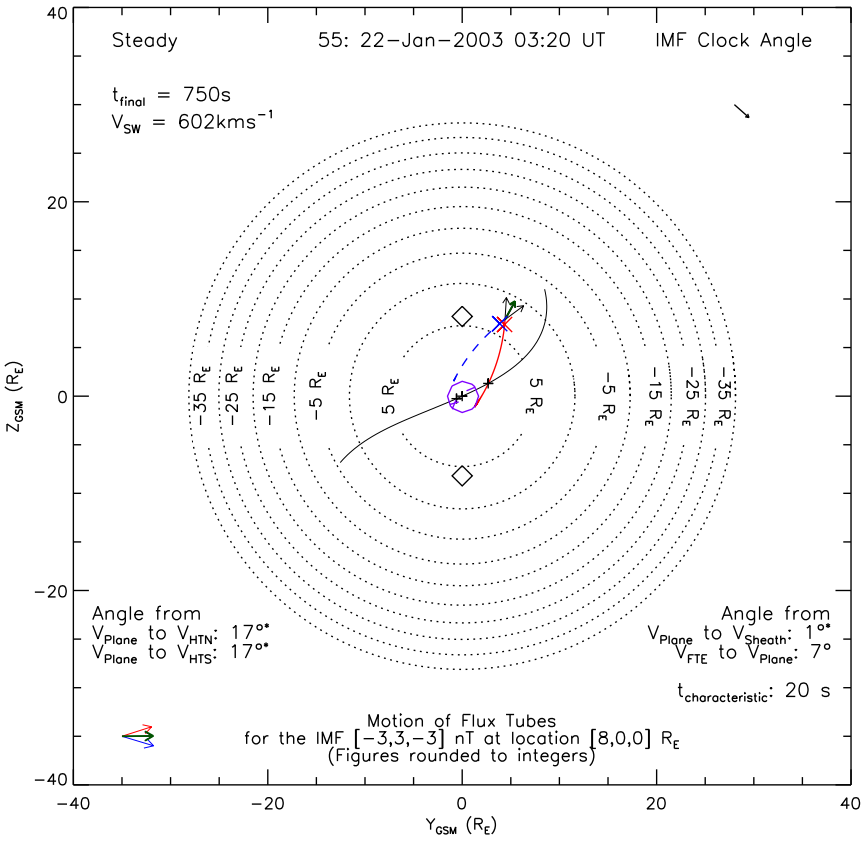
Steady
55: 22–Jan–2003 03:20 UT
IMF Clock Angle
t_{final} = 750s
V_{SW} = 602kms^{-1}
Angle from
V_{Plane} to V_{HTN}: 17°
V_{Plane} to V_{HTS}: 17°
Angle from
V_{Plane} to V_{Sheath}: 1°
V_{FTE} to V_{Plane}: 7°
$t_{characteristic}$: 20 s
Motion of Flux Tubes
for the IMF [−3,3,−3] nT at location [8,0,0] R_E
(Figures rounded to integers)
Z_{GSM} (R_E)
Y_{GSM} (R_E)

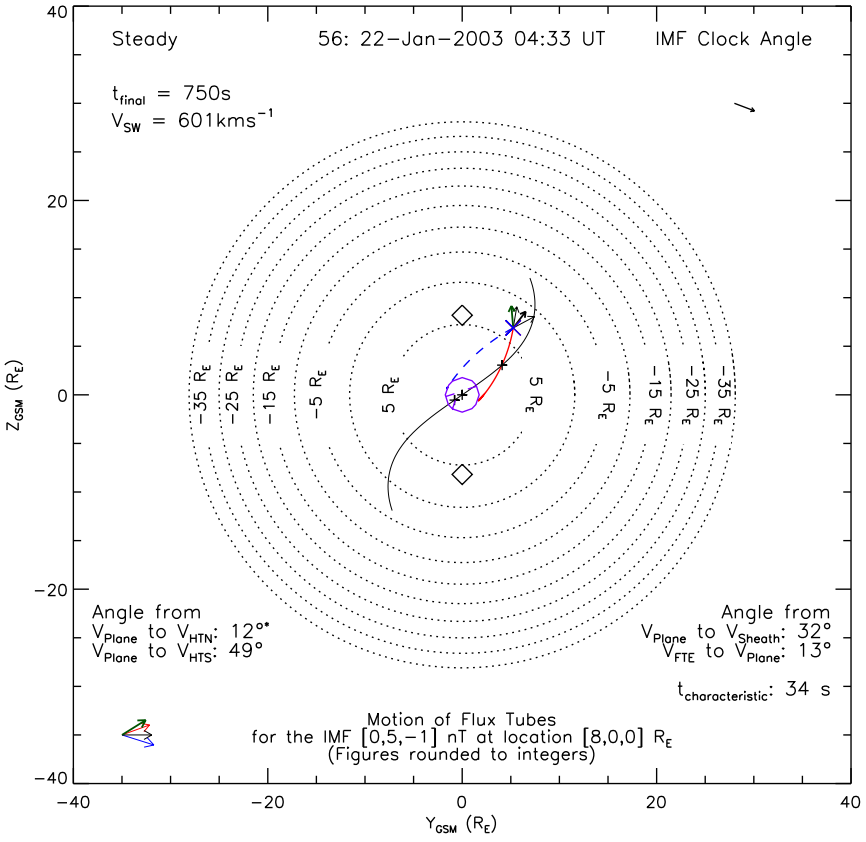
Steady
56: 22–Jan–2003 04:33 UT
IMF Clock Angle
t_{final} = 750s
V_{SW} = 601kms^{-1}
Angle from
V_{Plane} to V_{HTN}: 12°
V_{Plane} to V_{HTS}: 49°
Angle from
V_{Plane} to V_{Sheath}: 32°
V_{FTE} to V_{Plane}: 13°
$t_{characteristic}$: 34 s
Motion of Flux Tubes
for the IMF [0,5,−1] nT at location [8,0,0] R_E
(Figures rounded to integers)
Z_{GSM} (R_E)
Y_{GSM} (R_E)

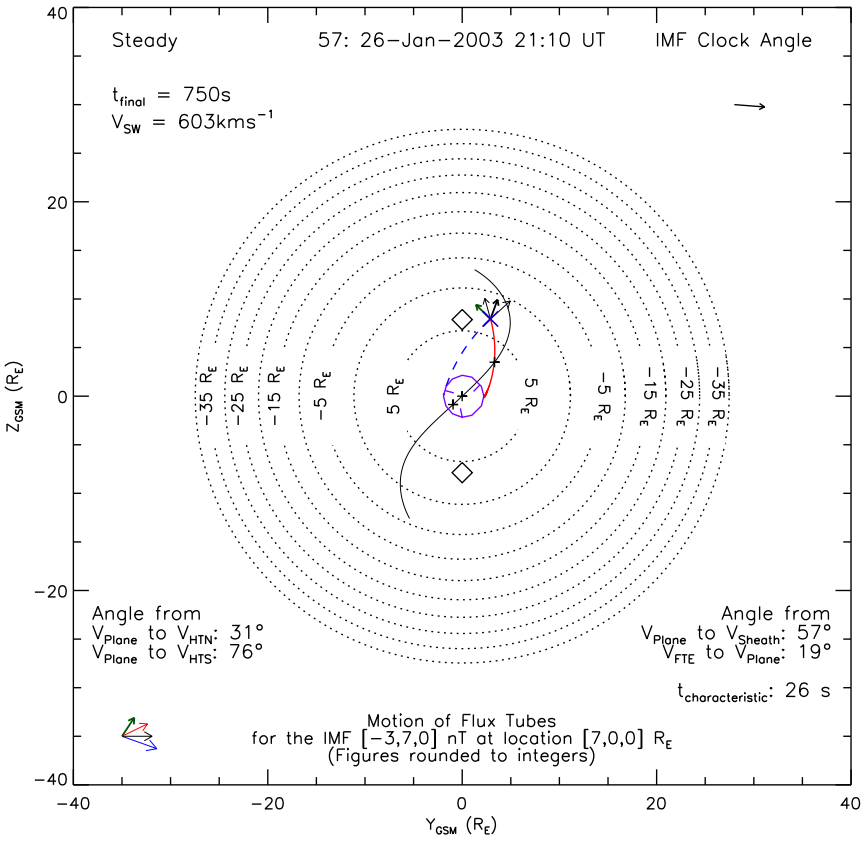
Steady
57: 26−Jan−2003 21:10 UT
IMF Clock Angle
t_{final} = 750s
V_{SW} = 603kms^{-1}
Angle from
V_{Plane} to V_{HTN}: 31°
V_{Plane} to V_{HTS}: 76°
Angle from
V_{Plane} to V_{Sheath}: 57°
V_{FTE} to V_{Plane}: 19°
$t_{characteristic}$: 26 s
Motion of Flux Tubes
for the IMF [−3,7,0] nT at location [7,0,0] R_E
(Figures rounded to integers)
Z_{GSM} (R_E)
Y_{GSM} (R_E)

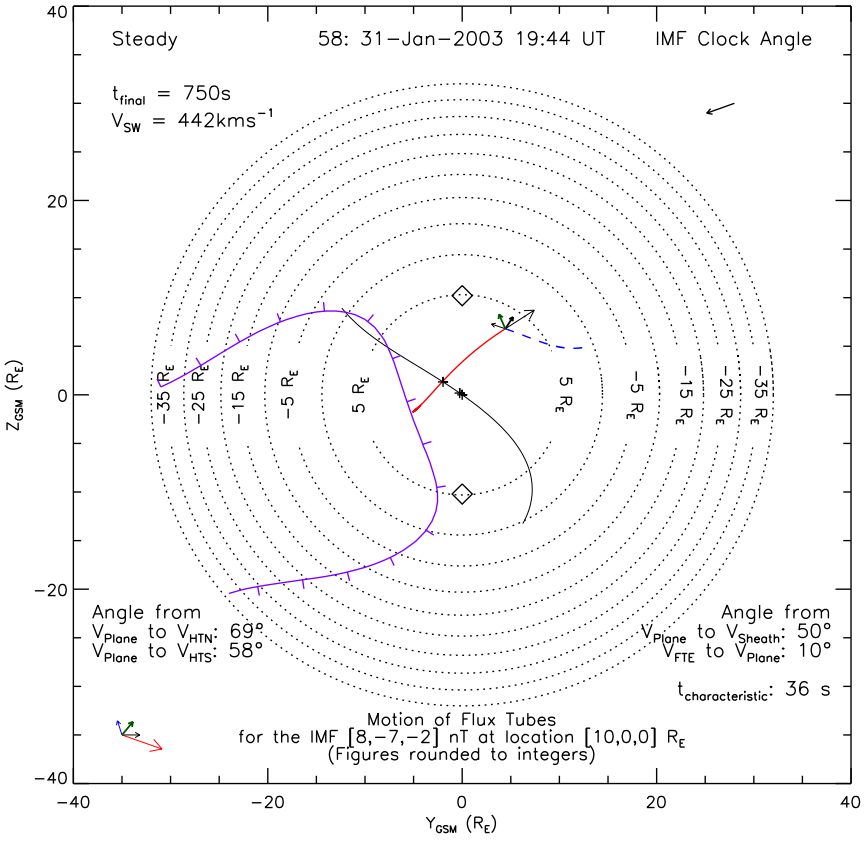
Steady
58: 31−Jan−2003 19:44 UT
IMF Clock Angle
t_{final} = 750s
V_{SW} = 442kms^{-1}
Angle from
V_{Plane} to V_{HTN}: 69°
V_{Plane} to V_{HTS}: 58°
Angle from
V_{Plane} to V_{Sheath}: 50°
V_{FTE} to V_{Plane}: 10°
$t_{characteristic}$: 36 s
Motion of Flux Tubes
for the IMF [8,−7,−2] nT at location [10,0,0] R_E
(Figures rounded to integers)
Z_{GSM} (R_E)
Y_{GSM} (R_E)

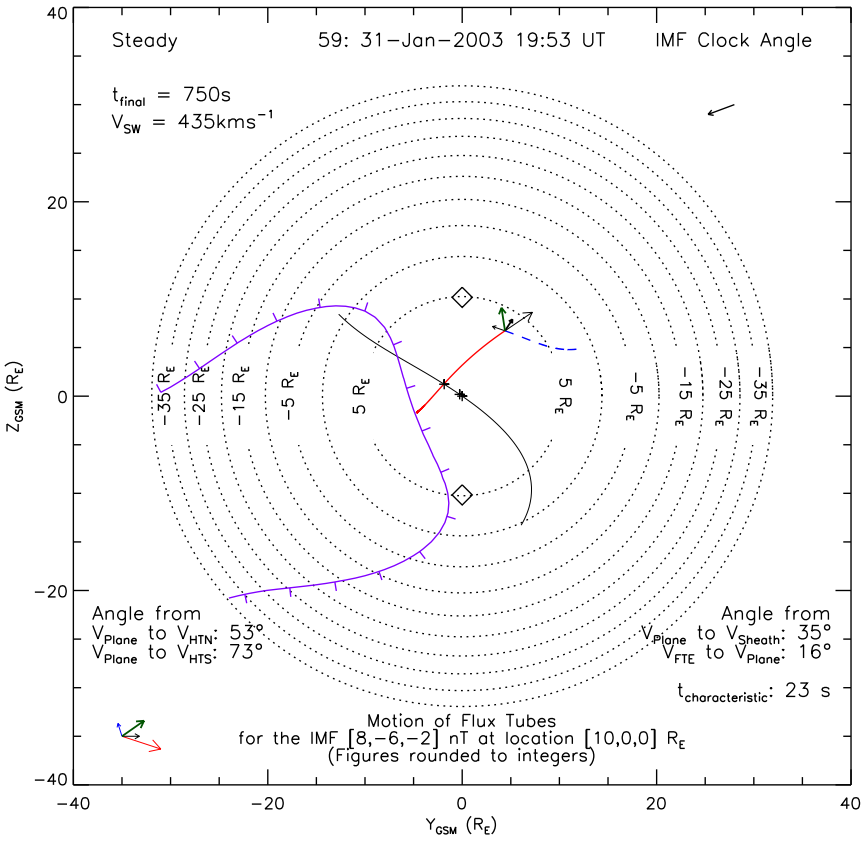
Steady
59: 31−Jan−2003 19:53 UT
IMF Clock Angle
t_{final} = 750s
V_{SW} = 435kms^{-1}
−35 R_E
−25 R_E
−15 R_E
−5 R_E
5 R_E
Angle from
V_{Plane} to V_{HTN}: 53°
V_{Plane} to V_{HTS}: 73°
Angle from
V_{Plane} to V_{Sheath}: 35°
V_{FTE} to V_{Plane}: 16°
$t_{characteristic}$: 23 s
Motion of Flux Tubes
for the IMF [8,−6,−2] nT at location [10,0,0] R_E
(Figures rounded to integers)
Z_{GSM} (R_E)
Y_{GSM} (R_E)

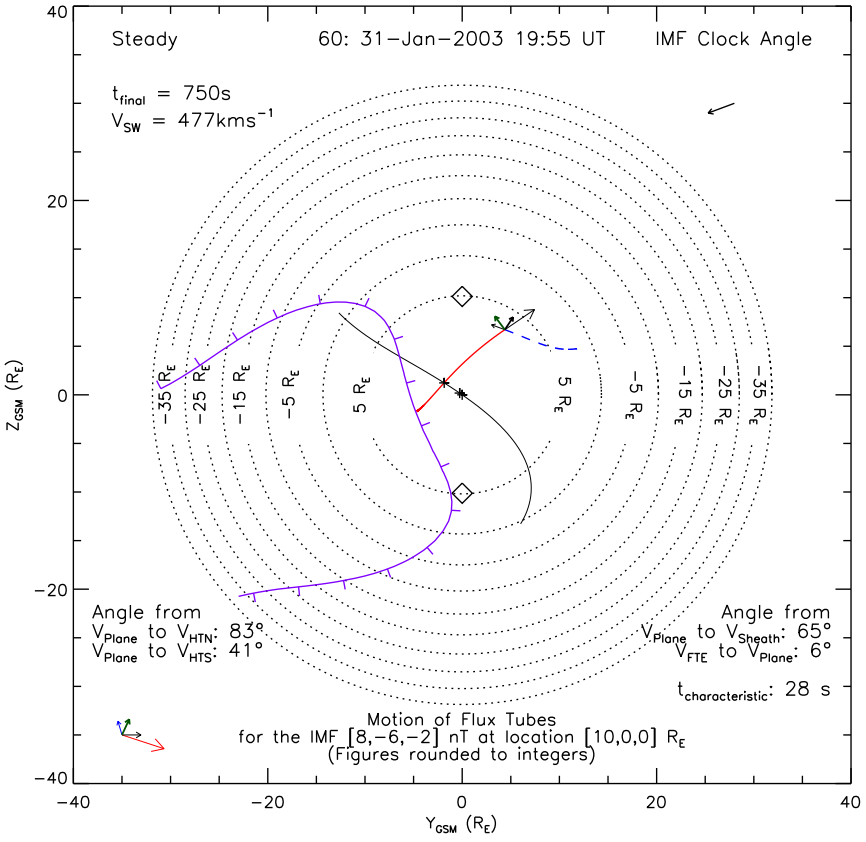
Steady
60: 31−Jan−2003 19:55 UT
IMF Clock Angle
t_{final} = 750s
V_{SW} = 477kms^{-1}
−35 R_E
−25 R_E
−15 R_E
−5 R_E
5 R_E
Angle from
V_{Plane} to V_{HTN}: 83°
V_{Plane} to V_{HTS}: 41°
Angle from
V_{Plane} to V_{Sheath}: 65°
V_{FTE} to V_{Plane}: 6°
$t_{characteristic}$: 28 s
Motion of Flux Tubes
for the IMF [8,−6,−2] nT at location [10,0,0] R_E
(Figures rounded to integers)
Z_{GSM} (R_E)
Y_{GSM} (R_E)

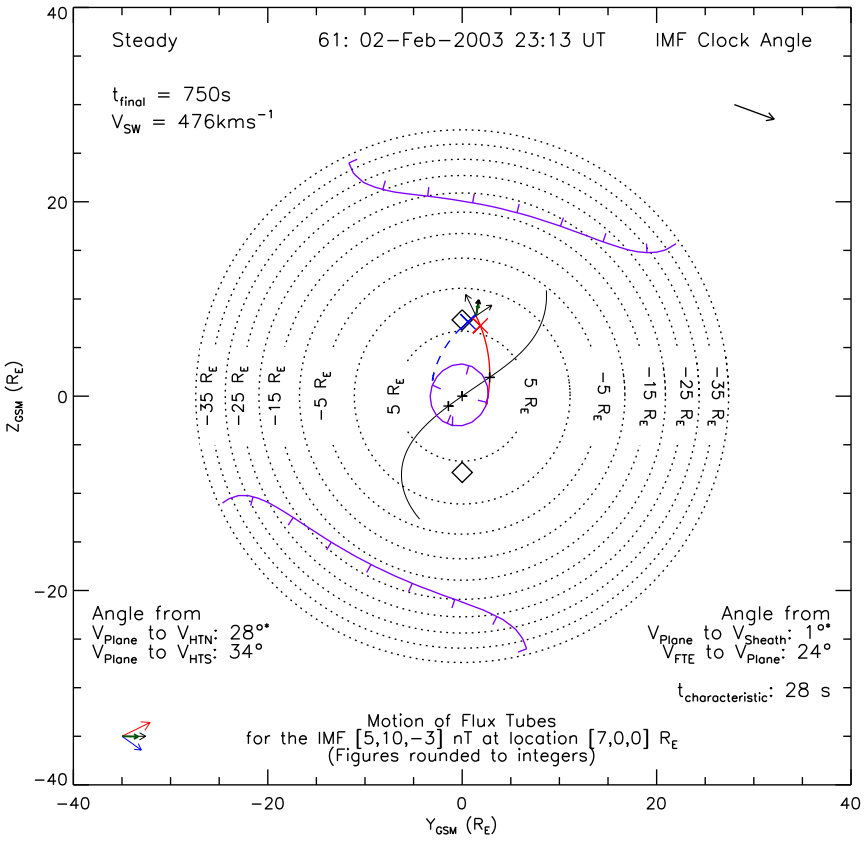
Steady
61: 02−Feb−2003 23:13 UT
IMF Clock Angle
t_{final} = 750s
V_{SW} = 476kms^{-1}
Angle from
V_{Plane} to V_{HTN}: 28°
V_{Plane} to V_{HTS}: 34°
Angle from
V_{Plane} to V_{Sheath}: 1°
V_{FTE} to V_{Plane}: 24°
$t_{characteristic}$: 28 s
Motion of Flux Tubes
for the IMF [5,10,−3] nT at location [7,0,0] R_E
(Figures rounded to integers)
Z_{GSM} (R_E)
Y_{GSM} (R_E)

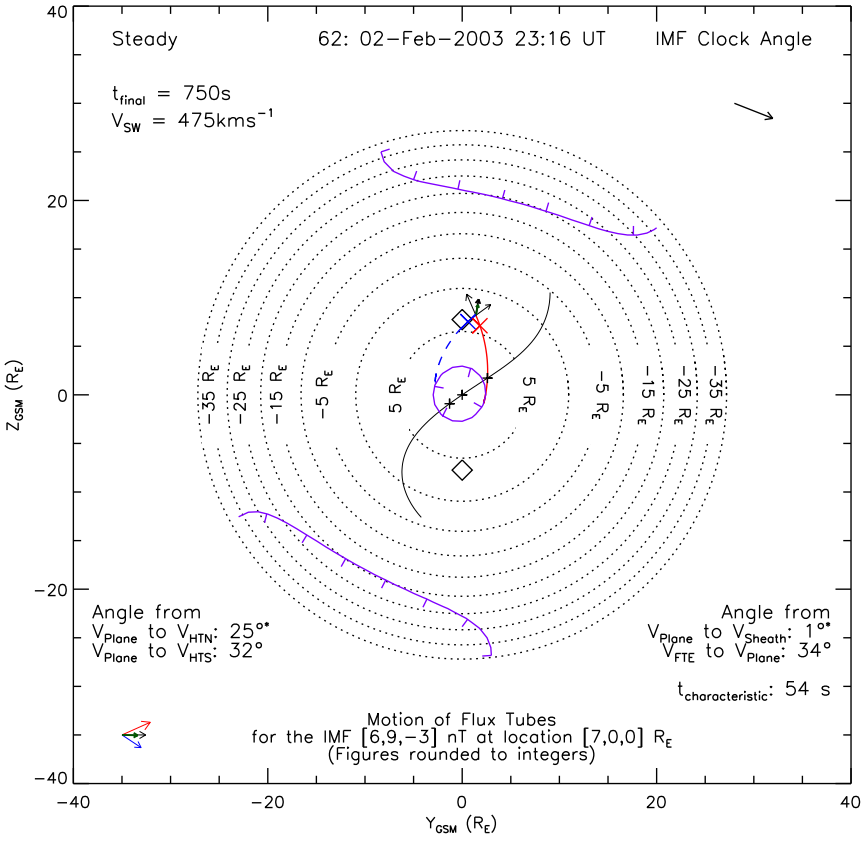
Steady
62: 02−Feb−2003 23:16 UT
IMF Clock Angle
t_{final} = 750s
V_{SW} = 475kms^{-1}
Angle from
V_{Plane} to V_{HTN}: 25°
V_{Plane} to V_{HTS}: 32°
Angle from
V_{Plane} to V_{Sheath}: 1°
V_{FTE} to V_{Plane}: 34°
$t_{characteristic}$: 54 s
Motion of Flux Tubes
for the IMF [6,9,−3] nT at location [7,0,0] R_E
(Figures rounded to integers)
Z_{GSM} (R_E)
Y_{GSM} (R_E)

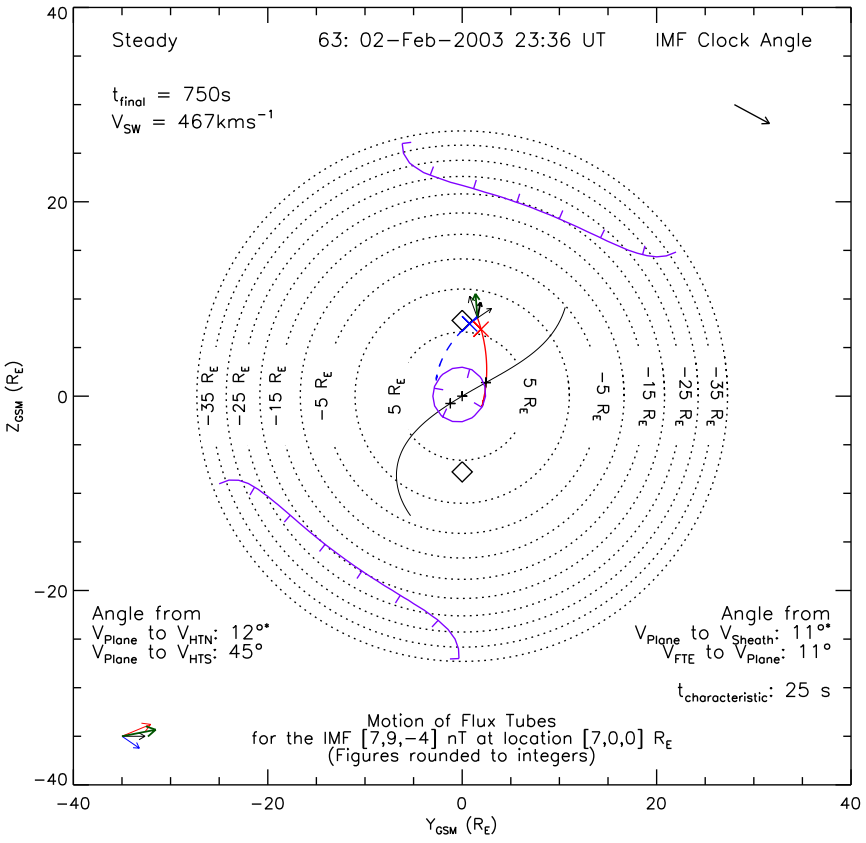
Steady
63: 02–Feb–2003 23:36 UT
IMF Clock Angle
t_{final} = 750s
V_{SW} = 467kms^{-1}
Angle from
V_{Plane} to V_{HTN}: 12°
V_{Plane} to V_{HTS}: 45°
Angle from
V_{Plane} to V_{Sheath}: 11°
V_{FTE} to V_{Plane}: 11°
$t_{characteristic}$: 25 s
Motion of Flux Tubes
for the IMF [7,9,−4] nT at location [7,0,0] R_E
(Figures rounded to integers)
Z_{GSM} (R_E)
Y_{GSM} (R_E)

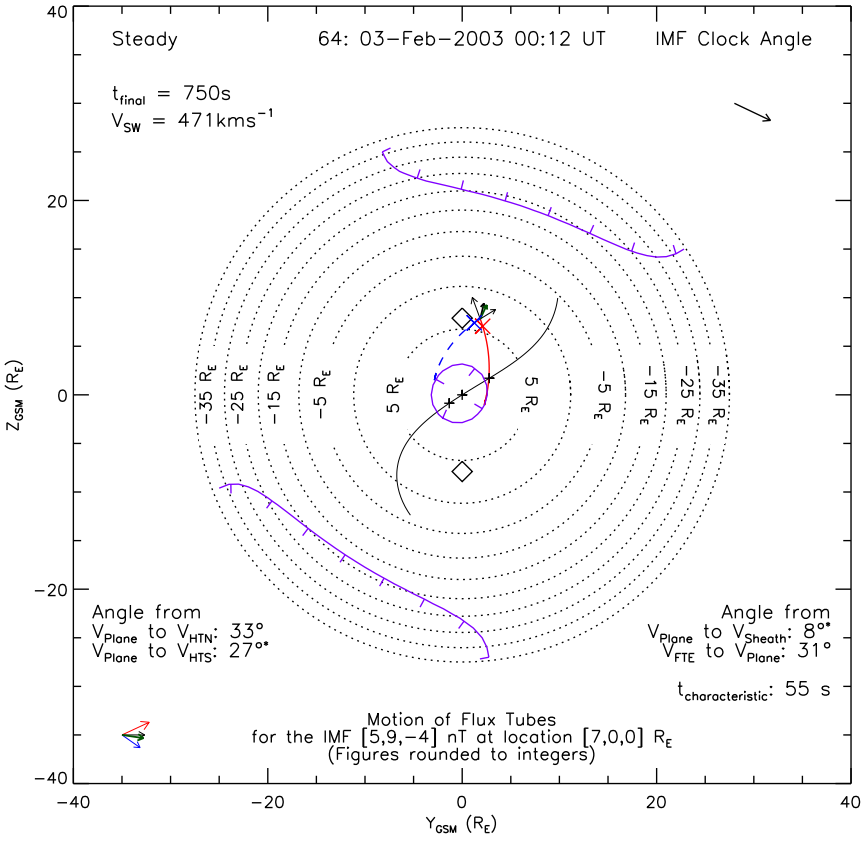
Steady
64: 03–Feb–2003 00:12 UT
IMF Clock Angle
t_{final} = 750s
V_{SW} = 471kms^{-1}
Angle from
V_{Plane} to V_{HTN}: 33°
V_{Plane} to V_{HTS}: 27°
Angle from
V_{Plane} to V_{Sheath}: 8°
V_{FTE} to V_{Plane}: 31°
$t_{characteristic}$: 55 s
Motion of Flux Tubes
for the IMF [5,9,−4] nT at location [7,0,0] R_E
(Figures rounded to integers)
Z_{GSM} (R_E)
Y_{GSM} (R_E)

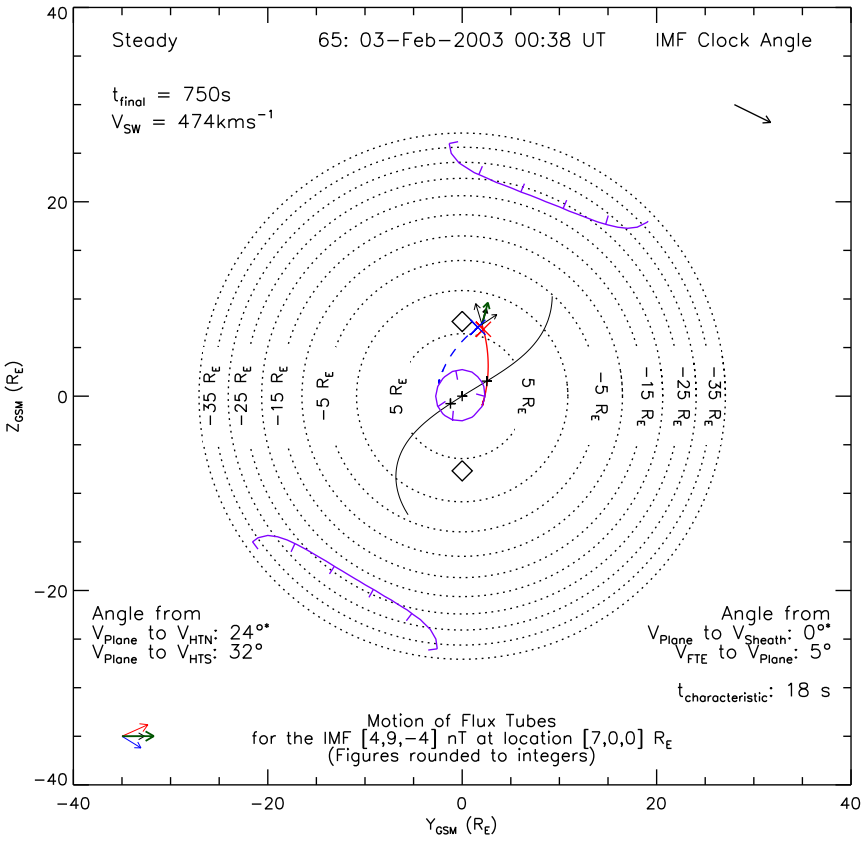
Steady
65: 03–Feb–2003 00:38 UT
IMF Clock Angle
t_{final} = 750s
V_{SW} = 474kms^{-1}
Angle from
V_{Plane} to V_{HTN}: 24°
V_{Plane} to V_{HTS}: 32°
Angle from
V_{Plane} to V_{Sheath}: 0°
V_{FTE} to V_{Plane}: 5°
$t_{characteristic}$: 18 s
Motion of Flux Tubes
for the IMF [4,9,−4] nT at location [7,0,0] R_E
(Figures rounded to integers)
Z_{GSM} (R_E)
Y_{GSM} (R_E)

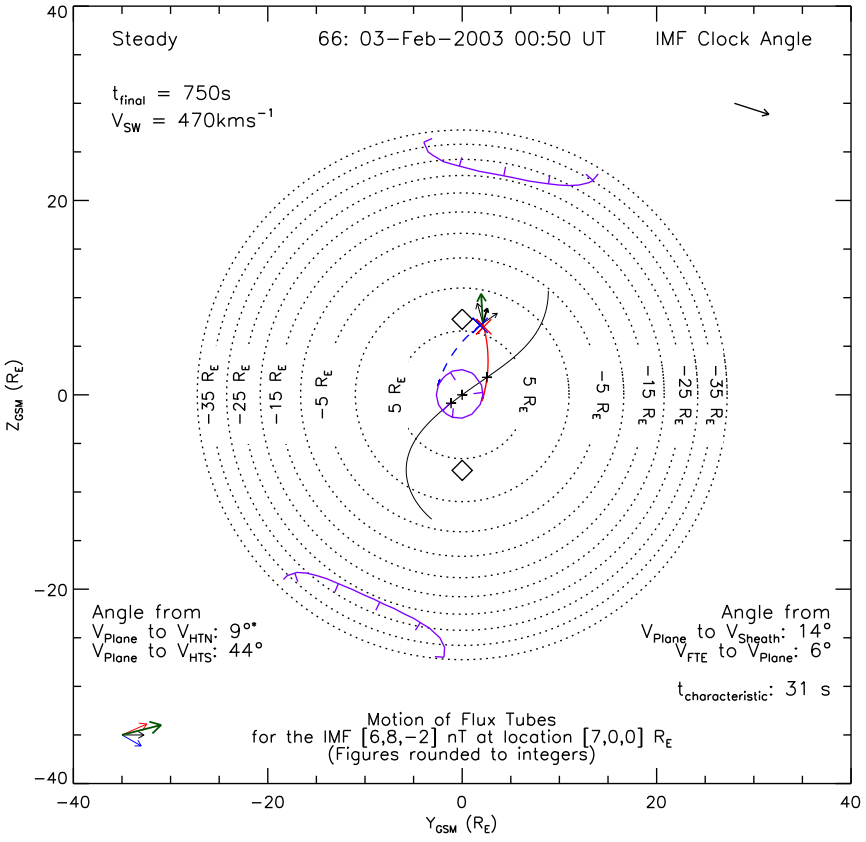
Steady
66: 03–Feb–2003 00:50 UT
IMF Clock Angle
t_{final} = 750s
V_{SW} = 470kms^{-1}
Angle from
V_{Plane} to V_{HTN}: 9°
V_{Plane} to V_{HTS}: 44°
Angle from
V_{Plane} to V_{Sheath}: 14°
V_{FTE} to V_{Plane}: 6°
$t_{characteristic}$: 31 s
Motion of Flux Tubes
for the IMF [6,8,−2] nT at location [7,0,0] R_E
(Figures rounded to integers)
Z_{GSM} (R_E)
Y_{GSM} (R_E)

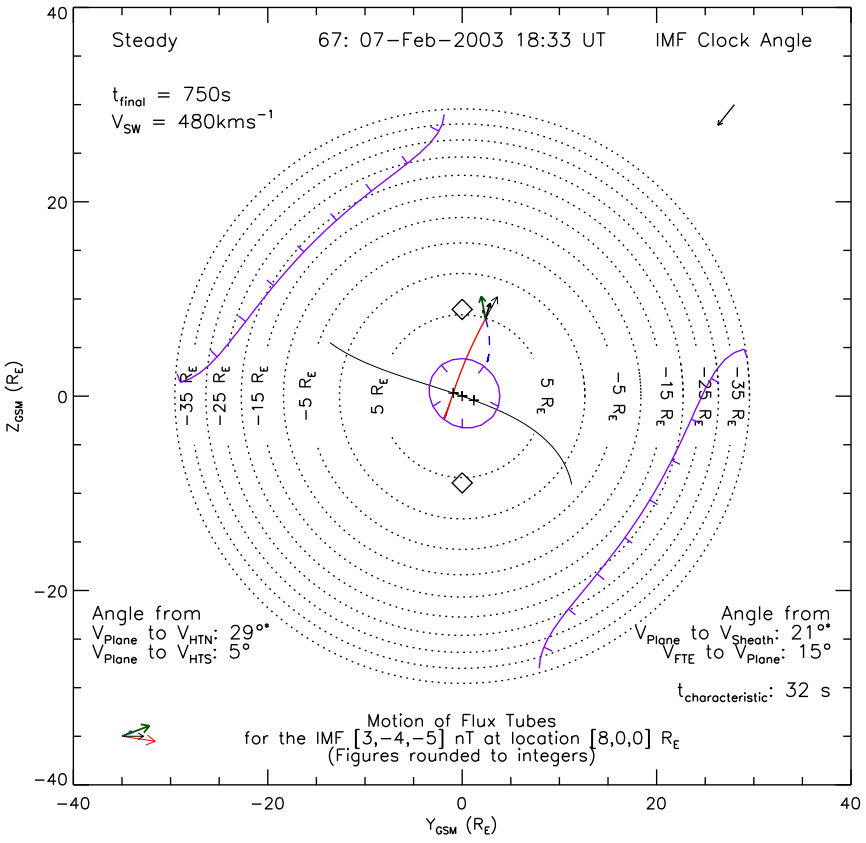
Steady
67: 07−Feb−2003 18:33 UT
IMF Clock Angle
t_{final} = 750s
V_{SW} = 480kms^{-1}
Angle from
V_{Plane} to V_{HTN}: 29°
V_{Plane} to V_{HTS}: 5°
Angle from
V_{Plane} to V_{Sheath}: 21°
V_{FTE} to V_{Plane}: 15°
$t_{characteristic}$: 32 s
Motion of Flux Tubes
for the IMF [3,−4,−5] nT at location [8,0,0] R_E
(Figures rounded to integers)
Z_{GSM} (R_E)
Y_{GSM} (R_E)

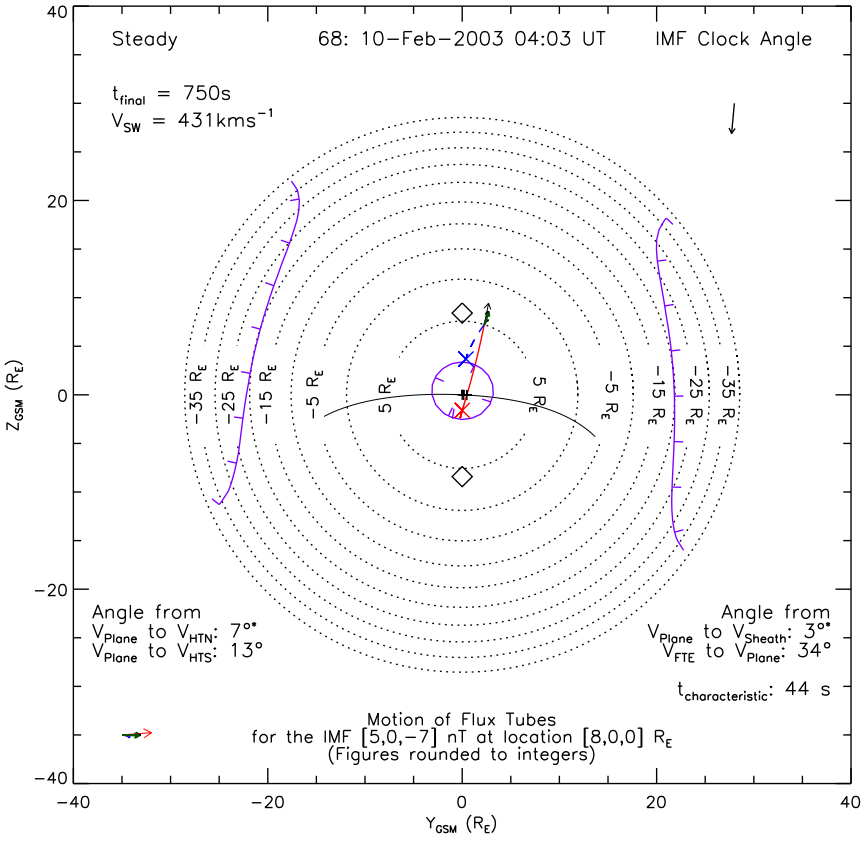
Steady
68: 10−Feb−2003 04:03 UT
IMF Clock Angle
t_{final} = 750s
V_{SW} = 431kms^{-1}
Angle from
V_{Plane} to V_{HTN}: 7°
V_{Plane} to V_{HTS}: 13°
Angle from
V_{Plane} to V_{Sheath}: 3°
V_{FTE} to V_{Plane}: 34°
$t_{characteristic}$: 44 s
Motion of Flux Tubes
for the IMF [5,0,−7] nT at location [8,0,0] R_E
(Figures rounded to integers)
Z_{GSM} (R_E)
Y_{GSM} (R_E)

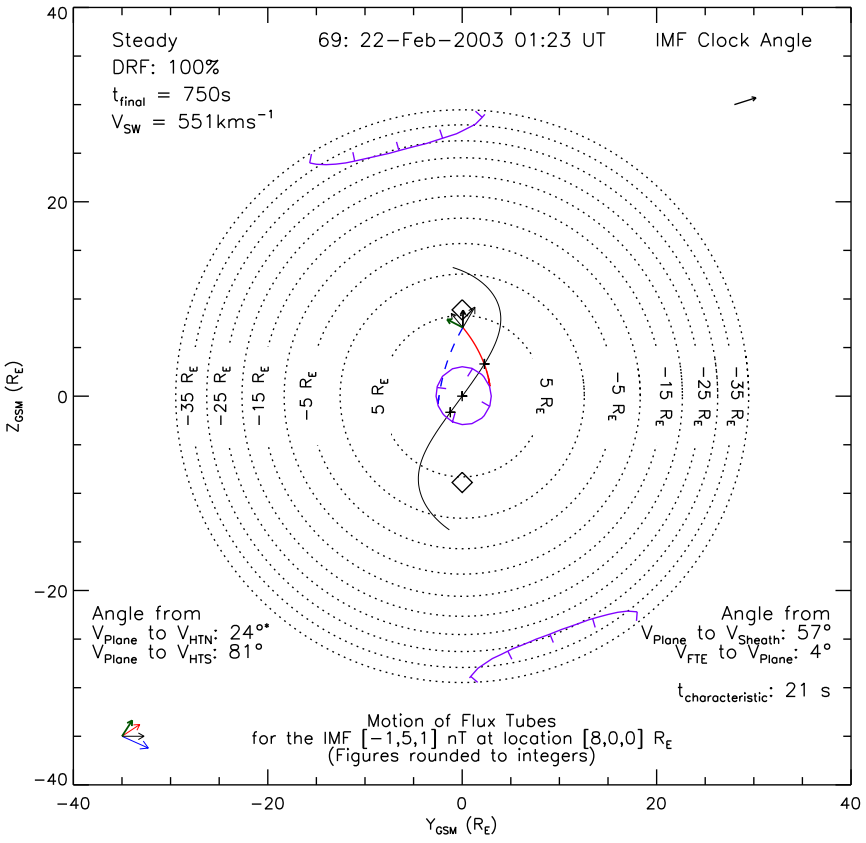
Steady
69: 22−Feb−2003 01:23 UT
IMF Clock Angle
DRF: 100%
t_{final} = 750s
V_{SW} = 551kms^{-1}
Angle from
V_{Plane} to V_{HTN}: 24°
V_{Plane} to V_{HTS}: 81°
Angle from
V_{Plane} to V_{Sheath}: 57°
V_{FTE} to V_{Plane}: 4°
$t_{characteristic}$: 21 s
Motion of Flux Tubes
for the IMF [−1,5,1] nT at location [8,0,0] R_E
(Figures rounded to integers)
Z_{GSM} (R_E)
Y_{GSM} (R_E)

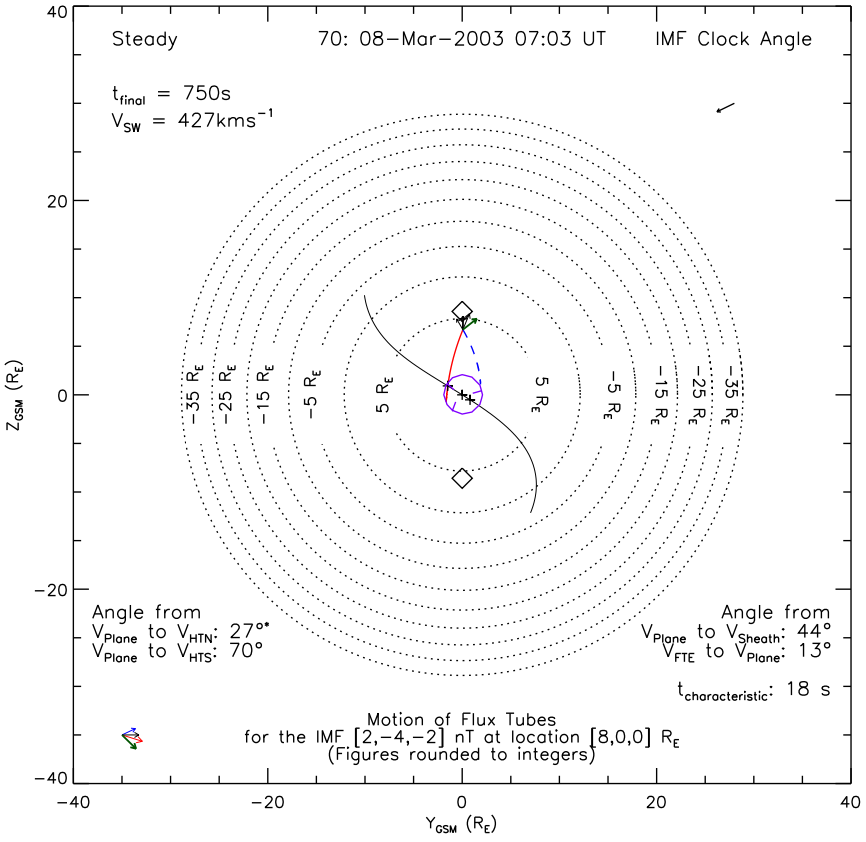
Steady
70: 08−Mar−2003 07:03 UT
IMF Clock Angle
t_{final} = 750s
V_{SW} = 427kms^{-1}
Angle from
V_{Plane} to V_{HTN}: 27°
V_{Plane} to V_{HTS}: 70°
Angle from
V_{Plane} to V_{Sheath}: 44°
V_{FTE} to V_{Plane}: 13°
$t_{characteristic}$: 18 s
Motion of Flux Tubes
for the IMF [2,−4,−2] nT at location [8,0,0] R_E
(Figures rounded to integers)
Z_{GSM} (R_E)
Y_{GSM} (R_E)

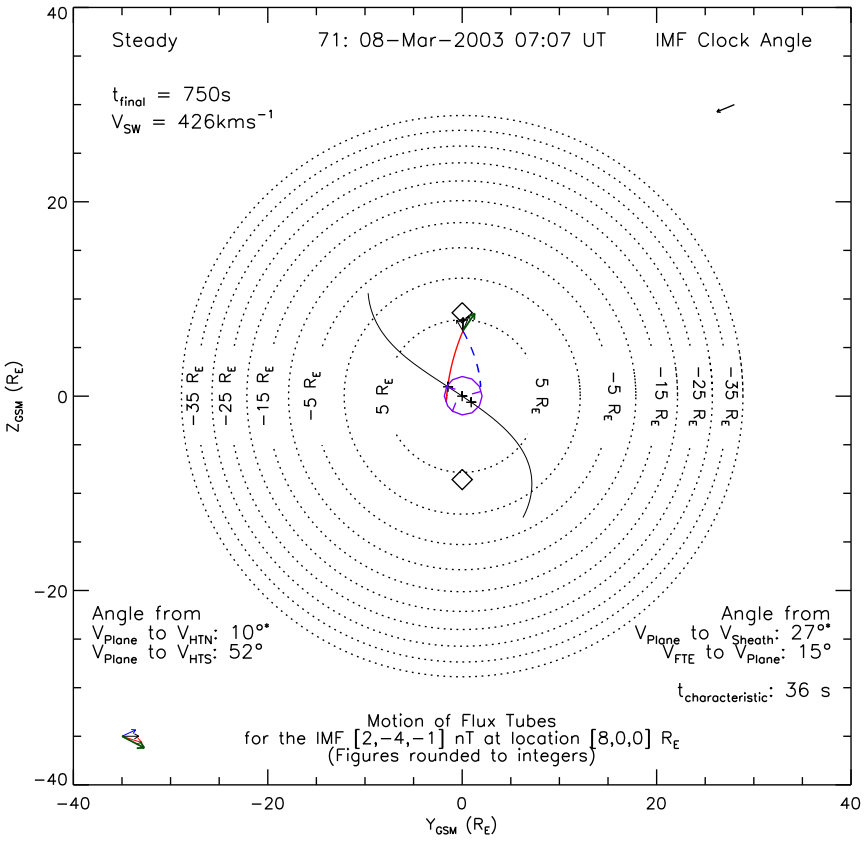
Steady
71: 08–Mar–2003 07:07 UT
IMF Clock Angle
t_{final} = 750s
V_{SW} = 426kms^{-1}
Angle from
V_{Plane} to V_{HTN}: 10°
V_{Plane} to V_{HTS}: 52°
Angle from
V_{Plane} to V_{Sheath}: 27°
V_{FTE} to V_{Plane}: 15°
$t_{characteristic}$: 36 s
Motion of Flux Tubes
for the IMF [2,−4,−1] nT at location [8,0,0] R_E
(Figures rounded to integers)
Z_{GSM} (R_E)
Y_{GSM} (R_E)

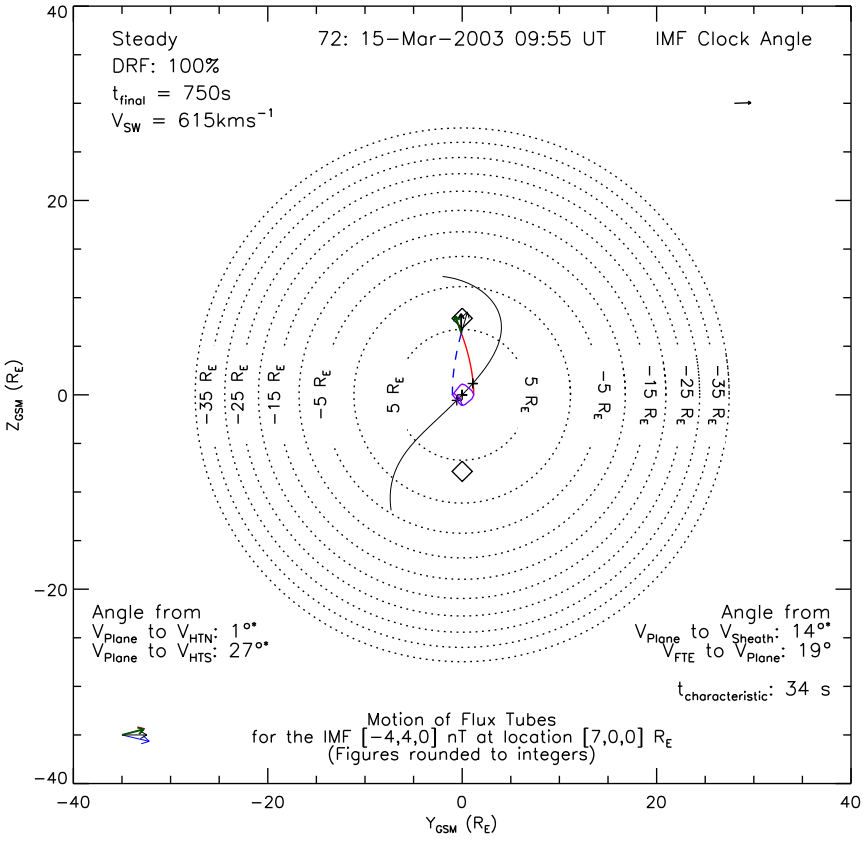
Steady
72: 15–Mar–2003 09:55 UT
IMF Clock Angle
DRF: 100%
t_{final} = 750s
V_{SW} = 615kms^{-1}
Angle from
V_{Plane} to V_{HTN}: 1°
V_{Plane} to V_{HTS}: 27°
Angle from
V_{Plane} to V_{Sheath}: 14°
V_{FTE} to V_{Plane}: 19°
$t_{characteristic}$: 34 s
Motion of Flux Tubes
for the IMF [−4,4,0] nT at location [7,0,0] R_E
(Figures rounded to integers)
Z_{GSM} (R_E)
Y_{GSM} (R_E)

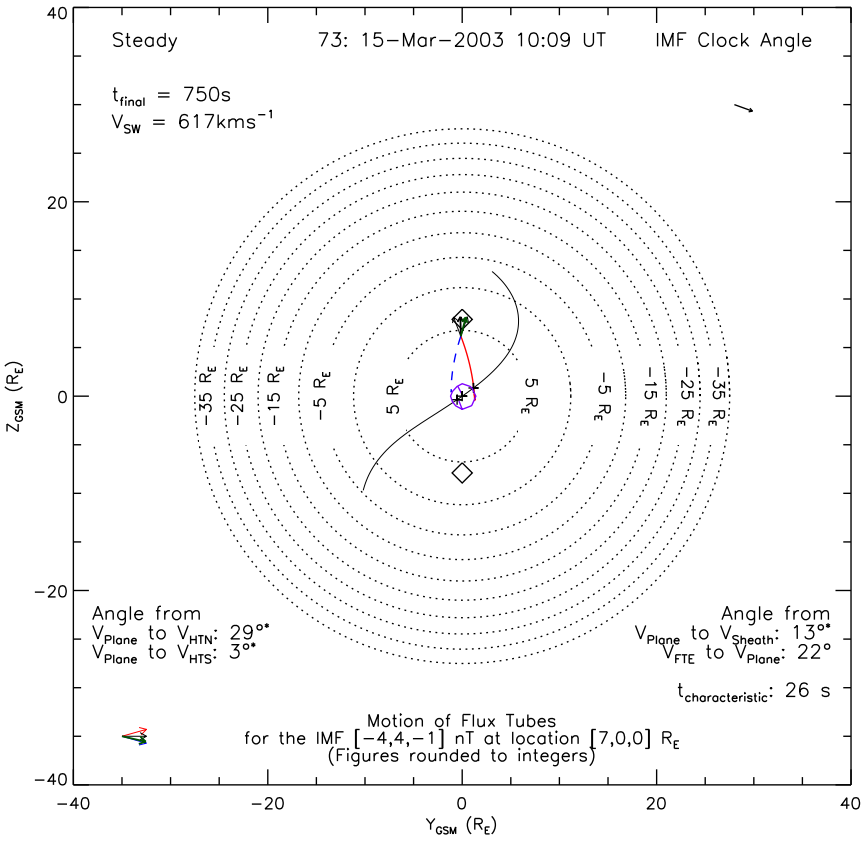
Steady
73: 15−Mar−2003 10:09 UT
IMF Clock Angle
t_{final} = 750s
V_{SW} = 617kms^{-1}
Angle from
V_{Plane} to V_{HTN}: 29°
V_{Plane} to V_{HTS}: 3°
Angle from
V_{Plane} to V_{Sheath}: 13°
V_{FTE} to V_{Plane}: 22°
$t_{characteristic}$: 26 s
Motion of Flux Tubes
for the IMF [−4,4,−1] nT at location [7,0,0] R_E
(Figures rounded to integers)
Z_{GSM} (R_E)
Y_{GSM} (R_E)

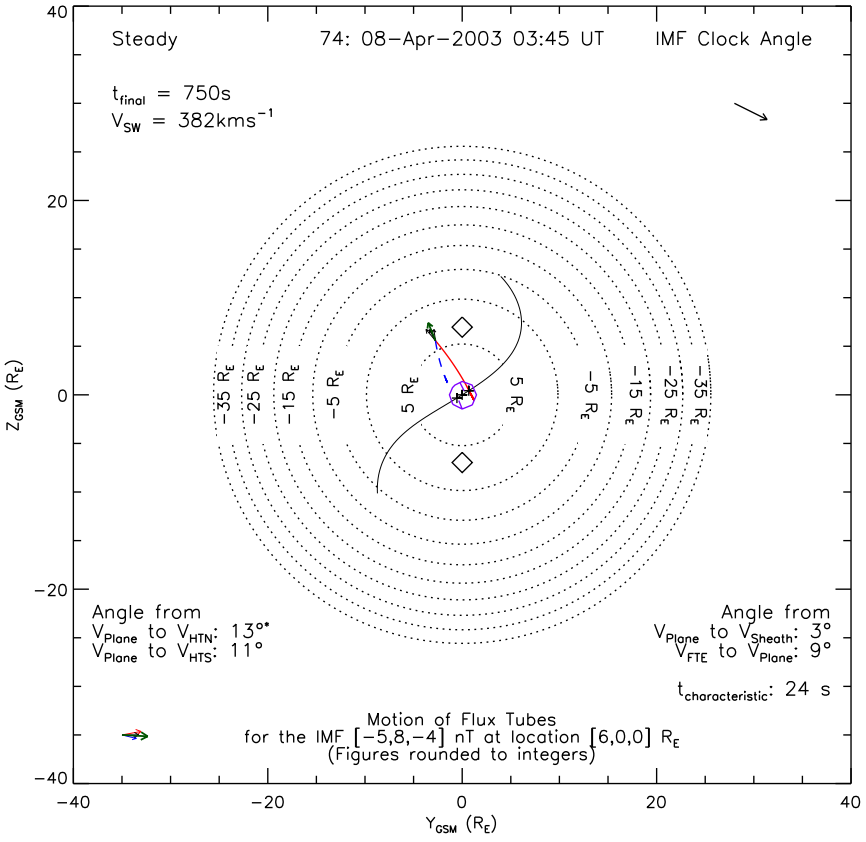
Steady
74: 08−Apr−2003 03:45 UT
IMF Clock Angle
t_{final} = 750s
V_{SW} = 382kms^{-1}
Angle from
V_{Plane} to V_{HTN}: 13°
V_{Plane} to V_{HTS}: 11°
Angle from
V_{Plane} to V_{Sheath}: 3°
V_{FTE} to V_{Plane}: 9°
$t_{characteristic}$: 24 s
Motion of Flux Tubes
for the IMF [−5,8,−4] nT at location [6,0,0] R_E
(Figures rounded to integers)
Z_{GSM} (R_E)
Y_{GSM} (R_E)

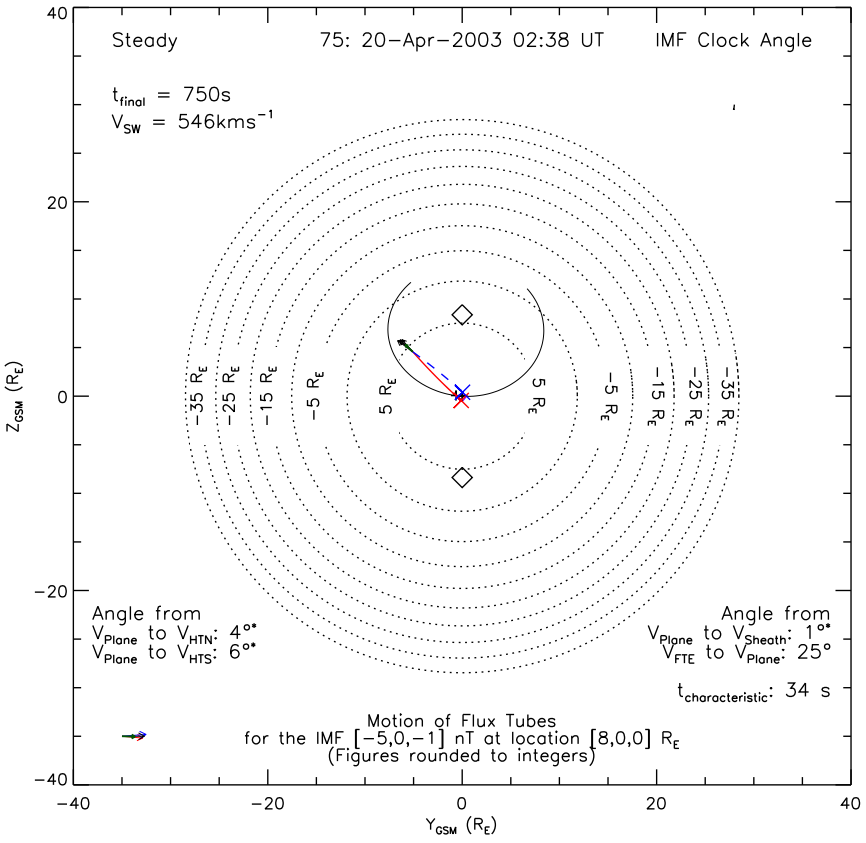
Steady
75: 20−Apr−2003 02:38 UT
IMF Clock Angle
t_{final} = 750s
V_{SW} = 546kms^{-1}
Angle from
V_{Plane} to V_{HTN}: 4°
V_{Plane} to V_{HTS}: 6°
Angle from
V_{Plane} to V_{Sheath}: 1°
V_{FTE} to V_{Plane}: 25°
$t_{characteristic}$: 34 s
Motion of Flux Tubes
for the IMF [−5,0,−1] nT at location [8,0,0] R_E
(Figures rounded to integers)
Z_{GSM} (R_E)
Y_{GSM} (R_E)

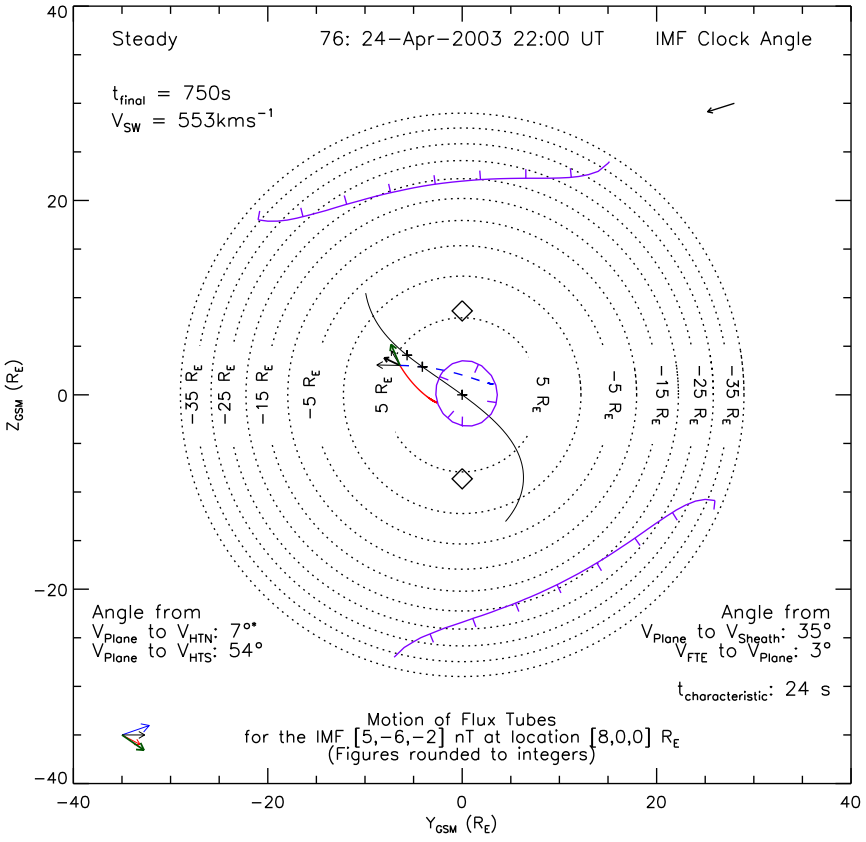
Steady
76: 24−Apr−2003 22:00 UT
IMF Clock Angle
t_{final} = 750s
V_{SW} = 553kms^{-1}
Angle from
V_{Plane} to V_{HTN}: 7°
V_{Plane} to V_{HTS}: 54°
Angle from
V_{Plane} to V_{Sheath}: 35°
V_{FTE} to V_{Plane}: 3°
$t_{characteristic}$: 24 s
Motion of Flux Tubes
for the IMF [5,−6,−2] nT at location [8,0,0] R_E
(Figures rounded to integers)
Z_{GSM} (R_E)
Y_{GSM} (R_E)

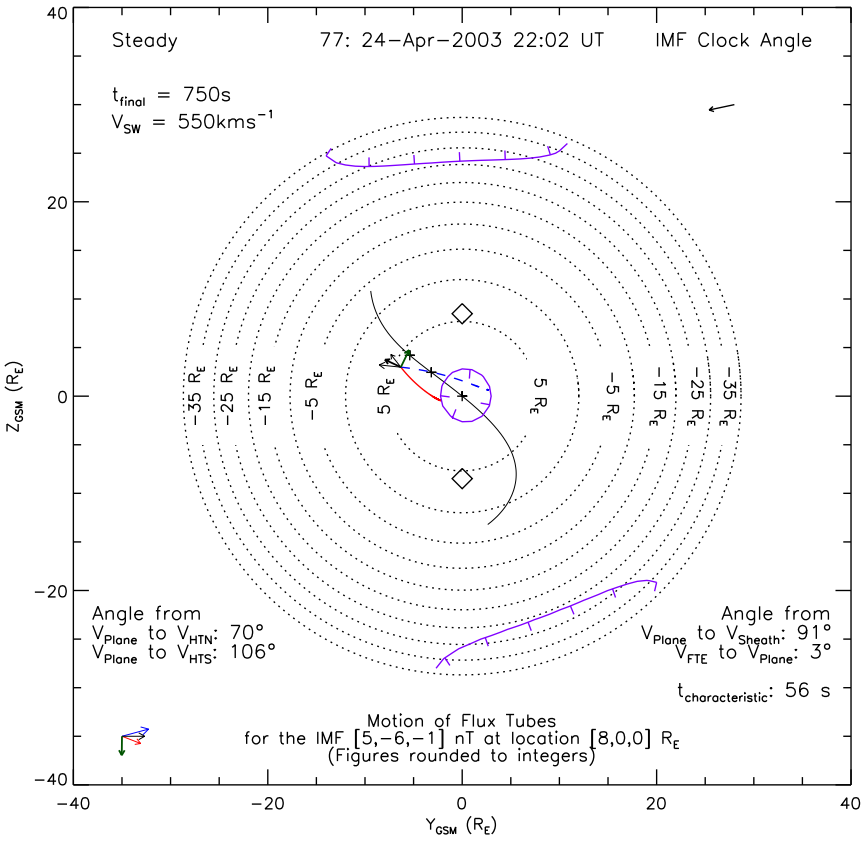
Steady
77: 24−Apr−2003 22:02 UT
IMF Clock Angle
t_{final} = 750s
V_{SW} = 550kms^{-1}
−35 R_E
−25 R_E
−15 R_E
−5 R_E
5 R_E
5 R_E
−5 R_E
−15 R_E
−25 R_E
−35 R_E
Angle from
V_{Plane} to V_{HTN}: 70°
V_{Plane} to V_{HTS}: 106°
Angle from
V_{Plane} to V_{Sheath}: 91°
V_{FTE} to V_{Plane}: 3°
$t_{characteristic}$: 56 s
Motion of Flux Tubes
for the IMF [5,−6,−1] nT at location [8,0,0] R_E
(Figures rounded to integers)
40
20
0
−20
−40
Z_{GSM} (R_E)
−40
−20
0
20
40
Y_{GSM} (R_E)

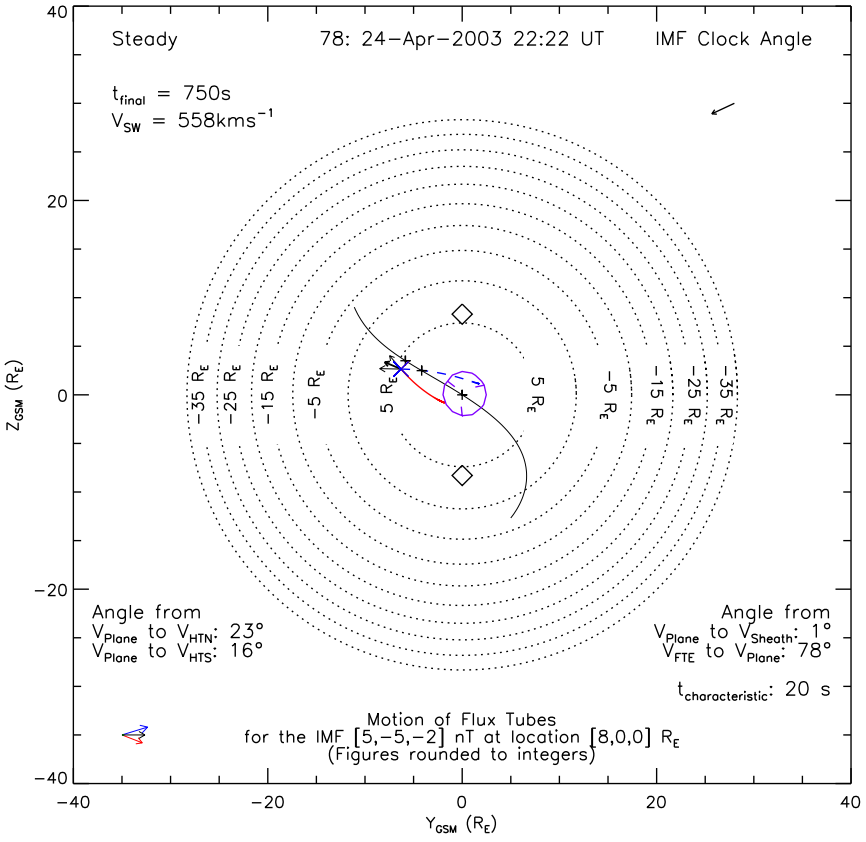
Steady
78: 24−Apr−2003 22:22 UT
IMF Clock Angle
t_{final} = 750s
V_{SW} = 558kms^{-1}
−35 R_E
−25 R_E
−15 R_E
−5 R_E
5 R_E
5 R_E
−5 R_E
−15 R_E
−25 R_E
−35 R_E
Angle from
V_{Plane} to V_{HTN}: 23°
V_{Plane} to V_{HTS}: 16°
Angle from
V_{Plane} to V_{Sheath}: 1°
V_{FTE} to V_{Plane}: 78°
$t_{characteristic}$: 20 s
Motion of Flux Tubes
for the IMF [5,−5,−2] nT at location [8,0,0] R_E
(Figures rounded to integers)
40
20
0
−20
−40
Z_{GSM} (R_E)
−40
−20
0
20
40
Y_{GSM} (R_E)

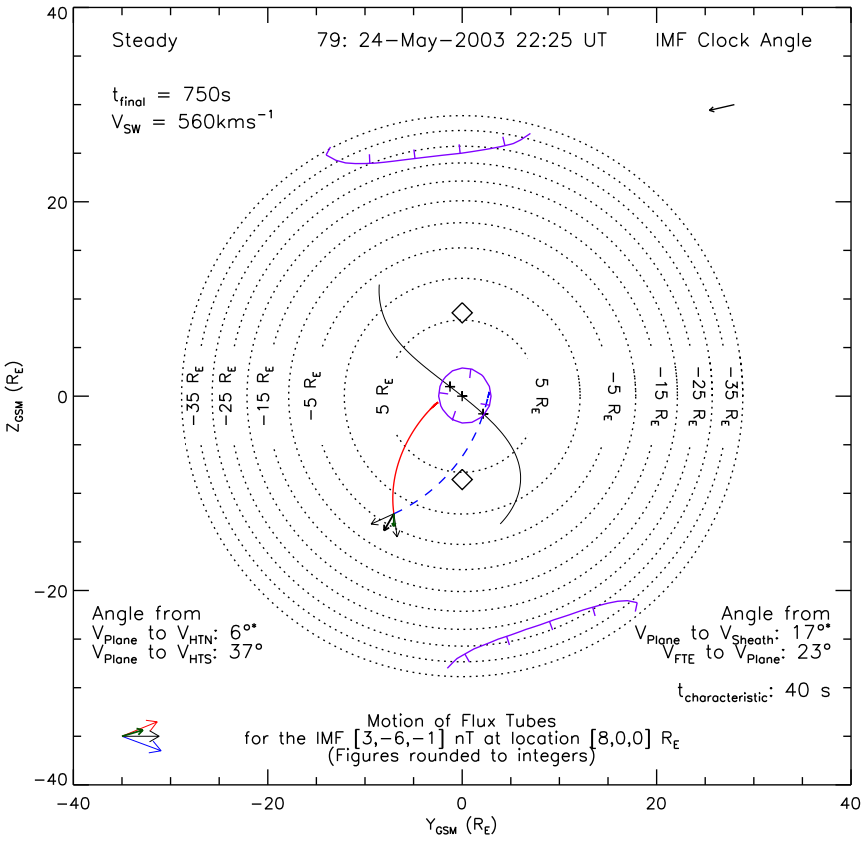
Steady
79: 24−May−2003 22:25 UT
IMF Clock Angle
t_{final} = 750s
V_{SW} = 560kms^{-1}
−35 R_E
−25 R_E
−15 R_E
−5 R_E
5 R_E
5 R_E
−5 R_E
−15 R_E
−25 R_E
−35 R_E
Angle from
V_{Plane} to V_{HTN}: 6°
V_{Plane} to V_{HTS}: 37°
Angle from
V_{Plane} to V_{Sheath}: 17°
V_{FTE} to V_{Plane}: 23°
$t_{characteristic}$: 40 s
Motion of Flux Tubes
for the IMF [3,−6,−1] nT at location [8,0,0] R_E
(Figures rounded to integers)
Z_{GSM} (R_E)
Y_{GSM} (R_E)
40
20
0
−20
−40

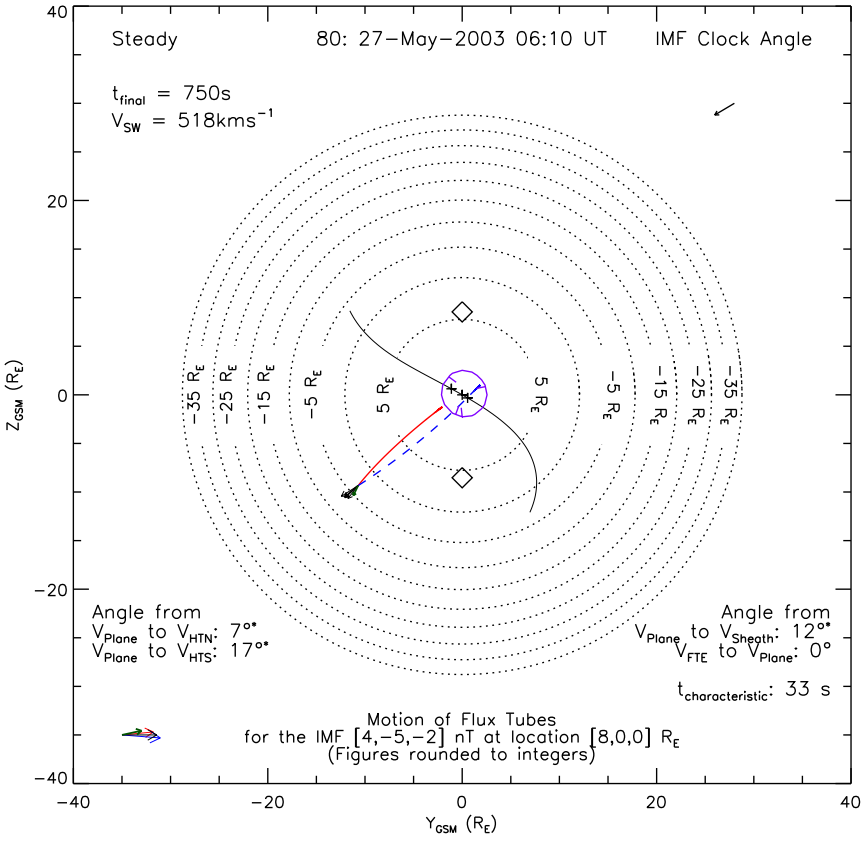
Steady
80: 27−May−2003 06:10 UT
IMF Clock Angle
t_{final} = 750s
V_{SW} = 518kms^{-1}
−35 R_E
−25 R_E
−15 R_E
−5 R_E
5 R_E
5 R_E
−5 R_E
−15 R_E
−25 R_E
−35 R_E
Angle from
V_{Plane} to V_{HTN}: 7°
V_{Plane} to V_{HTS}: 17°
Angle from
V_{Plane} to V_{Sheath}: 12°
V_{FTE} to V_{Plane}: 0°
$t_{characteristic}$: 33 s
Motion of Flux Tubes
for the IMF [4,−5,−2] nT at location [8,0,0] R_E
(Figures rounded to integers)
Z_{GSM} (R_E)
Y_{GSM} (R_E)
40
20
0
−20
−40

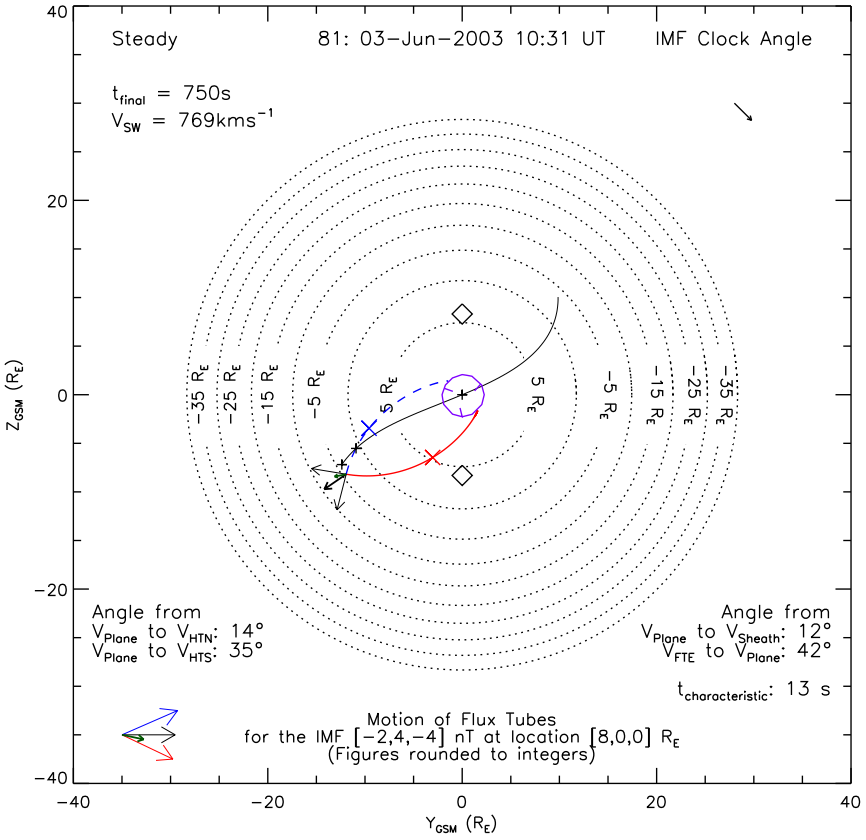
Steady
81: 03–Jun–2003 10:31 UT
IMF Clock Angle
t_{final} = 750s
V_{SW} = 769kms^{-1}
−35 R_E
−25 R_E
−15 R_E
−5 R_E
5 R_E
Angle from
V_{Plane} to V_{HTN}: 14°
V_{Plane} to V_{HTS}: 35°
Angle from
V_{Plane} to V_{Sheath}: 12°
V_{FTE} to V_{Plane}: 42°
$t_{characteristic}$: 13 s
Motion of Flux Tubes
for the IMF [−2,4,−4] nT at location [8,0,0] R_E
(Figures rounded to integers)
Z_{GSM} (R_E)
Y_{GSM} (R_E)
40
20
0
−20
−40

List of Abbreviations

Abbreviation	Details
AMPTE	Active Magnetospheric Particle Tracer Explorer
ASPOC	Active Spacecraft Potential Control
AU	Astronomical Unit (1.5×10^{11} m)
CCE	AMPTE Charge Composition Explorer
CIS	Cluster Ion Spectrometry experiment
CODIF	Composition and Distribution Function analyser
DPU	Data Processing Unit
EFW	Electric Fields and Waves experiment
FE	Fixed Energy
FGM	Fluxgate Magnetometer
GOES	Geostationary Operational Environmental Satellite
HAR	High Angular Resolution
HEEA	High Energy Electron Analyser
HEOS	Highly Eccentric Orbiting Satellite
HIA	Hot Ion Analyser
ICE	International Cometary Explorer
IEL	Inter-Experiment Link
IRM	AMPTE Ion Release Module
ISEE	International Sun-Earth Explorer
MAR	Medium Angular Resolution
MCP	Micro Channel Plate
MHD	Magnetohydrodynamic(s)
MSA	Micro Structure Analyser
LAR	Low Angular Resolution
LEEA	Low Energy Electron Analyser
PEACE	Plasma Electron and Current Experiment
R_E	Earth radius/radii (6378 km)
τ	Magnetopause transition parameter
t_{char}	FTE 'characteristic time'
UKS	AMPTE UK Sub-satellite

References

Axford, W. I. and Hines, C. O.: A unifying theory of high-latitude geophysical phenomena and geomagnetic storms, *Canadian Journal of Physics*, **39**, 1433, 1961.

Balogh, A., Dunlop, M. W., Cowley, S. W. H., Southwood, D. J., Thomlinson, J. G., Glassmeier, K. H., Musmann, G., Luhr, H., Buchert, S., Acuna, M. H., Fairfield, D. H., Slavin, J. A., Riedler, W., Schwingenschuh, K., and Kivelson, M. G.: The Cluster Magnetic Field Investigation, *Space Sci. Rev.*, **79**, 65–91, 1997.

Balogh, A., Carr, C. M., Acuña, M. H., Dunlop, M. W., Beek, T. J., Brown, P., Fornaçon, K.-H., Georgescu, E., Glassmeier, K.-H., Harris, J., Musmann, G., Oddy, T., and Schwingenschuh, K.: The Cluster Magnetic Field Investigation: Overview of in-flight performance and initial results, *Ann. Geophysicae*, **19**, 1207–1217, 2001.

Baumjohann, W. and Treumann, R. A.: Basic Space Plasma Physics, Imperial College Press, London, 1997.

Berchem, J. and Russell, C. T.: Flux transfer events on the magnetopause - spatial distribution and controlling factors, *J. Geophys. Res.*, **89**, 6689–6703, 1984.

Biermann, L.: Kometschweife und solare Korpuskularstrahlung, *Z. Astrophys.*, **29**, 274, 1951.

Birkeland, K. B.: The Norwegian Aurora Polaris Expedition, 1902-1903, H. Aschehoug & Co., Christiana, 1909.

Birkeland, K. O. B.: Are the Solar Corpuscular Rays that penetrate into the Earth's Atmosphere Negative or Positive Rays?, *Videnskapsselskapets Skrifter*, 1916.

Bosqued, J. M., Phan, T. D., Dandouras, I., Escoubet, C. P., Rème, H., Balogh, A., Dunlop, M. W., Alcaydé, D., Amata, E., Bavassano-Cattaneo, M. B., Bruno, R., Carlson, C., DiLellis, A. M., Eliasson, L., Formisano, V., Kistler, L. M., Klecker, B., Korth, A., Kucharek, H., Lundin, R., McCarthy, M., McFadden, J. P., Möbius, E., Parks, G. K., and Sauvaud, J. A.: Cluster observations of the

high-latitude magnetopause and cusp: Initial results from the CIS ion instruments, *Ann. Geophysicae*, **19**, 1545–1566, 2001.

Bowe, G. A., Hapgood, M. A., Lockwood, M., and Willis, D. M.: Short-term variability of solar-wind number density, speed and dynamic pressure as a function of the interplanetary magnetic field components - a survey over two solar cycles, *Geophys. Res. Lett.*, **17**, 1825–1828, 1990.

Bryant, D. A. and Riggs, S.: At the edge of the Earth's magnetosphere: A survey by AMPTE-UKS, *Phil. Trans. R. Soc. Lond. A.*, **328**, 43–56, 1989.

Chapman, S.: Notes on the Solar Corona and the Terrestrial Ionosphere, *Smithsonian Contributions to Astrophysics*, **2**, 1, 1957.

Chapman, S. and Ferarro, V. C. A.: A new theory of magnetic storms, *Nature*, **126**, 129, 1930.

Chen, F. F.: Introduction to Plasma Physics, Plenum Press, New York, 1974.

Coleman, I. J. and Freeman, M. P.: Fractal reconnection structures on the magnetopause, *Geophys. Res. Lett.*, **32**, L03 115, doi:10.1029/2004GL021779, 2005.

Coleman, I. J., Chisham, G., Pinnock, M., and Freeman, M. P.: An ionospheric convection signature of antiparallel reconnection, *J. Geophys. Res.*, **106**, 28 995–29 008, doi:10.1029/2001JA900084, 2001.

Cooling, B. M. A., Owen, C. J., and Schwartz, S. J.: Role of the magnetosheath flow in determining the motion of open flux tubes, *J. Geophys. Res.*, **106**, 18 763–18 776, 2001.

Cowley, S. W. H.: Comments on the merging of nonantiparallel magnetic fields, *J. Geophys. Res.*, **81**, 3455–3458, 1976.

Cowley, S. W. H.: A Beginner's Guide to the Earth's Magnetosphere, *Earth in Space*, **8**, 9, 1996.

Cowley, S. W. H. and Owen, C. J.: A simple illustrative model of open flux tube motion over the dayside magnetopause, *Planet. Space Sci.*, **37**, 1461–1475, 1989.

Cowley, S. W. H., Davies, J. A., Grocott, A., Khan, H., Lester, M., McWilliams, K. A., Milan, S. E., Provan, G., Sandholt, P. E., Wild, J. A., and Yeoman, T. K.: Solar-wind-magnetosphere-ionosphere interactions in the Earth's plasma environment, *Philos. Trans. R. Soc. London, Ser. A*, **361**, 113–126, 2003.

Crooker, N. U.: Dayside merging and cusp geometry, *J. Geophys. Res.*, **84**, 951–959, 1979.

Crooker, N. U.: Reverse convection, *J. Geophys. Res.*, **97**, 19 363–19 372, 1992.

Daly, P. W., Williams, D. J., Russell, C. T., and Keppler, E.: Particle signature of magnetic flux transfer events at the magnetopause, *J. Geophys. Res.*, **86**, 1628–1632, 1981.

Daly, P. W., Rijnbeek, R. P., Sckopke, N., Russell, C. T., and Saunders, M. A.: The distribution of reconnection geometry in flux transfer events using energetic ion, plasma and magnetic data, *J. Geophys. Res.*, **89**, 3843–3854, 1984.

Dungey, J. W.: Interplanetary magnetic field and the auroral zones, *Phys. Rev. Lett.*, **6**, 48–49, 1961.

Dungey, J. W.: The structure of the exosphere or adventures in velocity space, in The Earth's Environment, edited by C. DeWitt, J. Hieblot, and A. Lebeau, pp. 505–550, Gordon and Breach, New York, 1963.

Dungey, J. W.: The length of the geomagnetic tail, *J. Geophys. Res.*, **70**, 1753, 1965.

Dunlop, M. W., Balogh, A., Glassmeier, K.-H., and Robert, P.: Four-point Cluster application of magnetic field analysis tools: The Curlometer, *J. Geophys. Res.*, **107**, 1384, doi:10.1029/2001JA005088, 2002.

Einstein, A.: Über einen die Erzeugung und Verwandlung des Lichtes betreffenden heuristischen Gesichtspunkt, *Annalen der Physik*, **322**, 132–148, 1905.

Elphic, R. C.: Observations of flux transfer events: Are FTEs flux ropes, islands, or surface waves?, in Physics of Magnetic Flux Ropes, edited by C. T. Russell, E. R. Priest, and L. C. Lee, vol. 58 of *Geophysical Monograph*, pp. 455–471, AGU, Washington D. C., 1990.

Elphic, R. C.: Observations of flux transfer events: A review, in Physics of the Magnetopause, edited by P. Song, B. U. Ö. Sonnerup, and M. F. Thomsen, vol. 90 of *Geophysical Monograph*, pp. 225–233, AGU, Washington D. C., 1995.

Elphic, R. C., Baumjohann, W., Cattell, C. A., Lühr, H., and Smith, M. F.: A search for upstream pressure pulses associated with flux transfer events: An AMPTE/ISEE case study, *J. Geophys. Res.*, **99**, 13 521–13 527, 1994.

Escoubet, C. P., Fehringer, M., and Goldstein, M.: The Cluster mission, *Ann. Geophysicae*, **19**, 1197 – 1200, 2001.

Fairfield, D. H. and Cahill, L. J.: Transition Region Magnetic Field and Polar Magnetic Disturbances, *J. Geophys. Res.*, **71**, 155, 1966.

Fairfield, D. H., Baumjohann, W., Paschmann, G., Lühr, H., and Sibeck, D. G.: Upstream pressure variations associated with the bow shock and their effects on the magnetosphere, *J. Geophys. Res.*, **95**, 3773–3786, 1990.

Farrugia, C. J., Elphic, R. C., Southwood, D. J., and Cowley, S. W. H.: Field and flow perturbations outside the reconnected field line region in flux transfer events: Theory, *Planet. Space Sci.*, **35**, 227–240, 1987a.

Farrugia, C. J., Southwood, D. J., Cowley, S. W. H., Rijnbeek, R. P., and Daly, P. W.: Two-regime flux transfer events, *Planet. Space Sci.*, **35**, 737–744, 1987b.

Farrugia, C. J., Rijnbeek, R. P., Saunders, M. A., Southwood, D. J., Rodgers, D. J., Smith, M. F., Chaloner, C. P., Hall, D. S., Christiansen, P. J., and Woolliscroft, L. J. C.: A multi-instrument study of flux transfer event structure, *J. Geophys. Res.*, **93**, 14 465–14 477, 1988.

Fear, R. C., Fazakerley, A. N., Owen, C. J., Lahiff, A. D., Lucek, E. A., Balogh, A., Kistler, L. M., Mouikis, C., and Rème, H.: Cluster observations of boundary layer structure and a flux transfer event near the cusp, *Ann. Geophysicae*, **23**, 2605–2620, SRef-ID:1432-0576/ag/2005-23-2605, 2005a.

Fear, R. C., Fazakerley, A. N., Owen, C. J., and Lucek, E. A.: A survey of flux transfer events observed by Cluster during strongly northward IMF, *Geophys. Res. Lett.*, **32**, L18 105, doi:10.1029/2005GL023811, 2005b.

Freeman, M. P., Farrugia, C. J., Burlaga, L. F., Hairston, M. R., Greenspan, M. E., Ruohoniemi, J. M., and Lepping, R. P.: The interaction of a magnetic cloud with the Earth: Ionospheric convection in the northern and southern hemispheres for a wide range of quasi-steady interplanetary magnetic field conditions, *J. Geophys. Res.*, **98**, 7633–7655, 1993.

Gonzalez, W. D. and Mozer, F. S.: A quantitative model for the potential resulting from reconnection with an arbitrary interplanetary magnetic field, *J. Geophys. Res.*, **79**, 4186–4194, 1974.

Gosling, J. T., Thomsen, M. F., Bame, S. J., Elphic, R. C., and Russell, C. T.: Observations of reconnection of interplanetary and lobe magnetic field lines at the high-latitude magnetopause, *J. Geophys. Res.*, **96**, 14 097–14 106, 1991.

Gowen, R. A. and Birdseye, M. A.: Extracting Bulk Parameters of a Particle Distribution, Tech. rep., Mullard Space Science Laboratory, University College London, 1988.

Gringauz, K. L., Bezrukikh, V. V., Ozerov, V. D., and Rybchinskiy, R.: A Study of the Interplanetary Ionized Gas, High-Energy Electrons, and Corpuscular Radia-

tion from the Sun by Means of the Three-Electrode Trap for Charged Particles on the Second Cosmic Rocket, *Doklady Akad. Nauk SSSR*, **131**, 1301, 1960.

Gustafsson, G., André, M., Carozzi, T., Eriksson, A. I., Fälthammar, C.-G., Grard, R., Holmgren, G., Holtet, J. A., Ivchenko, N., Karlsson, T., Khotyaintsev, Y., Klimov, S., Laakso, H., Lindqvist, P.-A., Lybekk, B., Marklund, G., Mozer, F., Mursula, K., Pedersen, A., Popielawska, B., Savin, S., Stasiewicz, K., Tanskanen, P., Vaivads, A., and Wahlund, J.-E.: First results of electric field and density observations by Cluster EFW based on initial months of operation, *Ann. Geophysicae*, **19**, 1219–1240, 2001.

Haerendel, G., Paschmann, G., Sckopke, N., Rosenbauer, H., and Hedgecock, P. C.: The frontside boundary layer of the magnetosphere and the problem of reconnection, *J. Geophys. Res.*, **83**, 3195–3216, 1978.

Hapgood, M. A. and Bryant, D. A.: Re-ordered electron data in the low-latitude boundary layer, *Geophys. Res. Lett.*, **17**, 2043–2046, 1990.

Hapgood, M. A. and Bryant, D. A.: Exploring the magnetospheric boundary layer, *Planet. Space Sci.*, **40**, 1431–1459, 1992.

Hapgood, M. A. and Lockwood, M.: Rapid changes in LLBL thickness, *Geophys. Res. Lett.*, **22**, 77–80, 1995.

Harvey, C. C.: Spatial gradients and the volumetric tensor, in Analysis Methods for Multi-Spacecraft Data, edited by G. Paschmann and P. W. Daly, pp. 307–348, ISSI, 1998.

Heikkila, W. J.: Impulsive plasma transport through the magnetosphere, *Geophys. Res. Lett.*, **9**, 159–162, 1982.

Hertz, H.: Über einen Einfluss des ultravioletten Lichtes auf die electrische Entladung, *Annalen der Physik*, **267**, 983–1000, 1887.

Hill, T. W.: Magnetic merging in a collisionless plasma, *J. Geophys. Res.*, **80**, 4689–4699, 1975.

de Hoffmann, F. and Teller, E.: Magneto-hydrodynamic shocks, *Phys. Rev.*, **80**, 692, 1950.

Holzer, T. E. and Reid, G. C.: The response of the day side magnetosphere-ionosphere system to time-varying field line reconnection at the magnetosphere. I - Theoretical method., *J. Geophys. Res.*, **80**, 2041–2049, 1975.

Johnstone, A. D., Alsop, C., Burdge, S., Carter, P. J., Coates, A. J., Coker, A. J., Fazakerley, A. N., Grande, M., Gowen, R. A., Gurgiolo, C., Hancock, B. K.,

Narheim, B., Preece, A., Sheather, P. H., Winningham, J. D., and Woodliffe, R. D.: PEACE: A Plasma Electron And Current Experiment, *Space Sci. Rev.*, **79**, 351–398, 1997.

Kawano, H. and Russell, C. T.: Survey of flux transfer events observed with the ISEE 1 spacecraft: Rotational polarity and the source region, *J. Geophys. Res.*, **101**, 27,299–27,308, 1996.

Kawano, H. and Russell, C. T.: Survey of flux transfer events observed with the ISEE 1 spacecraft: Dependence on the interplanetary magnetic field, *J. Geophys. Res.*, **102**, 11 307–11 314, doi:10.1029/97JA00481, 1997a.

Kawano, H. and Russell, C. T.: Cause of postterminator flux transfer events, *J. Geophys. Res.*, **102**, 27 029–27 038, doi:10.1029/97JA02139, 1997b.

Kawano, H. and Russell, C. T.: Dual-satellite observations of the motions of flux transfer events: Statistical analysis with ISEE 1 and ISEE 2, *J. Geophys. Res.*, **110**, A07217, doi:10.1029/2004JA010821, 2005.

Kawano, H., Kokubun, S., and Takahashi, K.: Survey of transient magnetic field events in the dayside magnetosphere, *J. Geophys. Res.*, **97**, 10 677–10 692, 1992.

Kerr, R. A.: Voyager 1 Crosses a New Frontier and May Save Itself From Termination, *Science*, **308**, 1237–1238, doi:10.1126/science.308.5726.1237a, 2005.

Kivelson, M. G. and Russell, C. T., eds.: Introduction to Space Physics, Cambridge University Press, Cambridge, 1995.

Kobel, E. and Flückiger, E. O.: A model of the steady state magnetic field in the magnetosheath, *J. Geophys. Res.*, **99**, 23 617–23 622, 1994.

Krimigis, S. M., Decker, R. B., Hill, M. E., Armstrong, T. P., Gloeckler, G., Hamilton, D. C., Lanzerotti, L. J., and Roelof, E. C.: Voyager 1 exited the solar wind at a distance of ∼85AU from the Sun, *Nature*, **426**, 45–48, 2003.

Kuo, H., Russell, C. T., and Le, G.: Statistical studies of flux transfer events, *J. Geophys. Res.*, **100**, 3513–3519, 1995.

Lanzerotti, L. J.: Comment on "Solar wind dynamic pressure variations and transient magnetospheric signatures", *Geophys. Res. Lett.*, **16**, 1197–1199, 1989.

Lee, L. C. and Fu, Z. F.: A theory of magnetic flux transfer at the Earth's magnetopause, *Geophys. Res. Lett.*, **12**, 105–108, 1985.

Lee, L. C., Shi, Y., and Lanzerotti, L. J.: A mechanism for the generation of cusp region hydromagnetic waves, *J. Geophys. Res.*, **93**, 7578–7585, 1988.

Lemaire, J. and Roth, M.: Penetration of solar wind plasma elements into the magnetosphere, *J. Atmos. Terr. Phys.*, **40**, 331–335, 1978.

Lemaire, J., Rycroft, M. J., and Roth, M.: Control of impulsive plasma penetration of solar wind irregularities into the magnetosphere by the interplanetary magnetic field, *Planet. Space Sci.*, **27**, 47–57, 1979.

Lockwood, M.: Flux transfer events at the dayside magnetopause: Transient reconnection or magnetosheath dynamic pressure pulses?, *J. Geophys. Res.*, **96**, 5497–5509, 1991.

Lockwood, M. and Hapgood, M. A.: How the magnetopause transition parameter works, *Geophys. Res. Lett.*, **24**, 373–376, 1997.

Lockwood, M. and Hapgood, M. A.: On the cause of a magnetospheric flux transfer event, *J. Geophys. Res.*, **103**, 26 453–26 478, 1998.

Lockwood, M. and Moen, J.: Reconfiguration and closure of lobe flux by reconnection during northward IMF: Possible evidence for signatures in cusp/cleft auroral emissions, *Ann. Geophysicae*, **17**, 996–1011, 1999.

Lockwood, M. and Wild, M. N.: On the quasi-periodic nature of magnetopause flux transfer events, *J. Geophys. Res.*, **98**, 5935–5940, 1993.

Lockwood, M., Fazakerley, A. N., Opgenoorth, H., Moen, J., van Eyken, A. P., Dunlop, M., Bosqued, J. M., Lu, G., Cully, C., Eglitis, P., McCrea, I. W., Hapgood, M. A., Wild, M. N., Stamper, R., Denig, W., Taylor, M., Wild, J. A., Provan, G., Amm, O., Kauristie, K., Pulkkinen, T., Strømme, A., Prikryl, P., Pitout, F., Balogh, A., Rème, H., Behlke, R., Hansen, T., Greenwald, R., Frey, H., Morley, S. K., Alcaydé, D., Blelly, P. L., Donova, E., Engebretson, M., Lester, M., Watermann, J., and Marcucci, M. F.: Coordinated Cluster and ground-based instrument observations of transient changes in the magnetopause boundary layer during an interval of predominantly northward IMF: Relation to reconnection pulses and FTE signatures, *Ann. Geophysicae*, **19**, 1613–1640, 2001.

Longmore, M. M.: Multi-Spacecraft Observations of Earth's Bow Shock and a Survey of the Dayside Magnetosheath, Ph.D. thesis, Queen Mary, University of London, 2005.

Lundin, R., Sauvaud, J. A., Rème, H., Balogh, A., Dandouras, I., Bosqued, J. M., Carlson, C., Parks, G. K., Möbius, E., Kistler, L. M., Klecker, B., Amata, E., Formisano, V., Dunlop, M., Eliasson, L., Korth, A., Lavraud, B., and McCarthy, M.: Evidence for impulsive solar wind plasma penetration through the dayside magnetopause, *Ann. Geophysicae*, **21**, 457–472, 2003.

Marchaudon, A.: Étude Multi-Instrumentale de la Dynamique des Structures Aurorales Côté Jour et Côté Nuit: Couplage avec la Magnétosphère et le Milieu Interplanétaire, Ph.D. thesis, L'Université de Versailles-Saint-Quentin, 2003.

Marchaudon, A., Cerisier, J., Bosqued, J., Dunlop, M., Wild, J., Décréau, P., Förster, M., Fontaine, D., and Laakso, H.: Transient plasma injections in the dayside magnetosphere: One-to-one correlated observations by Cluster and SuperDARN, *Ann. Geophysicae*, **22**, 141–158, 2004.

Marchaudon, A., Owen, C. J., Bosqued, J.-M., Fear, R. C., Fazakerley, A. N., Dunlop, M. W., Lahiff, A. D., Carr, C., Balogh, A., Lindqvist, P.-A., and Rème, H.: Simultaneous Double Star and Cluster FTEs observations on the dawnside flank of the magnetosphere, *Ann. Geophysicae*, **23**, 2877–2888, SRef-ID:1432-0576/ag/2005-23-2877, 2005.

Maxwell, J. C.: A Treatise on Electricity and Magnetism, New York, Dover, Third edn., 2 vols., reprint (1954), 1891.

McComas, D. J., Bame, S. J., Barker, P., Feldman, W. C., Phillips, J. L., Riley, P., and Griffee, J. W.: Solar Wind Electron Proton Alpha Monitor (SWEPAM) for the Advanced Composition Explorer, *Space Sci. Rev.*, **86**, 563–612, 1998.

McDonald, F. B., Stone, E. C., Cummings, A. C., Heikkila, B., Lal, N., and Webber, W. R.: Enhancements of energetic particles near the heliospheric termination shock, *Nature*, **426**, 48–51, 2003.

Newell, P. T., Sibeck, D. G., and Meng, C.-I.: Penetration of the interplanetary magnetic field B_Y and magnetosheath plasma into the magnetosphere: Implications for the predominant magnetopause merging site, *J. Geophys. Res.*, **100**, 235–243, 1995.

Nishida, A.: Can random reconnection on the magnetopause produce the low latitude boundary layer?, *Geophys. Res. Lett.*, **16**, 227–230, 1989.

Owen, C. J. and Cowley, S. W. H.: Heikkila's mechanism for impulsive plasma transport through the magnetosphere: A re-examination, *J. Geophys. Res.*, **96**, 5565–5574, 1991.

Owen, C. J., Fazakerley, A. N., Carter, P. J., Coates, A. J., Krauklis, I. C., Szita, S., Taylor, M. G. G. T., Travnicek, P., Watson, G., Wilson, R. J., Balogh, A., and Dunlop, M. W.: Cluster PEACE observations of electrons during magnetospheric flux transfer events, *Ann. Geophysicae*, **19**, 1509–1522, 2001.

Parker, E. N.: Dynamics of the interplanetary gas and magnetic fields, *Astrophys. J.*, **128**, 664–676, 1958.

Parker, E. N.: The Solar-Flare Phenomenon and the Theory of Reconnection and Annihiliation of Magnetic Fields., *Ap. J. S.*, **8**, 177–211, 1963.

Paschmann, G., Sonnerup, B. U. Ö., Papamastorakis, I., Sckopke, N., Haerendel, G., Bame, S. J., Asbridge, J. R., Gosling, J. T., Russell, C. T., and Elphic, R. C.: Plasma acceleration at the Earth's magnetopause: Evidence for reconnection, *Nature*, **282**, 243–246, 1979.

Paschmann, G., Haerendel, G., Papamastorakis, I., Sckopke, N., Bame, S. J., Gosling, J. T., and Russell, C. T.: Plasma and magnetic field characteristics of magnetic flux transfer events, *J. Geophys. Res.*, **87**, 2159–2168, 1982.

Petrinec, S. M. and Fuselier, S. A.: On continuous versus discontinuous neutral lines at the dayside magnetopause for southward interplanetary magnetic field, *Geophys. Res. Lett.*, **30**, 26–1, doi:10.1029/2002GL016565, 2003.

Petschek, H. E.: Magnetic Field Annihilation, in The Physics of Solar Flares, pp. 425–439, 1964.

Phan, T.-D., Paschmann, G., Baumjohann, W., Sckopke, N., and Lühr, H.: The magnetosheath region adjacent to the dayside magnetopause: AMPTE/IRM observations, *J. Geophys. Res.*, **99**, 121–141, 1994.

Phillips, J. L., Bame, S. J., Feldman, W. C., Goldstein, B. E., Gosling, J. T., Hammond, C. M., McComas, D. J., Neugebauer, M., Scime, E. E., and Suess, S. T.: Ulysses Solar Wind Plasma Observations at High Southerly Latitudes, *Science*, **268**, 1030–1033, 1995.

Pudovkin, M. I. and Semenov, V. S.: Stationary frozen-in co-ordinate system, *Annales de Geophysique*, **33**, 429–433, 1977.

Rème, H., Aoustin, C., Bosqued, J. M., Dandouras, I., Lavraud, B., Sauvaud, J. A., Barthe, A., Bouyssou, J., Camus, T., Coeur-Joly, O., Cros, A., Cuvilo, J., Ducay, F., Garbarowitz, Y., Medale, J. L., Penou, E., Perrier, H., Romefort, D., Rouzaud, J., Vallat, C., Alcaydé, D., Jacquey, C., Mazelle, C., D'Uston, C., Möbius, E., Kistler, L. M., Crocker, K., Granoff, M., Mouikis, C., Popecki, M., Vosbury, M., Klecker, B., Hovestadt, D., Kucharek, H., Kuenneth, E., Paschmann, G., Scholer, M., Sckopke, N., Seidenschwang, E., Carlson, C. W., Curtis, D. W., Ingraham, C., Lin, R. P., McFadden, J. P., Parks, G. K., Phan, T., Formisano, V., Amata, E., Bavassano-Cattaneo, M. B., Baldetti, P., Bruno, R., Chionchio, G., di Lellis, A., Marcucci, M. F., Pallocchia, G., Korth, A., Daly, P. W., Graeve, B., Rosenbauer, H., Vasyliunas, V., McCarthy, M., Wilber, M., Eliasson, L., Lundin, R., Olsen, S., Shelley, E. G., Fuselier, S., Ghielmetti, A. G., Lennartsson, W., Escoubet, C. P., Balsiger, H., Friedel, R., Cao, J.-B., Kovrazhkin, R. A., Papamastorakis, I., Pellat,

R., Scudder, J., and Sonnerup, B.: First multispacecraft ion measurements in and near the Earth's magnetosphere with the identical Cluster Ion Spectrometry (CIS) experiment, *Ann. Geophysicae*, **19**, 1303–1354, 2001.

Rijnbeek, R. P. and Cowley, S. W. H.: Magnetospheric flux erosion events are flux transfer events, *Nature*, **309**, 135–138, 1984.

Rijnbeek, R. P., Cowley, S. W. H., Southwood, D. J., and Russell, C. T.: Observations of reverse polarity flux transfer events at the Earth's magnetopause, *Nature*, **300**, 23–26, 1982.

Rijnbeek, R. P., Cowley, S. W. H., Southwood, D. J., and Russell, C. T.: A survey of dayside flux transfer events observed by ISEE-1 and ISEE-2 magnetometers, *J. Geophys. Res.*, **89**, 786–800, 1984.

Rijnbeek, R. P., Farrugia, C. J., Southwood, D. J., Dunlop, M. W., Mier-Jedrzejowicz, W. A. C., Chaloner, C. P., Hall, D. S., and Smith, M. F.: A magnetic boundary signature within flux transfer events, *Planet. Space Sci.*, **35**, 871–878, 1987.

Roelof, E. C. and Sibeck, D. G.: Magnetopause shape as a bivariate function of interplanetary magnetic field B_Z and solar wind dynamic pressure, *J. Geophys. Res.*, **98**, 21,421–21,450, 1993.

Russell, C. T. and Elphic, R. C.: Initial ISEE magnetometer results: Magnetopause observations, *Space Sci. Rev.*, **22**, 681–715, 1978.

Russell, C. T. and Elphic, R. C.: ISEE observations of flux transfer events at the dayside magnetopause, *Geophys. Res. Lett.*, **6**, 33–36, 1979.

Russell, C. T. and McPherron, R. L.: The magnetotail and substorms, *Space Sci. Rev.*, **15**, 205–266, 1973.

Russell, C. T. and Walker, R. J.: Flux transfer events at Mercury, *J. Geophys. Res.*, **90**, 11 067–11 074, 1985.

Russell, C. T., Berchem, J., and Luhmann, J. G.: On the source region of flux transfer events, *Adv. Space Res.*, **5**, 363–368, 1985.

Saunders, M. A., Russell, C. T., and Sckopke, N.: Flux transfer events: Scale size and interior structure, *Geophys. Res. Lett.*, **11**, 131–134, 1984.

Scholer, M.: Magnetic flux transfer at the magnetopause based on single X-line bursty reconnection, *Geophys. Res. Lett.*, **15**, 291–294, 1988a.

Scholer, M.: Strong core magnetic fields in magnetopause flux transfer events, *Geophys. Res. Lett.*, **15**, 748–751, 1988b.

Senior, C., Cerisier, J.-C., Rich, F., Lester, M., and Parks, G. K.: Strong sunward propagating flow bursts in the night sector during quiet solar wind conditions: SuperDARN and satellite observations, *Ann. Geophysicae*, **20**, 771–779, 2002.

Sibeck, D. G.: A model for the transient magnetospheric response to sudden solar wind dynamic pressure variations, *J. Geophys. Res.*, **95**, 3755–3771, 1990.

Sibeck, D. G.: Transient events in the outer magnetosphere: Boundary waves or flux transfer events?, *J. Geophys. Res.*, **97**, 4009–4026, 1992.

Sibeck, D. G. and Newell, P. T.: Pressure-pulse driven surface waves at the magnetopause: A rebuttal, *J. Geophys. Res.*, **100**, 21 773–21 778, 1995.

Sibeck, D. G. and Newell, P. T.: Reply, *J. Geophys. Res.*, **101**, 13 351–13 352, 1996.

Sibeck, D. G., Baumjohann, W., Elphic, R. C., Fairfield, D. H., Fennell, J. F., Gail, W. B., Lanzerotti, L. J., Lopez, R. E., Luehr, H., Lui, A. T. Y., MacLennan, C. G., McEntire, R. W., Potemra, T. A., Rosenberg, T. J., and Takahashi, K.: The magnetospheric response to 8-minute period strong-amplitude upstream pressure variations, *J. Geophys. Res.*, **94**, 2505–2519, 1989.

Sibeck, D. G., Lopez, R. E., and Roelof, E. C.: Solar wind control of the magnetopause shape, location, and motion, *J. Geophys. Res.*, **96**, 5489–5495, 1991.

Slavin, J. A., Smith, E. J., Tsurutani, B. T., Sibeck, D. G., Singer, H. J., Baker, D. N., Gosling, J. T., Hones, E. W., and Scarf, F. L.: Substorm associated traveling compression regions in the distant tail - ISEE-3 geotail observations, *Geophys. Res. Lett.*, **11**, 657–660, 1984.

Slavin, J. A., Tanskanen, E. I., Hesse, M., Owen, C. J., Dunlop, M. W., Imber, S., Lucek, E. A., Balogh, A., and Glassmeier, K.-H.: Cluster observations of traveling compression regions in the near-tail, *J. Geophys. Res.*, **110**, A06 207, doi:10.1029/2004JA010878, 2005.

Smith, C. W., L'Heureux, J., Ness, N. F., Acuña, M. H., Burlaga, L. F., and Scheifele, J.: The ACE magnetic fields experiment, *Space Sci. Rev.*, **86**, 613–632, 1998.

Smith, M. F. and Curran, D. B.: On the correlation between a magnetopause penetration parameter and FTE occurrence, *Ann. Geophysicae*, **8**, 579–582, 1990.

Smith, M. F. and Owen, C. J.: Temperature anisotropies in a magnetospheric FTE, *Geophys. Res. Lett.*, **19**, 1907–1910, 1992.

Song, P., Le, G., and Russell, C. T.: Observational differences between flux transfer events and surface waves at the magnetopause, *J. Geophys. Res.*, **99**, 2309–2320, 1994.

Song, P., Le, G., and Russell, C. T.: Comment on "Pressure-pulse driven surface waves at the magnetopause: A rebuttal", *J. Geophys. Res.*, **101**, 13 349–13 350, 1996.

Sonnerup, B. U. O.: Transport mechanisms at the magnetopause, in Dynamics of the Magnetosphere, pp. 77–100, D. Reidel, Dordrecht, 1979.

Sonnerup, B. U. Ö.: On the stress balance in flux transfer events, *J. Geophys. Res.*, **92**, 8613–8620, 1987.

Sonnerup, B. U. O. and Scheible, M.: Minimum and maximum variance analysis, in Analysis Methods for Multi-Spacecraft Data, edited by G. Paschmann and P. W. Daly, pp. 185–220, ISSI, 1998.

Southwood, D. J.: The ionospheric signature of flux transfer events, *J. Geophys. Res.*, **92**, 3207–3213, 1987.

Southwood, D. J., Saunders, M. A., Dunlop, M. W., Mier-Jedrzejowicz, W. A. C., and Rijnbeek, R. P.: A survey of flux transfer events recorded by the UKS spacecraft magnetometer, *Planet. Space Sci.*, **34**, 1349–1359, 1986.

Southwood, D. J., Farrugia, C. J., and Saunders, M. A.: What are flux transfer events?, *Planet. Space Sci.*, **36**, 503–508, 1988.

Stone, E. C.: News from the Edge of Interstellar Space, *Science*, **293**, 55–56, 2001.

Sweet, P. A.: The neutral point theory of solar flares, in Electromagnetic Phenomema in Cosmical Physics, edited by B. Lehnert, pp. 123–134, Cambridge University Press, London, 1958.

Thompson, S. M., Kivelson, M. G., Khurana, K. K., Balogh, A., Rème, H., Fazakerley, A. N., and Kistler, L. M.: Cluster observations of quasi-periodic impulsive signatures in the dayside northern lobe: High-latitude flux transfer events?, *J. Geophys. Res.*, **109**, A02213, doi:10.1029/2003JA010138, 2004.

Torkar, K., Riedler, W., Escoubet, C. P., Fehringer, M., Schmidt, R., Grard, R. J. L., Arends, H., Rüdenauer, F., Steiger, W., Narheim, B. T., Svenes, K., Torbert, R., André, M., Fazakerley, A., Goldstein, R., Olsen, R. C., Pedersen, A., Whipple, E., and Zhao, H.: Active spacecraft potential control for Cluster - implementation and first results, *Ann. Geophysicae*, **19**, 1289–1302, 2001.

Trattner, K. J., Fuselier, S. A., and Petrinec, S. M.: Location of the reconnection line for northward interplanetary magnetic field, *J. Geophys. Res.*, **109**, A03219, doi:10.1029/2003JA009975, 2004.

Trattner, K. J., Fuselier, S. A., and Petrinec, S. M.: Reply to comment by G. A. Abel, M. P. Freeman, and G. Chisham on "Location of the reconnection line for northward interplanetary magnetic field", *J. Geophys. Res.*, **110**, A10209, doi:10.1029/2005JA011131, 2005.

Tsyganenko, N. A.: Modeling the Earth's magnetospheric magnetic field confined within a realistic magnetopause, *J. Geophys. Res.*, **100**, 5599–5612, 1995.

Vallance Jones, A.: Aurora, Reidel, Dordrecht, 1974.

Vasyliunas, V. M.: Theoretical models of magnetic field line merging. I, *Reviews of Geophysics and Space Physics*, **13**, 303–336, 1975.

Vontrat-Reberac, A., Bosqued, J. M., Taylor, M. G. G. T., Lavraud, B., Fontaine, D., Dunlop, M. W., Laakso, H., Cornilleau-Werhin, N., Canu, P., and Fazakerley, A.: Cluster observations of the high-altitude cusp for northward interplanetary magnetic field: A case study, *J. Geophys. Res.*, **108**, 1346, doi:10.1029/2002JA009717, 2003.

Walker, R. J. and Russell, C. T.: Flux transfer events at the Jovian magnetopause, *J. Geophys. Res.*, **90**, 7397–7404, 1985.

Wang, Y. L., Elphic, R. C., Lavraud, B., Taylor, M. G. G. T., Birn, J., Raeder, J., Russell, C. T., and Kawano, H.: The dependence of flux transfer events on geophysical parameters from three years of Cluster observations, *Geophys. Res. Lett.*, in press, 2005.

Wild, J. A., Cowley, S. W. H., Davies, J. A., Khan, H., Lester, M., Milan, S. E., Provan, G., Yeoman, T. K., Balogh, A., Dunlop, M. W., Fornaçon, K.-H., and Georgescu, E.: First simultaneous observations of flux transfer events at the high-latitude magnetopause by the Cluster spacecraft and pulsed radar signatures in the conjugate ionosphere by the CUTLASS and EISCAT radars, *Ann. Geophysicae*, **19**, 1491–1508, 2001.

Wild, J. A., Milan, S. E., Cowley, S. W. H., Bosqued, J. M., Rème, H., Nagai, T., Kokubun, S., Saito, Y., Mukai, T., Davies, J. A., Cooling, B. M. A., Balogh, A., and Daly, P. W.: Simultaneous in-situ observations of the signatures of dayside reconnection at the high- and low-latitude magnetopause, *Ann. Geophysicae*, **23**, 445–460, SRef-ID:1432-0576/ag/2005-23-445, 2005.